NUMERICAL PROCEDURE FOR PREDICTING THE TORSIONAL DYNAMIC RESPONSE OF SOLID MEDIA

by
Robert Henke

A dissertation submitted in partial fulfillment
of the requirements for the degree of
Doctor of Philosophy
(Civil Engineering)
in The University of Michigan
1980

Doctoral Committee:

Professor Frank E. Richart, Jr., Co-Chairman
Professor E. Benjamin Wylie, Co-Chairman
Professor Donald H. Gray
Professor Richard A. Scott
Professor Richard D. Woods

To My Wife,

Wanda,

and Son,

Michael

ACKNOWLEDGEMENTS

The author wishes to express his gratitude to Co-Chairman Prof. F. E. Richart, Jr. for suggesting the topic of this thesis and to Co-Chairman Prof. E. B. Wylie for suggesting to approach analytical work at the most fundamental level. The author is also grateful for the freedom given to him by these Professors in pursuing the investigation. A suitable problem, a point from which to start and freedom in solving the problem are essential to the success of an academic work. Also the continuous suggestions by these Professors throughout the study are appreciated. The author wishes to express his gratitude to Prof. Woods for his ideas concerning equipment, testing set ups and instrumentation. Without these ideas meaningful experiments would have been impossible. The author is also indebted to these Professors and Prof. H. E. Wahls for their significant efforts in presenting specialized courses from which the author developed his interests and which provided the background needed to carry out this study. The author

also wishes to thank Profs. D. H. Gray and R. A. Scott for comments on the writing of the thesis.

Special appreciation is given to Ben Bourland, Don Hutchings, and Lou North for many inventive ideas, for suggestions and especially for guidance in the design and construction of mechanical and electronic equipment.

The author is grateful to Dan Sinnott for assisting him in the setting up and performance of experiments, particularly on Saturdays. The author wishes to thank Rich Ray, Randy Laninga, and Bob Warner for help in the construction of equipment and Peter Bosscher for helpful comments.

Research was carried out under Grants Nos. NSF PFR 77-22219 and ENG. 76-01277 funded by the National Science Foundation. This support is appreciated greatly. The author wishes to thank the Department of Civil Engineering of The University of Michigan for teaching assistantships. In addition, the author is grateful to The University of Michigan for granting him a College of Engineering Fellowship and a Horace H. Rackham Predoctoral Fellowship.

TABLE OF CONTENTS

TABLE OF CONTENTS (Continued)

TABLE OF CONTENTS (Continued)

TABLE OF CONTENTS (Continued)

TABLE OF CONTENTS (Continued)

TABLE OF CONTENTS (Continued)

TABLE OF CONTENTS (Continued)

TABLE OF CONTENTS (Continued)

LIST OF TABLES

LIST OF FIGURES

LIST OF FIGURES (Continued)

LIST OF FIGURES (Continued)

LIST OF FIGURES (Continued)

LIST OF FIGURES (Continued)

LIST OF FIGURES (Continued)

LIST OF FIGURES (Continued)

LIST OF FIGURES (Continued)

LIST OF FIGURES (Continued)

LIST OF FIGURES (Continued)

LIST OF FIGURES (Continued)

LIST OF FIGURES (Continued)

LIST OF FIGURES (Continued)

LIST OF FIGURES (Continued)

LIST OF APPENDICES

NOMENCLATURE

A	point in medium
A_i	area assigned to ith node
A_l	lth arbitrary amplitude constant
$\overline{A}$	unknown multiplier
A'	area of base of disk or footing
$\overline{a}$	arbitrary coefficient
a_1, a_2, a_3, a_4, a_5, a_6, a_7	computed coefficients
B	point in medium
B_i	ith constant coefficient
$\overline{B}$	unknown multiplier
b_n	nth Fourier coefficient
$\overline{b}$	arbitrary coefficient
b_1, b_2, b_3, b_4, b_5, b_6, b_7	computed coefficients
C	point in medium
C^{++}, C^{+-}, C^{-+}, C^{--}	integration paths
C_1	parameter relating τ_y to τ_m ($\tau_y = C_1\tau_m$)
c	parameter defined by Reissner and Sagoci ($c = r_o\bar{\omega}\sqrt{\rho/G}$)
$\overline{c}$	apparent cohesion

c_1, c_2, c_3, c_4, c_5, c_6, c_7	computed coefficients
D	point in medium
$\overline{D}$	unknown multiplier
$\overline{d}$	arbitrary coefficient
d_1, d_2, d_3, d_4, d_5, d_6, d_7	computed coefficients
E_R	energy ratio
e	void ratio
e_1, e_2, e_3, e_4, e_5, e_6, e_7	computed coefficients
F_i	ith external force
F_x, F_y, F_z	forces in x-, y-, and z-direction, respectively
F_1, F_2	infinite series defined by Sagoci
f	frequency, Hz
f(t)	Fourier approximation of function
G	linear elastic shear modulus, psf
G_o	low amplitude shear modulus, psf
G_s	slope of line intersecting origin and point (τ, γ) of τ-stress vs. γ-strain curve obtained from Ramberg-Osgood equations
G_t	tangent modulus obtained from Ramberg-Osgood equations
G_{rt}	tangent modulus for deformations in horizontal planes
G_{zs}	slope of line intersecting origin and point (τ_z, γ_z) of τ_z-stress vs. γ_z-strain curve

G_{zsA}, G_{zsB}, G_{zsC}, G_{zsD}	values of G_{zs} in subcells A, B, C, and D, respectively
G_{zt}	tangent modulus for deformations in vertical surfaces
I	mass moment of inertia of disk or footing about vertical centerline (slugs-ft^2)
i	index
j	index
K	ratio of lateral normal stresses to vertical normal stresses
KE	kinetic energy of medium
KE_d	kinetic energy of disk or footing
k	index
k_o	parameter defined by Reissner ($k_o = \bar{\omega}\sqrt{\rho/G}$)
L	index used by Reissner and Sagoci
M	moment
M_A	moment applied to disk or footing
M_{max}	maximum moment applied to disk or footing
M_{net}	net moment acting on disk or footing
M_p	amplitude of harmonic point torque
M_R	resultant moment of τ_z-stress distribution along base of disk or footing
M_x, M_y, M_z	moments about x-, y-, and z-axis, respectively
m	index limit

N_1, N_2, N_3, N_4	shape functions for corners 1, 2, 3, and 4 of subcells, respectively
$N_1^{\gamma_r}$, $N_2^{\gamma_r}$, $N_3^{\gamma_r}$, $N_4^{\gamma_r}$	differentiated shape functions for corners 1, 2, 3, and 4 of subcells, respectively
$N_1^{\gamma_z}$, $N_2^{\gamma_z}$, $N_3^{\gamma_z}$, $N_4^{\gamma_z}$	differentiated shape functions for corners 1, 2, 3, and 4 of subcells, respectively
n	number of cycles of n^{th} Fourier component contained in one period of fictitious odd function used in Fourier analysis
P	point in medium
p	surcharge pressure
R	parameter in Ramberg-Osgood equations
$R_{1L}(-ic, i\xi)$	radial wave function
r	horizontal radius from axis of symmetry
r_A, r_B, r_C, r_D, r_P	radii at points A, B, C, D, and P, respectively
r_i	radius of inner wall of cylinder
r_o	radius of outer wall of cylinder
$\bar{r}_i$	radius of ith node
$\bar{r}_o$	radius of disk or footing
r_1, r_2, r_3, r_4	radii of corners 1, 2, 3, and 4 of subcells, respectively
$S_{1L}(-ic, \eta)$	angular wave function
SD	accumulated energy dissipated by slip

$SD_{\Delta t}$	incremental energy dissipated by slip
SH	accumulated hysteretic loss and instantaneous strain energy
$SH_{\Delta t}$	incremental hysteretic loss and change in instantaneous strain energy
s	distance
T'	length of record, sec
t	time, sec
U	displacement shape in horizontal planes
u	circumferential displacement
u_i	circumferential displacement of point of application of ith force
u'	circumferential displacement of disk or footing
u_1, u_2, u_3, u_4	displacements of corners, 1, 2, 3, and 4 of subcells, respectively
V	circumferential particle velocity
V_A, V_B, V_C, V_D, V_P	circumferential particle velocities at points A, B, C, D and P, respectively
V_{ave}	average particle velocity within subcell
V_i	circumferential particle velocity at ith node
V_m	amplitude of particle velocity
$\overline{V}$	volume of medium
v_s	shear wave velocity, fps

v_{sr}	shear wave velocity based upon G_{rt}
v_{srA}, v_{srB}, v_{srC}, v_{srD}	values of v_{sr} in subcells A, B, C, and D, respectively
v_{srm}	maximum value of v_{sr}
v_{sz}	shear wave velocity based upon G_{zt}
v_{szA}, v_{szB}, v_{szC}, v_{szD}	v_{sz} in subcells A, B, C, and D, respectively
v_{szm}	maximum value of v_{sz}
W	arbitrary physical parameter
W_A, W_B	W at points A and B, respectively
W_H	accumulated work done on half space by disk or footing
$W_{H\Delta t}$	incremental work done on half space by disk or footing
$W_{\Delta t}$	incremental work done
$W(t)$	accumulated work done
x	coordinate in (x, y, z) coordinate system
y	coordinate in (x, y, z) coordinate system
z	coordinate in (r, θ, z) and (x, y, z) coordinate systems
z_1, z_2, z_3, z_4	depths of corners 1, 2, 3, and 4 of subcells, respectively

α	parameter in Ramberg-Osgood equations
$\alpha_1, \alpha_2, \alpha_3, \alpha_4$	coefficients of approximating functions
β	infinite series defined by Sagoci
γ	unit weight of soil, pcf
γ_{ave}	general average shearing strain
$\gamma_r, \gamma_{r\theta}$	shearing strains in horizontal planes
γ_{rave}	average γ_r-strain
$\gamma_z, \gamma_{z\theta}$	shearing strains in vertical surfaces
γ_{zave}	average γ_z-strain
γ'	infinite series defined by Sagoci
$\bar{\gamma}$	wave number
γ_1	shearing strain level at reversal in Ramberg-Osgood model
Δ	phase shift between M_R and $\phi(t)$ defined by Sagoci
$\Delta A_i'$	finite area assigned to ith node along interface
ΔM_{iRS}	incremental moment about vertical centerline caused by ith slipping node
Δr	$2\Delta\bar{r}$
$\Delta\bar{r}$	distance interval of grid in r-direction
Δs	change in distance
Δt	increment of time
$\Delta\bar{V}_j$	volume of jth subcell

$\Delta W_{A \to B}$	change in W between points A and B
$\Delta \bar{z}$	distance interval of grid in z-direction
η	oblate spheroidal coordinates
θ	angle of rotation about axis of symmetry, rad
$\theta_x, \theta_y, \theta_z$	angles of rotation about x-, y- and z-axis, respectively
$\bar{\theta}$	angular displacement of disk or footing, rad
λ	wavelength along longitudinal axis of cylinder
ξ	oblate spheroidal coordinate
ρ	mass density, slugs/ft^3
$\bar{\sigma}_o$	average effective normal stress, psf
$\bar{\sigma}_v$	vertical effective normal stress psf
τ_m	shearing strength of soil, psf
$\tau_r, \tau_{r\theta}$	shearing stresses causing deformation in horizontal planes
$\tau_{rA}, \tau_{rB}, \tau_{rC}, \tau_{rD}$	τ_r-stresses at points A, B, C, D, and P, respectively
τ_{ri}	τ_r-stress at ith node
τ_{rm}	shearing strength of soil in horizontal planes, psf
τ_Y	parameter in Ramberg-Osgood equations
$\tau_z, \tau_{z\theta}$	shearing stresses causing deformation in vertical surfaces

$\tau_{zA}, \tau_{zB}, \tau_{zC}, \tau_{zD}, \tau_{zP}$	τ_z-stress at points A, B, C, D, and P, respectively
τ_{zi}	τ_z-stress at ith node
τ_{zm}	shearing strength of soil in vertical surfaces, psf
τ_{zslip}	slip-stress
$\bar{\tau}_{rm}$	amplitude of harmonic shearing stress excitation
τ_1	stress level at reversal in Ramberg-Osgood model
$\tau_{r1}, \tau_{r2}, \tau_{r3}, \tau_{r4}$	τ_r-stresses at corners 1, 2, 3, and 4 of subcells, respectively
$\bar{\Phi}$	amplitude of harmonic angular displacement of disk
$\bar{\Phi}(r,z)$	approximating function
$\bar{\phi}$	angle of internal friction of soil, deg
$\phi(t)$	angular displacement of disk or footing, rad
$\phi_1, \phi_2, \phi_3, \phi_4$	values of general function at corners 1, 2, 3, and 4 of subcells, respectively
ω	angular velocity of disk, of footing, or of horizontal plane rotating rigidly about axis of symmetry, rad/sec
$\bar{\omega}$	circular frequency, rad/sec

CHAPTER I

INTRODUCTION

The dynamic response of a foundation is affected significantly by the supporting soil. The dynamic behavior of a soil deposit may be described by the multi-dimensional equations of motion for a continuum and the equations identifying the stress-strain properties of the soil.

Foundations may be subjected to loads ranging in intensity from machine vibrations to nuclear explosions. Under this range of loadings the shearing stress-strain properties of a soil may vary from linear elastic to highly nonlinear inelastic. Thus to predict accurately the dynamic response of foundations this variation in properties must be taken into account.

The first objective of this thesis was to develop a practical method of solving the equations describing the dynamic behavior of either a linear elastic or nonlinear inelastic multi-dimensional continuum. This method was to be applied to the equations representing the axisymmetric, torsional

behavior of a medium. Axisymmetric torsion is the simplest behavior of a three-dimensional medium; thus torsion provides an effective means of evaluating this proposed method. In addition, only shearing stresses develop during torsional motions therefore the effects of shearing stress-strain properties are studied easily.

Using this method, developed in Chapters III and V, the equations describing the torsional behavior of a medium are transformed to a different set of equations which may be solved numerically. The transformation, which is very simple, introduces no approximations. The numerical procedure gives stresses and particle velocities at selected points (nodes) within the medium. Because, at least in the linear case, very few approximations are introduced by solving the transformed equations numerically, this procedure is very accurate.

First, the numerical procedure is formulated for linear behavior. A number of numerical solutions are obtained and each is compared to a theoretical solution. Then, the numerical procedure is formulated for nonlinear inelastic behavior. Numerical solutions are obtained using Ramberg-Osgood equations to model nonlinear inelasticity. These nonlinear solutions are confirmed using an energy balance.

The second objective of this thesis was to demonstrate the ability of the nonlinear numerical model to predict the response of a model foundation-soil system. For this purpose laboratory experiments were conducted in which a rigid circular footing resting on a granular test bed was excited torsionally. The applied loading, the motion of the footing, and the motions of the test bed at selected locations were measured.

The properties needed to define the nonlinear shearing stress-strain behavior of the test bed were also obtained experimentally. Then, the experiment was modeled numerically using these soil properties and the measured loads and numerical responses were compared with measured responses.

CHAPTER II

REVIEW OF LITERATURE

Streeter, Wylie and Richart (1974) have adapted the one-dimensional method of characteristics to predict the response of soil deposits. Because of its success in solving the equations governing the motions of one-dimensional linear elastic and nonlinear inelastic media, this adaptation was used as the basis for the new multi-dimensional approach. This new approach cannot, however, be classified as the multi-dimensional method of characteristics which has been applied to hydrodynamic problems by Butler (1960), Richardson (1964), Fox (1962), Shin and Valentin (1978), and Lai (1977). In the multi-dimensional method of characteristics integrations are carried out along bicharacteristics to obtain a solution at a point. These bicharacteristics define paths along which waves may travel. Through each point within the medium there are an infinite number of bicharacteristics. Since each bicharacteristic defines one equation, at any point within a medium there are an infinite number of equations available from which to

obtain a solution for a finite number of unknowns. When results are compared with accepted theory, even for one dimensional conditions, agreement is not obtained (Shin and Valentin, 1978). Ziv (1969) has applied the two-dimensional method of characteristics to solid media.

As pointed out by Richart, Hall and Woods (1970), Hardin and Drnevich (1972), and Richart (1975), soils behave as nonlinear inelastic materials. Richart (1975), Richart and Wylie (1975) and Richart (1977) have demonstrated that, by selecting certain values for various parameters, the Ramberg-Osgood equations may be used to model the nonlinear inelastic shearing-stress strain properties of a soil.

A number of studies involving the motions of soil masses have been conducted using this model. Streeter, Wylie and Richart (1974), Richart and Wylie (1975), and Wylie and Henke (1979) considered the one-dimensional response of soil deposits subjected to earthquake excitations. Papadakis, Streeter and Wylie (1974) used surface seismograms to compute bedrock motions for one-dimensional deposits. Papadakis and Wylie (1975) have obtained one-dimensional solutions giving the response of an earth dam subjected to seismic excitation. Wylie et al (1974) obtained two-dimensional solutions giving the motions of various nonlinear

inelastic soil masses by treating these masses as lattice works of one-dimensional line elements which interacted at nodes. With this approach they identified zones within a two-dimensional dam which developed permanent deformations during earthquake excitation.

CHAPTER III

FORMULATION OF LINEAR ELASTIC NUMERICAL PROCEDURE

A. Introduction

In this chapter the equations governing axisymmetric torsional wave propagation within an elastic continuum are presented. These equations are transformed to a new set of equations from which a practical numerical procedure is developed. This procedure may be used to obtain solutions of the original equations in terms of particle velocities and stresses. A discussion of the treatment of boundary conditions is also given.

B. Definitions

Terms and parameters frequently encountered in this study are defined in this section. All work is carried out with respect to a cylindrical coordinate system having coordinates r, θ, and z as shown in Fig. 3.1. Axisymmetry refers to a condition for which there is no variation with the θ-coordinate, and an axisymmetric torsional wavefield consists of axisymmetric displacements and stresses. As shown in Fig. 3.1, the

only displacements, u, which occur are horizontal and perpendicular to horizontal radii extending from the z-axis. From the resulting deformations, two types of shearing stresses arise. The first of these, denoted $\tau_{r\theta}$, acts on vertical cylindrical surfaces centered along the z-axis and on vertical radial planes, while the second, $\tau_{z\theta}$, acts on horizontal and vertical radial planes. In axisymmetric torsion, compressional and shearing disturbances generated by centrifugal effects are neglected.

C. Derivation and Discussion of Governing Equations

One form of the equations governing axisymmetric torsional wave propagation in an isotropic, homogeneous, elastic medium consists of an equation of motion relating element stresses to element acceleration and two stress-strain relations relating stresses and strains in each coordinate direction. In order to develop these relationships, only stresses and displacements pertinent to axisymmetric torsion are considered.

An element showing the shearing stresses and the variations in shearing stresses is given in Fig. 3.2. The net force on the element caused by various force imbalances in the direction of the displacement is

equated to the mass times the acceleration of the element in this direction:

$$\left(\tau_{r\theta}+\frac{\partial\tau_{r\theta}}{\partial r}dr\right)(r+dr)\,d\theta dz-\tau_{r\theta}\,r d\theta\,dz+\left(\tau_{\theta r}+\frac{\partial\tau_{\theta r}}{\partial\theta}d\theta\right)dr dz\sin\frac{d\theta}{2}+\tau_{\theta r}\,dr dz\sin\frac{d\theta}{2}+\left(\tau_{z\theta}+\frac{\partial\tau_{z\theta}}{\partial z}dz\right)r d\theta\,dr-\tau_{z\theta}r d\theta\,dr=\rho r d\theta dr dz\frac{\partial V}{\partial t} \tag{3.1}$$

in which ρ is the mass density of the material and V is the particle velocity in the u-direction. Following expansion, cancellation, neglect of higher order terms, substitutions based upon small angle approximations ($\sin d\theta/2 \sim d\theta/2$), and considerations of symmetry ($\partial/\partial\theta = 0$), Eq. (3.1) reduces to

$$\frac{\partial\tau_{r\theta}}{\partial r}r d\theta dr dz+\tau_{r\theta}\,d\theta dr dz+\tau_{\theta r}\,d\theta dr dz+\frac{\partial\tau_{z\theta}}{\partial z}r d\theta dr dz=\rho r d\theta dr dz\frac{\partial V}{\partial t} \tag{3.2}$$

Physically each of the terms on the left of Eq. (3.2) represents some force acting on the element. The first term is that force component arising from the difference in stress, $\partial\tau_{r\theta}/\partial r\,dr$, occurring between the inner and outer vertical cylindrical surfaces and distributed over an area, $r d\theta dz$, equal to that of the inner surface. Clearly, even under conditions of constant $\tau_{r\theta}$-stress,

there will be a net force acting on the element due to $\tau_{r\theta}$ because of the change in area, $drdedz$, of the vertical cylindrical surface occurring over element length, dr. The second term represents this force. The third term is the net force acting on the element caused by the components of the forces in the u-direction, $\tau_{\theta r}drdz$, due to stresses acting on each of the vertical radial planes of area $drdz$. The approximation of $2\sin d\theta/2$, $d\theta/2$, transforms the force, $\tau_{\theta r}drdz$, into the u-direction component. The net force due to the stress difference, $\partial\tau_{z\theta}/\partial z dz$, occurring over the depth of the element and acting on horizontal planes of area, $rdrd\theta$, is given by the fourth term, and the term on the right hand side is equal to the mass times the acceleration of the element in the u-direction, $\partial V/\partial t$. Simplifying Eq. (3.2), and noting that from rotational considerations, $\tau_{r\theta} = \tau_{\theta r}$, Eq. (3.2) becomes

$$\frac{\partial\tau_{r\theta}}{\partial r} + 2\frac{\tau_{r\theta}}{r} + \frac{\partial\tau_{z\theta}}{\partial z} = \rho\frac{\partial V}{\partial t} \qquad (3.3)$$

Stresses create variations in the displacement field as shown in Fig. 3.3, and the spatial rates of change of this displacement field may be used to define the two strains, $\gamma_{r\theta}$ and $\gamma_{z\theta}$, as follows:

$$\gamma_{r\theta} = \frac{u + \frac{\partial u}{\partial r} dr - u}{dr} - \frac{u}{r} = \frac{\partial u}{\partial r} - \frac{u}{r} \tag{3.4}$$

and

$$\gamma_{z\theta} = \frac{u + \frac{\partial u}{\partial z} dz - u}{dz} = \frac{\partial u}{\partial z} \tag{3.5}$$

In Eq. (3.4), u/r represents a rigid body rotational component contained in the quantity, $\partial u/\partial r$, which must be subtracted from this quantity to obtain strain, which is a measure of deformation only. In Figs. 3.4 and 3.5 are shown deformation modes corresponding to each of the strains.

Stresses and strains are linearly related through the shear modulus, G. Assuming homogeneity and isotropy, the stress-strain relations for axisymmetric torsion are

$$\tau_{r\theta} = G\gamma_{r\theta} = G\left(\frac{\partial u}{\partial r} - \frac{u}{r}\right) \tag{3.6}$$

and

$$\tau_{z\theta} = G\gamma_{z\theta} = G\frac{\partial u}{\partial z} \tag{3.7}$$

A simplified notation, $\tau_r = \tau_{r\theta}$, $\tau_z = \tau_{z\theta}$, $\gamma_r = \gamma_{r\theta}$, and $\gamma_z = \gamma_{z\theta}$, will be used hereafter.

Equations (3.3), (3.6) and (3.7), presented together below, are the equations governing torsional axisymmetric wave propagation in a linearly elastic, homogeneous, isotropic medium.

$$\frac{\partial \tau_r}{\partial r} + 2\frac{\tau_r}{r} + \frac{\partial \tau_z}{\partial z} = \rho \frac{\partial V}{\partial t} \tag{3.3}$$

$$\tau_r = G\left(\frac{\partial u}{\partial r} - \frac{u}{r}\right) \tag{3.6}$$

$$\tau_z = G\frac{\partial u}{\partial z} \tag{3.7}$$

To demonstrate the validity of these equations, making use of the fact that $V = \partial u/\partial t$, these equations are combined as follows:

$$\frac{\partial}{\partial r}\left\{G\left(\frac{\partial u}{\partial r} - \frac{u}{r}\right)\right\} + \frac{2}{r}G\left(\frac{\partial u}{\partial r} - \frac{u}{r}\right) + \frac{\partial}{\partial z}\left(G\frac{\partial u}{\partial z}\right) = \rho\frac{\partial}{\partial t}\left(\frac{\partial u}{\partial t}\right) \tag{3.8}$$

After differentiating and collecting terms, this gives

$$G\left\{\frac{\partial^2 u}{\partial r^2} + \frac{1}{r}\frac{\partial u}{\partial r} - \frac{u}{r^2} + \frac{\partial^2 u}{\partial z^2}\right\} = \rho\frac{\partial^2 u}{\partial t^2} \tag{3.9}$$

Equation (3.9) is identical to the undamped, axisymmetric torsional wave equation as presented by Reissner (1937) and Kolsky (1963) in terms of displacements.

D. Transformation

In this section the equation of motion, Eq. (3.3), and the two stress-strain relations, Eqs. (3.6)

and (3.7), are transformed to an equation set from which a numerical solution procedure may be developed. Theoretical background is discussed prior to this transformation with an emphasis on physical interpretations.

Fundamental to the transformation is the relationship between partial derivatives and total differentials. Consider the coordinate system shown in Fig. 3.6 with mutually perpendicular r-, z- and t-axes. With respect to this figure it is assumed that a physical parameter, W, which might represent velocity, stress, pressure, etc., is known for all (r,z,t) and attention is directed at point A. It is desired to determined the difference in W, $\Delta W_{A\to B}$, between locations A and B based upon information available at A. For this purpose a path is constructed between A and B which consists of 3 segments, AC, CD and DB, each of which parallels one of the coordinate axes. As illustrated in Fig. 3.6, each segment represents one of the coordinate axis components of Δs, the direct path distance between A and B. The change, $\Delta W_{A\to B}$, may be expressed as the sum of the changes in W along each of the component segments, i.e.

$$\Delta W_{A\to B} = \Delta W_{A\to C} + \Delta W_{C\to D} + \Delta W_{D\to B} \qquad (3.10)$$

where $\Delta W_{i\to j}$ is the change in W along a linear path between points i and j. Each of these component changes may be approximated by the product of the rate of change of the physical quantity, W, with respect to the coordinate direction of interest at point A, i.e. $\partial W/\partial r|_A$, and the component of the path Δs in that direction, i.e. $\Delta r_{A\to B}$. Thus Eq. (3.10) may be written as

$$\Delta W_{A\to B} \cong \frac{\partial W}{\partial r}\Big|_A \Delta r_{A\to B} + \frac{\partial W}{\partial z}\Big|_A \Delta z_{A\to B} + \frac{\partial W}{\partial t}\Big|_A \Delta t_{A\to B} \quad (3.11)$$

where $\Delta r_{A\to B}$, $\Delta z_{A\to B}$, and $\Delta t_{A\to B}$ are the components in the coordinate directions of the linear path, Δs, between points A and B, and $\partial W/\partial r|_A$, $\partial W/\partial z|_A$, and $\partial W/\partial t|_A$ are the rates of change of W at point A with respect to changes in each coordinate direction while holding the other coordinates constant (partial derivative of W with respect to each of the coordinate directions at A). The approximation of Eq. (3.11), which improves as Δr, Δz, and Δt approach zero, is strictly valid only if $\partial W/\partial r$, $\partial W/\partial z$, and $\partial W/\partial t$ are continuous. Clearly, it is incorrect to estimate the change in a quantity between two points based upon the rate of change at one point, if the rate of change of the quantity between the two points is discontinuous.

Defining $\Delta W_{A\to B}$ as dw, $\Delta r_{A\to B}$ as dr, $\Delta z_{A\to B}$ as dz and $\Delta t_{A\to B}$ as dt, Eq. (3.11) may be expressed in differential form as

$$dW_{A\to B} = \left.\frac{\partial W}{\partial r}\right|_A dr + \left.\frac{\partial W}{\partial z}\right|_A dz + \left.\frac{\partial W}{\partial t}\right|_A dt \qquad (3.12)$$

giving the approximate total change in W along path AB as a sum of the changes in W along each of the components of this path.

An objective in the following development is to replace the sum,

$$\bar{a}\frac{\partial W}{\partial r} + \bar{b}\frac{\partial W}{\partial z} + \bar{d}\frac{\partial W}{\partial t} \qquad (3.13)$$

by the total change, dW, where coefficients $\bar{a}$,$\bar{b}$, and $\bar{d}$ in expression (3.13) are numbers. Expression (3.13) is equal to the change in the function, dW, but only for the path having components dr = $\bar{a}$, dz = $\bar{b}$, and dt = $\bar{d}$. Should the path, (dr, dz, dt) take on values other than these, then expression (3.13) would not predict dW along this different path.

The preceding discussion may also be extended to the time rates of change of W, dW/dt. Dividing Eq. (3.12) by dt and dropping subscripts:

$$\frac{dW}{dt} = \frac{(\partial W/\partial r)\,dr}{dt} + \frac{(\partial W/\partial z)\,dz}{dt} + \frac{(\partial W/\partial t)\,dt}{dt} \qquad (3.14)$$

Equation (3.14) states that the total time rate of change of physical quantity, W, due to a change in coordinates (dr, dz, dt) occurring in time, dt, is equal to the sum of the coordinate axis components of the time rate of change of W. Rewriting Eq. (3.14) gives

$$\frac{dW}{dt} = \frac{\partial W}{\partial r}\frac{dr}{dt} + \frac{\partial W}{\partial z}\frac{dz}{dt} + \frac{\partial W}{\partial t} \tag{3.15}$$

A more rigorous development of Eq. (3.15) is given by Streeter and Wylie (1975, Appendix B).

From the previous discussion and Eq. (3.15), $\bar{e}(\partial W/\partial r)+\bar{f}(\partial W/\partial z)+\partial W/\partial t$ correctly gives dW/dt only for the path having component time rates of change, $dr/dt = \bar{e}$, $dz/dt = \bar{f}$, and $dt/dt = 1$.

The equations to be transformed are, in simplified notation,

$$\frac{\partial \tau_r}{\partial r} + 2\frac{\tau_r}{r} + \frac{\partial \tau_z}{\partial z} = \rho\frac{\partial V}{\partial t}$$

$$\tau_r = G\left(\frac{\partial u}{\partial r} - \frac{u}{r}\right) \tag{3.16b}$$

$$\tau_z = G\frac{\partial u}{\partial z} \tag{3.16c}$$

The dependent variables for this equation set include τ_r, τ_z, u, and V, and the objective of the transformation is to simplify this equation set by replacing

combinations of partial derivatives of the dependent variables with total derivatives.

The following partial derivatives are present in Eqs. (3.16): $\partial\tau_r/\partial r$, $\partial\tau_z/\partial z$, and $\partial V/\partial t$. To form the combinations of partial derviatives necessary to substitute total derivatives, $\partial\tau_r/\partial z$, $\partial\tau_r/\partial t$, $\partial\tau_z/\partial t$, $\partial\tau_z/\partial r$, $\partial V/\partial r$, and $\partial V/\partial z$ are required. These are generated by partial differentiation of Eqs. (3.16b) and (3.16c). Differentiating the first of these with respect to time gives a relationship between the time rate of change of τ_r -stress and the time rate of change of γ_r-strain at a fixed point in space.

$$\frac{\partial\tau_r}{\partial t} = G\left(\frac{\partial^2 u}{\partial t\partial r} - \frac{1}{r}\frac{\partial u}{\partial t}\right) \tag{3.17}$$

Since $V = \partial u/\partial t$, and imposing continuity of the second derivatives of displacement so that the order of differentiation is immaterial, i.e. $\partial^2 u/\partial t\partial r = \partial^2 u/\partial r\partial t$ Eq. (3.17) may be interpreted as

$$\frac{\partial\tau_r}{\partial t} = G\left(\frac{\partial V}{\partial r} - \frac{V}{r}\right) \tag{3.18}$$

Eq. (3.18) may be rewritten as

$$\frac{\partial\tau_r}{\partial t} - G\frac{\partial V}{\partial r} + G\frac{V}{r} = 0 \tag{3.19}$$

To obtain $\partial\tau_r/\partial z$, Eq. (3.16 b) is differentiated with respect to z, giving a relationship between the rate of

change of τ_r-stress with respect to depth and the rate of change of γ_r-strain with respect to depth at a given time and radius.

$$\frac{\partial \tau_r}{\partial z} = G\left(\frac{\partial^2 u}{\partial z \partial r} - \frac{1}{r}\frac{\partial u}{\partial z}\right) \tag{3.20}$$

Again, imposing continuity of second derivatives of displacement, so that $\partial^2 u/\partial r \partial z = \partial^2 u/\partial z \partial r$, yields

$$\frac{\partial \tau_r}{\partial z} = \frac{\partial}{\partial r}\left(G\frac{\partial u}{\partial z}\right) - \frac{1}{r} G \frac{\partial u}{\partial z} \tag{3.21}$$

Substituting Eq. (3.16c) into Eq. (3.21) and rearranging terms,

$$\frac{\partial \tau_r}{\partial z} - \frac{\partial \tau_z}{\partial r} + \frac{1}{r}\tau_z = 0 \tag{3.22}$$

is obtained. In order to obtain a positive partial derivative, $\partial \tau_z/\partial r$, the following relation is used:

$$\frac{\partial \tau_z}{\partial r} - \frac{\partial \tau_z}{\partial r} = 0 \tag{3.23}$$

The partial derivative, $\partial \tau_z/\partial t$, is obtained by differentiating Eq. (3.16c) with respect to time, giving a relationship between the time rate of change of τ_z-stress and the time rate of change of γ_z-strain at a point in space:

$$\frac{\partial \tau_z}{\partial t} = G\frac{\partial^2 u}{\partial t \partial z}$$

Since $V = \partial u/\partial t$ and since the second partial derivatives of displacement have been assumed to be continuous, the equation above may be rewritten as

$$\frac{\partial \tau_z}{\partial t} - G \frac{\partial V}{\partial z} = 0 \tag{3.24}$$

Finally, the equation of motion is rearranged to give

$$\frac{\partial \tau_r}{\partial r} + 2\frac{\tau_r}{r} + \frac{\partial \tau_z}{\partial z} - \rho \frac{\partial V}{\partial t} = 0 \tag{3.25}$$

Since the five equations developed above, Eqs. (3.19), (3.22), (3.23), (3.24) and (3.25), are all equal to zero, each may be multiplied by an unknown constant and combined linearly to give a single equation also equal to zero. Thus

$$1\left(\frac{\partial \tau_r}{\partial r} + \frac{\partial \tau_z}{\partial z} + \frac{2}{r}\tau_r - \rho\frac{\partial V}{\partial t}\right) + \bar{A}\left(\frac{\partial \tau_r}{\partial t} - G\frac{\partial V}{\partial r} + G\frac{V}{r}\right) + \bar{B}\left(\frac{\partial \tau_r}{\partial z} - \frac{\partial \tau_z}{\partial r} + \frac{\tau_z}{r}\right) + \bar{C}\left(\frac{\partial \tau_z}{\partial t} - G\frac{\partial V}{\partial z}\right) + \bar{D}\left(\frac{\partial \tau_z}{\partial r} - \frac{\partial \tau_z}{\partial r}\right) = 0 \tag{3.26}$$

where $\bar{A}$, $\bar{B}$, $\bar{C}$, and $\bar{D}$ are unknown multipliers. Performing manipulations necessary to collect groups of partial derivatives, Eq. (3.26) may be rewritten as

$$\bar{A}\left(\frac{1}{\bar{A}}\frac{\partial \tau_r}{\partial r}+\frac{\bar{B}}{\bar{A}}\frac{\partial \tau_r}{\partial z}+\frac{\partial \tau_r}{\partial t}\right)+\bar{C}\left(\frac{\bar{D}}{\bar{C}}\frac{\partial \tau_z}{\partial r}+\right.$$

$$\left.\frac{1}{\bar{C}}\frac{\partial \tau_z}{\partial z}+\frac{\partial \tau_z}{\partial t}\right)-\rho\left(\frac{\bar{A}G}{\rho}\frac{\partial V}{\partial r}+\frac{\bar{C}G}{\rho}\frac{\partial V}{\partial z}+\frac{\partial V}{\partial t}\right)+2\frac{\tau_r}{r} \qquad (3.27)$$

$$+\bar{A}G\frac{V}{r}+\frac{\bar{B}}{r}\tau_z-\bar{B}\frac{\partial \tau_z}{\partial r}-\bar{D}\frac{\partial \tau_z}{\partial r}=0$$

Based in general upon the discussion of the relationship between partial and total derivatives, and in particular upon Eq. (3.15), in order to interpret the groups of partial derivatives in Eq. (3.27) as total time derivatives, the time rates of change of coordinates, dr/dt, dz/dt, and dt/dt, must be given the values of the appropriate coefficients of the partial derivatives in Eq. (3.27). Thus, for this interpretation,

$$\frac{dr}{dt}=\frac{1}{\bar{A}}=\frac{\bar{D}}{\bar{C}}=\frac{\bar{A}G}{\rho} \qquad (3.28a)$$

$$\frac{dz}{dt}=\frac{\bar{B}}{\bar{A}}=\frac{1}{\bar{C}}=\frac{\bar{C}G}{\rho} \qquad (3.28b)$$

$$\frac{dt}{dt}=1 \qquad (3.28c)$$

Under the conditions of Eqs. (3.28), Eq. (3.27) may be written as

$$\bar{A}\left(\frac{dr}{dt}\frac{\partial\tilde{\tau}_r}{\partial r}+\frac{dz}{dt}\frac{\partial\tilde{\tau}_r}{\partial z}+\frac{\partial\tilde{\tau}_r}{\partial t}\right)+\bar{C}\left(\frac{dr}{dt}\frac{\partial\tilde{\tau}_z}{\partial r}+\frac{dz}{dt}\frac{\partial\tau_z}{\partial z}\right.$$

$$\left.+\frac{\partial\tilde{\tau}_z}{\partial t}\right)-\rho\left(\frac{dr}{dt}\frac{\partial V}{\partial r}+\frac{dz}{dt}\frac{\partial V}{\partial z}+\frac{\partial V}{\partial t}\right)+2\frac{\tilde{\tau}_r}{r}+ \qquad (3.29)$$

$$\bar{A}G\frac{V}{r}+\frac{\bar{B}}{r}\tau_z-\bar{B}\frac{\partial\tilde{\tau}_z}{\partial r}-\bar{D}\frac{\partial\tau_z}{\partial r}=0$$

Each of the groups of partial derivative terms of Eq. (3.29) is in the form of Eq. (3.15), and this permits the replacement of these groups by total time derivatives. The paths in space and time along which the groups may be so interpreted are those having component time rates of change dr/dt, dz/dt, and dt/dt as defined by Eqs. (3.28). For a given time increment, dt, these paths therefore have component lengths (dr, dz, dt) = $\left(\frac{dr}{dt}dt\,,\ \frac{dz}{dt}dt\ ,\ \frac{dt}{dt}dt\right)$. Note that by virtue of the repetitive equalities in Eqs. (3.28a) and (3.28b), each of the groups become total time derivatives along the same path.

The conditions of Eqs. (3.28) permit Eq. (3.27) to be written as

$$\bar{A}\frac{d\tilde{\tau}_r}{dt}+\bar{C}\frac{d\tilde{\tau}_z}{dt}-\rho\frac{dV}{dt}+2\frac{\tilde{\tau}_r}{r}+\bar{A}G\frac{V}{r}+$$

$$\bar{B}\frac{\tilde{\tau}_z}{r}-(\bar{B}+\bar{D})\frac{\partial\tau_z}{\partial r}=0$$

or

$$d\tau_r + \frac{\bar{C}}{\bar{A}} d\tau_z - \frac{\rho}{\bar{A}} dV + \frac{2}{\bar{A}} \frac{\tau_r}{r} dt + \frac{\bar{B}}{\bar{A}} \frac{\tau_z}{r} dt + G \frac{V}{r} dt - \frac{(\bar{B}+\bar{D})}{\bar{A}} \frac{\partial \tau_z}{\partial r} dt = 0 \tag{3.30}$$

Solving for the coefficients $\bar{A}$, $\bar{B}$, $\bar{C}$ and $\bar{D}$ by use of Eqs. (3.28a) and (3.28b) gives

$$\begin{aligned} \bar{A} &= \pm\sqrt{\frac{\rho}{G}} = \pm \frac{1}{V_s} \\ \bar{C} &= \pm\sqrt{\frac{\rho}{G}} = \pm \frac{1}{V_s} \\ \bar{B} &= \pm 1 \\ \bar{D} &= \pm 1 \end{aligned} \tag{3.31}$$

where v_s is defined as $\sqrt{G/\rho}$, the velocity of a shear wave in an elastic medium. From Eqs. (3.31), (3.28a) and (3.28b) there arise four possible paths along which the conversion from partial differentiation to total differentiation may take place. The time rates of change of the components of these paths in the coordinate directions are given by the four possible combinations of the following set:

$$\frac{dr}{dt} = \pm v_s \tag{3.32a}$$

$$\frac{dz}{dt} = \pm v_s \tag{3.32b}$$

$$\frac{dt}{dt} = 1 \tag{3.32c}$$

The four paths defined by Eqs. (3.32) are

$$(dr, dz, dt) = \begin{cases} (v_s dt, v_s dt, dt) \\ (v_s dt, -v_s dt, dt) \\ (-v_s dt, v_s dt, dt) \\ (-v_s dt, -v_s dt, dt) \end{cases} \tag{3.33}$$

Introducing separately each combination of Eqs. (3.32) into Eq. (3.30) and also applying Eqs. (3.31) gives four equations, each valid along a different one of the four paths described by Eqs. (3.33). These equations along with path identifiers (C^{++}, C^{+-}, C^{-+}, and C^{--}), path rates, and paths are presented below:

C^{++}: Path rate: $\frac{dr}{dt} = v_s$, $\frac{dz}{dt} = v_s$, $\frac{dt}{dt} = 1$

Path: $(dr, dz, dt) = (v_s dt, v_s dt, dt)$

Equation:

$$d\tau_r + d\tau_z - \rho v_s dV - 2\frac{\partial \tau_z}{\partial r} dr + 2\frac{\tau_r}{r} dr + \frac{\tau_z}{r} dr + \rho v_s \frac{V}{r} dr = 0 \qquad (3.34a)$$

C^{+-}: Path rate: $\frac{dr}{dt} = v_s$, $\frac{dz}{dt} = -v_s$, $\frac{dt}{dt} = 1$

Path: $(dr, dz, dt) = (v_s dt, -v_s dt, dt)$

Equation:

$$d\tau_r - d\tau_z - \rho v_s dV + 2\frac{\partial \tau_z}{\partial r} dr + 2\frac{\tau_r}{r} dr - \frac{\tau_z}{r} dr + \rho v_s \frac{V}{r} dr = 0 \qquad (3.34b)$$

C^{-+}: Path rate: $\frac{dr}{dt} = -v_s$, $\frac{dz}{dt} = v_s$, $\frac{dt}{dt} = 1$

Path: $(dr, dz, dt) = (-v_s dt, v_s dt, dt)$

Equation:

$$d\tau_r - d\tau_z + \rho v_s dV + 2\frac{\partial \tau_z}{\partial r} dr + 2\frac{\tau_r}{r} dr - \frac{\tau_z}{r} dr - \rho v_s \frac{V}{r} dr = 0 \qquad (3.34c)$$

C^{--}: Path rate: $\frac{dr}{dt} = -v_s$, $\frac{dz}{dt} = -v_s$, $\frac{dt}{dt} = 1$

$$\text{Path}: (dr, dz, dt) = (-v_s dt, -v_s dt, dt)$$

Equation:

$$d\tilde{\tau}_r + d\tilde{\tau}_z + \rho v_s dV - 2\frac{\partial \tilde{\tau}_z}{\partial r} dr + \tag{3.34d}$$

$$2\frac{\tilde{\tau}_r}{r} dr + \frac{\tilde{\tau}_z}{r} dr - \rho v_s \frac{V}{r} dr = 0$$

E. Numerical Procedure

To develop a numerical procedure capable of solving Eqs. (3.16), each of the four major differential equations of Eqs. (3.34) is integrated over a finite change in space and time along an appropriate path also defined in Eqs. (3.34). With reference to Fig. 3.7, an example integration is carried out over a finite distance from point A to P along the C^{++} path for which $(\Delta r, \Delta z, \Delta t) = (v_s \Delta t, v_s \Delta t, \Delta t)$.

$$\int_A^P d\tilde{\tau}_r + \int_A^P d\tilde{\tau}_z - \rho v_s \int_A^P dV - 2\int_A^P \frac{\partial \tilde{\tau}_z}{\partial r} dr + \tag{3.35}$$

$$2\int_A^P \frac{\tilde{\tau}_r}{r} dr + \int_A^P \frac{\tilde{\tau}_z}{r} dr + \rho v_s \int_A^P \frac{V}{r} dr = 0$$

Integrating Eq. (3.35) in accordance with the trapezoidal rule, which introduces a numerical approximation, gives,

$$(\tilde{\tau}_{rp} - \tilde{\tau}_{rA}) + (\tilde{\tau}_{zp} - \tilde{\tau}_{zA}) - \rho v_s (V_p - V_A) -$$

$$\left(\frac{\partial \tau_z}{\partial r}\Big|_P + \frac{\partial \tau_z}{\partial r}\Big|_A\right)(r_P - r_A) + \left(\frac{\tau_{rP}}{r_P} + \frac{\tau_{rA}}{r_A}\right)(r_P - r_A)$$

$$+\left(\frac{\tau_{zP}}{r_P} + \frac{\tau_{zA}}{r_A}\right)\left(\frac{r_P - r_A}{2}\right) + \frac{\rho V_s}{2}\left(\frac{V_P}{r_P} + \frac{V_A}{r_A}\right)(r_P - r_A) \quad (3.36)$$

$$= 0$$

The appended subscripts, A and P, indicate the location along the path at which a quantity is defined. The other three equations of Eqs. (3.34) may be integrated similarly along C^{+-}, C^{-+}, and C^{--} paths.

To obtain a solution at a point in space and time, as shown in Fig. 3.8, the origins of the four paths are selected such that, for a given change in time, the terminal points of each path occupy the same point in space and time. If all the variables, V, τ_r, τ_z, and $\partial\tau_z/\partial r$, are known at the origin of each path and unknown at the terminal point, then, by integrating Eqs. (3.34) along these four paths, four algebraic equations may be obtained in the four unknowns: τ_{zP}, V_P, τ_{rP}, and $\partial\tau_z/\partial r|_P$. This equation set may be solved simultaneously and the solution may be interpreted as an estimate of the values of τ_z, τ_r, V and $\partial\tau_z/\partial r$ at a point in space and time based upon known values of these

variables at a finite number of distinct locations at an earlier time.

The implementation of the numerical procedure involves defining a grid in the (r,z,t) coordinate system. In this grid, any r-z plane represents space at a particular time, and each r-z plane of this grid consists of a regular array of nodes at which variables are known or are to be computed. Each r-z plane is separated by a preselected time increment, Δt, which also fixes the distance interval between nodes, $\Delta \bar{r}$ and $\Delta \bar{z}$.

Two types of grids, square and staggered, have been used to obtain linearly elastic solutions and are shown in Fig. 3.9. For each grid, values are computed at the starred nodes.

At any time, $t + \Delta t$, computations are carried out for all nodes in the r-z plane corresponding to this time. These computations are based upon the values of the variables, τ_z, τ_r, V, and $\partial \tau_z / \partial r$, obtained at nodes within the r-z plane corresponding to time t, either from previous computations or initial conditions. Fig. 3.10 focuses on the details of an isolated cell used for computations at a point, P, having coordinates (r_p, z_p, $t + \Delta t$). The four integration paths, C^{++}, C^{+-}, C^{-+}, and C^{--}, are shown originating from points A, B, C, and D each in the same time plane and terminating at point

P. The distance intervals of the grid, $\Delta\bar{r}$ and $\Delta\bar{z}$, are chosen such that, for the time increment selected, each of the paths extends from an appropriate originating node to the terminating node, P. Since, for a given time increment, Δt, each path has component magnitudes $(|\Delta r|, |\Delta z|, \Delta t) = (V_S \Delta t, V_S \Delta t, \Delta t)$, the required distance interval is $\Delta\bar{r} = \Delta\bar{z} = V_S \Delta t$. All variables are known at nodes A, B, C and D permitting a solution to be obtained for τ_{rp}, τ_{zp}, V_p, and $\partial\tau_z/\partial r|_p$ by solving the following equation set representing the systematic form of the integrated path equations:

$$
\begin{aligned}
a_1\tau_{rp} + b_1\tau_{zp} + c_1 V_p + d_1 \frac{\partial\tau_z}{\partial r}\Big|_p &= e_1 \\
a_3\tau_{rp} + b_3\tau_{zp} + c_3 V_p + d_3 \frac{\partial\tau_z}{\partial r}\Big|_p &= e_3 \\
a_5\tau_{rp} + b_5\tau_{zp} + c_5 V_p + d_5 \frac{\partial\tau_z}{\partial r}\Big|_p &= e_5 \\
a_7\tau_{rp} + b_7\tau_{zp} + c_7 V_p + d_7 \frac{\partial\tau_z}{\partial r}\Big|_p &= e_7
\end{aligned}
\qquad (3.37)
$$

The quantities a_1 through e_7 may be computed and are functions of the nodal coordinates, nodal variables and material properties. Equations for these coefficients are given in Appendix I. Equations (3.37) are solved at each nodal point in the r-z plane corresponding to time $t + \Delta t$, time is then incremented and the entire process is repeated. In this manner, values are

obtained for the variables τ_r, τ_z, V, and $\partial\tau_z/\partial r$, for each node in the space-time region of interest.

F. Development of Boundary Conditions

Boundary conditions may be given either directly or indirectly. A direct boundary condition is one for which one of the unknowns, V, τ_r, τ_z or $\partial\tau_z/\partial r$, is given known values at a point or node. In an indirect boundary condition, quantities other than one of the four main variables are specified and these quantities are introduced into accepted differential equations which relate the main variables to these specified quantities. This gives a relationship between the main variables. As an example of a useful indirect boundary condition, $\partial\tau_r/\partial z$ may be given at a point yielding a relationship between the two main variables $\partial\tau_z/\partial r$ and τ_z, through the equation

$$\frac{\partial\tau_r}{\partial z} - \frac{\partial\tau_z}{\partial r} + \frac{\tau_z}{r} = 0 \qquad (3.38)$$

which is the differentiated form of Eq. (3.16b). It is of interest to note that partial derivatives, which may be specified as boundary conditions, are fully defined at a point rather than being determined as a finite change of a dependent variable with respect to a finite change in one independent variable.

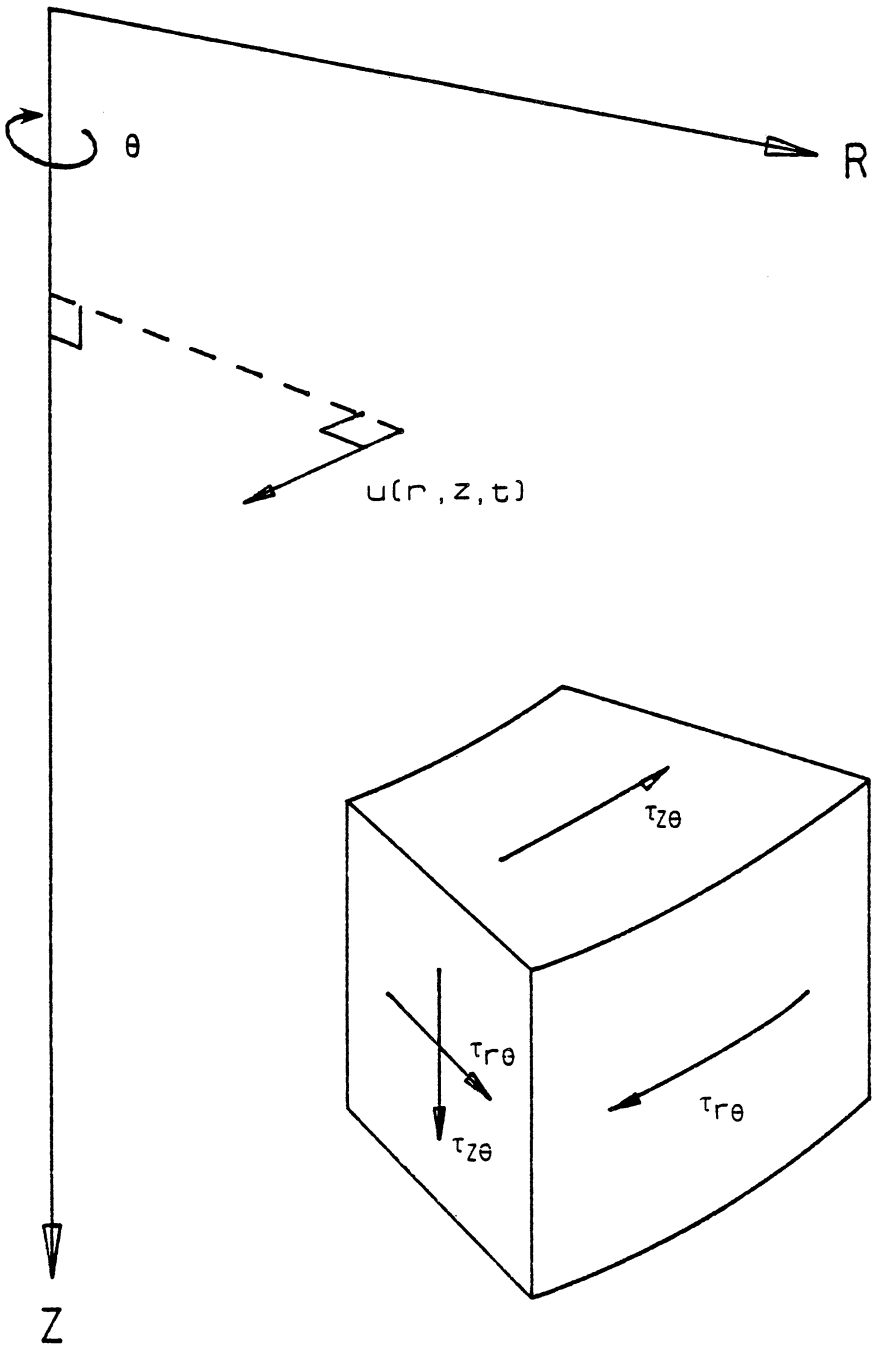

Fig. 3.1: Axisymmetric Torsional Displacement and Stress Fields Given in Cylindrical Coordinate System.

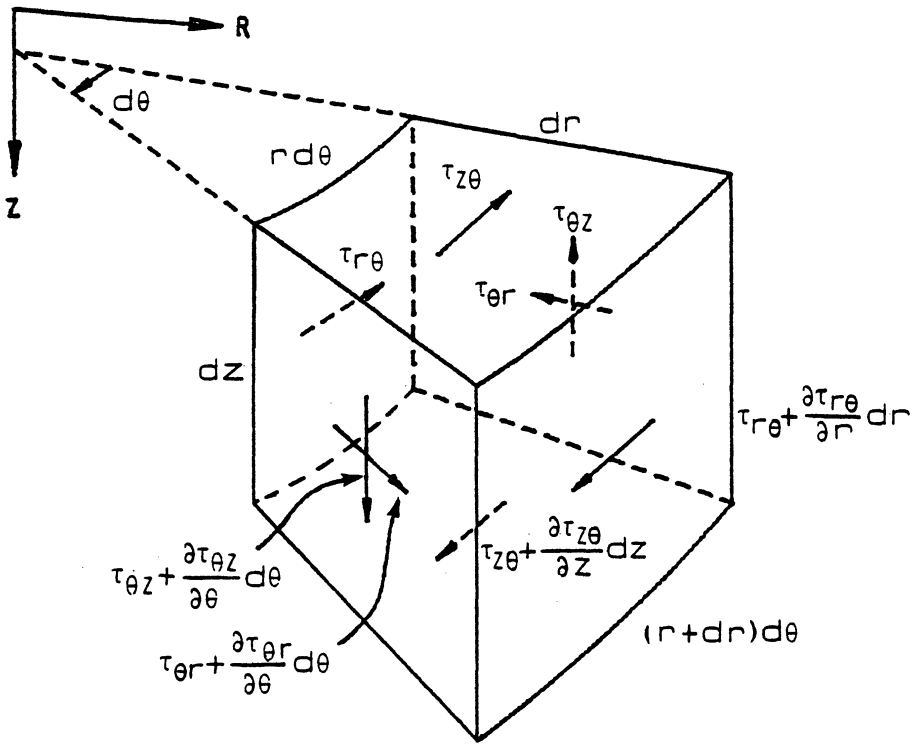

Fig. 3.2: Element with Stresses.

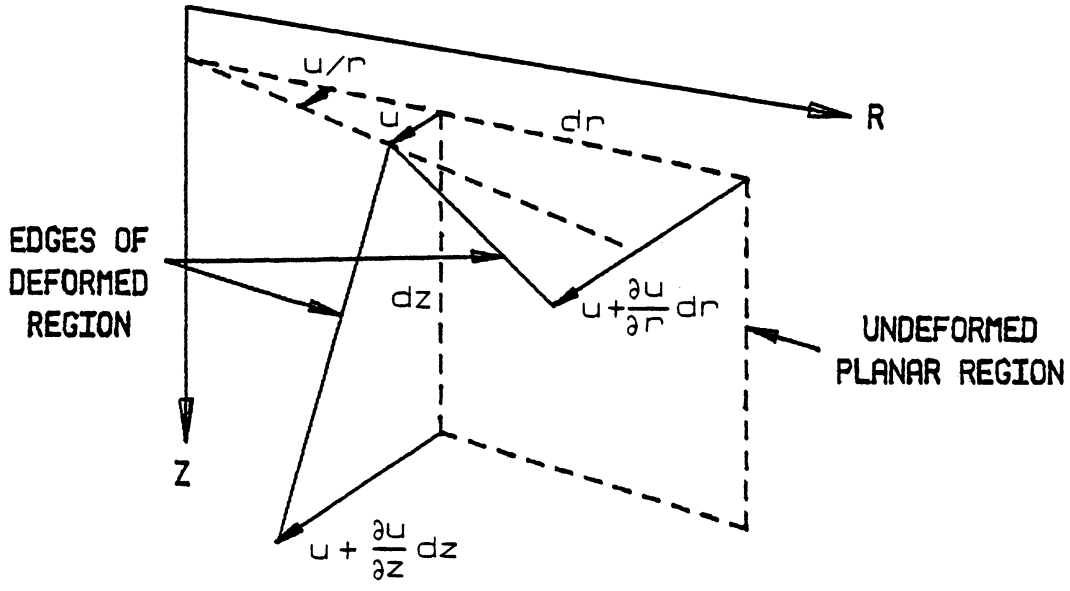

Fig. 3.3: Deformation of Region in r-z Plane.

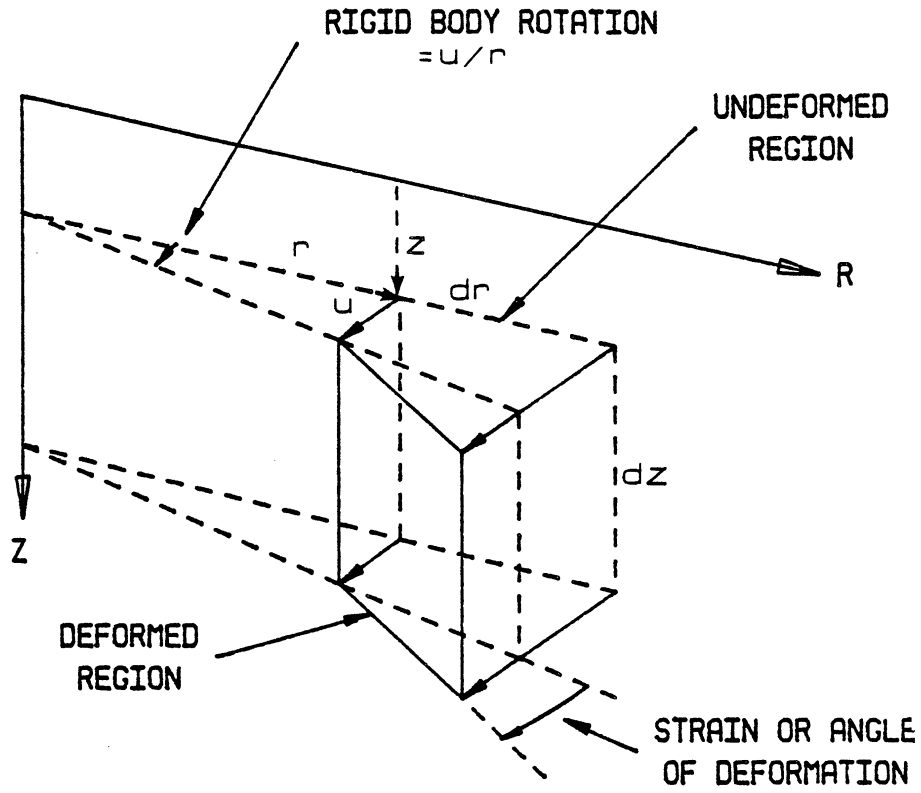

Fig. 3.4: Region in r-z Plane Having $\gamma_{r\theta}$-Strain in Absence of $\gamma_{z\theta}$-Strain.

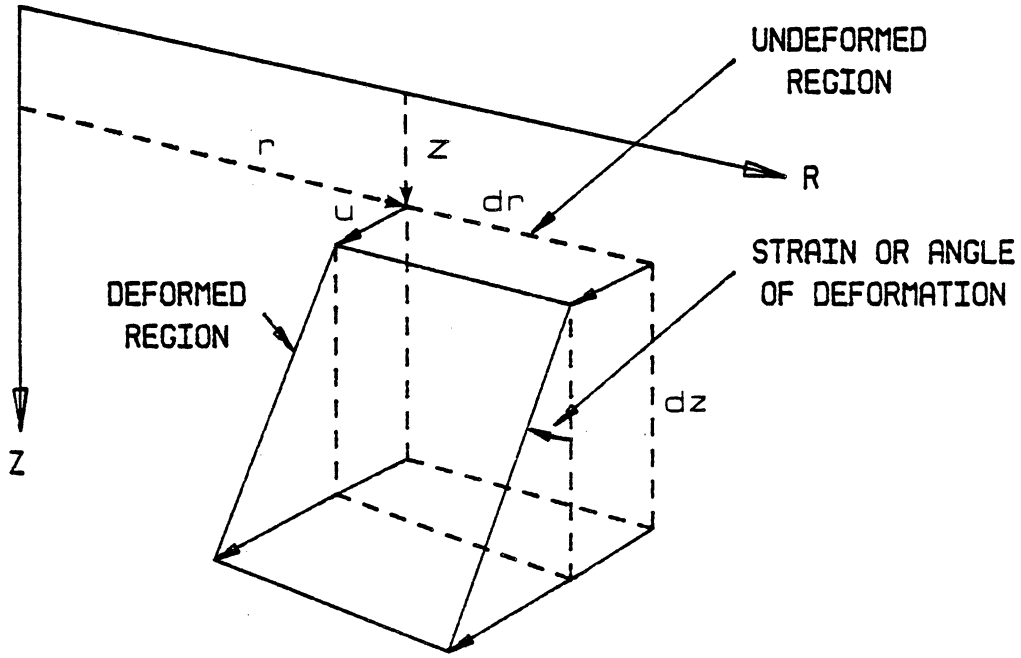

Fig. 3.5: Region in r-z Plane Having $\gamma_{z\theta}$-Strain in Absence of $\gamma_{r\theta}$-Strain.

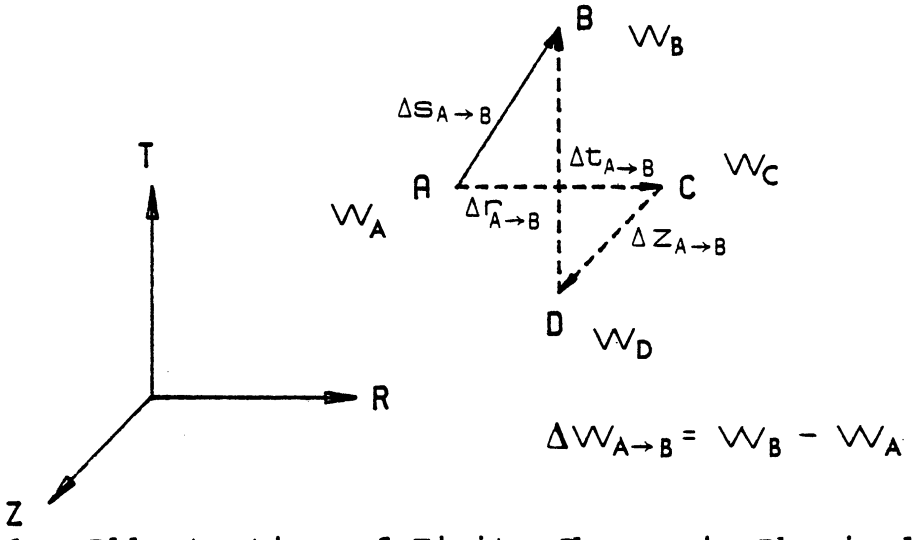

Fig. 3.6: Illustration of Finite Change in Physical Parameter, W, over Path, A→B, in Space and Time Having Components, $\Delta r_{A\to B}$, $\Delta z_{A\to B}$, and $\Delta t_{A\to B}$.

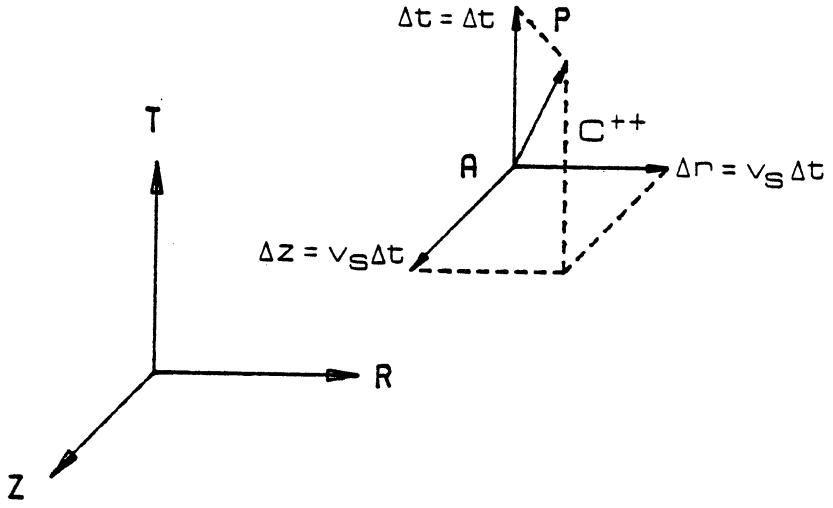

Fig. 3.7: Integration Path (C^{++}) Having Finite Length.

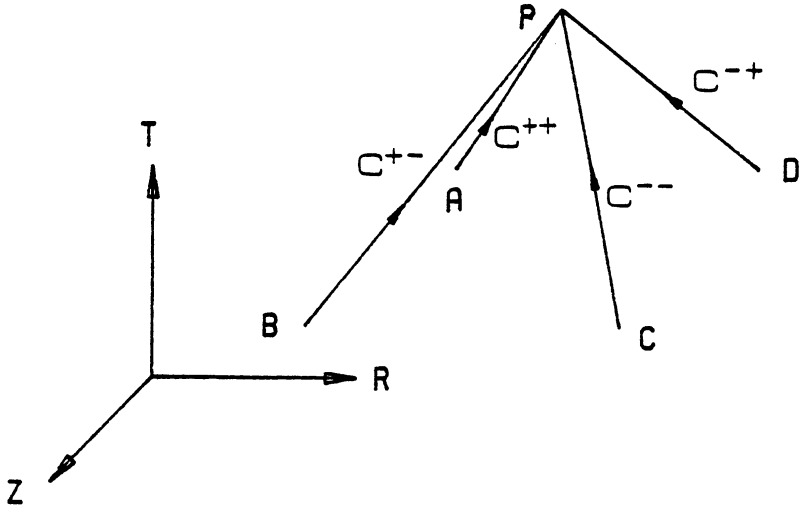

Fig. 3.8: Integration Paths (C^{++}, C^{+-}, C^{-+}, C^{--}) Intersecting at Common Point P.

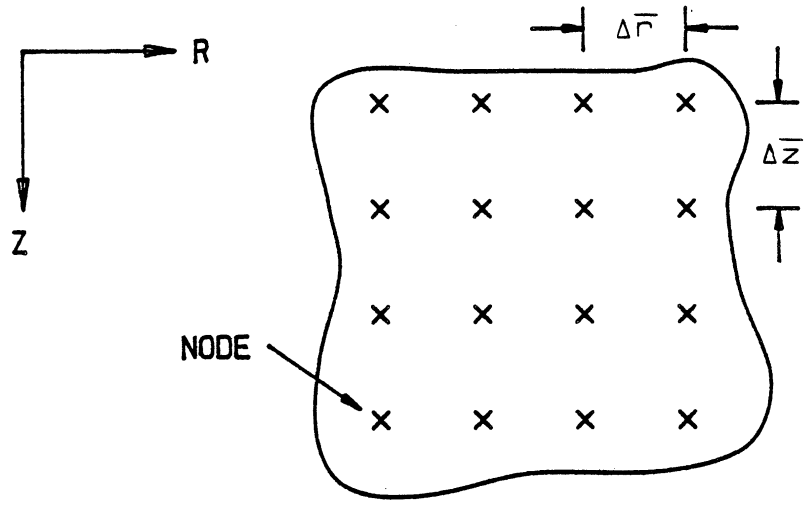

(a) Square Grid

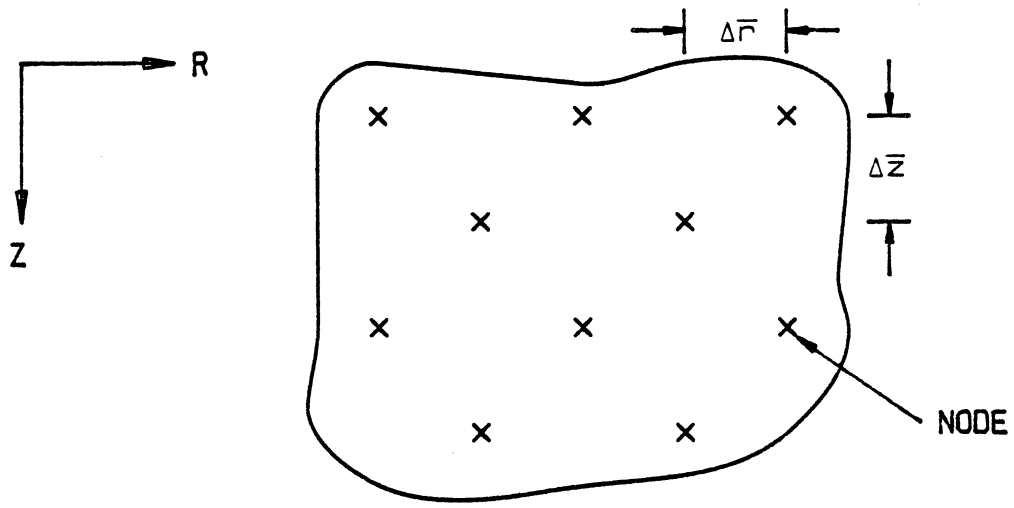

(b) Staggered Grid

Fig. 3.9: Segments of Grids Used to Obtain Numerical Solutions in r-z Planes at Instants in Time.

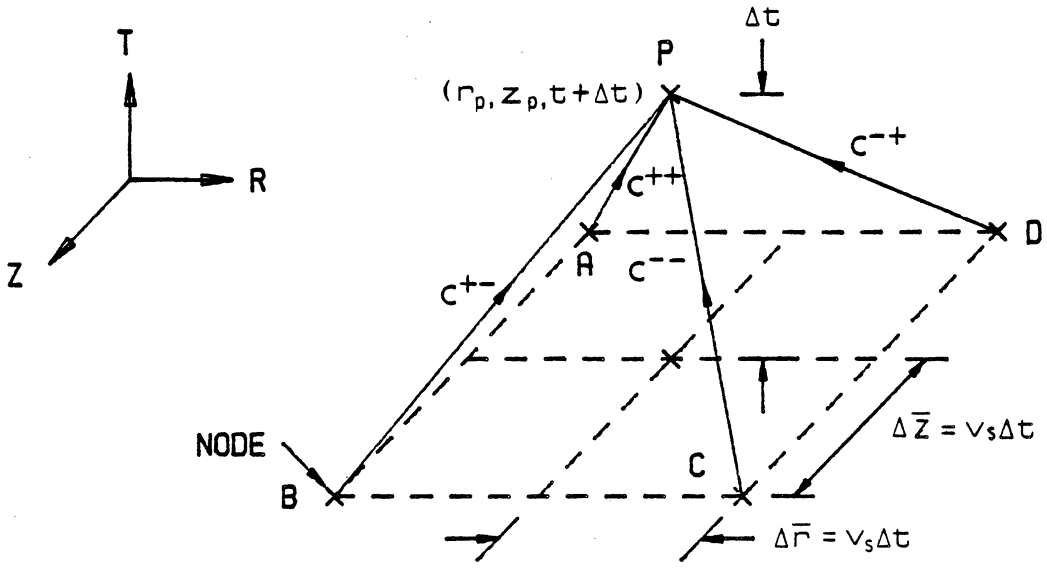

Fig. 3.10: Isolated Computational Cell for Computations at Point P.

CHAPTER IV

EXAMPLES OF LINEAR ELASTIC BEHAVIOR

A. Introduction

In this chapter, numerical solutions obtained using the numerical procedure developed in Chapter III are presented for a number of examples involving torsional wave propagation in a homogeneous, isotropic, elastic continuum. These examples range in difficulty from simple one-dimensional, to complex two-dimensional problems. Each example is discussed from theoretical, physical and numerical standpoints and numerical result are compared with analytical solutions.

B. One-Dimensional Examples

Under certain conditions, one-dimensional shear wave propagation may be approximated by axisymmetric, torsional wave propagation. In the following two sections, these conditions are imposed and one-dimensional shear wave propagation is simulated numerically in the radial and z-directions.

1. Radial Direction

a. Theory -- The propagation of torsional shear waves through the thickness of a thin walled, infinitely long cylinder having a large radius (see Fig. 4.1) approximates one-dimensional shear wave propagation. The thin wall and the large radius reduce the geometric decay of waves due to propagation into a larger area. These torsional waves are generated by applying, uniformly, either τ_r or V disturbances along the inner or outer wall of the cylinder. Only τ_r and V develop within the cylinder and the direction of wave propagation and the mode of deformation are shown in Fig. 4.1.

The known relationship between particle velocity, V, and shearing stress, τ, for plane shear wave propagation, in the absence of reflections, is given as

$$V = \frac{\tau V_s}{G} \tag{4.1}$$

b. Description of Example -- An example was solved numerically in which a time dependent stress was applied uniformly along the inner surface of the cylinder. To demonstrate the treatment of boundaries, the outer wall was fixed uniformly. Using the square

grid shown in Fig. 4.2, a solution was obtained by applying boundary and initial conditions at the nodes of the grid.

Initially, the entire region defined by the grid was undisturbed. At each boundary node two algebraic equations are available from the interior of the medium. Therefore, to obtain a solution at these nodes two independent boundary conditions are needed. The inner boundary was excited by applying a sinusoidally varying shearing stress uniformly along the inner wall of the cylinder. Mathematically, this condition is given by

$$\tau_r = \bar{\tau}_{rm} \sin 2\pi f t \tag{4.2}$$

$$\frac{\partial \tau_r}{\partial z} = 0 \tag{4.3}$$

where $\bar{\tau}_{rm}$ and f are the amplitude and the frequency of the excitation, respectively. The first condition, Eq. (4.2), is a direct boundary condition. The second condition, Eq. (4.3), insures uniformity of the applied stress with respect to depth and is an indirect boundary condition. From this equation a relationship may be obtained between useful unknowns. Rewriting one of the basic equations, Eq. (3.22),

$$\frac{\partial \tau_r}{\partial z} - \frac{\partial \tau_z}{\partial r} + \frac{1}{r}\tau_z = 0 \qquad (3.22)$$

and substituting Eq. (4.3) into Eq. (3.22) gives

$$\frac{\partial \tau_z}{\partial r} = \frac{\tau_z}{r} \qquad (4.4)$$

Equation (4.4) was applied at each node along the inner wall. Note that specifying τ_r to be identical at each of these nodes does not imply that $\partial \tau_r / \partial z = 0$, thus Eqs. (4.2) and (4.3) are independent conditions.

The boundary conditions describing the uniformly fixed outer wall are given by Eq. (4.3) and

$$V = 0 \qquad (4.5)$$

The first condition is an indirect boundary condition leading to the application of Eq. (4.4) at each node along this boundary, and Eq. (4.5) is a direct boundary condition.

Under one-dimensional conditions in the radial direction, behavior does not vary with depth. In order to model this condition, as well as the infinite extensions of the cylinder in depth, values computed along the horizontal center plane of the grid were applied to the upper and lower boundaries.

Considering plane wave propagation in the positive direction of an arbitrary radius, the theoretical one-dimensional response of the medium to the excitation given by Eq. (4.2) is

$$\tau_r(r,t) = \bar{\tau}_{rm} \sin 2\pi f\left(t - \frac{(r-r_i)}{V_s}\right) \qquad (4.6)$$

$$V(r,t) = -\frac{V_s}{G}\,\bar{\tau}_{rm} \sin 2\pi f\left(t - \frac{(r-r_i)}{V_s}\right) \qquad (4.7)$$

where r_i is the radius of the inner boundary. These equations are valid in the absence of reflections and apply behind the plane wavefront, which travels at the shear wave velocity. With the convention used, positive r causes negative V for waves traveling in the positive radial direction.

At a fixed boundary, the stress of an incident wave and its reflection are equal in magnitude and sign. Superimposing these waves gives the theoretical stress at the outer boundary as

$$\tau_r(r_o,t) = 2\bar{\tau}_{rm} \sin 2\pi f\left(t - \frac{(r_o-r_i)}{V_s}\right) \qquad (4.8)$$

where r_o is the radius of the outer boundary. Equation (4.8) is valid prior to the arrival of reflected reflections.

c. Solution of Example -- A numerical solution was obtained using a grid, shown in Fig. 4.2, having 5 rows and 11 columns of nodes. The following values were used for parameters: ρ = 3.11 slugs/ft^3, G = 1,200,000 psf, r_i = 10,000 ft, r_o = 10,006.21 ft, $\bar{\tau}_{rm}$ = 500 psf, f = 300 cps and v_s = 621.17 fps. The wall of the cylinder was thin enough and the radius large enough so that the geometric decay of the dependent variables with increasing radius was negligible.

Numerically and analytically obtained values of τ_r and V are presented in Figs. 4.3 through 4.5. Values of τ_z and $\partial\tau_z/\partial r$ were found to be insignificant, as would be expected, and are not plotted.

Plots of V and τ_r vs. time are given in Fig. 4.3 for a radius of 10,001.242 ft. The finite time prior to the arrival of the disturbance is equal to the time it takes for a disturbance, traveling at the shear wave velocity, to travel from the inner boundary to this radius.

Figure 4.4 gives plots of τ_r and V vs. radius at a given time of 0.0089975 sec. The distance traveled by the wavefront in this time, 5.59 ft., is equal to the distance traveled by a shear wave in this time.

Figure 4.5 gives τ_r vs. time at the rigid boundary. The disturbance also arrives at this boundary at the correct time.

2. Z-Direction

a. Theory--One dimensional shear wave propagation may also be approximated by a shearing disturbance traveling longitudinally along a cylinder having a large radius and a thin wall. With a large radius, the relative changes in the dependent variables for a given change in radius are small and with a thin wall, the differences between the dependent variables at the outer and inner walls are small. Shown in Fig. 4.6 is a segment of such a cylinder which extends infinitely in the positive z-direction from the z = 0 plane. Approximate one-dimensional waves may be generated by applying radially proportional values of τ_z or V to the upper horizontal surface of the cylinder. Only τ_z and V develop within the cylinder and the direction of wave propagation and the mode of deformation is shown in Fig. 4.6.

b. Description of Example--An example was worked using the square grid shown in Fig. 4.7. Initially, the entire region defined by the grid was taken to be free of disturbance. Direct boundary

conditions were applied to each node along the upper surface of the cylinder. The first of these conditions imposed a distribution of particle velocities which varied sinusoidally with time. In this distribution, the particle velocity was proportional to radius, a condition which corresponds to the rotation of the upper plane as a rigid plane about the axis of symmetry. This boundary condition may be expressed as

$$V(r,t) = \omega r \sin 2\pi f t = V_m(r) \sin 2\pi f t \qquad (4.9)$$

where ω is the angular velocity of the rigid rotation and $V_m(r)$ is the amplitude of the particle velocity as a function of radius. There can be no shearing deformation in a rigidly behaving plane, thus, $\gamma_r = 0$ along the upper surface of the cylinder giving the second boundary condition along this surface as

$$\tau_r = 0 \qquad (4.10)$$

The inner and outer boundaries were treated as being uniformly free of τ_r-stress. This condition may be expressed by Eq. (4.3), which leads to Eq. (4.4), and by Eq. (4.10).

For each of the nodes at the intersections between the upper surfaces and the walls, three boundary conditions are needed because only one algebraic

equation is available from within the medium. Equations (4.3), (4.9) and (4.10), which are a combination of boundary conditions from the upper surface and the walls, were applied at these nodes.

The lower boundary models the infinite extension of the cylinder. For one-dimensional propagation in the direction of infinite extension, events taking place in any plane perpendicular to the z-axis, at any given time, take place in any other parallel plane further along the direction of propagation at a later time. This later time is equal to the given time plus the travel time of the wave between these planes. Accordingly, at time $t + \Delta t$ the dependent variables along the lower boundary were assigned the values of the dependent variables computed at time t along the horizontal plane one distance interval above this boundary.

The theoretical, one-dimensional response to the excitation, given by Eq. (4.9), is given as

$$V(z,t) = V_m \sin 2\pi f \left(t - \frac{z}{V_s}\right) \qquad (4.11)$$

and

$$\tau_z(z,t) = -\frac{G V_m}{V_s} \sin 2\pi f \left(t - \frac{z}{V_s}\right) \qquad (4.12)$$

These equations are valid, in the absence of reflections, behind the wavefront which propagates in the positive z-direction at the shear wave velocity.

With the convention used, positive particle velocities result in negative shearing stresses for waves traveling in the positive z-direction.

c. Solution of Example--An example was solved numerically using a square grid having 11 nodal rows with 6 nodes in each row and shown in Fig. 4.7. For this example G = 1,200,000 psf, ρ = 3.11 slugs/ft^3, ω = 0.00005 rad/sec, r_i = 10,000 ft, r_o = 10,001.035 ft, f = 300 cps, and v_s = 621.17 fps.

Results from the numerical solution as well as from the corresponding analytical solution are given in Fig. 4.8 and 4.9. Only curves involving τ_z and V are presented since τ_r and $\partial\tau_z/\partial r$ were found to be negligibly small, as expected. Values of τ_z and V obtained numerically were taken from the inner surface of the cylinder. Because of the large radius and the thin wall of the cylinder, differences between the values of these variables along the inner and outer walls were negligibly small.

In Fig. 4.8, plots of τ_z and V vs. time are given for a depth of 0.207 ft and Fig. 4.9 gives V and τ_z vs. depth at the time 0.00333 sec. As in the preceding example, the wavefront was found to travel at the velocity of a shear wave.

C. Longitudinal Wave Propagation in a Solid Cylinder

In this section, the problem of the propagation of torsional waves along the longitudinal axis of a solid cylinder is studied. In this problem, waves propagate as planes; however, the problem is more complicated than that of one-dimensional wave propagation because the dependent variables vary along the propagating planes. A second feature of this problem is that a solution is obtained in the vicinity of the axis of symmetry.

1. Theory

The application of an axisymmetric distribution of shearing stresses or particle velocities along a plane surface perpendicular to the longitudinal axis of a solid cylinder gives rise to torsional waves which propagate along this axis. The mode of deformation and the direction of wave propagation is shown in Fig. 4.10 which shows a wedge of a solid cylinder excited along its upper suface by a distribution of particle velocity which is proportional to radius.

Kolsky (1963) presents a steady state solution for the propagation of torsional waves along an elastic solid cylinder of infinite length. This solution, obtained by solving the axisymmetric torsional wave

equation, Eq. (3.9), using the separation of variables technique is given as

$$u(r,z,t) = U(r)\, e^{i(\bar{\gamma} z + \bar{\omega} t)} \tag{4.13}$$

where U(r) is the displacement shape in planes perpendicular to the z-axis, $\bar{\gamma}$ is the wave number, λ is the wavelength along the longitudinal axis of the cylinder and $\bar{\omega}$ is the circular frequency of the excitation. Equation (4.13) gives the solution for a wave traveling in the negative z-direction. Numerical solutions were obtained for waves traveling in the positive z-direction and the corresponding theoretical solution, based upon Eq. (4.13), is given as

$$u(r,z,t) = U(r)\, e^{i(\bar{\omega} t - \bar{\gamma} z)} \tag{4.14}$$

Expressing Eq. (4.14) in sinusoidal form by use of Euler's identity gives

$$u(r,z,t) = U(r)\cos(\bar{\omega} t - \bar{\gamma} z) + i\, U(r)\sin(\bar{\omega} t - \bar{\gamma} z) \tag{4.15}$$

Solutions corresponding to the real portion of the response,

$$u(r,z,t) = U(r)\cos(\bar{\omega} t - \bar{\gamma} z) \tag{4.16}$$

were considered and attention was directed towards the first mode of vibration. In this mode the displacements

within all planes perpendicular to the z-axis are proportional to the radius, thus these planes rotate about this axis as rigid disks. In this mode, the displacement shape may be expressed as

$$U(r) = A\,r \tag{4.17}$$

where A is an arbitrary constant.

Several manipulations are carried out to present the solution in a more convenient form. Since $\bar{\gamma} = 2\pi/\lambda$ and $\lambda = V_s/f$,

$$\bar{\gamma} = \frac{2\pi f}{V_s} \tag{4.18}$$

Combining Eqs. (4.16), (4.17), and (4.18) and substituting $2\pi f$ for $\bar{\omega}$ gives

$$u(r,z,t) = A\,r\cos 2\pi f\left(t - \frac{z}{V_s}\right) \tag{4.19}$$

The variables V, τ_r, τ_z and $\partial\tau_z/\partial r$, for which values are obtained in the numerical procedure, may be obtained by differentiating Eq. (4.19) in accordance with basic definitions. For example,

$$\tau_r = G\left(\frac{\partial u}{\partial r} - \frac{u}{r}\right)$$

$$\tau_r = G\left[A\cos 2\pi f\left(t - \frac{z}{V_s}\right) - \frac{A\,r\cos 2\pi f\left(t - \frac{z}{V_s}\right)}{r}\right]$$

Cancelling terms gives $\tau_r = 0$, which is expected in this mode in which deformations are not permitted in planes

perpendicular to the z-axis. The remaining variables are given as

$$\tau_z = G\frac{\partial u}{\partial z} = \frac{2\pi f G A r}{V_s} \sin 2\pi f\left(t - \frac{z}{V_s}\right) \qquad (4.20)$$

$$V = \frac{\partial u}{\partial t} = -2\pi f A r \sin 2\pi f\left(t - \frac{z}{V_s}\right) \qquad (4.21)$$

and

$$\frac{\partial \tau_z}{\partial r} = \frac{2\pi f G A}{V_s} \sin 2\pi f\left(t - \frac{z}{V_s}\right) \qquad (4.22)$$

2. Description of Example

A numerical example was worked using the square grid shown in Fig. 4.11. To avoid divisions by zero in the numerical process, the cylinder was given an inner radius having a very small value. Thus the solid cylinder was approximated by a very thick-walled hollow cylinder. All boundaries as well as the interior region were treated as described in the preceding example. The particle velocities applied to the upper surface of the cylinder correspond to the particle velocities given by Eq. (4.21) along this plane. The initially undisturbed state of the solid cylinder in the numerical solution contrasts the initial state of the cylinder in the steady state analytical solution. The initial state used in the numerical solution was chosen in order to demonstrate the propagation of the wavefront.

3. Solution of Example

A numerical solution was obtained using the following values for parameters: G = 1,200,000 psf, = 3.11 slugs/ft^3, r_i = 0.01 ft, r_o = 1.045 ft, $\bar{\omega}$ = 0.04784 rad/s, and f = 300 cps. Numerically and analytically obtained values for the variables V, τ_z and $\partial\tau_z/\partial r$ are plotted in Figs. 4.12 to 4.14. The variable, τ_r, was not plotted since it was found to be insignificant, as expected from theory. The numerical solution gives the theoretical solution for all variables along the plane of excitation for all time, indicating that the upper boundary used in the numerical solution models effectively the influence of the upper semi-infinite portion of the cylinder, $z < 0$, which is present in the analytical model.

In Figs. 4.12 and 4.14(a) are shown plots of V, τ_z and $\partial\tau_z/\partial r$ as functions of time at a depth of 0.207 ft and a radius of 0.838 ft. The steady state theoretical solution was compared to the numerical solution for times greater than the arrival time of the disturbance at this depth, and the agreement indicates that steady state conditions were developed immediately in the numerical solution. The repetition of the response in Figs. 4.12 and 4.14(a), after one cycle, indicates that the response is identical whether the wave

propagates into a disturbance-free field or into a field corresponding to steady state conditions.

The plots of Figs. 4.13 and 4.14(b) give numerical and analytical solutions for the variables V, τ_z and $\partial\tau_z/\partial r$ as functions of depth for a time of 0.00333 sec and a radius of 0.631 ft. All comparisons were made behind the wavefront of the numerical solution and this wavefront was found to travel at the velocity of shear waves.

D. Two-Dimensional Examples

The most complex solutions of the axisymmetric torsional wave equation are two-dimensional solutions in which all dependent variables are nonuniform functions of all possible independent variables, and in which wave propagation is nonplanar. Two examples of this type of solution are presented in the following sections. Each of these examples involves the steady state response of a homogeneous, isotropic, linearly elastic half space. In the first example, a sinusoidal point torque is applied to the surface of a half space and in the second, a sinusoidal angular displacement is applied to a rigid massless disk attached to the surface of the half space. Numerical and analytical solutions are presented for each example.

1. Torsional Point Source

a. Theory--A portion of a half space is shown in Fig. 4.15 to show the manner in which waves propagate from a torsional point source acting on the surface of the half space. In response to steady state, sinusoidal excitation, alternating crests and troughs in the dependent variables propagate at the shear wave velocity within the half space. In accordance with Huygens' principle and as shown in region ABCD, some distance from the point source in Fig. 4.15, these crests and troughs propagate as circles perpendicular to rays extending from the point source. The dependent variables are not uniform in value along these crests and troughs.

Reissner (1937) presents the steady state displacements within a linearly elastic, isotropic, homogeneous half space loaded by a sinusoidal point torque, $M_p \cos \bar{\omega} t$, applied to the surface of the half space. This solution represents an approximation which improves with distance from the source and is given as

$$u(r,z,t) = \frac{M_p}{4\pi G} \frac{r}{r^2+z^2} \left\{ k_o \sin[\bar{\omega} t - k_o (r^2+z^2)^{1/2}] + \frac{1}{(r^2+z^2)^{1/2}} \cos[\bar{\omega} t - k_o (r^2+z^2)^{1/2}] \right\} \quad (4.23)$$

where M_p is the magnitude of the applied torque and $k_o = \bar{\omega}\sqrt{\rho/G}$. The variables V, τ_r, τ_z and $\partial\tau_z/\partial r$, which are obtained in the numerical solution, may be obtained from the analytical solution by differentiating Eq. (4.23) in accordance with basic definitions. These variables are given as

$$\tau_r = G\left(\frac{\partial u}{\partial r} - \frac{u}{r}\right) = \frac{M_p}{4\pi}\left\{\left[-\frac{r^2 k_o}{(r^2+z^2)^2}\right]\sin\left[\bar{\omega}t - k_o(r^2+z^2)^{1/2}\right] - \left[\frac{(3r^2)/(r^2+z^2) + r^2k_o^2}{(r^2+z^2)^{3/2}}\right]\cos\left[\bar{\omega}t - k_o(r^2+z^2)^{1/2}\right]\right. \tag{4.24a}$$

$$\tau_z = G\frac{\partial u}{\partial z} = \frac{M_p}{4\pi}\left\{\left[-\frac{rzk_o}{(r^2+z^2)^2}\right]\sin\left[\bar{\omega}t - k_o(r^2+z^2)^{1/2}\right] + \left[-\frac{rzk_o^2}{(r^2+z^2)^{3/2}} - \frac{3rz}{(r^2+z^2)^{5/2}}\right]\cos\left[\bar{\omega}t - k_o(r^2+z^2)^{1/2}\right]\right\} \tag{4.24b}$$

$$\frac{\partial\tau_z}{\partial r} = \frac{M_p}{4\pi}\left\{\left[-\frac{z^3k_o}{(r^2+z^2)^3} - \frac{r^2zk_o^3}{(r^2+z^2)^2}\right]\sin\left[\bar{\omega}t - k_o(r^2+z^2)^{1/2}\right] + \left[\frac{-z^3k_o^2 + 3r^2zk_o^2}{(r^2+z^2)^{5/2}} - \frac{3z^3 - 12zr^2}{(r^2+z^2)^{7/2}}\right]\cos\left[\bar{\omega}t - k_o(r^2+z^2)^{1/2}\right] \tag{4.24c}$$

$$V = \frac{\partial u}{\partial t} = \frac{Mp}{4\pi G}\left\{\left[\frac{r k_o \bar{\omega}}{r^2+z^2}\right]\cos\left[\bar{\omega}t - k_o(r^2+z^2)^{1/2}\right] - \left[\frac{r\bar{\omega}}{(r^2+z^2)^{3/2}}\right]\sin\left[\bar{\omega}t - k_o(r^2+z^2)^{1/2}\right]\right. \qquad (4.24d)$$

b. Description of Example--A numerical solution was obtained within region ABCD, shown in Fig. 4.15, using the staggered grid. A segment of this grid is shown in Fig. 3.9(b). In the staggered grid suggested by Wylie (1979), much fewer computations are needed than in an equivalent square grid which actually consists of two independent staggered grids offset from one another by one distance interval.

For the initial conditions, the theoretical solution, Eqs. (4.24), was applied over the entire region and boundaries of square ABCD. After the initial time, the theoretical solution was applied only along boundaries AB, BC, and CD of this square. The boundary AD, along the free surface, was described by the following direct boundary conditions:

$$\tau_z = 0 \tag{4.25}$$

$$\frac{\partial \tau_z}{\partial r} = 0 \tag{4.26}$$

A numerical solution was obtained for a time span of sufficient length to demonstrate cyclic behavior. A satisfactory numerical solution was one which agreed with theory for the duration of a cycle and returned to the initial state after one cycle.

c. Solution of Example--An example was solved using the following parameters: M_p = 1000 ft-lb, G = 700253 psf, ρ= 3.17 slugs/ft^3 and f = 300 cps. The period of the excitation was 0.00333 sec and a solution was obtained for a time span of 0.0035 sec.

One wavelength, λ, is 1.56 ft in length and corner A of region ABCD, shown in Fig. 4.15, is three wavelengths, 4.68 ft, from the z-axis. Each edge of this square region is three wavelengths in length and, as shown in Fig. 4.16, a grid having 31 rows, each consisting of 31 nodes, was used to obtain a solution. A square subregion having edges one wavelength in length and located centrally within region ABCD is unaffected, for the duration of the first cycle, by the excitation applied to the boundaries of region ABCD. This is

because it takes a minimum time of one period of the excitation for a disturbance originating along the boundaries of region ABCD to reach this subregion.

Values of the variables, τ_z, τ_r, V, and $\partial\tau_z/\partial r$, at the initial state, as obtained from the analytical solution and the values of these variables at a time equal to one period of the excitation, as obtained numerically and analytically, are plotted in Figs. 4.17 and 4.18. All values presented in these figures were obtained either along lines 1-1 or 2-2 contained in region ABCD shown in Fig. 4.15.

Figures 4.17(a) and (b) show τ_z, τ_r, V and $\partial\tau_z/\partial r$ as functions of radius at a constant depth of 2.34 ft, along line 1-1 shown in Fig. 4.15. Along this line the numerical solution returns to the initial state at the end of one cycle and similar agreement between analytical and numerical results is observed at intermediate times.

As shown in Figs. 4.17(a) and (b), the apparent wavelength of the disturbance along line 1-1 is relatively short. This is because, as shown in Fig. 4.15, line 1-1 cuts primarily across the crests and troughs of the waves. Since line 1-1 is located near the surface of the half space along which $\tau_z = 0$, the quantity τ_z is found to be much smaller in magnitude along line 1-1

than τ_r. Also apparent in Figs. 4.17(a) and (b) is the significant geometric decay of each of the dependent variables with increasing radius.

Figures 4.18(a) and (b) show τ_z, τ_r, V and $\partial\tau_z/\partial r$ as functions of depth at a constant radius of 7.02 ft, along line 2-2 shown in Fig. 4.15. The agreement between numerical and analytical results is similar to that found along line 1-1.

As shown in Figs. 4.18(a) and (b), the values of the variables along line 2-2 have a longer apparent wavelength than those along line 1-1 since line 2-2 cuts primarily along the crests and troughs of the waves. Near the surface, τ_z is small because the surface is stress-free, and τ_r is large. At the surface the velocity does not change with depth. This is because at the surface $\gamma_z = 0$ and therefore the rate of change of displacement with depth, $\partial u/\partial z$, and also the rate of change of velocity with depth are equal to zero.

2. Massless Disk on Half Space

a. Theory--As shown in Fig. 4.19, if a rigid, massless disk, attached to the surface of an elastic half space, rotates about the axis of symmetry, an axisymmetric distribution of τ_z-shearing stresses develops within the half space along the disk-half space

interface. The resultant moment of these stresses about the axis of symmetry gives the torsional reaction or resistance of the half space to rotation of the disk. Motion of the disk also causes an axisymmetric torsional wavefield to propagate within the half space and since the disk has a finite area, this wavefield propagates from the disk in ellipse-like fronts in accordance with Huygens' principle.

Sagoci (1944) presents a steady state solution giving the response of an isotropic, homogeneous, elastic half space to the forced rotations of a rigid massless disk attached to the surface of the half space. This solution was derived from a general solution giving the displacement field of a half space obtained by solving the axisymmetric torsional wave equation, Eq. (3.9), using the separation of variables technique and oblate spheroidal coordinates. This displacement field is a complicated function of position, time, elastic properties of the half space, exciting frequency and the radius of the disk, and is given as

$$u = \epsilon^{i\bar{\omega}t} \sum_{\ell}^{\infty} A_{\ell} S_{1\ell}(-ic, \eta) R_{1\ell}(-ic, i\xi) \tag{4.27}$$

where

$$c = \bar{r}_o \bar{\omega} \sqrt{\frac{\rho}{G}} \tag{4.28}$$

$\bar{r}_o$ is the radius of the disk, A_ℓ is an arbitrary amplitude constant, η and ξ are oblate spheroidal coordinates which are related to the r- and z-coordinates, $S_{1\ell}(-ic, \eta)$ is an angular wave function, and $R_{1\ell}(-ic, i\xi)$ is a radial wave function. The angular and the radial wave functions are infinite series in which the terms are multiples of tabulated numerical coefficients for oblate spheroidal wave functions and associated Legendre polynomials and Bessel functions, respectively.

The forcing function imposed on the disk is given as

$$\phi(t) = \bar{\Phi}\, e^{i\bar{\omega}t} \tag{4.29}$$

where $\bar{\omega}$ is the circular frequency of the excitation, $\phi(t)$ is the angular displacement of the disk, and $\bar{\Phi}$ is the amplitude of this angular displacement. By introducing Eq. (4.29) into Eq. (4.27) an expression was obtained giving the displacement field of the half space in response to the forcing function given by Eq. (4.29). Sagoci obtained the τ_z-stress distribution along the interface by differentiating this expression for the displacement field with respect to z, evaluating the resulting expression along the interface, and substituting this result into the basic relationship, Eq.

(3.7). The expression for the τ_z-stress along the interface is given as

$$\tau_z = \frac{2}{3} \Phi G (-F_2 \cos \bar{\omega} t + F_1 \sin \bar{\omega} t) \tag{4.30}$$

where F_1 and F_2 are infinite series involving angular and radial wave functions. Physically, $-F_2$ and F_1, which are functions of the properties of the half space, the excitation frequency, and indirectly functions of radius, are measures of the components in- and 90° out-of-phase, respectively, with the excitation, Eq. (4.29). The magnitude of τ_z, $|\tau_z|$, may be obtained from Eq. (4.30) and is given as

$$|\tau_z| = \frac{2}{3} \Phi G \sqrt{F_1^2 + F_2^2} \tag{4.31}$$

Sagoci also obtained the resultant moment of the τ_z-stress distribution, M_R, by integrating the incremental moment, caused by τ_z acting over an infinitesimally thin ring centered on the z-axis, over the radius of the disk. This integration may be expressed as

$$M_R = \int_0^{\bar{r}_o} \tau_z (2\pi r^2) dr \tag{4.32}$$

From this integration, Sagoci obtained the following relationship between the amplitude of this resultant moment, $|M_R|$, and the angular displacement of the disk:

$$\phi = \frac{9|M_R|}{16\pi G \bar{r}_o^3} (\beta^2 + \gamma'^2)^{-1/2} \cos(\bar{\omega}t - \Delta) \tag{4.33}$$

where β and γ' are infinite series involving the radial wave functions and the numerical coefficients for the oblate spheroidal wave functions, and Δ is the phase shift between ϕ and M_R. In order to compare numerical and analytical solutions, an equation relating the amplitudes of the resultant moment and the angular displacement was obtained from Eq. (4.33) and is given as

$$|M_R| = \frac{16\pi G \bar{r}_o^3 \Phi \sqrt{\beta^2 + \gamma'^2}}{9} \tag{4.34}$$

Only a few terms were evaluated in each of the series, F_1, F_2, γ' and β, thus the values of $|\tau_z|$ and $|M_R|$ obtained from Eqs. (4.31) and (4.34) are approximate. Sagoci gives a discussion of the accuracy of his solutions, and some of this discussion is paraphrased herein. The accuracy of each series depends upon the value of the quantity c as determined by Eq. (4.28). As c decreases, the accuracy of the values of F_1 and F_2 increase but the convergence of F_2 is much less rapid than that of F_1. In the numerical example which was studied, the parameters were chosen such that the value of F_2 was much larger than that of F_1; thus, the

accuracy of the theoretical solution to which the numerical solution was compared was controlled by F_2. Sagoci stated that 1.0 is the largest value of c for which the value of F_2, a function of radius, is known to within 4 or 5 percent. The parameters in the numerical example were chosen to give a value of 1.0 for c; thus, the corresponding theoretical value of $|\tau_z|$, obtained from Eq. (4.31) and also a function of radius, is also known to within approximately 4 or 5 percent.

The γ' and β series each have two terms and the values of these series are known fairly accurately. For c = 2.0, the values of the second terms of the γ' and β series are 8.8×10^{-3} percent and 3.2 percent of the values of the total two-term γ' and β series, respectively, whereas for c = 0.2 the values of the second terms of each of these series are negligible fractions of the values of the total series. Therefore, for c = 1.0, the value of $|M_R|$, obtained from Eq. (4.34), is quite accurate.

b. Description of Examples--Examples were solved numerically using the staggered grid shown in Fig. 4.20. The region in which a solution was obtained is also shown schematically in Fig. 4.21. The motion of the rigid, massless disk was modeled by imposing rigid

rotations on the surface of the half space along the interface, AB in Fig. 4.20. To obtain the particle velocities along the interface corresponding to the rotation of the rigid disk given by Eq. (4.29), this equation was differentiated with respect to time and then multiplied by radius. The real portion of these particle velocities is given as

$$V = r\frac{d\phi}{dt} = -r\,\Phi\,\bar{\omega}\sin\bar{\omega}t \tag{4.35}$$

Since deformations are not permitted along the interface, the second boundary condition along the interface is given as

$$\tau_r = 0 \tag{4.10}$$

The boundary conditions along the free surface, BC in Fig. 4.20, are

$$\tau_z = 0 \tag{4.25}$$

$$\frac{\partial \tau_z}{\partial r} = 0 \tag{4.26}$$

For an axisymmetric displacement field to be continuous along the axis of symmetry, displacements and, therefore, $\partial u/\partial z$ and $\partial u/\partial t$ must approach zero as the radius approaches zero. Since these derivatives define γ_z and V, respectively, the inner boundary

conditions, applied along line AE in Fig. 4.20, may be expressed as

$$\tau_z = 0 \tag{4.25}$$

$$V = 0 \tag{4.5}$$

To avoid division by zero in the numerical procedure, an insignificantly small radius must be assigned to the inner boundary.

To reduce computational storage space and time, a floating boundary, CDE in Figs. 4.20 and 4.21, was used. With this scheme, computations are carried out only over region ACDE, which is initially given as line AB. The grid functions in two modes. In the expanding mode, numerical front CD advances horizontally while numerical front ED advances vertically, each at the shear wave velocity. A contracting mode is initiated by simultaneously reversing the direction of motion of the two floating boundaries at a time such that at the instant the grid returns to its original state, all required information has been obtained at the disk. In either mode, computations are always based upon a correct set of nodal values.

The relationship between the numerical fronts of an expanding grid and the curved physical wavefront, as

derived from Huygens' principle, is shown in Fig. 4.21 for some instant of time. Along rays 1, 5 and 6, also shown in this figure, the numerical front and the physical wavefront travel together. Along rays 2, 3, and 4, however, the numerical front extends beyond the physical front, and therefore, in the region of these rays, computations are carried out ahead of the wavefront. To examine why computations must be carried out ahead of the physical wavefront in some directions, an isolated C^{++} path, along which Eq. (3.34a) is integrated, is shown in Fig. 4.22 projected onto the r-z plane. From Eqs. (3.33) each of the spatial coordinate components of this path for a given time increment, Δt, are given as $v_s \Delta t$. Based upon these components, the spatial length of the C^{++} path, as shown in Fig. 4.22, is given as

$$\Delta s = \sqrt{2}\, v_s \Delta t \tag{4.36}$$

Dividing Eq. (4.36) by Δt gives the rate at which the integration takes place in space along the C^{++} path:

$$\frac{\Delta s}{\Delta t} = \sqrt{2}\, v_s \tag{4.37}$$

Similar results may be obtained for each of the remaining integration paths. Thus within a single computation cell and also within an entire grid

information is transmitted at the shear wave velocity in the coordinate directions, at $\sqrt{2}\, v_s$ in a direction $\pm$ 45° to the coordinate directions and at an intermediate rate in all other directions. In the example involving a torsional point source, disturbances within the half space propagate in directions other than those of the coordinate axes. The agreement between theory and numerical results in that example confirms, for steady state conditions, the concept of integrating at a rate greater than the wave velocity.

c. Solutions of Examples--Numerical solutions were obtained using the following values for parameters: G = 700253 psf, ρ = 3.17 slugs/ft^3 $\bar{r}_o$ = 0.3334 ft, r_i = 0.0001 ft, $\bar{\omega}$ = 0.77557 rad/sec and f = 224.43 cps. With these values, the value of c, from Eq. (4.28), is 1.0. Using the grid scheme shown in Fig. 4.20, solutions were obtained using grids having 5, 15, 25, 35, and 45 distance intervals or 3, 8, 13, 18, and 23 nodes along the interface. The items which are examined include the distribution of τ_z-shearing stresses along the interface, the resultant moment of these stresses and the propagation of the disturbance within the half space.

The application of the particle velocity distribution, given by Eq. (4.35), to the interface gives a constant and a steady state oscillating component in the angular displacement of the interface. Transient as well as constant and steady state oscillating components appear in the stress distribution along the interface and in the resultant moment of this stress distribution. The theoretical solutions, Eqs. (4.31) and (4.34) relate only the amplitudes of steady state oscillating quantities. To compare numerical results to theory, it was necessary to subtract the constant components from the numerical steady state solutions in order to obtain the required numerical steady state oscillating components.

In the examples, the amplitude of the oscillating component of the angular displacement of the disk was 0.00055 rad. The shearing stress at the interface at the radius of 0.26674 ft. is plotted in Fig. 4.23 as a function of time for each analysis. The rough behavior in the solution obtained using the coarsest grid is characteristic of an inadequate grid. In each analysis, computations were carried out only for a time span of sufficient length to determine the amplitude of the steady state oscillating component. Results using the two coarsest grids were obtained for a period of

0.0095 sec. Using the horizontal dashed lines in Fig. 4.23 for assistance in relating peaks to peaks and troughs to troughs, this figure shows that steady state conditions were developed either at or prior to the time of the first peak. In order to insure that the value of the first trough had stabilized, the analysis using 25 distance intervals along the interface was conducted for a time span sufficient to include this trough, 0.005 sec. Since this trough was found to stabilize, it was only necessary to obtain the first peak in the remaining solutions to obtain the desired steady state oscillating components.

The results given in Fig. 4.23 indicate a convergence to a limiting stress vs. time curve with increasing fineness of the grid. Convergence is further demonstrated in Fig. 4.24, which gives the amplitude of the steady state oscillating component of the shearing stress at the interface at a radius of 0.26674 ft as a function of the number of distance intervals along the interface. The theoretical value of this amplitude is also shown in this figure and using the finest grid, the value of the numerically obtained amplitude is within 3.5 percent of this theoretical value. In his discussion on accuracy, Sagoci states that as the number of terms in the F_2 series, the dominant series in this

example, is increased, the magnitude of F_2 as a function of radius is expected to increase. From Eq. (4.31) it follows that the theoretical amplitude of the stress given in Fig. 4.24 is underestimated and thus the estimate of the error in the numerical solution is conservative.

The amplitude of the steady state oscillating component of the shearing stress is plotted in Fig. 4.25 as a function of the dimensionless radius, r/R_o, along the interface for the theoretical solution and two numerical solutions; one using a relatively coarse grid and the other using the finest grid. The quantity R_o is the radius of the disk and for radii less than R_o, as the fineness of the grid is increased the numerical solution approaches the theoretical solution. In Fig. 4.26, the percentage difference between the theoretical stress amplitudes and the numerically obtained stress amplitudes, using the finest grid, is given as a function of the dimensionless radius along the interface. As shown in this figure, the accuracy of the numerical solution is greatest for radii some distance from the center and the edge of the disk. At the edge of the disk, because displacements are assumed to be continuous within the half space, the theoretical amplitude of the

stress is infinite and the numerical procedure cannot give this result.

In order to determine the resultant moment of the shearing stress distribution along the interface, Eq. (4.32) was evaluated numerically using the following relation:

$$M_R(t+\Delta t) = \sum_{i=1}^{n} (2\pi \bar{r}_i \Delta r) \tau_{zi}(t+\Delta t) r_i \qquad (4.38)$$

where i refers to the ith node along the interface, $\bar{r}_i$ is the radius of this node, $\tau_{zi}(t + \Delta t)$ is the stress at this node, Δr is the finite width of a ring the thickness of which is centered on the ith node and the center of which is centered on the axis of symmetry and n is the number of nodes along the interface. The value of Δr is equal to the length of two distance intervals.

The resultant moment of the stress distribution along the interface as obtained numerically is shown in Fig. 4.27 as a function of time for each analysis. These curves are similar to those given in Fig. 4.23 for shearing stresses because the shearing stresses along the interface and the resultant moment of these shearing stresses are directly related. As shown in Fig. 4.27, the resultant moment vs. time curve approaches a limiting value with increasing grid fineness.

The amplitude of the resultant moment vs. the number of distance intervals along the interface is given in Fig. 4.28 along with the theoretical value of this amplitude. The value of this amplitude as obtained numerically using the finest grid is within 3.5 percent of the theoretical value which is known fairly accurately.

Sagoci did not obtain information concerning the propagation of waves within the half space from his solution; thus, such information obtained from the numerical solution is not compared with a theoretical solution. One objective in studying the propagation of waves within the half space is to determine whether the numerically obtained wavefront travels at the correct speed even though the rate at which information is transmitted within a grid is generally greater than the wave speed. In Figs. 4.29 and 4.30 are shown the particle velocities, obtained using the grid having 15 distance intervals along the interface, as functions of distance along various rays within the half space at an instant of time, 0.00268 sec. These rays, originating from point B in Fig. 4.21 and designated 2, 3 and 4, are rays along which computations are carried out ahead of the physical wavefront as located by Huygens' principle. As shown in Figs. 4.29 and 4.30 the agreement between

the location of this physical wavefront and the location at which particle velocities become significant is quite good along each ray.

Wavefronts may be viewed as locations along which discontinuities may occur in the first derivatives of the dependent variables. In the development of the equations upon which the numerical procedure is based it was assumed that the first derivatives of the dependent variables were continuous. Thus, in obtaining a numerical solution, the entire solution region, which generally includes wavefronts, is treated as having continuous first derivatives. If, theoretically, discontinuities in derivatives exist, the numerical procedure is an approximation with respect to this factor. A second objective, then, in studying the propagation of waves within the half space would be to evaluate the adequacy of this approximation. However, since a theoretical solution giving the propagation of transient disturbances within a half space was not found this second objective was not carried out.

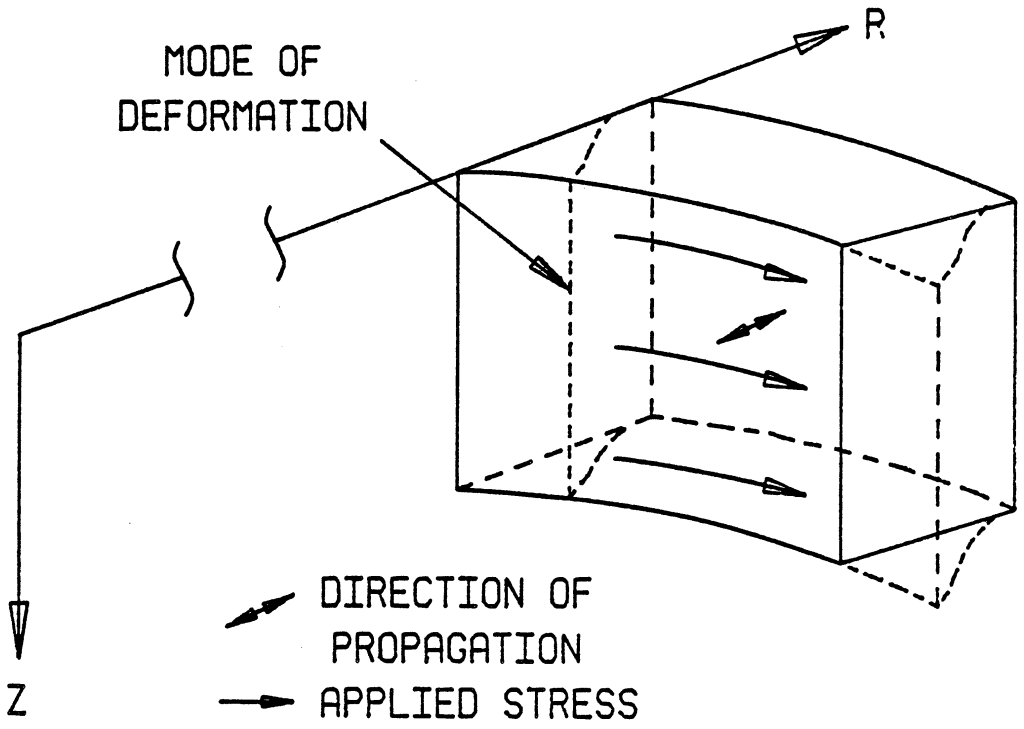

Fig. 4.1: Radial Wave Propagation: Segment of Infinitely Long Cylinder Having Large Radius.

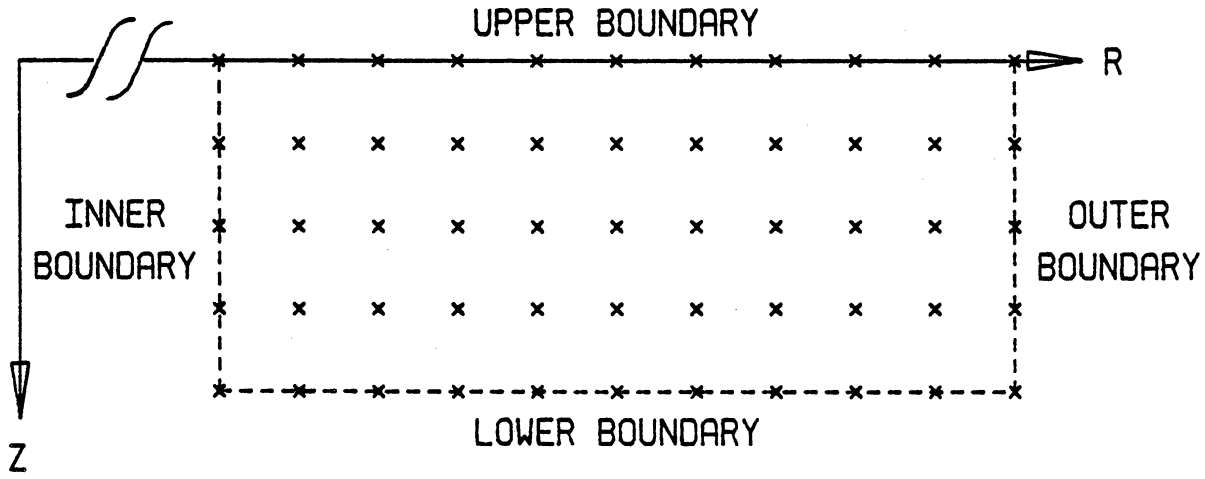

Fig. 4.2: Square Grid Used for Example of One-Dimensional Radial Propagation of Shear Waves.

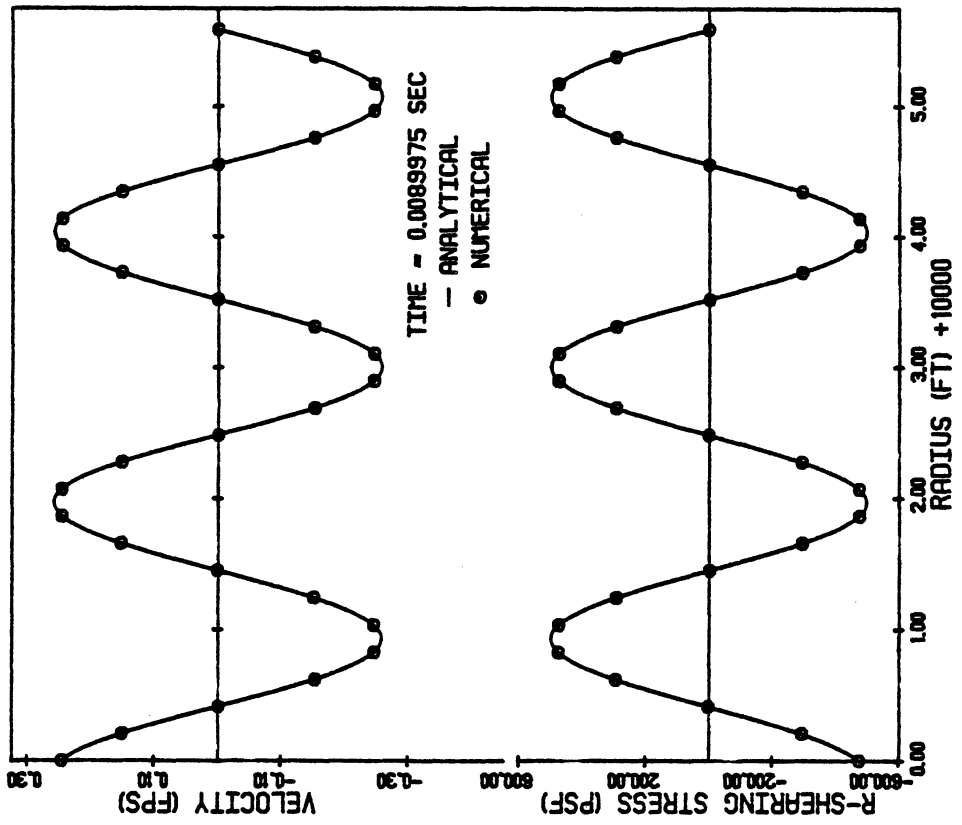

Fig. 4.4: Radial Wave Propagation: Dependent Variables vs. Radius at Time of 0.00899 sec.

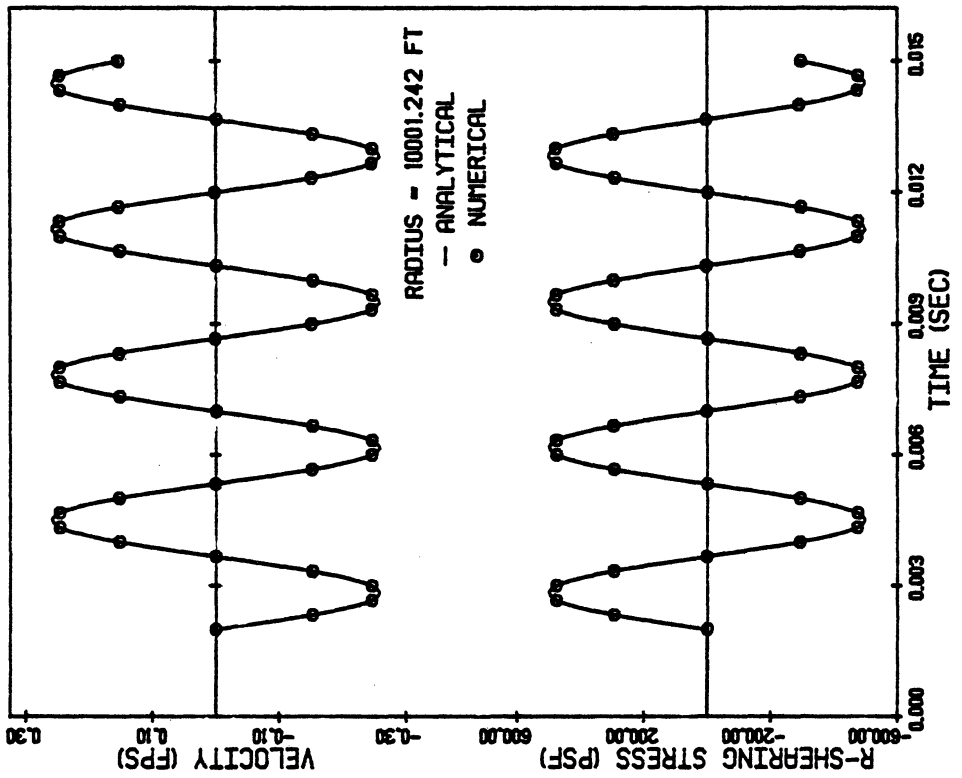

Fig. 4.3: Radial Wave Propagation: Dependent Variables vs. Time at r = 10001.242 ft.

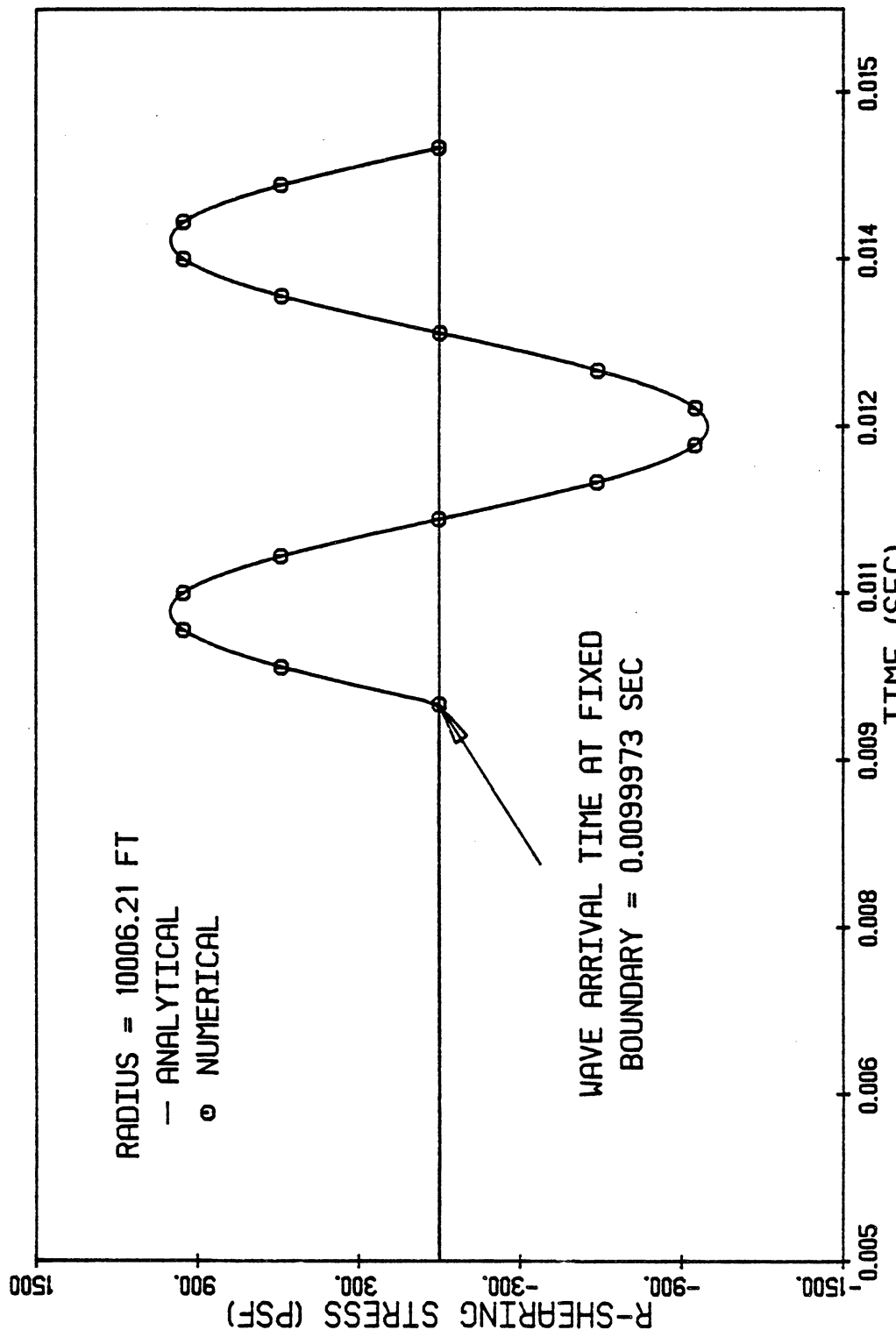

Fig. 4.5: Radial Wave Propagation: Dependent Variables vs. Time at Fixed Outer Boundary.

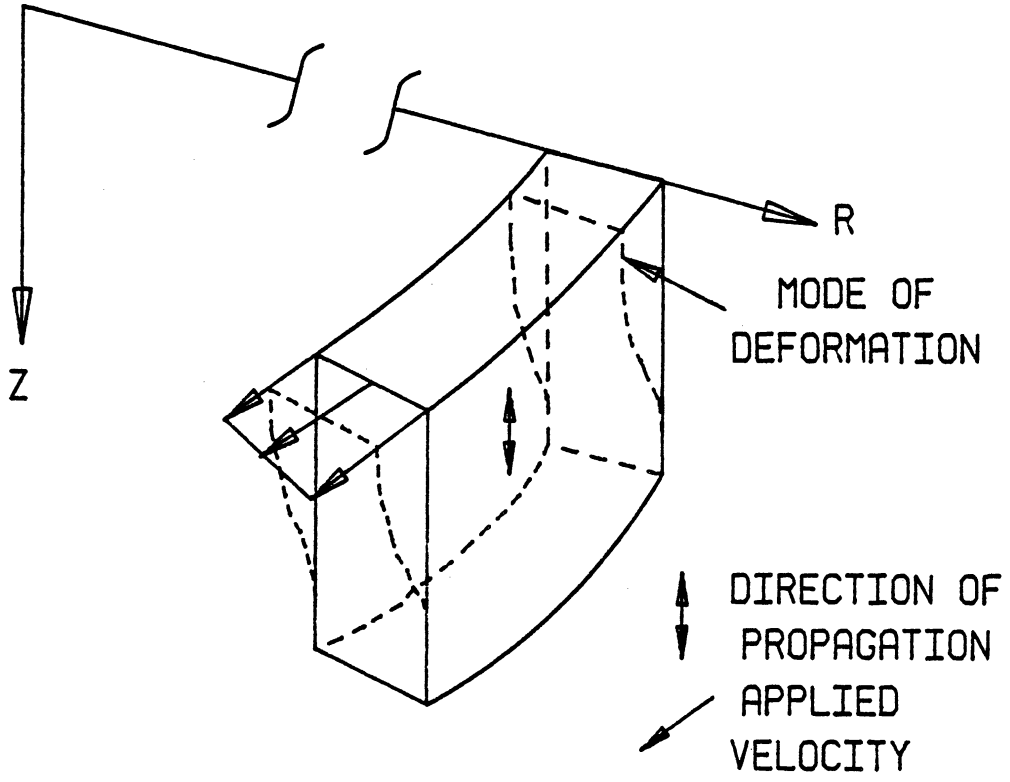

Fig. 4.6: Propagation of Waves in z-Direction: Segment of Thin-Walled Cylinder Having Large Radius.

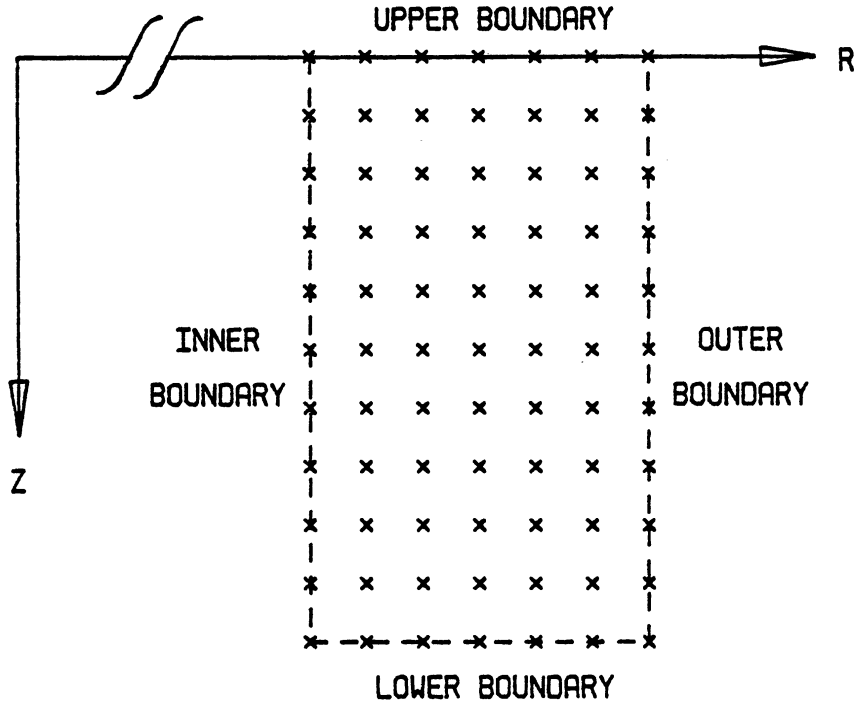

Fig. 4.7: Square Grid Used for Example of One-Dimensional Propagation of Shear Waves in z-Direction.

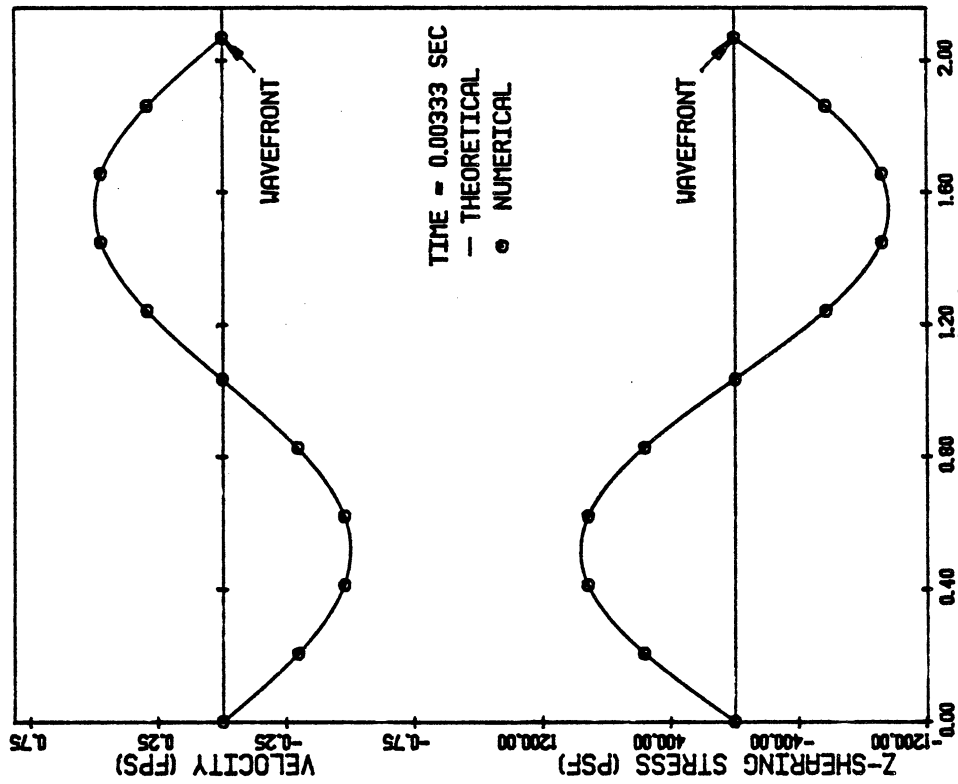

Fig. 4.9: Propagation of Waves in z-Direction: Dependent Variables vs. z at Time of 0.00333 sec.

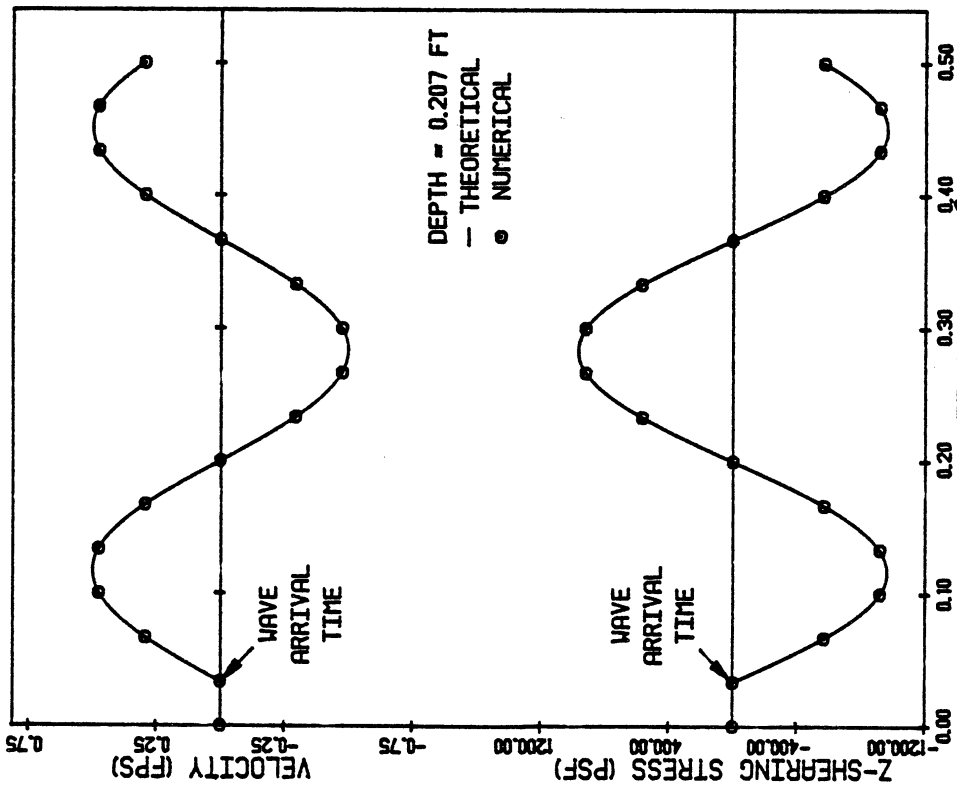

Fig. 4.8: Propagation of Waves in z-Direction: Dependent Variables vs. Time at z = 0.207 ft.

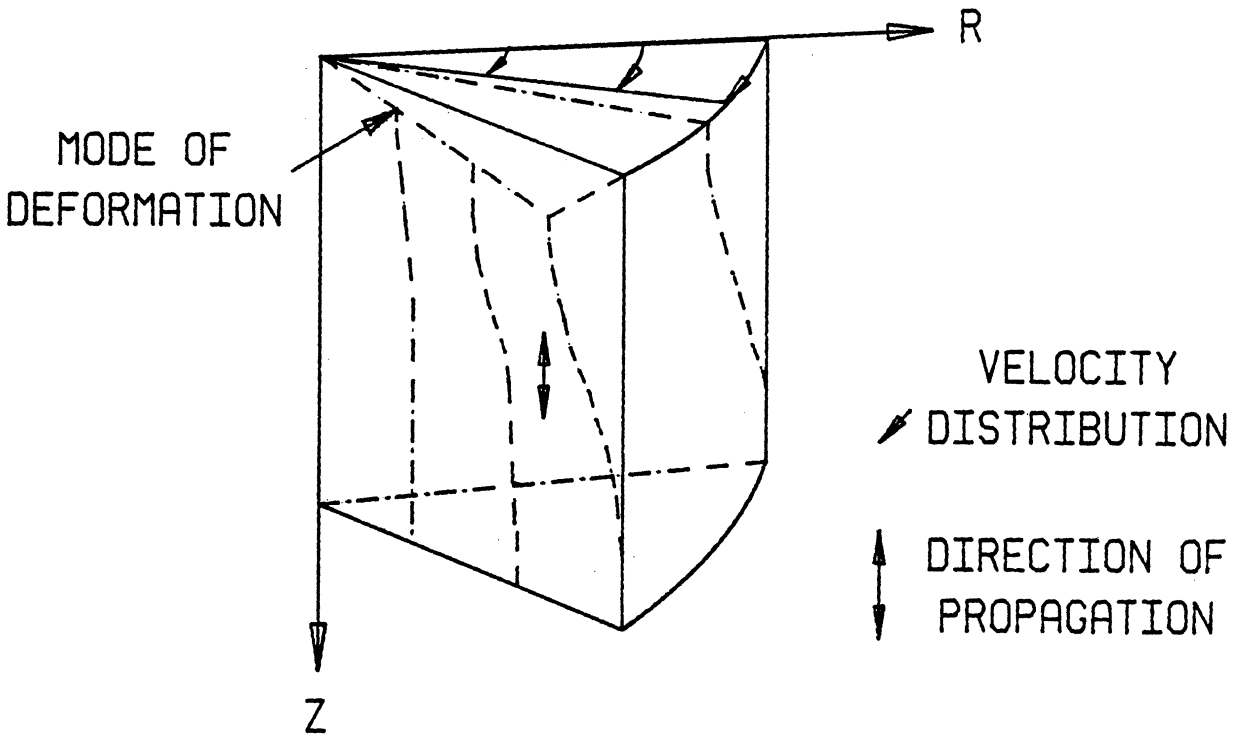

Fig. 4.10: Longitudinal Wave Propagation: Slice of Solid Cylinder.

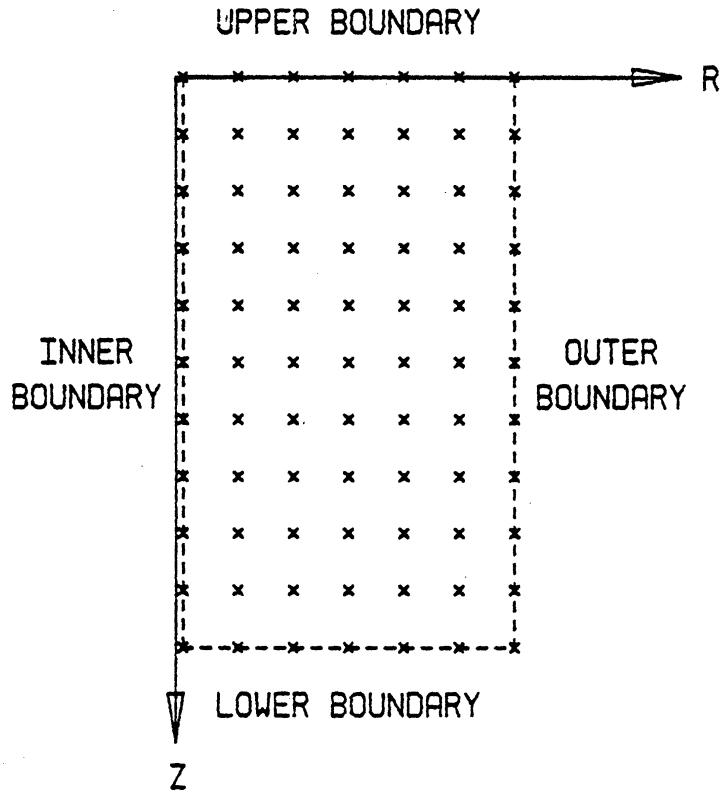

Fig. 4.11: Square Grid Used for Example of Longitudinal Wave Propagation in Solid Cylinder.

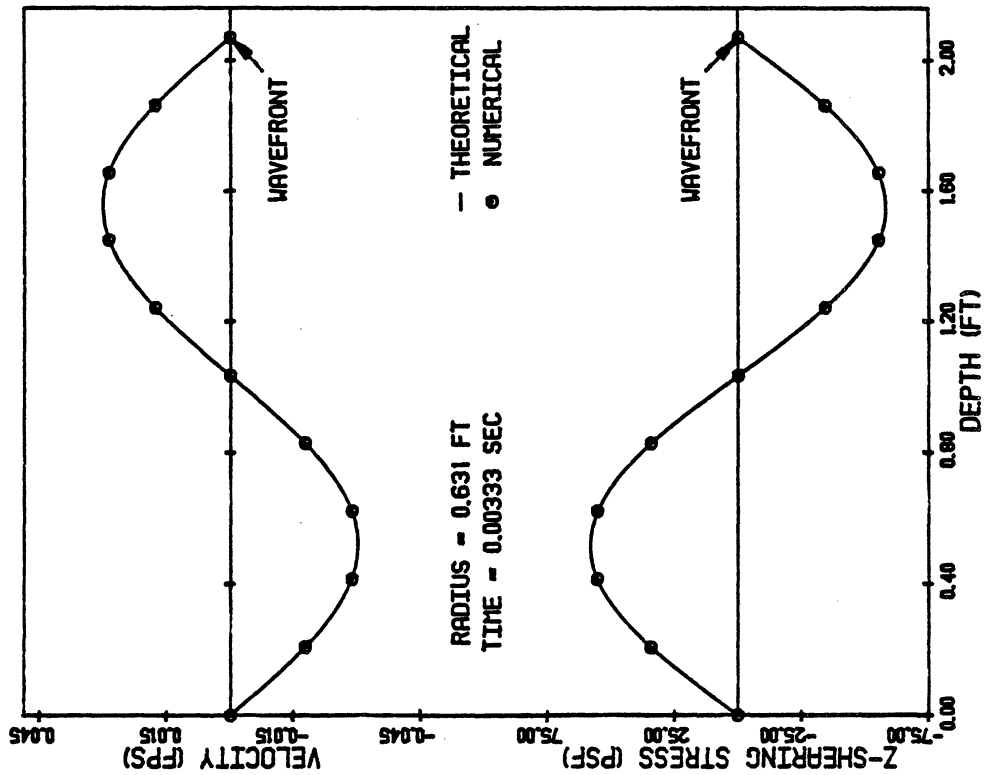

Fig. 4.13: Longitudinal Wave Propagation: Dependent Variables vs. z at r = 0.631 ft and Time of 0.00333 sec.

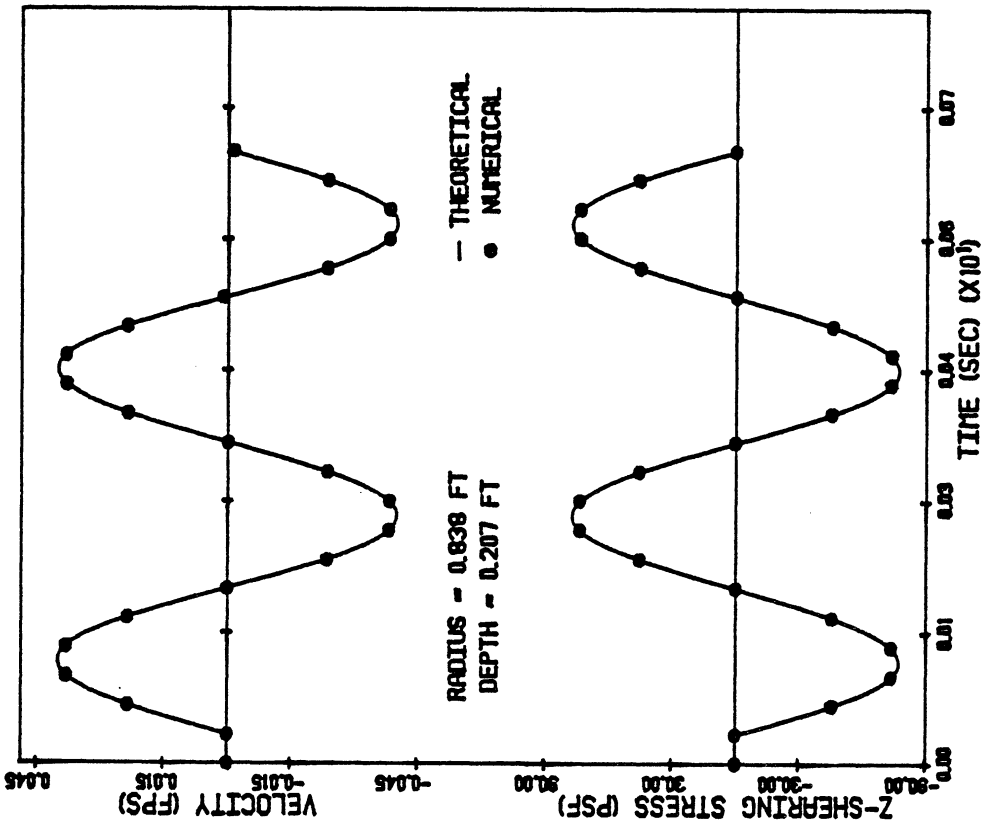

Fig. 4.12: Longitudinal Wave Propagation: Dependent Variables vs. Time at r = 0.838 ft and z = 0.207 ft.

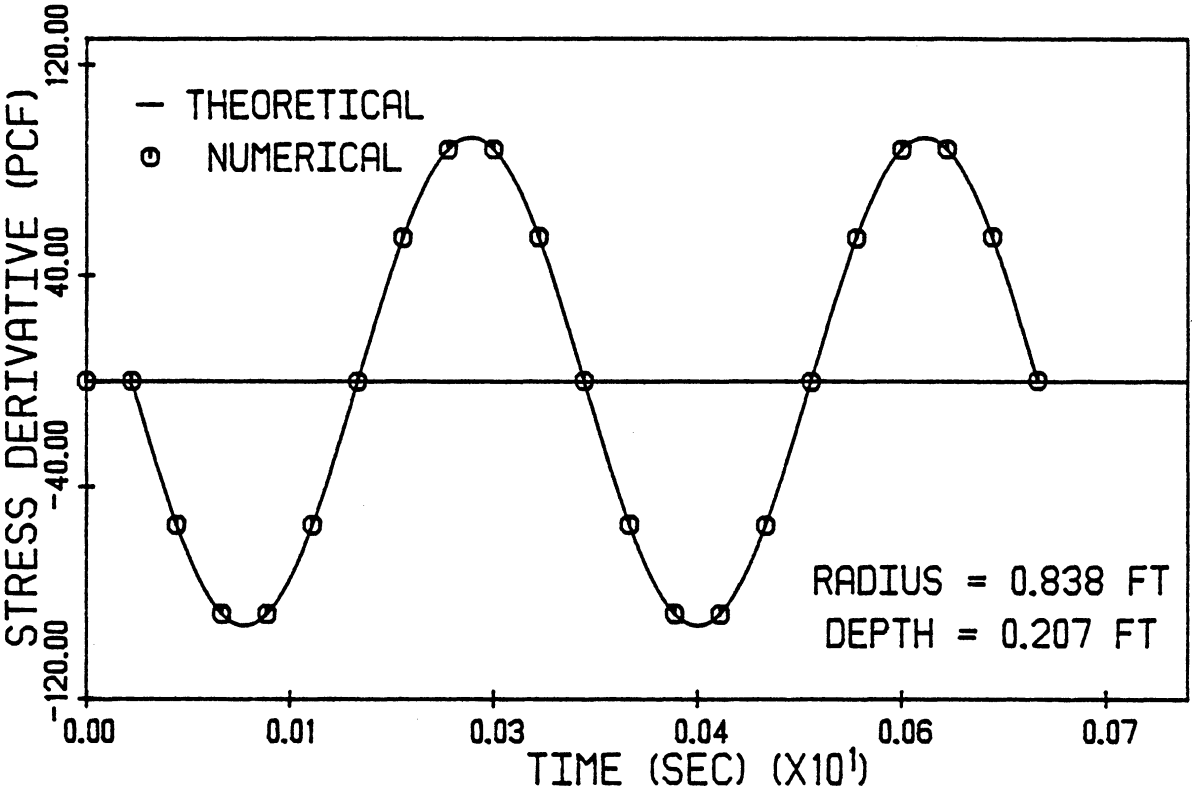

(a)

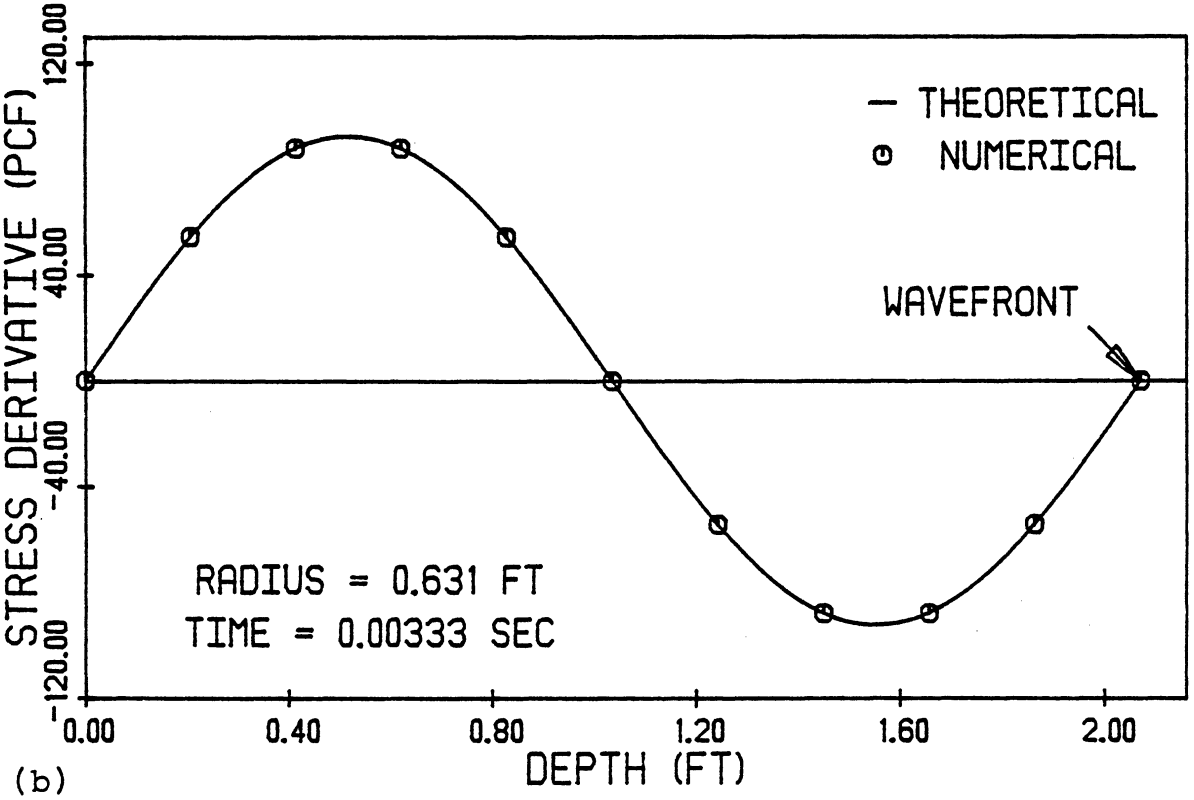

(b)

Fig. 4.14: Longitudinal Wave Propagation: Dependent Variables as Functions of Indicated Independent Variables for Indicated Values of Independent Variables.

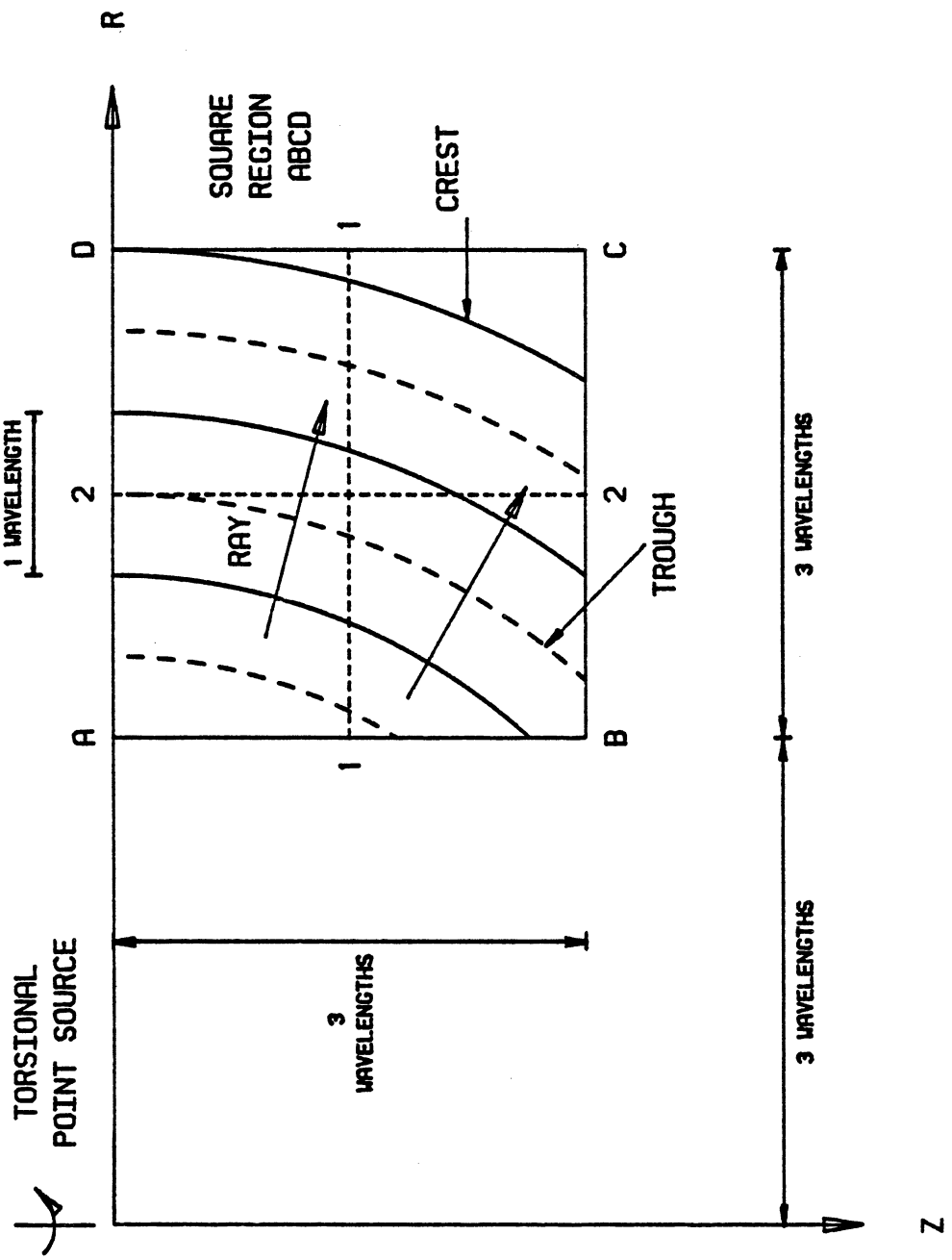

Fig. 4.15: Coordinate System Used for Half Space Subjected to Loading by Torsional Point Source. Shows Isolated Region ABCD Drawn to Scale.

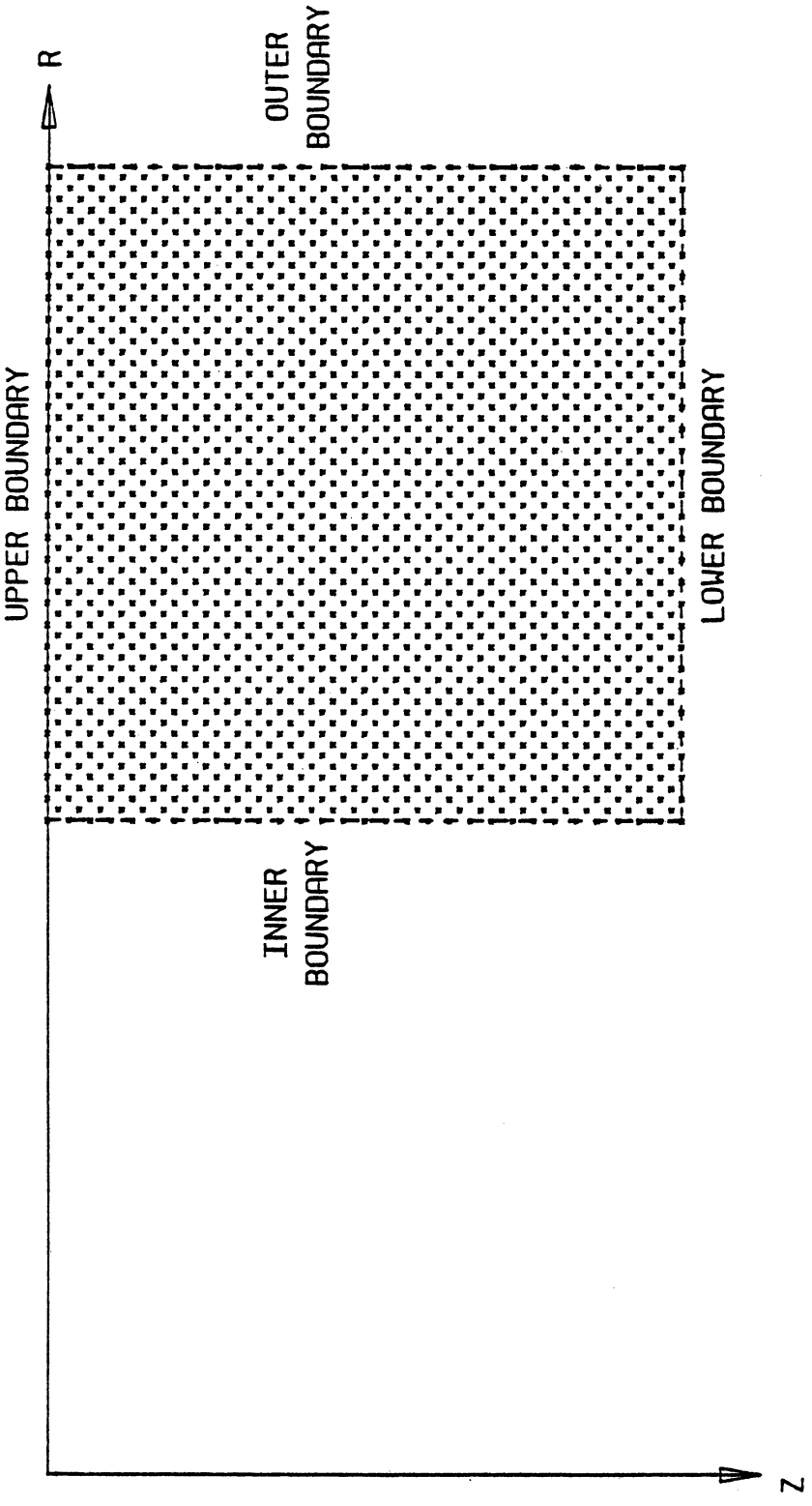

Fig. 4.16: Staggered Grid Used in Example of Half Space Loaded by Torsional Point Source.

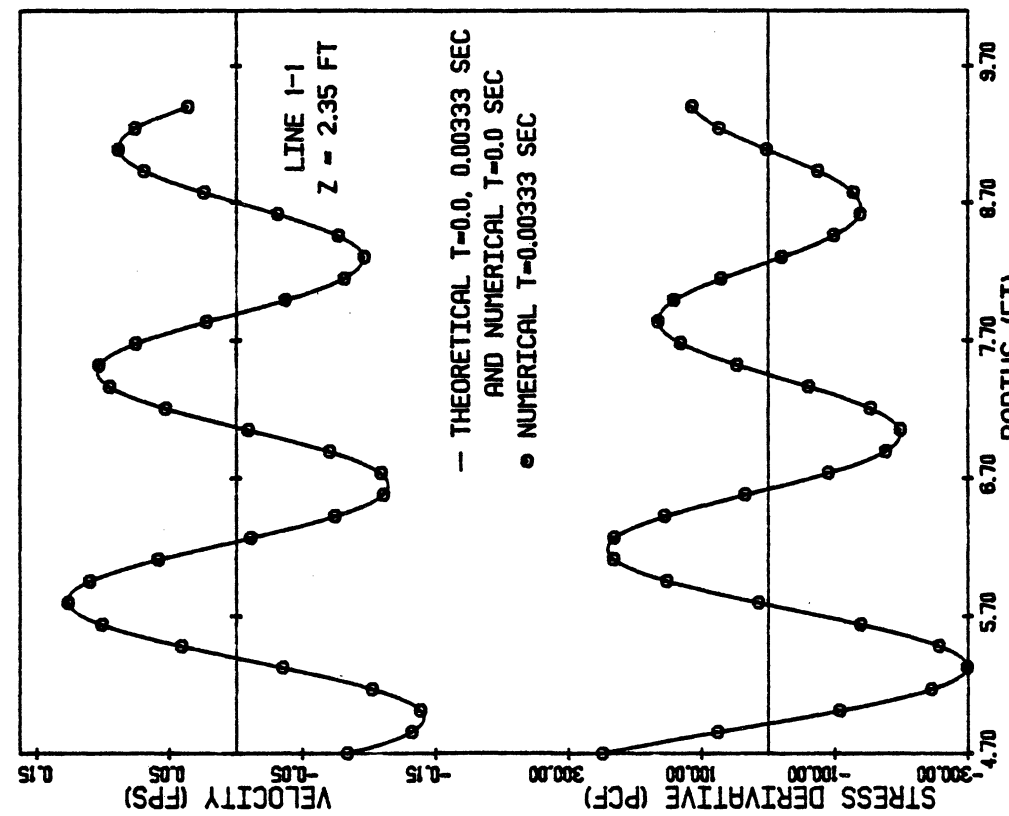

(b)

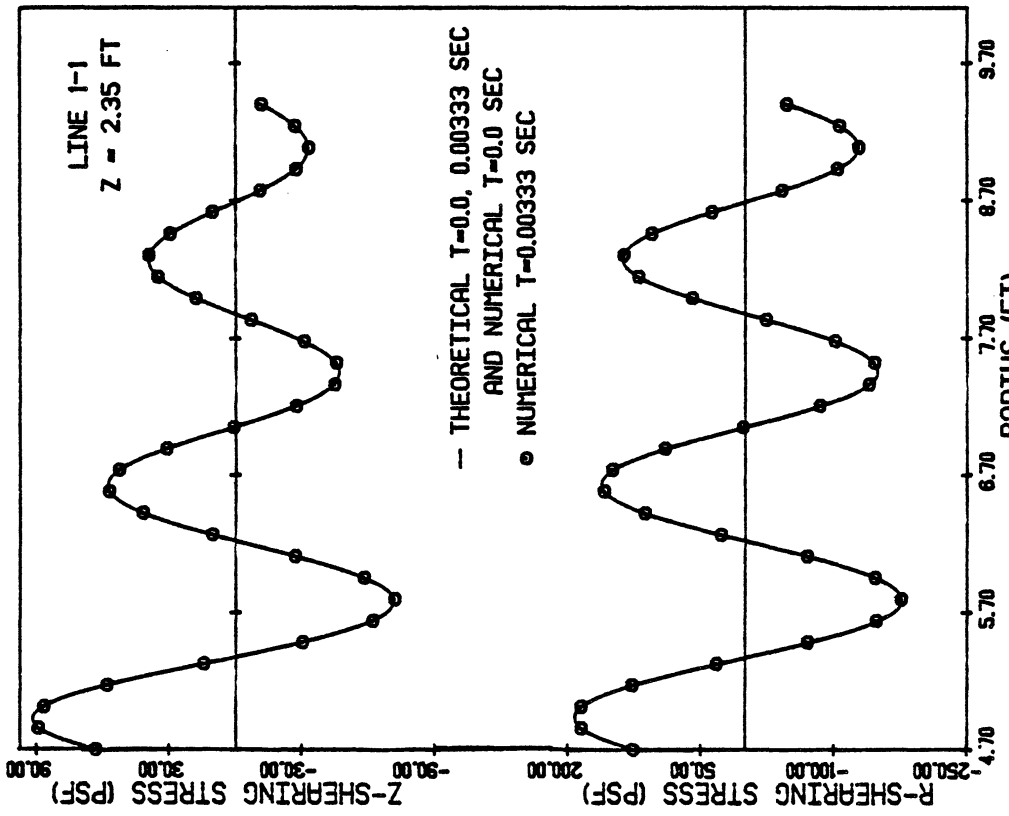

(a)

Fig. 4.17: Wave Propagation from Torsional Point Source: Dependent Variables vs. r along Line 1-1 (Fig. 4.15) for Indicated Times.

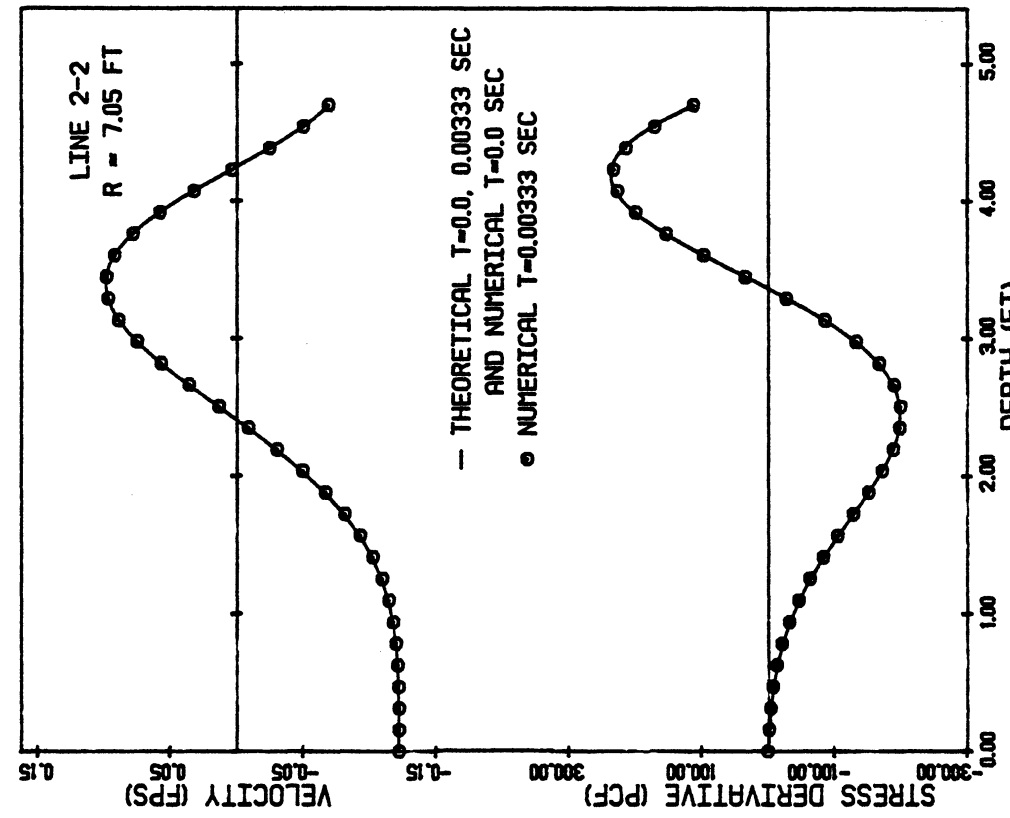

(b)

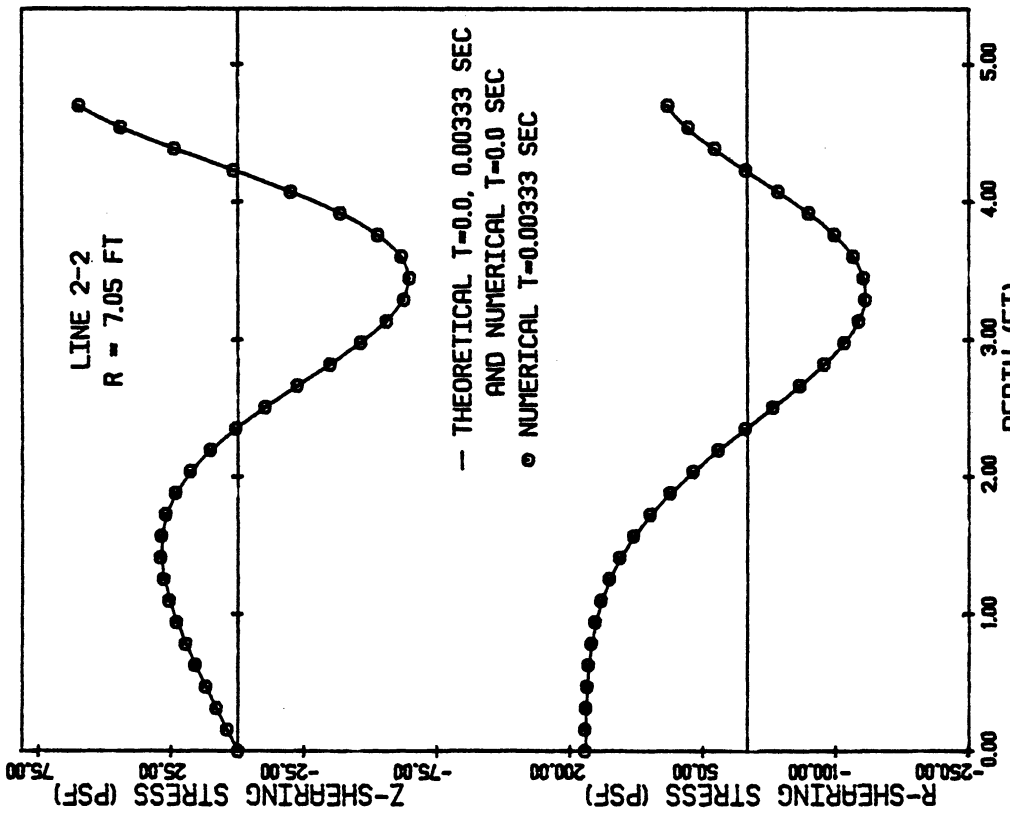

(a)

Fig. 4.18: Wave Propagation from Torsional Point Source: Dependent Variables vs. z along Line 2-2 (Fig. 4.15) for Indicated Times.

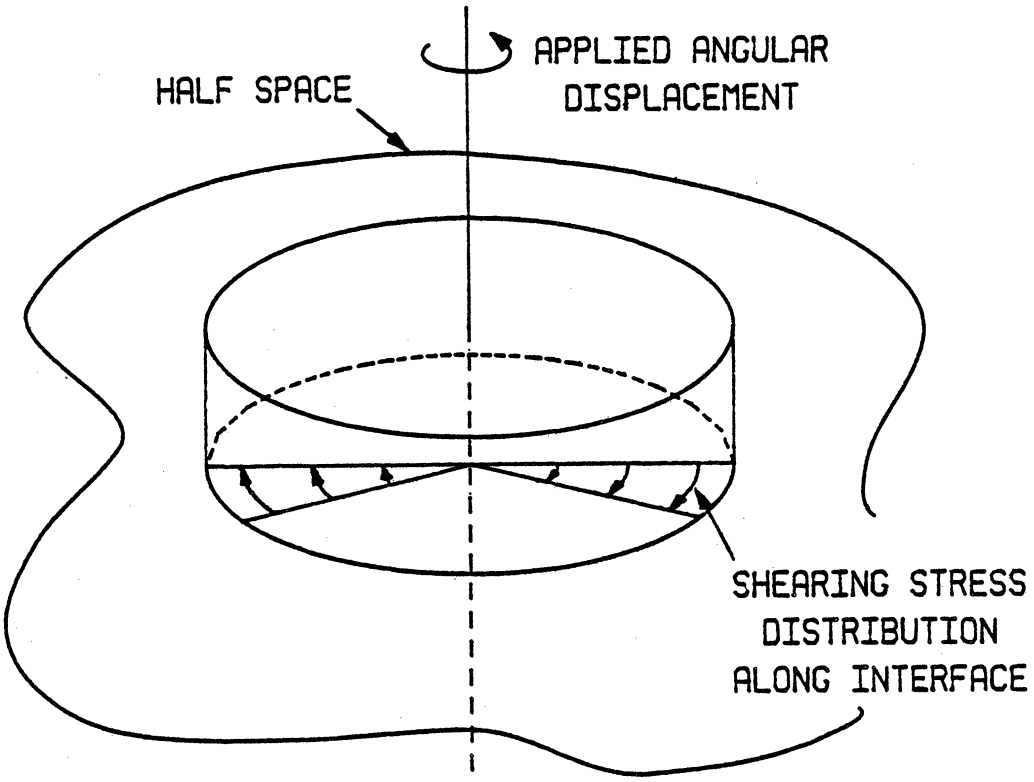

Fig. 4.19: Disk on Half Space.

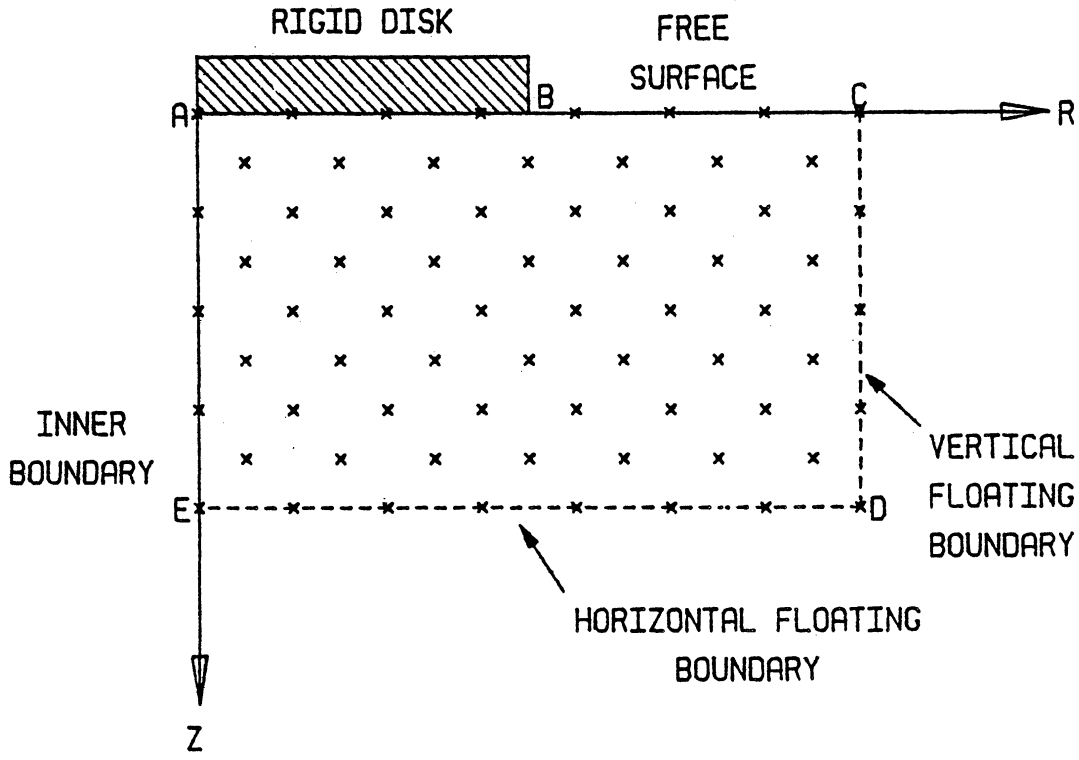

Fig. 4.20: Staggered Grid Used for Examples Involving Rigid Massless Disk on Elastic Half Space.

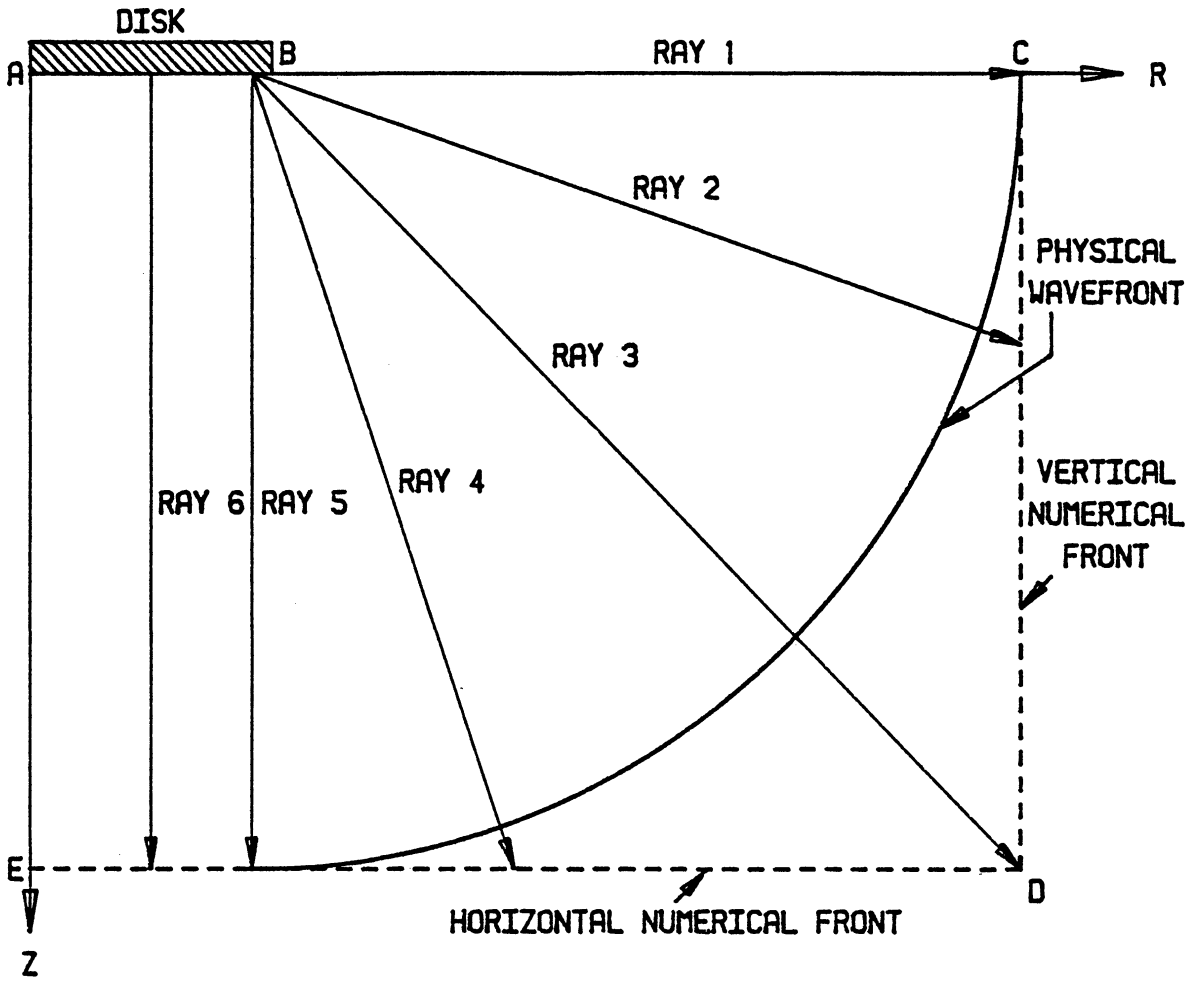

Fig. 4.21: Schematic Diagram Showing Numerical Fronts and Physical Wavefront Originating from Disk and Propagating into Half Space.

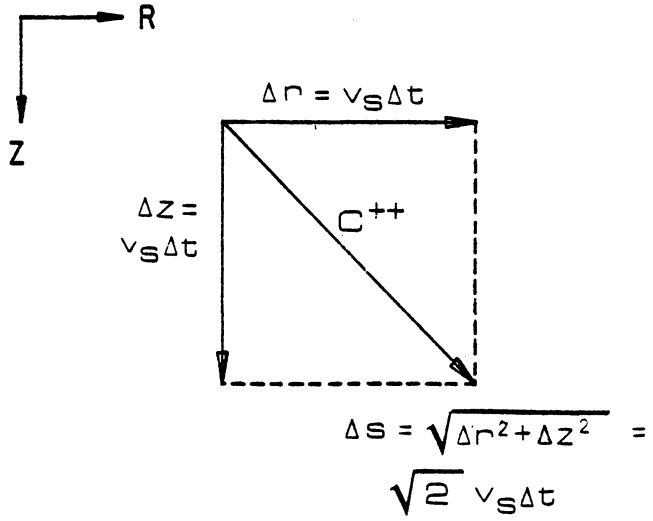

Fig. 4.22: Integration Path (C^{++}) for Finite Time Increment, Δt, Projected onto r-z Plane and Spatial Components of Path.

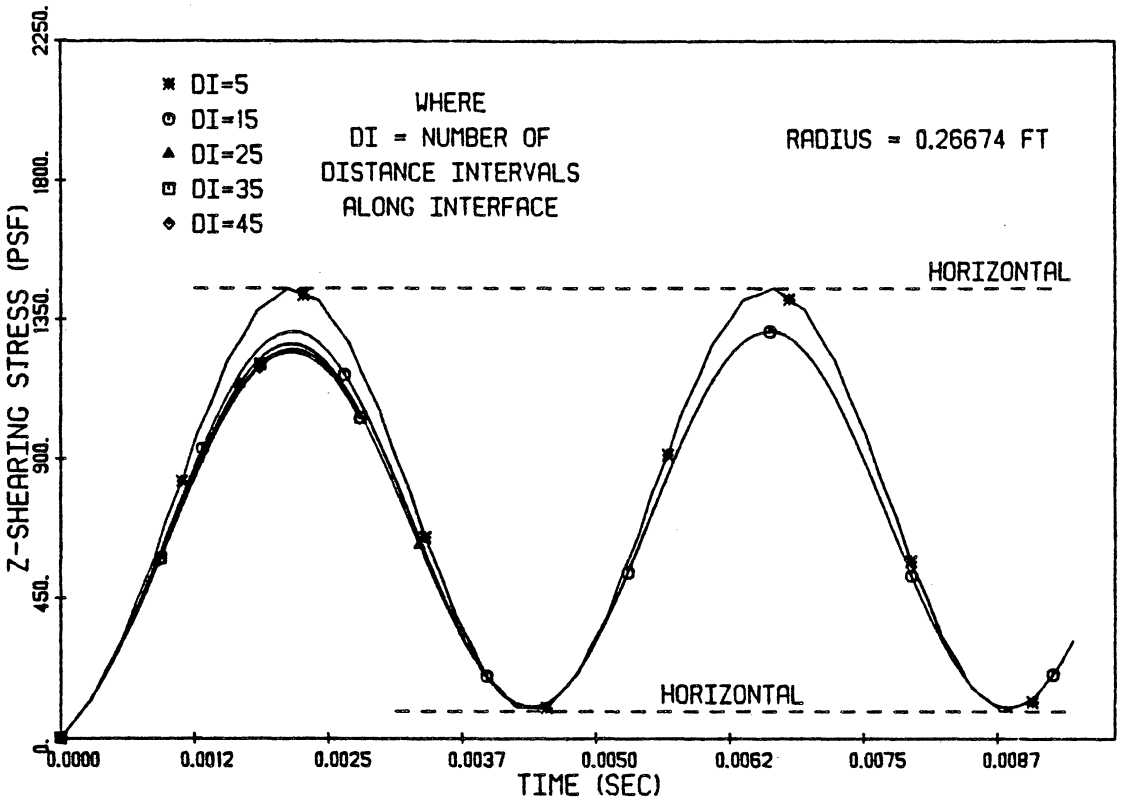

Fig. 4.23: Problem of Disk on Half Space: τ_z-Stress at Interface vs. Time for r = 0.26674 ft. Not All Points Shown.

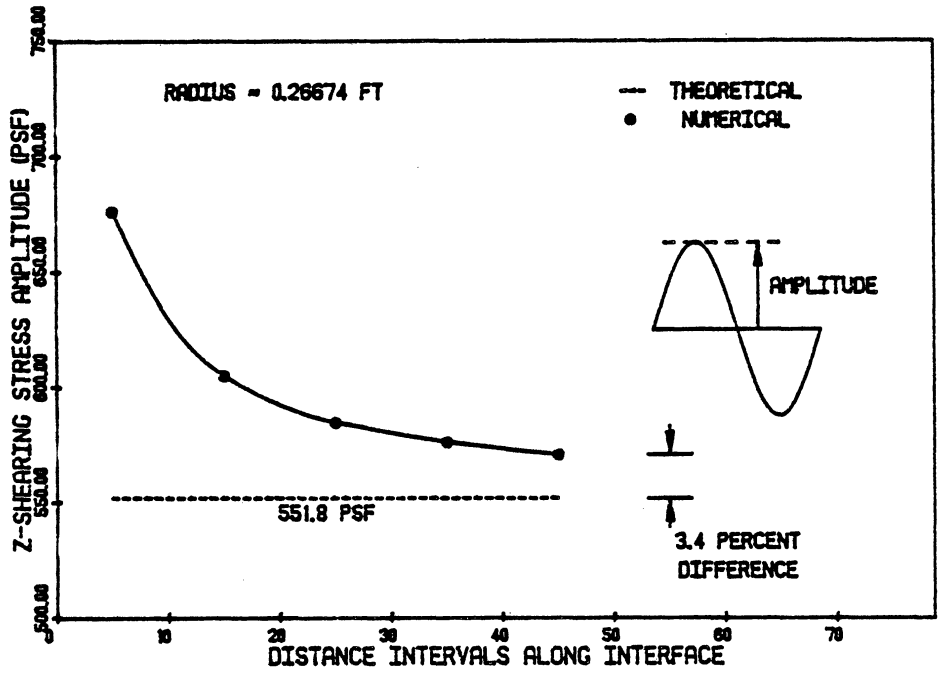

Fig. 4.24: Problem of Disk on Half Space: Amplitude of Steady State Oscillating Component of τ_z-Stress at Interface at r = 0.26674 ft vs. Number of Distance Intervals Along Interface.

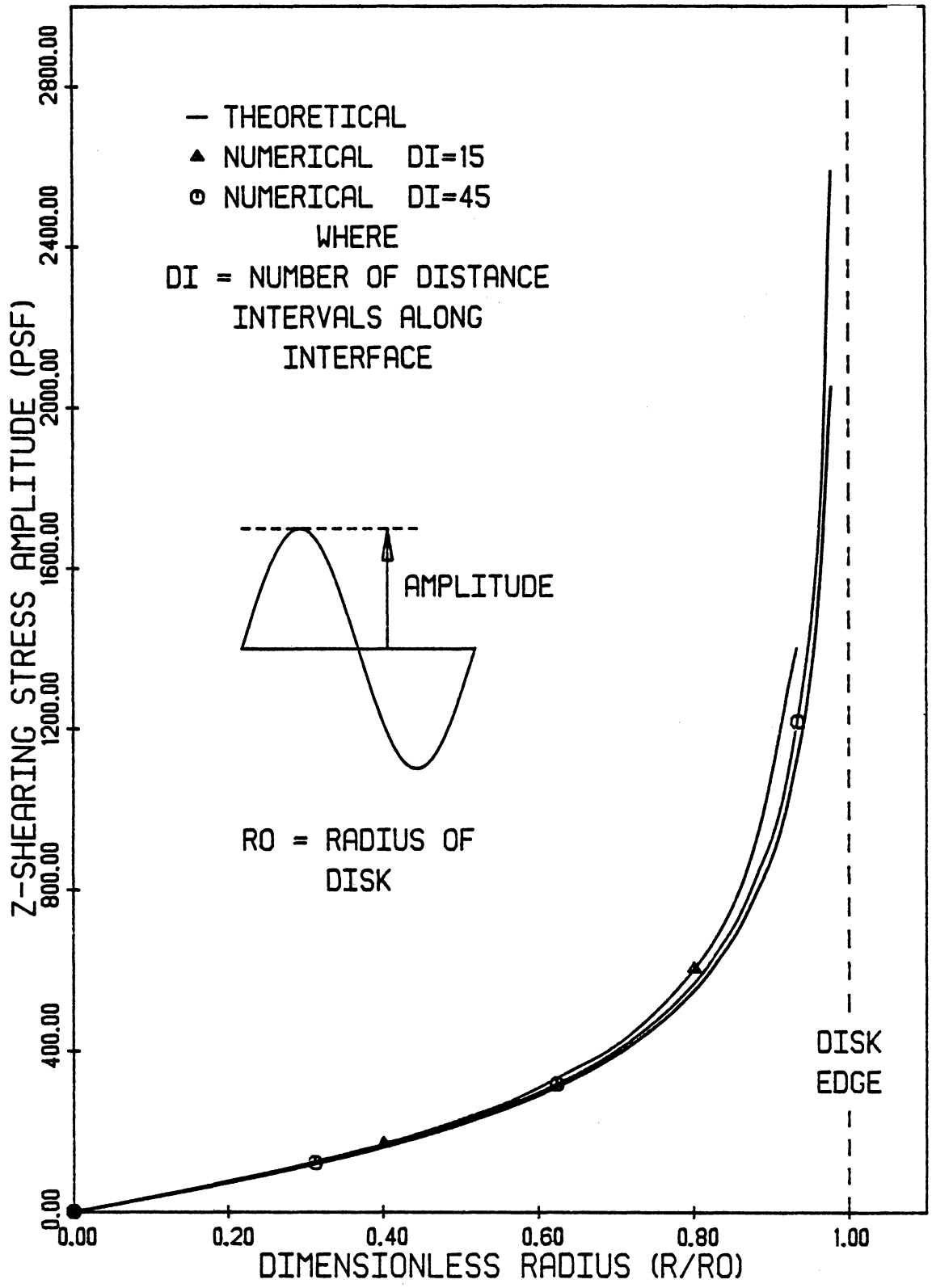

Fig. 4.25: Problem of Disk on Half Space: Amplitude of Steady State Oscillating Component of τ_z-Stress vs. Dimensionless Radius. Not All Points Shown.

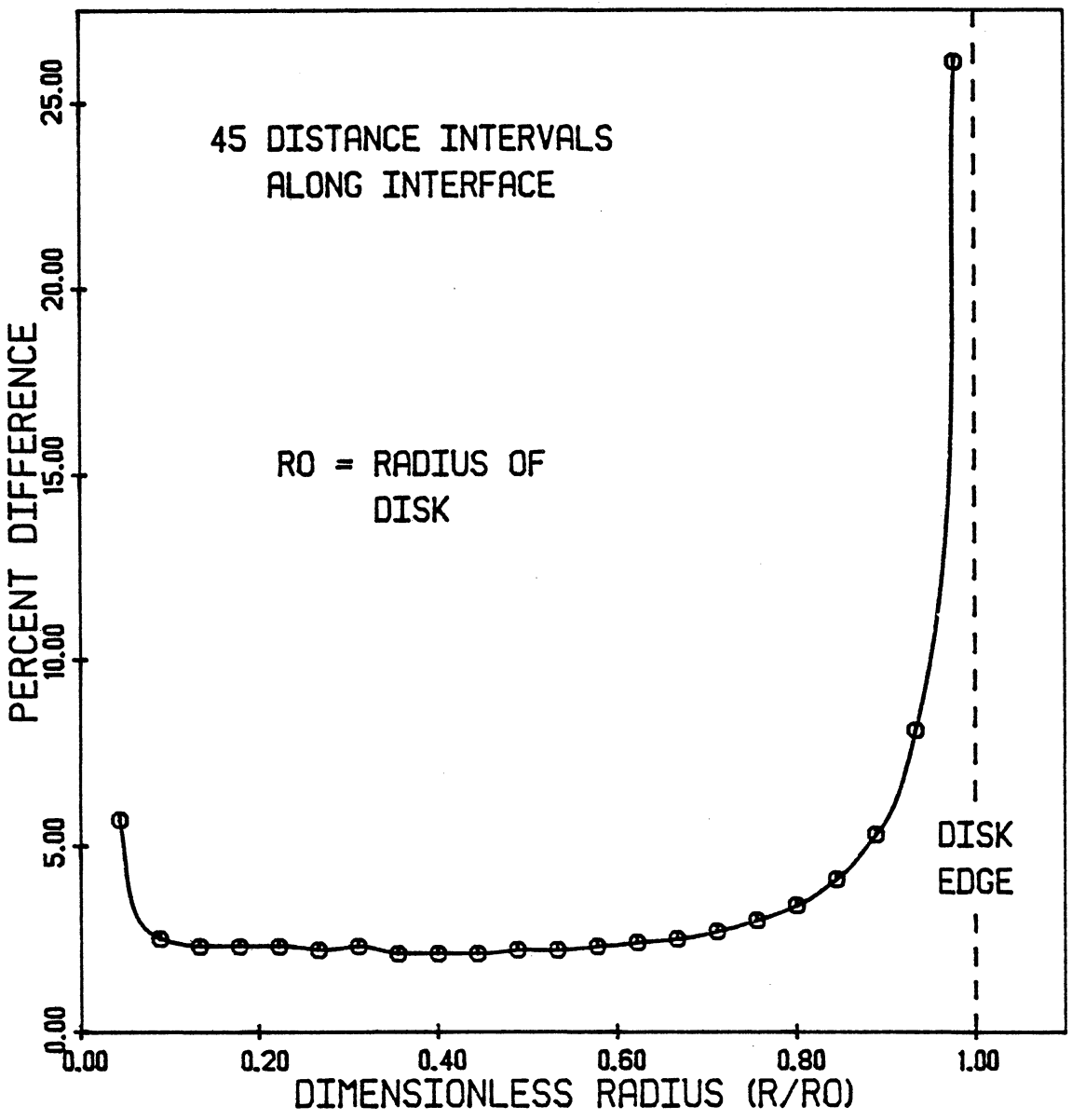

Fig. 4.26: Problem of Disk on Half Space: Percentage Difference between Amplitudes of Steady State Component of τ_z-Stress Along Interface as Determined by Numerical Procedure and Theory vs. Dimensionless Radius.

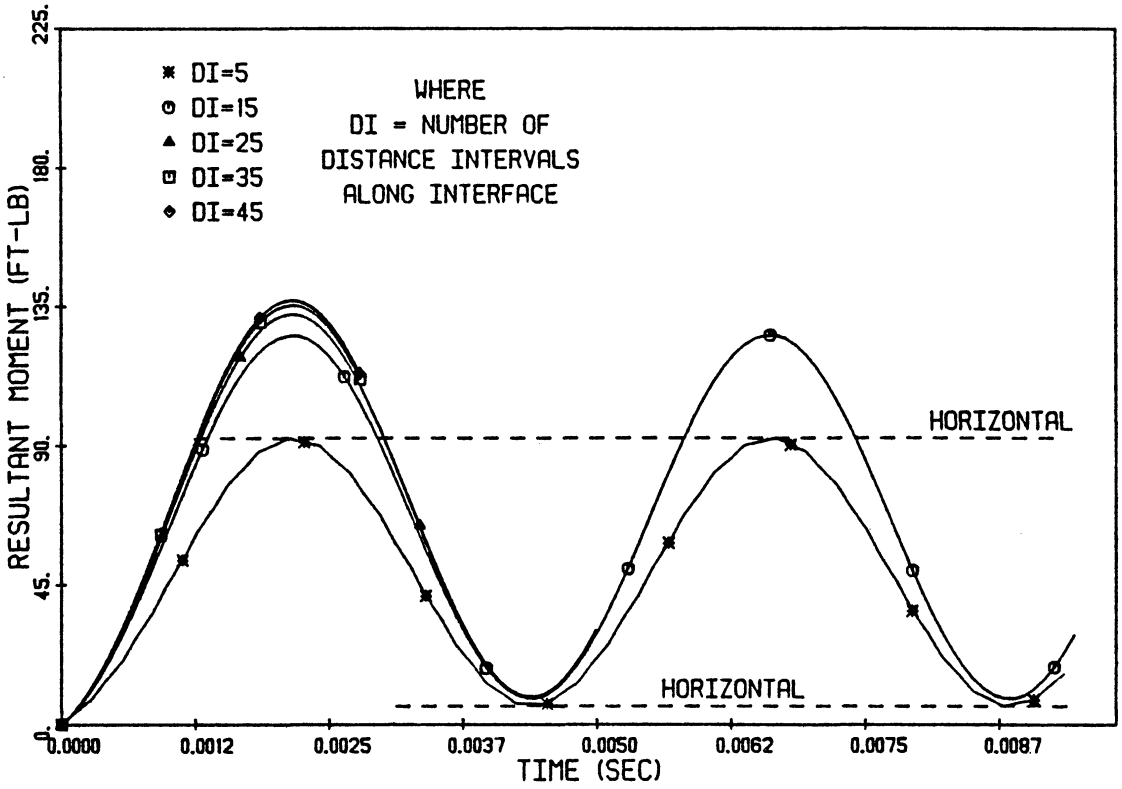

Fig. 4.27: Problem of Disk on Half Space: Resultant Moment of τ_z-Stress Distribution vs. Time. Not All Points Shown.

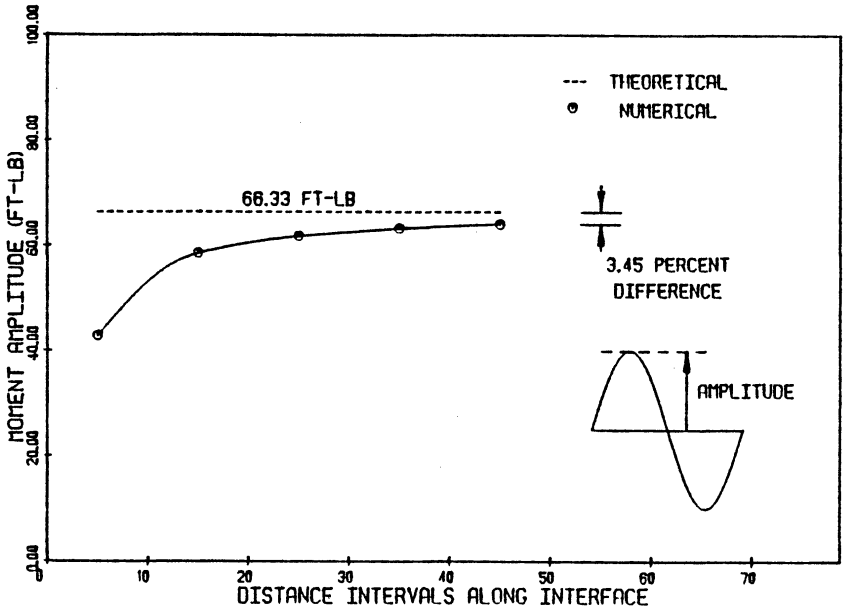

Fig. 4.28: Problem of Disk on Half Space: Amplitude of Resultant Moment of Shearing Stresses Along Interface vs. Number of Distance Intervals Along Interface.

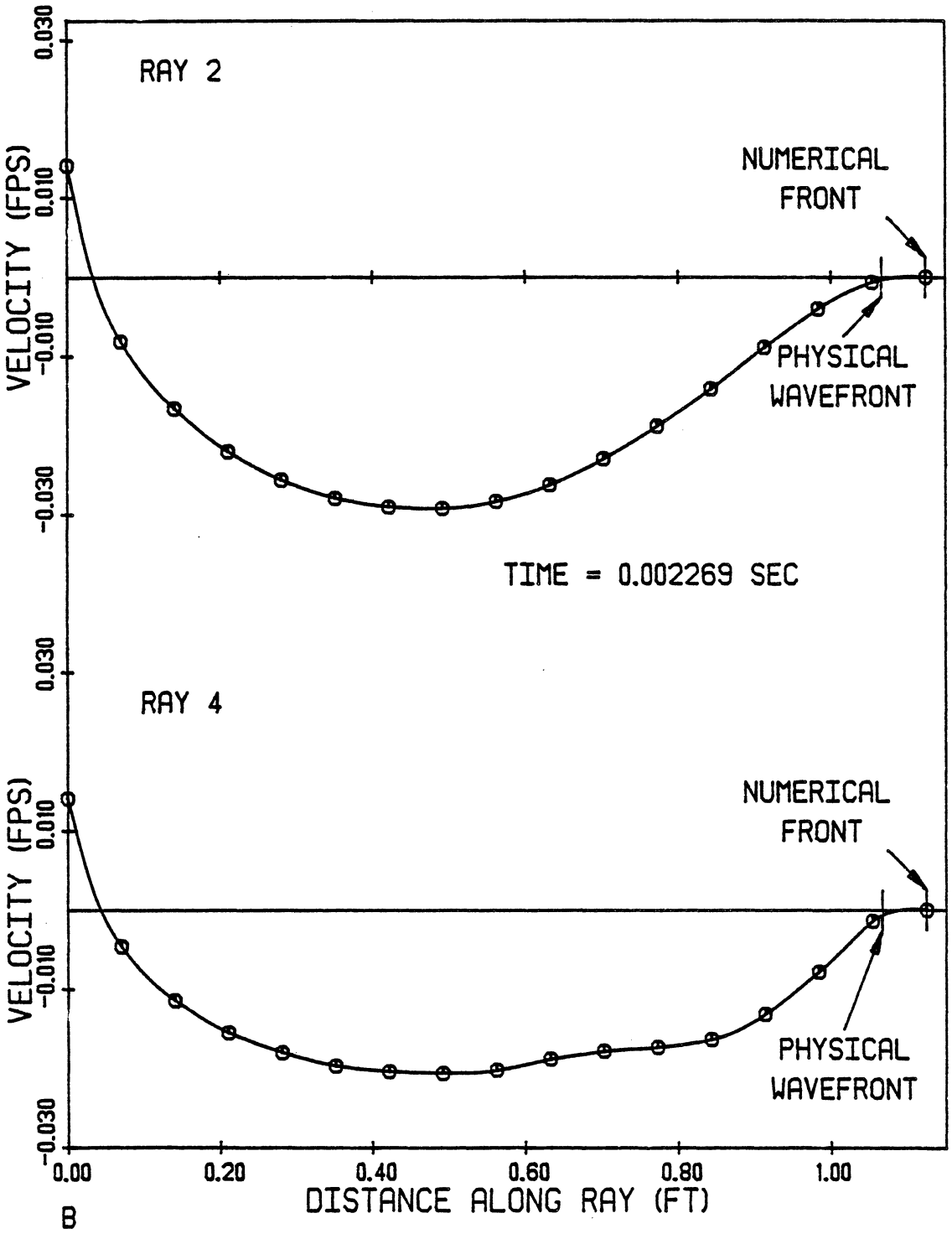

Fig. 4.29: Problem of Disk on Half Space: Particle Velocities vs. Distance Along Rays 2 and 4 Originating from Point B in Fig. 4.21.

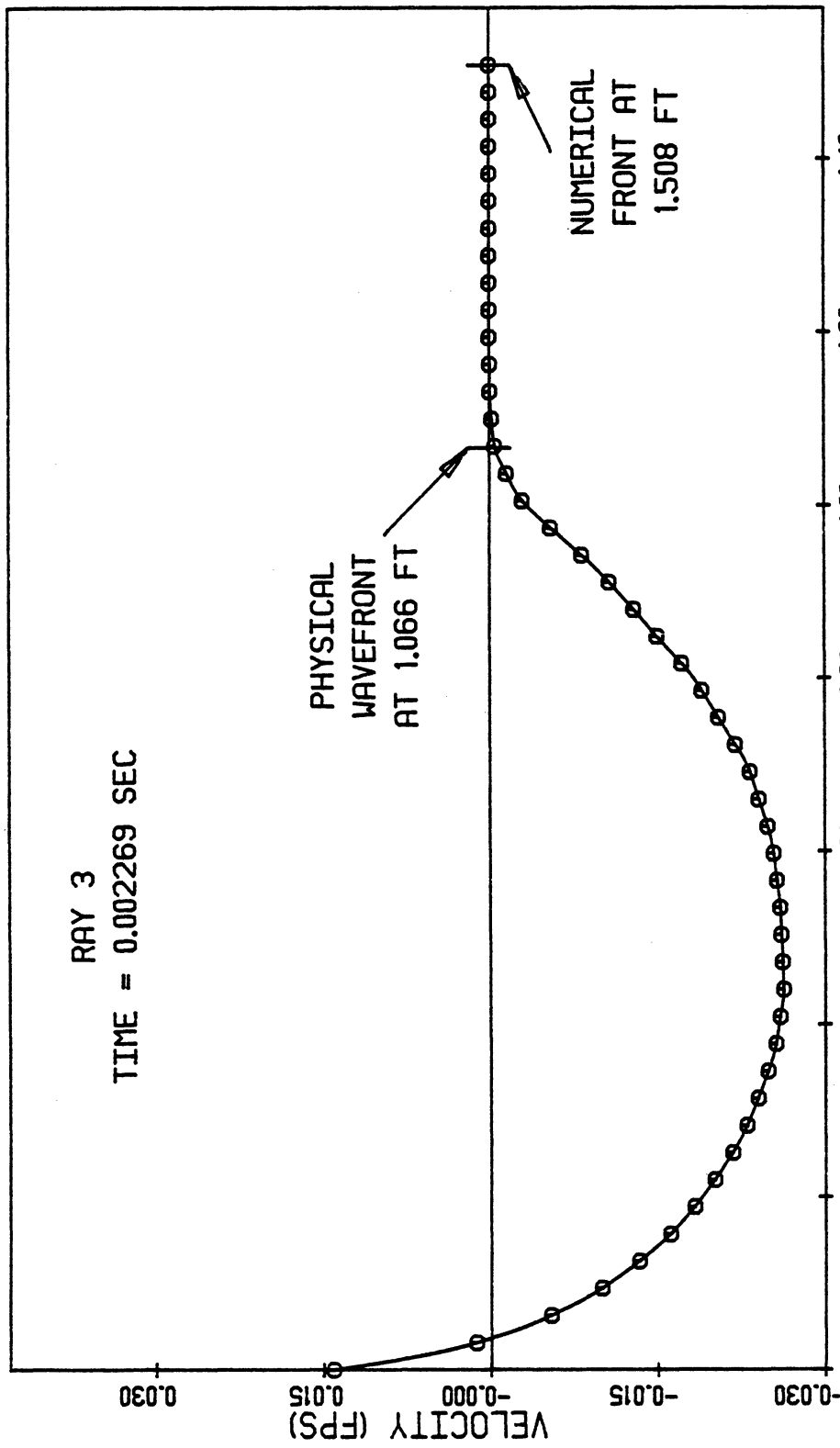

Fig. 4.30: Problem of Disk on Half Space: Particle Velocity vs. Distance Along Ray 3 Originating from Point B in Fig. 4.21.

CHAPTER V

FORMULATION OF NONLINEAR INELASTIC NUMERICAL PROCEDURE

A. Introduction

In Chapter IV the problem of a massless, rigid disk oscillating on an elastic half space was discussed. The rotation of the disk causes infinite shearing stresses to develop at the periphery. A great deal of attention was directed towards the resultant moment of the distribution of shearing stresses along the interface between the disk and the half space. Because large stresses act at the outer edge of the disk, a major portion of the resultant moment is developed by these stresses.

Soils cannot withstand infinite stresses and the resultant moment is extremely important in predicting the response of a disk having mass. Therefore, the elastic theory cannot provide a realistic solution for torsional motions of real foundations resting on soils.

A more practical analysis is one in which shearing stresses are limited to finite values. Stresses may be limited by assigning nonlinear inelastic properties to a material by using shear moduli which vary with shearing stress and strain. In this chapter the basic analytical development given in Chapter III is reformulated to allow the use of variable shear moduli. Shearing stresses may also be limited in the problem of a disk on a half space by permitting slip along the interface. The adaptation of the numerical analysis to include slip is presented in Chapter VI.

B. Governing Equations

The equations governing axisymmetric torsional wave propagation in a medium having variable moduli consist of the equation of motion and two shearing stress-strain relationships. These are given as

$$\frac{\partial \tau_r}{\partial r} + \frac{\partial \tau_z}{\partial z} + \frac{2}{r}\tau_r = \rho \frac{\partial v}{\partial t} \tag{3.3}$$

and

$$\frac{d\tau_r}{d\gamma_r} = G_{rt}(\tau_r, \tau_z, \gamma_r, \gamma_z) \tag{5.1}$$

$$\frac{d\tau_z}{d\gamma_z} = G_{zt}(\tau_r, \tau_z, \gamma_r, \gamma_z) \tag{5.2}$$

where $G_{rt}(\tau_r, \tau_z, \gamma_r, \gamma_z)$ and $G_{zt}(\tau_r, \tau_z, \gamma_r, \gamma_z)$ are tangent shear moduli in the subscripted coordinate directions. Each of Eqs. (5.1) and (5.2) defines a shear modulus in one of the coordinate directions as the rate of change of shearing stress with shearing strain and each shear modulus depends upon shearing stresses and strains.

C. Transformation

In this section, in an initial step towards the formulation of a numerical procedure capable of solving Eqs. (3.3), (5.1), and (5.2), these equations are transformed to a different set of equations. From basic calculus, Eq. (5.1) may be interpreted as

$$\frac{d\tau_r}{d\gamma_r} = G_{rt} = \frac{\partial \tau_r}{\partial t} \cdot \frac{\partial t}{\partial \gamma_r}$$

which leads to

$$\frac{\partial \tau_r}{\partial t} = G_{rt} \frac{\partial \gamma_r}{\partial t} \tag{5.3}$$

Equation (5.3) relates a time rate of change of τ_r-stress to a time rate of change of γ_r-strain at a fixed point in space. Recalling Eq. (3.4), Eq. (5.3) is rewritten as

$$\frac{\partial \tau_r}{\partial t} = G_{rt} \frac{\partial}{\partial t}\left(\frac{\partial u}{\partial r} - \frac{u}{r}\right)$$

Differentiations are carried out giving

$$\frac{\partial \tau_r}{\partial t} = G_{rt}\left(\frac{\partial^2 u}{\partial r \partial t} - \frac{1}{r}\frac{\partial u}{\partial t}\right) \tag{5.4}$$

Continuity of second derivatives of the displacement field is imposed. Thus, the order of differentiation is immaterial, and, noting that $V = \partial u/\partial t$, Eq. (5.4) may be interpreted as

$$\frac{\partial \tau_r}{\partial t} = G_{rt}\left(\frac{\partial V}{\partial r} - \frac{1}{r}V\right)$$

or, in an alternate form, as

$$\frac{\partial \tau_r}{\partial t} - G_{rt}\frac{\partial V}{\partial r} + G_{rt}\frac{V}{r} = 0 \tag{5.5}$$

Equation (5.2) may be interpreted as

$$\frac{d\tau_z}{d\gamma_z} = G_{zt} = \frac{\partial \tau_z}{\partial t}\cdot\frac{\partial t}{\partial \gamma_z}$$

which may be rewritten as

$$\frac{\partial \tau_z}{\partial t} = G_{zt}\frac{\partial \gamma_z}{\partial t} \tag{5.6}$$

Equation (5.6) relates the time rate of change of τ_z-stress to the time rate of change of γ_z-strain at a point in space. Substituting Eq. (3.5) into Eq. (5.6) gives

$$\frac{\partial \tau_z}{\partial t} = G_{zt}\frac{\partial}{\partial t}\left(\frac{\partial u}{\partial z}\right)$$

which, with the assumption of continuous second derivatives of the displacement field, may be interpreted as

$$\frac{\partial \tau_z}{\partial t} = G_{zt} \frac{\partial v}{\partial z}$$

This is rearranged to give

$$\frac{\partial \tau_z}{\partial t} - G_{zt} \frac{\partial v}{\partial z} = 0 \qquad (5.7)$$

Equation (5.1) may be interpreted alternatively as

$$\frac{d\tau_r}{d\gamma_r} = G_{rt} = \frac{\partial \tau_r}{\partial z} \frac{\partial z}{\partial \gamma_r}$$

which may be rewritten as

$$\frac{\partial \tau_r}{\partial z} = G_{rt} \frac{\partial \gamma_r}{\partial z} \qquad (5.8)$$

Equation (5.8) gives the rate of change of τ_r-stress with respect to depth in terms of the rate of change of γ_r-strain with respect to depth at a given radius and time. Introducing Eq. (3.4) into Eq. (5.8) gives

$$\frac{\partial \tau_r}{\partial z} = G_{rt} \frac{\partial}{\partial z} \left(\frac{\partial u}{\partial r} - \frac{u}{r} \right)$$

which, when differentiated results in

$$\frac{\partial \tau_r}{\partial z} = G_{rt} \left(\frac{\partial^2 u}{\partial r \partial z} - \frac{1}{r} \frac{\partial u}{\partial z} \right) \qquad (5.9)$$

Continuity of second derivatives of the displacement field and substitution of Eq. (3.5) into Eq. (5.9) permits the following interpretation of Eq. (5.9):

$$\frac{\partial \tau_r}{\partial z} = G_{rt}\left(\frac{\partial \gamma_z}{\partial r} - \frac{\gamma_z}{r}\right) \tag{5.10}$$

For the purpose of expressing Eq. (5.10) in a different form, Eq. (5.2) is interpreted as

$$\frac{d\tau_z}{d\gamma_z} = \frac{\partial \tau_z}{\partial r}\frac{\partial r}{\partial \gamma_z} = G_{zt}$$

which may be rewritten as

$$\frac{\partial \gamma_z}{\partial r} = \frac{1}{G_{zt}}\frac{\partial \tau_z}{\partial r} \tag{5.11}$$

Equation (5.11) relates the rate of change of γ_z-strain with respect to radius to the rate of change of τ_z-stress with respect to radius at a given depth and time. In addition, γ_z-strain is written as a function of τ_z-stress as follows:

$$\gamma_z = \frac{\tau_z}{G_{zs}(\tau_r, \tau_z, \gamma_r, \gamma_z)} \tag{5.12}$$

Herein, $G_{zs}(\tau_r, \tau_z, \gamma_r, \gamma_z)$, corresponding to stress-strain level $(\tau_r, \tau_z, \gamma_r, \gamma_z)$ is defined as the slope of a line intersecting the origin and the coordinate (τ_z, γ_z) of the τ_z-stress-γ_z-strain curve. Substituting Eqs. (5.12) and (5.11) into Eq. (5.10) gives

$$\frac{\partial \tau_r}{\partial z} = G_{rt}\left(\frac{1}{G_{zt}}\frac{\partial \tau_z}{\partial r} - \frac{1}{r}\frac{\tau_z}{G_{zs}}\right)$$

which may be rewritten as

$$\frac{\partial \tau_r}{\partial z} - \frac{G_{rt}}{G_{zt}} \frac{\partial \tau_z}{\partial r} + \frac{1}{r} \frac{G_{rt}}{G_{zs}} \tau_z = 0 \tag{5.13}$$

A fourth relationship needed in the development is

$$\frac{\partial \tau_z}{\partial r} - \frac{\partial \tau_z}{\partial r} = 0 \tag{5.14}$$

and a final equation is the rearranged equation of motion,

$$\frac{\partial \tau_r}{\partial r} + \frac{\partial \tau_z}{\partial z} + \frac{2}{r} \tau_r - \rho \frac{\partial V}{\partial t} = 0 \tag{5.15}$$

Each of Eqs. (5.5), (5.7), (5.13), (5.14), and (5.15) may be multiplied by known or unknown constants and added together resulting in

$$1\left(\frac{\partial \tau_r}{\partial r} + \frac{\partial \tau_z}{\partial z} + \frac{2}{r} \tau_r - \rho \frac{\partial V}{\partial t}\right) + \bar{A}\left(\frac{\partial \tau_r}{\partial t} - G_{rt} \frac{\partial V}{\partial r} + G_{rt} \frac{V}{r}\right)$$

$$+ \bar{B}\left(\frac{\partial \tau_r}{\partial z} - \frac{G_{rt}}{G_{zt}} \frac{\partial \tau_z}{\partial r} + \frac{1}{r} \frac{G_{rt}}{G_{zs}} \tau_z\right) + \bar{C}\left(\frac{\partial \tau_z}{\partial t} - \right. \tag{5.16}$$

$$\left. G_{zt} \frac{\partial V}{\partial z}\right) + \bar{D}\left(\frac{\partial \tau_z}{\partial r} - \frac{\partial \tau_z}{\partial r}\right) = 0$$

where $\bar{A}$, $\bar{B}$, $\bar{C}$, and $\bar{D}$ are unknown constants. Rearranging Eq. (5.16) to group related partial derivatives gives

$$\bar{A}\left(\frac{1}{A}\frac{\partial\tau_r}{\partial r}+\frac{\bar{B}}{A}\frac{\partial\tau_r}{\partial z}+\frac{\partial\tau_r}{\partial t}\right)+\bar{C}\left(\frac{\bar{D}}{C}\frac{\partial\tau_z}{\partial r}+\frac{1}{C}\frac{\partial\tau_z}{\partial z}+\frac{\partial\tau_z}{\partial t}\right)$$
$$-\rho\left(\frac{\bar{A}G_{rt}}{\rho}\frac{\partial V}{\partial r}+\frac{\bar{C}G_{zt}}{\rho}\frac{\partial V}{\partial z}+\frac{\partial V}{\partial t}\right)+\frac{2}{r}\tau_r+\frac{\bar{A}G_{rt}}{r}V \qquad (5.17)$$
$$+\frac{\bar{B}}{r}\frac{G_{rt}}{G_{zs}}\tau_z-\left(\bar{B}\frac{G_{rt}}{G_{zt}}+\bar{D}\right)\frac{\partial\tau_z}{\partial r}=0$$

To allow total derivative interpretations, the time rates of change of coordinates, dr/dt, dz/dt, and dt/dt, are equated to the appropriate coefficients of the partial derivatives in Eq. (5.17), giving

$$\frac{dr}{dt}=\frac{1}{\bar{A}}=\frac{\bar{D}}{\bar{C}}=\frac{\bar{A}G_{rt}}{\rho} \qquad (5.18a)$$

$$\frac{dz}{dt}=\frac{\bar{B}}{\bar{A}}=\frac{1}{\bar{C}}=\frac{\bar{C}G_{zt}}{\rho} \qquad (5.18b)$$

$$\frac{dt}{dt}=1 \qquad (5.18c)$$

Imposing Eqs. (5.18) permits Eq. (5.17) to be written as

$$\bar{A}\left(\frac{dr}{dt}\frac{\partial\tau_r}{\partial r}+\frac{dz}{dt}\frac{\partial\tau_r}{\partial z}+\frac{\partial\tau_r}{\partial t}\right)+\bar{C}\left(\frac{dr}{dt}\frac{\partial\tau_z}{\partial r}+\frac{dz}{dt}\frac{\partial\tau_z}{\partial z}\right.$$
$$\left.+\frac{\partial\tau_z}{\partial t}\right)-\rho\left(\frac{dr}{dt}\frac{\partial V}{\partial r}+\frac{dz}{dt}\frac{\partial V}{\partial z}+\frac{\partial V}{\partial t}\right)+\frac{2}{r}\tau_r \qquad (5.19)$$
$$+\frac{\bar{A}G_{rt}}{r}V+\frac{\bar{B}}{r}\frac{G_{rt}}{G_{zs}}\tau_z-\left(\bar{B}\frac{G_{rt}}{G_{zt}}+\bar{D}\right)\frac{\partial\tau_z}{\partial r}=0$$

The replacement of the groups of partial derivatives in Eq. (5.19) with total derivatives gives

$$\bar{A}\frac{d\tau_r}{dt} + \bar{C}\frac{d\tau_z}{dt} - \rho\frac{dV}{dt} + \frac{2}{r}\tau_r + \frac{\bar{A}G_{rt}}{r}V + \frac{\bar{B}}{r}\frac{G_{rt}}{G_{zs}}\tau_z - \left(\bar{B}\frac{G_{rt}}{G_{zt}} + \bar{D}\right)\frac{\partial\tau_z}{\partial r} = 0$$

which, when multiplied by $dt/\bar{A}$, results in

$$d\tau_r + \frac{\bar{C}}{\bar{A}}d\tau_z - \frac{\rho}{\bar{A}}dV + \frac{2}{\bar{A}r}\tau_r\,dt + \frac{G_{rt}}{r}V\,dt + \frac{\bar{B}}{\bar{A}r}\frac{G_{rt}}{G_{zs}}\tau_z\,dt - \left(\frac{\bar{B}}{\bar{A}}\frac{G_{rt}}{G_{zt}} + \frac{\bar{D}}{\bar{A}}\right)\frac{\partial\tau_z}{\partial r}\,dt = 0 \tag{5.20}$$

Equation (5.20) is valid along paths having components in the (r,z,t) coordinate system which have the time rates of change given by Eqs. (5.18). Defining the quantities V_{sr} and V_{sz} as

$$V_{sr} = \sqrt{\frac{G_{rt}}{\rho}} \tag{5.21a}$$

and

$$V_{sz} = \sqrt{\frac{G_{zt}}{\rho}} \tag{5.21b}$$

Eqs. (5.18) may be solved to give

$$\bar{A} = \pm \frac{1}{V_{sr}}$$

$$\bar{C} = \pm \frac{1}{V_{sz}}$$

$$\bar{D} = \pm \frac{V_{sr}}{V_{sz}} \qquad (5.22)$$

$$\bar{B} = \pm \frac{V_{sz}}{V_{sr}}$$

Substitution of Eqs. (5.21) and (5.22) into Eqs. (5.18) leads to four paths along which the conversion from partial to total differentiation may take place. The components of these paths in the (r,z,t) coordinate system have the following time rates of change:

$$\frac{dr}{dt} = \pm V_{sr} \qquad (5.23a)$$

$$\frac{dz}{dt} = \pm V_{sz} \qquad (5.23b)$$

$$\frac{dt}{dt} = 1 \qquad (5.23c)$$

and the paths are given as

$$(dr, dz, dt) = \begin{cases} (v_{sr}dt, v_{sz}dt, dt) \\ (v_{sr}dt, -v_{sz}dt, dt) \\ (-v_{sr}dt, v_{sz}dt, dt) \\ (-v_{sr}dt, -v_{sz}dt, dt) \end{cases} \quad (5.24)$$

The combinations of Eqs. (5.23) along with Eqs. (5.18) and Eq. (5.20) results in four equations, one for each path. These equations are presented below along with the paths, the identifiers of the paths and the rates of the paths:

C^{++} : Path rate: $\frac{dr}{dt} = v_{sr}, \frac{dz}{dt} = v_{sz}, \frac{dt}{dt} = 1$

Path : $dr = v_{sr}dt,\ dz = v_{sz}dt,\ dt = dt$ (5.25a)

Equation:

$$d\tilde{\tau}_r + \frac{v_{sr}}{v_{sz}} d\tilde{\tau}_z - \rho v_{sr} dV + \frac{2\tilde{\tau}_r}{r} dr + \frac{\rho v_{sr} V}{r} dr + \frac{\rho v_{sz} v_{sr} \tilde{\tau}_z}{r \Theta_{zs}} dr - 2 \frac{v_{sr}}{v_{sz}} \frac{\partial \tilde{\tau}_z}{\partial r} dr = 0 \quad (5.25b)$$

C^{+-} : Path rate: $\frac{dr}{dt} = v_{sr}, \frac{dz}{dt} = -v_{sz}, \frac{dt}{dt} = 1$

Path : $dr = v_{sr}dt,\ dz = -v_{sz}dt,\ dt = dt$

$$d\tilde{\tau}_r - \frac{v_{sr}}{v_{sz}} d\tilde{\tau}_z - \rho v_{sr} dV + \frac{2\tilde{\tau}_r}{r} dr + \frac{\rho v_{sr} V}{r} dr$$

$$-\frac{\rho V_{sr} V_{sz} \tilde{\tau}_z}{r G_{zs}} dr + 2 \frac{V_{sr}}{V_{sz}} \frac{\partial \tilde{\tau}_z}{\partial r} dr = 0$$

C^{-+}: Path rate: $\frac{dr}{dt} = -V_{sr}$, $\frac{dz}{dt} = V_{sz}$, $\frac{dt}{dt} = 1$

Path: $dr = -V_{sr}\,dt$, $dz = V_{sz}\,dt$, $dt = dt$

$$d\tilde{\tau}_r - \frac{V_{sr}}{V_{sz}} d\tilde{\tau}_z + \rho V_{sr}\, dV + \frac{2\tilde{\tau}_r}{r} dr - \frac{\rho V_{sr} V}{r} dr - \frac{\rho V_{sr} V_{sz} \tilde{\tau}_z}{r G_{zs}} dr + 2 \frac{V_{sr}}{V_{sz}} \frac{\partial \tilde{\tau}_z}{\partial r} dr = 0 \qquad (5.25c)$$

C^{--}: Path rate: $\frac{dr}{dt} = -V_{sr}$, $\frac{dz}{dt} = -V_{sz}$, $\frac{dt}{dt} = 1$

Path: $dr = -V_{sr}\,dt$, $dz = -V_{sz}\,dt$, $dt = dt$ (5.25d)

$$d\tilde{\tau}_r + \frac{V_{sr}}{V_{sz}} d\tilde{\tau}_z + \rho V_{sr}\, dV + \frac{2\tilde{\tau}_r}{r} dr - \frac{\rho V_{sr} V}{r} dr + \frac{\rho V_{sr} V_{sz} \tilde{\tau}_z}{r G_{zs}} dr - 2 \frac{V_{sr}}{V_{sz}} \frac{\partial \tilde{\tau}_z}{\partial r} dr = 0$$

The four paths are similar to those of the constant modulus case which are shown in Fig. 3.8. With variable moduli, however, V_{sr} and V_{sz} vary with shearing stress and strain and therefore so do the directions of the paths. In a medium having a single constant modulus,

$$G_{zt} = G_{rt} = G_{zs} = G$$

resulting in

$$V_{sr} = V_{sz} = V_s = \sqrt{\frac{G}{\rho}}$$

Under these conditions, Eqs. (5.25) reduce to Eqs. (3.34), the equations for a medium having a constant modulus.

D. Numerical Solution of Transformed Equations

Similar to solutions in which moduli are constant, numerical solutions in which moduli vary are obtained as a function of space for each time of a pre-selected sequence of times. Because the integration paths change in direction when moduli change, however, details between the two solution procedures differ significantly. In the following sections, various aspects of the numerical procedure which, in concept, is similar to that used by Streeter, Wylie and Richart (1974) in a variable moduli, one-dimensional analysis, are discussed.

1. Characteristics of Grid

Figure 5.1 shows a typical computational cell used to obtain the dependent variables at node P at time $t+\Delta t$. Each of the four integration paths originates from one of four zones, termed subcells, and intersects node P. The subcells are regions in the r-z plane corresponding to time t, and are designated along with corresponding path origins as A, B, C and D. Using the stability criterion used in the one-dimensional method

of characteristics as a guide (Wylie and Streeter, 1978), the distance intervals of the grid are selected such that the origin of each path may reach, but not extend beyond the boundary of its subcell. As shown in Fig. 5.1, with this restriction the dimensions of a subcell, $\Delta\bar{r}$ and $\Delta\bar{z}$, are given as

$$\Delta\bar{r} = |V_{srm}|\,\Delta t$$
$$\Delta\bar{z} = |V_{szm}|\,\Delta t \qquad (5.26)$$

where $|V_{srm}|$ and $|V_{szm}|$ are the absolute, maximum values of V_{sr} and V_{sz} as determined by the maximum moduli in the r and z directions.

2. Algebraic Equations

In addition to the four available path equations, three algebraic equations describing the deformation properties of the material are required. These equations give shear moduli in terms of immediate and past stresses and strains and depend upon the modeling of the material. To avoid iterations needed to solve this combination of seven equations, a simplified procedure is used to obtain a solution. Prior to computations for a given node, each related subcell is

assigned single average values of shear moduli. These values are based solely on the dependent variables existing at the initial time of the increment and remain constant throughout the increment. Under these conditions, computations for shear moduli are independent of each other and independent of those for the dependent variables. Thus, at each node, a simultaneous solution of only four algebraic equations in four unknowns, τ_r, τ_z, $\partial\tau_z/\partial r$, and V, is required.

The simplified simultaneous equations are obtained by integrating each of Eqs. (5.25) along appropriate paths shown in Fig. 5.1. As an example, Eq. (5.25a) is integrated along the C^{++} path from point A to node P:

$$\int_A^P d\tau_r + \frac{V_{srA}}{V_{szA}} \int_A^P d\tau_z - \rho V_{srA} \int_A^P dV - 2\frac{V_{srA}}{V_{szA}} \int_A^P \frac{\partial \tau_z}{\partial r} dr + 2\int_A^P \frac{\tau_r}{r} dr + \frac{\rho V_{srA} V_{szA}}{G_{zsA}} \int_A^P \frac{\tau_z}{r} dr + \rho V_{srA} \int_A^P \frac{V}{r} dr = 0 \tag{5.27}$$

Subscripts appended to V_{sr}, V_{sz}, and G_{zs} identify the subcell in which the path originates. Integrating Eq. (5.27) using the trapezoidal rule gives

$$\tau_{rp} - \tau_{rA} + \frac{V_{srA}}{V_{szA}}(\tau_{zp} - \tau_{zA}) - \rho V_{srA}(V_p - V_A)$$
$$- \frac{V_{srA}}{V_{szA}}\left(\frac{\partial \tau_z}{\partial r}\Big|_p + \frac{\partial \tau_z}{\partial r}\Big|_A\right)(r_p - r_A) + \left(\frac{\tau_{rp}}{r_p} + \frac{\tau_{rA}}{r_A}\right)(r_p - r_A) + \frac{\rho V_{srA} V_{szA}}{2 G_{zsA}}\left(\frac{\tau_{zp}}{r_p} + \frac{\tau_{zA}}{r_A}\right)(r_p - r_A) + \frac{\rho V_{srA}}{2}\left(\frac{V_p}{r_p} + \frac{V_A}{r_A}\right)(r_p - r_A) = 0 \qquad (5.28)$$

Subscripts appended to the dependent variables and radii identify points along the C^{++} path. Similar integrations are performed for the remaining paths and the resulting equations may be arranged to give the systematic equations, Eqs. (3.37). The coefficients of these equations, a_1 through e_7, are defined in Appendix I for the case of variable moduli. If conditions are imposed in which moduli are constant, the coefficients reduce to those for the case of constant moduli.

3. Solution of Algebraic Equations

In order to determine the coefficients in Eqs. (3.37) needed to obtain a solution at a node, the average values of the moduli, V_{sz} and V_{sr} within subcells, the origins of the paths and the values of the

dependent variables at these origins are required at the start of a time increment. To obtain these values related functions must be defined over the entire area of each subcell, and shape functions are used for this purpose.

a. Shape Functions--As discussed by Zienkiewicz (1971) and Gallagher (1975), a function may be approximated over a rectangular region of the r-z plane, using only the values of this function at the corners of this region, by use of the expression

$$\Phi(r,z) = \alpha_1 + \alpha_2 r + \alpha_3 z + \alpha_4 r z \qquad (5.29)$$

where $\Phi(r,z)$ represents the approximating function. The α coefficients are constants which depend on the shape and size of the rectangle and the values of the actual function at the corners. These coefficients may be determined by solving simultaneously the four equations obtained by substituting the coordinates of each corner and the values of the function at the corners into Eq. (5.29). With these α coefficients, Eq. (5.29) gives the exact values of the function at the corners of the region and approximate values at all other locations.

An approximating function defined over a rectangular subcell is shown in Fig. 5.2 (a) for an

arbitrary set of function values, ϕ_1 through ϕ_4, at the corners. This approximating function may be written as

$$\Phi(r,z) = N_1(r,z)\phi_1 + N_2(r,z)\phi_2 + N_3(r,z)\phi_3 + N_4(r,z)\phi_4 \quad (5.30)$$

where $N_1(r,z) \rightarrow N_4(r,z)$ are shape functions and the subscripts identify the corners of the subcell.

As shown in Fig. 5.2(b), each shape function describes a function defined over the region and generated by a unit value of function at one of the corners and a zero value at all others. The shape functions are given as

$$\begin{aligned} N_1(r,z) &= \frac{(r-r_4)(z-z_2)}{4\Delta r \Delta z} \\ N_2(r,z) &= -\frac{(r-r_4)(z-z_1)}{4\Delta r \Delta z} \\ N_3(r,z) &= \frac{(r-r_1)(z-z_1)}{4\Delta r \Delta z} \\ N_4(r,z) &= -\frac{(r-r_1)(z-z_2)}{4\Delta r \Delta z} \end{aligned} \quad (5.31)$$

where $2\Delta r$ and $2\Delta z$ are the dimensions of the subcell and $r_1 \rightarrow r_4$ and $z_1 \rightarrow z_4$ are the coordinates of the corners. As shown in Fig. 5.2(c), the ϕ's are the

amplitudes of the shape functions. Thus, each term of Eq. (5.30) represents an approximating function caused by the value of the original function at one of the corners and zero at the others.

To apply the concept of the shape function, values of the dependent variables are needed at each of the corners of each subcell. As shown in Fig. 5.1, the numerical procedure gives only two of these values per subcell, and these are at opposing corners. Values at the remaining two corners are obtained by averaging values from the four surrounding nodes. At boundaries only the two appropriate nodal values are averaged.

b. Average Stresses and Strains--To obtain the moduli for a subcell, the average strains within the subcell are needed. These strains are determined by differentiating and then averaging the approximate displacement field within the subcell. The nodal displacements needed to obtain this displacement field are obtained by integrating the nodal velocities with respect to time using the trapezoidal rule;

$$u_t = \int_{t-\Delta t}^{t} V\,dt + u_{t-\Delta t} \qquad (5.32)$$

$$= \frac{1}{2}\left(V_{t-\Delta t} + V_t\right)\Delta t + u_{t-\Delta t}$$

The quantity u is the displacement and the subscripts reference time. The approximate displacement field within a subcell, based on Eq. (5.30), is given by

$$u(r,z) = N_1(r,z)\,u_1 + N_2(r,z)\,u_2 + N_3(r,z)\,u_3 + N_4(r,z)\,u_4 \tag{5.33}$$

To obtain the γ_r-strain field within the subcell in terms of these displacements, Eq. (5.33) is differentiated in accordance with the defining relation, Eq. (3.4), giving

$$\gamma_r(r,z) = \frac{\partial u}{\partial r} - \frac{u}{r} = N_1^{\gamma r}(r,z)\,u_1 + N_2^{\gamma r}(r,z)\,u_2 + N_3^{\gamma r}(r,z)\,u_3 + N_4^{\gamma r}(r,z)\,u_4 \tag{5.}$$

where

$$N_1^{\gamma r} = \frac{\partial N_1}{\partial r} - \frac{N_1}{r} = \frac{r_4}{4r\Delta r\Delta z}(z - z_2)$$

$$N_2^{\gamma r} = \frac{\partial N_2}{\partial r} - \frac{N_2}{r} = -\frac{r_4}{4r\Delta r\Delta z}(z - z_1)$$

$$N_3^{\gamma r} = \frac{\partial N_3}{\partial r} - \frac{N_3}{r} = \frac{r_1}{4r\Delta r\Delta z}(z - z_1)$$

$$N_4^{\gamma r} = \frac{\partial N_4}{\partial r} - \frac{N_4}{r} = -\frac{r_1}{4r\Delta r\Delta z}(z - z_2)$$

Similarly the γ_z-strain field is obtained by differentiating Eq. (5.33) in accordance with Eq. (3.5) giving

$$\gamma_z(r,z) = \frac{\partial u}{\partial z} = N_1^{\gamma_z}(r,z)\,u_1 + N_2^{\gamma_z}(r,z)\,u_2 + N_3^{\gamma_z}(r,z)\,u_3 + N_4^{\gamma_z}(r,z)\,u_4 \tag{5.35}$$

where

$$N_1^{\gamma_z} = \frac{\partial N_1}{\partial z} = \frac{1}{4\Delta z\Delta r}(r-r_4)$$

$$N_2^{\gamma_z} = \frac{\partial N_2}{\partial z} = -\frac{1}{4\Delta z\Delta r}(r-r_4)$$

$$N_3^{\gamma_z} = \frac{\partial N_3}{\partial z} = \frac{1}{4\Delta z\Delta r}(r-r_1)$$

$$N_4^{\gamma_z} = \frac{\partial N_4}{\partial z} = -\frac{1}{4\Delta z\Delta r}(r-r_1)$$

Each of the strain fields given by Eqs. (5.34) and (5.35) are averaged over the subcell by integrating

each field with respect to area over the entire area of the subcell and dividing this quantity by this area. These steps may be expressed as

$$\gamma_{AVE} = \frac{1}{4\Delta r \Delta z} \int_{r_1}^{r_4} \int_{z_1}^{z_2} \gamma(r,z)\, dz\, dr \qquad (5.36)$$

where $\gamma(r,z)$ represents either the γ_r- or γ_z-strain field as expressed by Eqs. (5.34) or (5.35), respectively, and γ_{AVE} is the corresponding average strain within the subcell. These integrations give

$$\gamma_{rAVE} = -\frac{\ln(r_4/r_1)}{8\Delta r^2}\left[r_4(u_1+u_2) - r_1(u_3+u_4)\right] \qquad (5.37)$$

and

$$\gamma_{zAVE} = \frac{1}{4\Delta z}(u_2 - u_1 + u_3 - u_4) \qquad (5.38)$$

Average values of each of the τ_r- and τ_z-stresses are needed within subcells to obtain the moduli of the subcells. These averages may be obtained using shape functions, but simple averaging of the values of these stresses at the corners of a subcell gives identical results.

c. Solution Procedure--The current and past averages of the stresses and strains within each subcell are used to compute the moduli within each subcell.

From these moduli, V_{Sr} and V_{Sz} are computed for each subcell using Eqs. (5.21) and then these quantities are used to locate the origin of each integration path. As demonstrated in Fig. 5.3, which shows a C^{++} path projected onto the r-z plane, the origin of this path, (r_A, z_A), is obtained by subtracting from the coordinates of the terminal point, (r_p, z_p), the spatial components of the C^{++} path giving

$$r_A = r_p - V_{SrA}\,\Delta t$$
$$z_A = z_p - V_{SzA}\,\Delta t \tag{5.39}$$

The spatial length of this path, Δs, is

$$\Delta s = \sqrt{V_{SrA}^2 + V_{SzA}^2}\;\Delta t \tag{5.40}$$

The remaining paths are treated similarly.

To determine the values of the dependent variables at the origin of each path the fields of the dependent variables are first approximated within each subcell using Eq. (5.30). As an example, the approximate τ_r-stress field within a subcell is given as

$$\tau_r(r,z) = N_1(r,z)\,\tau_{r1} + N_2(r,z)\,\tau_{r2} + N_3(r,z)\,\tau_{r3} + N_4(r,z)\,\tau_{r4} \tag{5.41}$$

The values of the dependent variables are then determined at the origin of each path by introducing the coordinates of the origin into these field equations.

The steps which have been discussed permit the coefficients of Eqs. (3.37) to be computed and solving these equations gives the solution at a node. Each node within a medium is treated similarly and nodes along the boundary are treated as described in Chapters III and IV for the case of constant moduli.

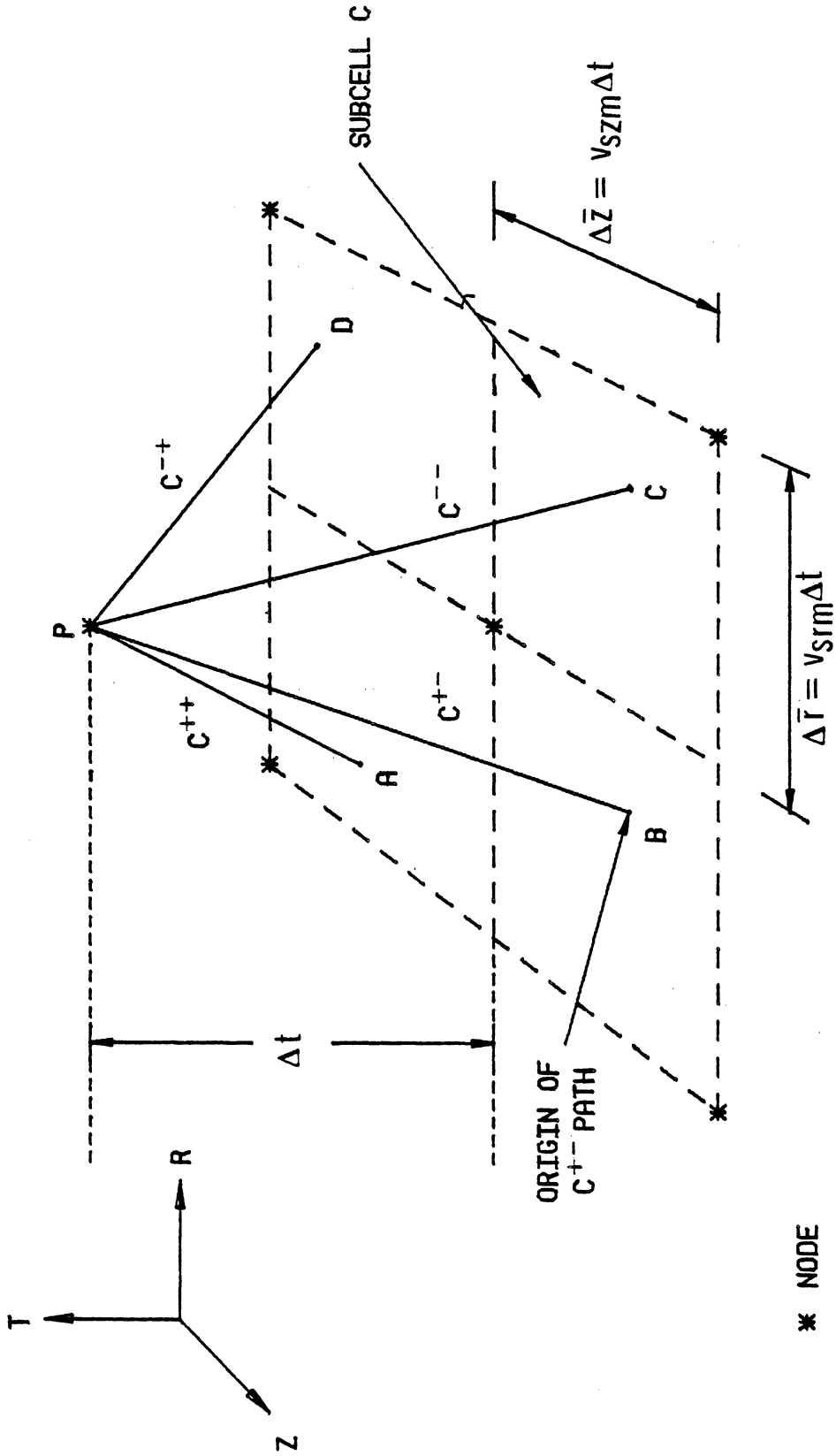

Fig. 5.1: Isolated Computation Cell for Variable Moduli Solution at Node P at Time t + Δt.

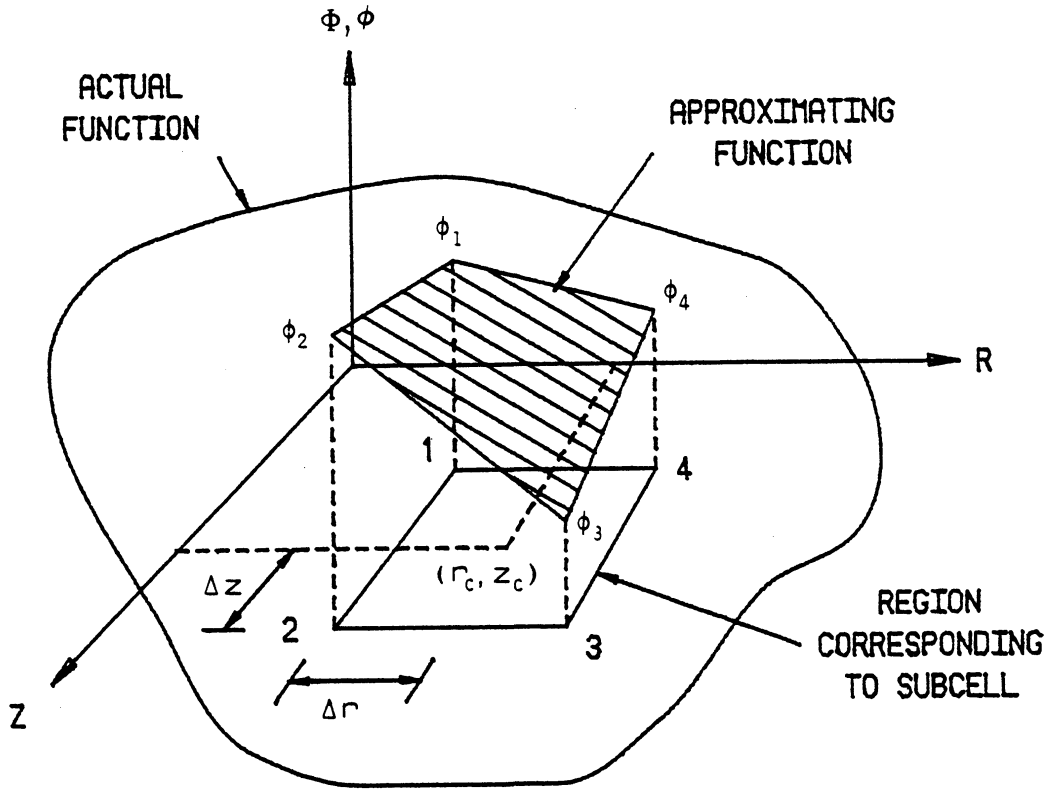

(a) Approximating Function, $\Phi(r, z)$.

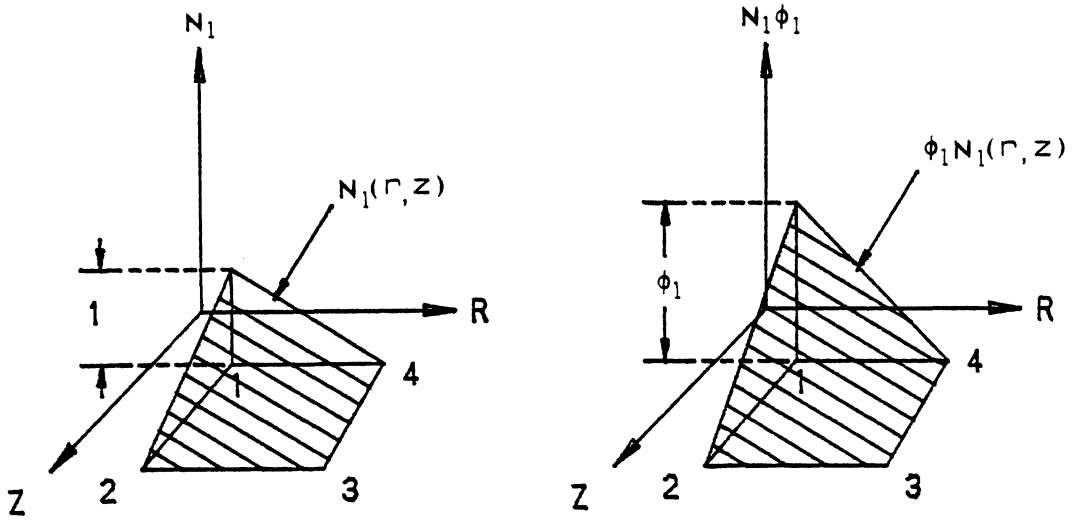

(b) Shape Function for Corner 1.

(c) Contribution of Value of Function at Corner 1, ϕ_1, to Approximating Function.

Fig. 5.2: Shape Function Concepts Applied to Subcell Having Corners 1, 2, 3, and 4 in r-z Plane.

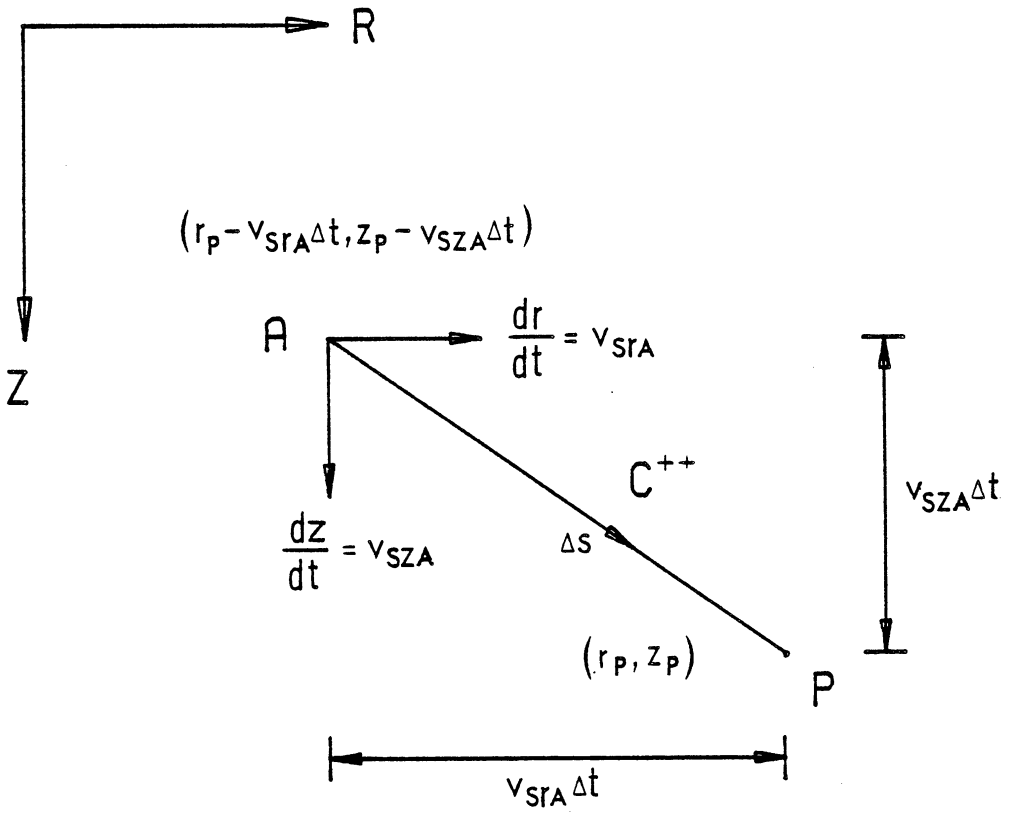

Fig. 5.3: Projection of C^{++} Path Having Origin, A, and Terminal Point, P, onto r-z Plane.

CHAPTER VI

EXAMPLES OF NONLINEAR INELASTIC BEHAVIOR

A. Introduction

In this chapter, the numerical procedure developed in Chapter V is used to obtain solutions to several examples. These examples range in difficulty from simple one-dimensional radial wave propagation to the torsional response of a disk with mass resting on a half space. In order to determine the effects of the properties of the medium on dynamic response, the medium in these examples was treated first as a linear elastic material, and then as a nonlinear inelastic material. Relevant theoretical background and equations are also given.

An energy balance was used to check the numerical solutions with respect to concept and grid adequacy. The development of this energy balance is also presented.

B. Equations for Variable Moduli

Ramberg-Osgood equations were used to determine the variable moduli needed in the numerical analysis.

These equations describe the effects of nonlinear inelasticity on the properties of a material and have been discussed by Richart (1975).

As shown in Fig. 6.1, hysteretic shearing stress-strain behavior may be modeled using two Ramberg-Osgood equations; one desribing a skeleton curve and a second describing extended branches. The tangent modulus, G_t, is obtained from these equations as

$$G_t = \frac{d\tau}{d\gamma} = G_o\left(\frac{1}{1 + \alpha R|\tau/\tau_y|^{R-1}}\right) \qquad (6.1a)$$

along skeleton curves, and

$$G_t = \frac{d\tau}{d\gamma} = G_o\left(\frac{1}{1 + \alpha R|(\tau-\tau_1)/2\tau_y|^{R-1}}\right) \qquad (6.1b)$$

along extended branches. The quantity τ_y is a parameter related to the shearing strength of the material ($\tau_y = C_1\tau_m$), γ_1 and τ_1 define origins of the extended branches at stress reversals and R and α are parameters which describe the shape of the curves. The quantity G_s, defined in Chapter V and shown in Fig. 6.1, is also obtained from the Ramberg-Osgood equations and is given as

$$G_s = \frac{\tau}{\gamma} = G_o\left(\frac{1}{1 + \alpha|\tau/\tau_y|^{R-1}}\right) \qquad (6.2a)$$

along the skeleton curve, and

$$G_s = \frac{\tau}{\gamma} = G_o\left\{(\tau/\tau_y)/\left[((\tau-\tau_1)/\tau_y)\left(1+\alpha\left|(\tau-\tau_1)/2\tau_y\right|^{R-1}\right)+G_o\gamma_1/\tau_y\right]\right\} \qquad (6.2b)$$

along extended branches.

Along an extended branch the magnitude of G_s may take on the values of zero and infinity. To avoid computing difficulties, the value of G_s was given absolute upper and lower bounds. During preliminary work, however, it was observed that insignificant reversals of strain triggered very large changes in the value of G_s which caused erratic results. To prevent this difficulty, the terms in which G_s appeared were linearized by assigning to this quantity the constant value of the elastic shear modulus. This improved results considerably. Clearly, the less the strain amplitude, the better will be this approximation. Also, the value of the term involving G_s (see Eq. (5.20)) is inversely proportional to the radius. Therefore the relative effect of this term decreases with increasing radius. All results presented are based upon this approximation.

C. Energy Development

At any instant of time during a transient, the accumulated work done on a solid medium by applied stresses must be equal to the sum of the accumulated

energy lost and the instantaneous energy stored by the medium. Energy may be stored as kinetic and elastic strain energy. Energy is lost when the medium deforms plastically.

The external work accumulated at time $t + \Delta t$ is given as

$$W(t+\Delta t) = W_{\Delta t} + W(t) \tag{6.3}$$

where $W(t + \Delta t)$ and $W(t)$ represent work accumulated at the indicated times. The quantity $W_{\Delta t}$ is the incremental work done during time increment, Δt, and is given as

$$W_{\Delta t} = \sum_{i=1}^{n} \int_{u_i(t)}^{u_i(t+\Delta t)} F_i(t)\, du_i \tag{6.4}$$

The quantity $F_i(t)$ is the ith instantaneous external force and du_i is the infinitesimal displacement in the direction of this force. The displacements, $u_i(t)$ and $u_i(t + \Delta t)$, at the point of application and in the direction of the force occur at times t and $t + \Delta t$, respectively. The quantity n is equal to the number of forces which are applied. In a numerical solution, external forces are obtained from stresses developed at the nodes along the boundaries and acting over the areas assigned to these nodes. Thus for a numerical solution the i in Eq. (6.4) refers to the ith node. By changing

variables from u to t and writing forces in term of nodal stresses, Eqs. (6.3) and (6.4) may be combined to give

$$W(t+\Delta t) = \sum_{i=1}^{n} \left[- \int_{t}^{t+\Delta t} (\tau_{ri} + \tau_{zi}) A_i V_i \, dt \right] + W(t) \qquad (6.5)$$

where A_i is the area assigned to the ith node. The negative sign is needed because of the sign convention used. Equation (6.5) is integrated numerically using the trapezoidal rule to give the accumulated work as

$$W(t+\Delta t) = \sum_{i=1}^{n} \left\{ - \frac{A_i \Delta t}{2} \left[\tau_{ri}(t+\Delta t) V_i(t+\Delta t) + \tau_{ri}(t) V_i(t) + \tau_{zi}(t+\Delta t) V_i(t+\Delta t) + \tau_{zi}(t) V_i(t) \right] \right\} + W(t) \qquad (6.6)$$

With the Ramberg-Osgood stress-strain model, accumulated hysteretic loss and instantaneous elastic strain energy are combined. The sum of these quantities for the medium at time $t + \Delta t$, $SH(t + \Delta t)$, may be written in the same form as Eq. (6.3) giving

$$SH(t + \Delta t) = SH_{\Delta t} + SH(t) \qquad (6.7)$$

The incremental quantity, $SH_{\Delta t}$, may be obtained from the area under the stress-strain curve corresponding to a change in strain at a point by integrating this area

with respect to volume. Mathematically, this process is described by

$$SH_{\Delta t} = \int_{\bar{V}} \left(\int_{\gamma_r}^{\gamma_r + \Delta\gamma_r} \tau_r \, d\gamma_r + \int_{\gamma_z}^{\gamma_z + \Delta\gamma_z} \tau_z \, d\gamma_z \right) d\bar{V} \tag{6.8}$$

where $\bar{V}$ is the volume of the medium. For use in the numerical analysis, Eq. (6.8) may be written as

$$SH_{\Delta t} = \sum_{j=1}^{m} \left(\int_{\gamma_{rave}}^{(\gamma_r + \Delta\gamma_r)_{ave}} \tau_{rave} \, d\gamma_{rave} + \int_{\gamma_{zave}}^{(\gamma_z + \Delta\gamma_z)_{ave}} \tau_{zave} \, d\gamma_{zave} \right) \Delta\bar{V}_j \tag{6.9}$$

where j refers to the jth subcell and $\bar{V}_j$ its volume. The symbol m represents the total number of subcells and the subscript "ave" indicates the average value of a quantity over a subcell, as obtained by use of either shape functions or simple averaging. Integrating Eq. (6.9) over time increment, Δt, using the trapezoidal rule, and substituting the result into Eq. (6.7) gives

$$\begin{aligned} SH(t+\Delta t) = \sum_{j=1}^{m} \frac{\Delta\bar{V}_j}{2} \Big\{ & \left[\tau_r(t+\Delta t) + \tau_r(t) \right]_{ave} \left[\gamma_r(t+\Delta t) \right. \\ & - \gamma_r(t) \Big]_{ave} + \left[\tau_z(t+\Delta t) + \tau_z(t) \right]_{ave} \left[\gamma_z(t+\Delta t) \right. \\ & \left. - \gamma_z(t) \Big]_{ave} \Big\}_j + SH(t) \end{aligned} \tag{6.10}$$

The instantaneous kinetic energy of the medium at time $t + \Delta t$, $KE(t + \Delta t)$, is given as

$$KE(t+\Delta t) = \frac{1}{2}\int_{\bar{V}} \rho V^2 \, d\bar{V} \tag{6.11}$$

For use in the numerical analysis, Eq. (6.11) may be expressed as

$$KE(t+\Delta t) = \sum_{j=1}^{m} \frac{1}{2} \rho \left[V_{ave}^2 (t+\Delta t) \right]_j \Delta \bar{V}_j \tag{6.12}$$

The degree to which work and energy balance at time, $t + \Delta t$, may be given by an energy ratio, $E_R(t + \Delta t)$, defined as

$$E_R(t+\Delta t) = \frac{KE(t+\Delta t) + SH(t+\Delta t)}{W(t+\Delta t)} \tag{6.13}$$

At any instant during a transient the value of this quantity is equal theoretically to 1.0. A value other than 1.0 indicates error in either the numerical solution or the energy balance, or both.

D. Radial Wave Propagation

In this section, the propagation of one-dimensional waves is simulated in the radial direction in the manner described in Chapter IV. Only boundary conditions which differ from those used in Chapter IV to model this condition are discussed. Numerical solutions to examples are also presented and discussed.

1. Boundary Conditions

The configuration of the staggered grid used to obtain numerical solutions was similar to that of the square grid shown in Fig. 4.2. In order to excite the body, a particle velocity which varied with time was applied to each node along the inner boundary. Since conditions do not vary with depth, both the rate of change of displacement with respect to depth, $\partial u/\partial z$, and, from Eq. (3.5), γ_z-strains, are equal to zero. Therefore, the second boundary condition at the inner surface is

$$\tau_z = 0 \tag{6.14}$$

Equation (6.14) was also applied to the nodes along the outer boundary for similar reasons. The outer boundary was modeled as a free surface; thus, the second boundary condition at this boundary is

$$\tau_r = 0 \tag{6.15}$$

2. Examples

Two examples which differed only in the properties of the material were solved. In one example the material was treated as a nonlinear, inelastic material and in the other example as a linear elastic material.

The low amplitude shear modulus, G_o, in the nonlinear model was given the value of the elastic shear modulus used in the linear model (G_o = 700250 psf = 4860 psi). The shearing strength in the nonlinear model was assumed as 62.5 psf (0.43 psi).

For each example, the radii of the inner and outer boundaries were 1000.0 and 1004.7 ft, respectively. In order to study the effects of the fineness of the grid, solutions were obtained using coarse, medium and fine grids consisting of 13, 25, and 49 nodes per row, respectively. For the linear case, solutions were obtained using the coarse and medium grids while the medium and fine grids were used to obtain nonlinear solutions.

A sinusoidal particle velocity having an amplitude which varied linearly over the first cycle and was constant thereafter was used to excite the body. The constant amplitude of the excitation was 0.05 fps and the frequency was 200 cps. Results from these examples are presented in Figs. 6.2 through 6.7.

a. Stress-Strain Curves--Average $\tilde{\gamma}_r$-stress vs. γ_r-strain curves obtained from a subcell located 0.75 ft from the inner boundary are given in Fig. 6.2

for the linear and nonlinear cases. Both curves are based on results obtained using the medium grid.

In the elastic case, the slope of the stress-strain curve is within 0.4 percent of the given elastic shear modulus. This difference decreases and the peaks of the stress-strain curves increase with increasing grid fineness. A small amount of artificial hysteresis was observed in the stress-strain curves obtained from subcells along the inner boundary. This effect, which decreases with increasing grid fineness, is thought to be caused by inconsistencies in obtaining values of the dependent variables at the corners of subcells located along boundaries.

In the nonlinear case, peak values of the stress-strain curves increase and the smoothness of the curves improves with increases in grid fineness. It was also found that the greater the degree of nonlinearity the finer is the grid needed to obtain smooth stress-strain curves.

b. Dependent Variables--Particle velocity and τ_r-stress are plotted for the two models in Figs. 6.3 through 6.6, as functions of time at a given radius, 1000.78 ft, and as functions of radius at a given time, 0.00916 sec. The excitation curve is included in Figs.

6.3 and 6.4. Values of τ_z-stress and $\partial\tau_z/\partial r$ are not plotted since these values were small.

The influence of grid fineness on the values of the plotted dependent variables is fairly small, especially in the linear elastic case. Therefore, the dependence of the stress-strain curves on grid fineness is due primarily to approximations introduced in obtaining quantities for the subcells rather than approximations in the numerical solution.

As shown in Figs. 6.3 through 6.6, within each medium disturbances propagate with a shape and an amplitude which depend on the properties of each medium. In the linearly elastic case, each increment of disturbance caused by an increment of excitation propagates at the same speed. Thus, as shown in Figs. 6.3 through 6.6, within the elastic medium the shape of the disturbance is similar to that of the excitation in radius and time.

In a nonlinear medium, because the wave velocity varies with stress level, the rates at which increments of disturbance propagate from the excitation boundary depend on the stress level at which these increments are introduced into the medium. In addition, as described by Kolsky (1963), within a strain softening, bilinear, inelastic, one-dimensional finite medium which is loaded

and then unloaded at one boundary, a complex series of internal reflections develop. These reflections take place when the rapidly propagating increments of disturbance caused by unloading the medium under elastic modulus conditions overtake the more slowly traveling increments of disturbance which developed during loading. As a result of these factors the form of the disturbance within the nonlinear medium does not resemble the form of the excitation in either radius or time.

As shown in Figs. 6.3 through 6.6, the amplitudes of the disturbance within the nonlinear medium are smaller than those in the linear medium. One source of these lower amplitudes is the loss in rigidity or the reduction in shear modulus which takes place in the nonlinear medium. The interactions between the loading and unloading increments of disturbance also cause reductions in amplitude.

c. Energy Balance--The results of the energy balance are given in Fig. 6.7 as plots of energy ratio vs. time for each solution. In both models, as the fineness of the grid is increased, the energy ratio approaches 1.0; thus, work and energy approach a state of balance. The elastic solutions converge to this value more rapidly than the nonlinear solutions and as

the degree of nonlinearity is increased, a finer grid is needed to develop a given energy ratio.

Since the values of the dependent variables are relatively insensitive to the changes in the fineness of the grid, in the examples presented, improvements in the energy ratio with increasing fineness of the grid are due primarily to improvements in the accuracy of the energy computations.

Work done is the most accurate of the quantities in the energy balance because it is computed directly from the values of the dependent variables. The various energies are computed using average stresses, strains and velocities. Each of these quantities depends on shape functions and the grid scheme both of which introduce errors. The average strains, discussed in Chapter V, involve the greatest number of approximations, and therefore, are the least accurately known quantities used in the energy computations. The sum of the accumulated hysteretic loss and the instantaneous strain energy, which depends on average strains, is the energy quantity which is most sensitive to changes in the fineness of the grid.

Inaccuracy in the values of average stress and strain is the major cause of the decay in the energy ratio which occurs with time in the nonlinear models

(see Fig. 6.7). These average values are based on the sharply changing disturbances which occur in the nonlinear case (see Fig. 6.5 and 6.6) and the peaks of these disturbances are difficult to approximate in the subcells. These peaks determine the peaks of the stress-strain curves for the subcells which in turn affect significantly the sum of the accumulated hysteretic loss and the instantaneous strain energy. As the number of peaks of the disturbance in the medium increases the ability to represent this sum decreases and therefore the energy ratio is in a transient state. Only when the number of peaks within the medium stabilizes does the energy ratio stabilize. In the nonlinear examples this occurs at a time of about 0.020 sec, when reflections from the outer boundary arrive at the excitation boundary. As the fineness of the grid is increased and the size of the subcells decrease, the average values of stress and strain improve and, as shown in Fig. 6.7, the magnitude of the decay in the energy ratio decreases.

The properties of the material influence the amount and distribution of energy introduced into the medium for the given excitation. Based upon the solutions using the medium grid, the energy introduced into the linear medium was 30 percent greater than that

introduced into the nonlinear medium during the same period.

Energy in the linear elastic medium is stored entirely as instantaneous elastic strain and kinetic energies. In the nonlinear inelastic medium, energy is dissipated by the permanent deformation of the medium as well as stored. A measure of the amount of energy dissipated per unit volume at a point is given by the area enclosed by the stress-strain curves. As shown in Fig. 6.2, in the nonlinear case this area is large.

The convergence of the energy ratio to the value which is correct theoretically gives a great deal of credibility to the nonlinear numerical solutions. Since the convergence of the dependent variables is more rapid, however, the energy ratio provides only a conservative means of estimating the adequacy of a grid. The balance of energy has been found to be very sensitive to seemingly minor details in the analysis. Therefore, the energy balance has been extremely useful in identifying program errors and in evaluating the influence and correctness of changes in the analysis. In addition, energy computations are useful for interpreting a solution physically since these computations give information on the amount and distribution of energy in a medium.

E. Wave Propagation Along a Cylinder

In this section the propagation of τ_z-stresses and γ_z-strains along the longitudinal axis of a semi-infinite solid cylinder is considered. The assumed boundary conditions are discussed briefly and results obtained from an example are presented and discussed.

1. Boundary Conditions

For convenience, the grid used in the problem of a rigid disk resting on a half space was used to model the solid cylinder. Details of the grid, shown schematically in Fig. 6.8, and a discussion of boundary conditions are given in Section F.1. As shown in Fig. 6.8, the grid is divided into two cylindrical zones. One zone has the same outer radius as the disk and represents the solid cylinder. The other zone surrounds the solid cylinder and is made much less rigid than the solid cylinder by assigning to this zone much smaller shear moduli. Because of its low relative rigidity this zone does not develop significant stresses and most of the wave energy created by exciting the top of the solid cylinder remains within the bounds of the cylinder. Thus the less rigid surrounding zone has very little influence on the response of the inner cylinder. The system is excited by applying a torque to the disk which

rotates in response, and excites the top of the solid cylinder with a distribution of particle velocities which is proportional to the radius.

2. Examples

In this section results are presented from an example in which the solid cylinder was treated as a nonlinear inelastic material. Since these results are similar to those from the example of nonlinear radial wave propagation given in Section D.2 only a very brief discussion is given. Results are not presented for a linear solid cylinder since these results are similar to the linear results given in Section D.2.

As shown in Fig. 6.8, the radius of the solid cylinder is 0.375 ft. To avoid division by zero, the inner boundary was given a very small non-zero value: 0.001 ft. The grid, which consists of 55 nodal rows, each containing 34 nodes, represents an area extending 1.90 ft in the radial direction and 1.56 ft in depth. The disk was excited by a sinusoidal torque having an amplitude which increased linearly with time. The amplitude of this excitation after one cycle is 40 ft-lb and the frequency is 300 cps. The low amplitude shear moduli and the shearing strength ($\gamma_m = \gamma_y/0.8$) of the solid cylinder were given values of 700,250 psf (4860

psi) and 44 psf (.31 psi), respectively. The low amplitude shear moduli of the less rigid zone were assigned the value of 70 psf which is equal to one ten thousandth of those of the solid cylinder.

A curve of τ_z-stress vs. γ_z-strain obtained from a subcell located within the cylinder at a radius of 0.288 ft and a depth of 0.0288 ft is plotted in Fig. 6.9. Both τ_r-stresses and γ_r-strains were found to be small. The energy ratio vs. time is plotted in Fig. 6.10 and since neither the excitation nor the disturbance within the cylinder had stabilized over the span of the analysis, the energy ratio is in a transient state. Plots of the angular velocity of the disk, and the particle velocity and the τ_z-stress within the cylinder at a depth of 0.115 ft and radius of 0.289 ft vs. time are given in Fig. 6.11. Particle velocity and τ_z-stress within the cylinder at a radius of 0.289 ft and a time of 0.00263 sec vs. depth is plotted in Fig. 6.12.

F. Disk Resting on a Half Space

In the following section, boundary conditions are formulated for a nonlinear, inelastic half space on the surface of which rests a rigid disk having mass. Torsional loadings may be applied to this disk and slip

is permitted along the interface between the disk and the half space. The energy balance is then adapted to this problem and solutions to examples in which a torsional pulse was applied to the disk are presented and discussed.

1. Boundary Conditions

Except at the disk, boundary conditions are identical with those presented in Chapter IV for the massless disk on an elastic half space and are not repeated. The grid used to obtain solutions is also similar to that used in Chapter IV and shown in Fig. 4.20.

Moments are applied to the rigid disk and as a result the disk rotates. This rotation is resisted by the inertia of the disk and shearing stresses which develop within the half space and act along the interface. Figure 6.13 shows the sign convention for the applied moment, M_A, the angular velocity of the disk, ω, and the resultant moment, M_R, of the stresses along the interface.

Values of the angular velocity of the disk and of the shearing stresses and particle velocities within the half space along the interface are obtained as a function of time by applying Newton's Second Law to the disk. Newton's Second Law is given as

$$M_{net}(t) = I \frac{d\omega}{dt} \tag{6.16}$$

where I is the mass moment of inertia of the disk about its vertical centerline and $M_{net}(t)$ is the instantaneous net moment acting on the disk.

In the numerical analysis both the net moment and the angular acceleration, $d\omega/dt$, are averaged over the finite increment of time, Δt, starting at time t and ending at time $t + \Delta t$. Thus, Eq. (6.16) is expressed numerically, in an expanded form, as

$$\frac{M_A(t+\Delta t) + M_R(t+\Delta t) + M_A(t) + M_R(t)}{2} = I \frac{\omega(t+\Delta t) - \omega(t)}{\Delta t} \tag{6.17}$$

in which $M_R(t + \Delta t)$ and $\omega(t + \Delta t)$ are unknown.

By the use of the C^{+-} and C^{--} path equations, $M_R(t + \Delta t)$ may be expressed in terms of $\omega(t + \Delta t)$ and Eq. (6.17) may then be solved for $\omega(t + \Delta t)$. In order to obtain an expression for the resisting moment at time $t + \Delta t$ in terms of the angular velocity of the rigid disk at this time, first a condition of no slip is assumed along the interface. Under this condition the half space does not deform along the interface; thus, along the interface $\gamma_r = 0$ and

$$\tau_r = 0 \tag{6.18}$$

Also, under this condition, the particle velocity of the half space at each node along the interface may be expressed in terms of the angular velocity of the disk at time $t + \Delta t$ as

$$V_i(t + \Delta t) = \omega(t + \Delta t)\,\bar{r}_i \tag{6.19}$$

where the index i refers to the ith node along the interface. An assumption is made that the node at the centerline does not influence the motion of the disk; therefore, this node is treated independently. Substituting the two boundary conditions, Eqs. (6.18) and (6.19), into each of the two path equations from each of the k remaining nodes along the interface gives 2k equations in 2k + 1 unknowns: $\partial\tau_z/\partial r|_i(t + \Delta t)$, $\tau_{zi}(t + \Delta t)$ and $\omega(t + \Delta t)$. At each of these nodes the two path equations may be combined to eliminate $\partial\tau_z/\partial r|_i(t + \Delta t)$, giving $\tau_{zi}(t + \Delta t)$ in terms of $\omega(t + \Delta t)$ at each of these nodes. As described in Chapter IV for the problem of a massless disk on a half space, the resisting moment $M_R(t + \Delta t)$, may be written in terms of the nodal stresses, $\tau_{zi}(t + \Delta t)$, using Eq. (4.38). Expressing $\tau_{zi}(t + \Delta t)$ in terms of $\omega(t + \Delta t)$

and absorbing all constants into one, Eq. (4.38) may be written as

$$M_R(t+\Delta t) = \sum_{i=1}^{k} B_i\, \omega(t+\Delta t) \tag{6.20}$$

where B_i is a constant. Substituting Eq. (6.20) into Eq. (6.17) permits Eq. (6.17) to be solved for $\omega(t + \Delta t)$ which may be introduced into the path equations giving values for $\tau_{zi}(t + \Delta t)$. The magnitude of each of these stresses is compared with the magnitude of the stress needed to cause slip along the interface. If this magnitude is not exceeded then the solution along the interface is completed by computing nodal velocities using Eq. (6.19) and solving for $\partial\tau_z/\partial r|_i(t + \Delta t)$ by substituting the values of $\tau_{zi}(t + \Delta t)$ and $V_i(t + \Delta t)$ into the original path equations.

If, after obtaining the values of $\tau_{zi}(t + \Delta t)$, it is found that the magnitude of the slip-stress is exceeded at some node along the interface, the magnitude of the stress at this node is replaced by the slip-stress while the sign is retained. Mathematically, this is stated as

$$\tau_{zi}(t+\Delta t) = \frac{\tau_{zi}(t+\Delta t)}{|\tau_{zi}(t+\Delta t)|}\,|\tau_{z\,slip}| \tag{6.21}$$

where τ_{zslip} is the slip-stress. The value of the incremental moment caused by the stress at the ith slipping node, $M_{iRS}(t + \Delta t)$, may be obtained directly as

$$\Delta M_{iRS}(t+\Delta t) = (2\pi r_i \Delta r)\bar{r}_i \tau_{zi}(t+\Delta t) \quad (6.22)$$

The resultant moment may then be expressed as the sum of two components: one caused by the stresses at nodes at which slip occurs and a second caused by stresses at nodes at which slip does not occur. The latter component is a function of the unknown, $\omega(t + \Delta t)$. The resultant moment is given as

$$M_R(t+\Delta t) = \sum_{\substack{\text{non} \\ \text{slipping} \\ \text{nodes}}} B_i \omega(t+\Delta t) + \sum_{\substack{\text{slipping} \\ \text{nodes}}} \Delta M_{iRS}(t+\Delta t) \quad (6.23)$$

Equation (6.23) is substituted into Eq. (6.17) and a solution is again obtained for $\omega(t + \Delta t)$. This quantity is substituted into Eq. (6.19) to obtain the particle velocities of the half space along the interface at each node at which slip does not occur. These particle velocities are then substituted back into the path equations and $\tau_{zi}(t + \Delta t)$ is computed for each of these nodes.

The development of slip at any node causes a redistribution of stress along the interface which may cause slip at other nodes along the interface.

Therefore, it is necessary to check the values of $\tau_{zi}(t + \Delta t)$ to determine whether further slip has taken place. If further slip has taken place, the procedure for obtaining values of $\tau_{zi}(t + \Delta t)$ under conditions of slip and checking these stresses against the slip-stress is repeated. This process continues until no further slip takes place, after which the remaining unknowns along the interface are computed.

To obtain a complete solution at slipping nodes, a second boundary condition, in addition to that specifying the slip-stress, is needed. At each of these nodes the particle velocity of the half space is an independent unknown. Also, as shown in Fig. 9.18, deformations which cause τ_r-stresses develop in slipping zones. For the second boundary condition the assumption is made that, since the slip-stress is a maximum stress, at slipping nodes the rate of change of τ_z-stress with respect to radius is equal to zero. Mathematically, this is given as

$$\frac{\partial \tau_z}{\partial r} = 0 \tag{6.24}$$

If the magnitudes of the τ_z-stresses at slipping nodes fall below the slip-stress, slip ceases and at these nodes the half space and the disk have the same velocities. Without slip the half space cannot deform

in the plane of the interface; therefore, τ_r-stresses are locked into the interface at these nodes until further slip takes place. The τ_r-stresses at these nodes are assigned the values of the τ_r-stresses existing immediately prior to the return to the no-slip condition. These values are retained until further slip takes place at these nodes.

At the inner node along the interface three boundary conditions are needed. For one of these, the half space is assumed to behave rigidly along the interface leading to Eq. (6.18). For the other two boundary conditions, the half space is assumed to follow the motion of the disk without developing τ_z-stress. This condition may be expressed by Eq. (6.19) and

$$\tau_z = 0 \tag{6.25}$$

The boundary conditions along the interface are summarized schematically in Fig. 6.14.

The edge of the disk lies between two nodes. Similar to all points centered between nodes, values of the dependent variable are needed at this location. Because at this location, functions such as τ_z-stress and the slopes of functions such as particle velocity are discontinuous theoretically, a parabolic extrapolation rather than the simple averaging of values from

surrounding nodes is used to obtain values of the dependent variables. The extrapolation is parabolic because of the nature of the functions in this region. To obtain the values of the dependent variables at this location for use in the outer subcell beneath the disk, the extrapolation is based upon the values of the dependent variables at the outer three nodes along the interface. To obtain values of the dependent variables at this location for use in the inner subcell along the free surface, the extrapolation is based upon the values of the dependent variables at the inner three nodes along the free surface.

2. Energy Development

In this section the energy balance presented in Section C is adapted to the problem of a disk on a half space.

At any instant during a transient the accumulated work done by the disk on the half space must equal the sum of the instantaneous energy stored within the half space and the accumulated loss of energy caused by slip at the interface and inelasticity of the half space.

An expression for the incremental work done on the half space by the disk, $W_{H\Delta t}$, in rotating from angular displacement $\bar{\Theta}(t)$ to $\bar{\Theta}(t + \Delta t)$ is given by

$$W_{H\Delta t} = \int_{\bar{\Theta}(t)}^{\bar{\Theta}(t+\Delta t)} [-M_R(t)] \, d\bar{\Theta} \tag{6.26}$$

The negative sign in Eq. (6.26) takes into account the sign convention used. A change of variables from $\bar{\Theta}$ to t and the introduction of Eq. (6.26) into Eq. (6.3) gives

$$W_H(t+\Delta t) = -\int_{t}^{t+\Delta t} M_R(t)\, \omega(t)\, dt + W_H(t) \tag{6.27}$$

where $W_H(t + \Delta t)$ and $W_H(t)$ are accumulated work done on the half space. Expressing $M_R(t)$ in terms of τ_z-stress using Eq. (4.38), substituting the result into Eq. (6.27), and integrating in accordance with the trapezoidal rule gives

$$W_H(t+\Delta t) = -\tfrac{1}{2}\Big[\Big(\sum_{i=1}^{k} \tau_{zi}(t+\Delta t)\, A_i \bar{r}_i\Big)\, \omega(t+\Delta t) + \Big(\sum_{i=1}^{k} \tau_{zi}(t)\, A_i \bar{r}_i\Big)\, \omega(t)\Big]\Delta t + W(t) \tag{6.28}$$

where k represents the number of nodes along the interface.

If slip occurs between the disk and the half space, the work done by the disk on the half space will

differ from the work done by the stresses along the interface on the half space. This is because, while the stresses acting on the disk and the half space along the interface are equal, the displacements of these bodies along the interface are not. Energy is lost along the interface in an amount equal to the difference between these works. An expression for the incremental energy dissipated by slip, $SD_{\Delta t}$, during finite time increment, Δt, is given by

$$SD_{\Delta t} = -\left(\int_0^{A'u'(t+\Delta t)} \int_{u'(t)} \tau_{zslip}\, dA\, du' \Big|_{\substack{\text{disk} \\ \text{base}}} - \int_0^{A'u(t+\Delta t)} \int_{u(t)} \tau_{zslip}\, dA\, du \Big|_{\text{medium}} \right) \tag{6.29}$$

in which the first integral is the work done by the disk on the half space and the second integral is the work done by the stresses along the interface on the half space. The first negative sign in Eq. (6.29) is necessary because of the sign convention used. The notation, dA, represents the differential area of a concentric ring upon which the stress, τ_{zslip}, acts. The quantity, A', is the total area of the interface, and u and u' represent the circumferential displacements of the half space along the interface and the disk, respectively.

Using the form of Eq. (6.3) and integrating Eq. (6.29) numerically gives the accumulated loss of energy due to slip, SD(t + Δt), as

$$SD(t+\Delta t) = \sum_{\substack{\text{Slipping} \\ \text{nodes}}} \{ [u(t+\Delta t) - u(t)]_i \tau_{z\,slip} - [u'(t+\Delta t) - u'(t)]_i \tau_{z\,slip} \} \Delta A_i + SD(t) \qquad (6.30)$$

where ΔA_i is the finite area of the ring corresponding to node i at which slip occurs.

The corresponding energy ratio is given as

$$E_R(t+\Delta t) = \frac{SD(t+\Delta t) + SH(t+\Delta t) + KE(t+\Delta t)}{W_H(t+\Delta t)} \qquad (6.31)$$

The theoretical value of this energy ratio during a transient is 1.0.

Some energy quantities, including the work done on the disk by the applied moment and the kinetic energy of the disk, were not needed in the energy ratio but were computed throughout an analysis. The incremental work of the applied moment as the disk rotates from angle $\bar{\theta}(t)$ to $\bar{\theta}(t + \Delta t)$, $W_{\Delta t}$, during time increment, Δt, is given by

$$W_{\Delta t} = \int_{\bar{\theta}(t)}^{\bar{\theta}(t+\Delta t)} M \, d\theta \tag{6.32}$$

Changing variables from $\bar{\theta}$ to t and substituting the result into Eq. (6.3) gives

$$W(t+\Delta t) = \int_{t}^{t+\Delta t} M\omega \, dt + W(t) \tag{6.33}$$

where $W(t+\Delta t)$ and $W(t)$ are accumulated work done on the disk. The integral in Eq. (6.33) is integrated by the trapezoidal rule leading to

$$W(t+\Delta t) = \frac{1}{2}\left[M(t+\Delta t)\,\omega(t+\Delta t) + M(t)\omega(t)\right]\Delta t + W(t). \tag{6.34}$$

The instantaneous kinetic energy of the disk at time $t+\Delta t$, $KE_d(t+\Delta t)$, is given as

$$KE_d(t+\Delta t) = \frac{1}{2} I \omega^2(t+\Delta t) \tag{6.35}$$

3. Examples

In this section solutions are presented for several examples in which a torsional impulse was applied to a circular disk resting on a half space. In order to illustrate the influence of the properties of the half space on dynamic response, in these examples, only the properties of the half space were varied. The

half space was treated as a linearly elastic material, a nonlinear inelastic material, and a nonlinear inelastic material with slip permitted along the interface.

a. Description--The grid used to obtain the solutions consists of 83 rows, each row having 49 nodes. This grid represents a depth of 1.82 ft and width of 2.13 ft. A total of eight nodes are located along the disk which has a radius of 0.334 ft and a moment of inertia of 0.155 slugs-ft^2. With these properties, the disk models an actual model foundation. The time increment of the solution is 4.72 x 10-5 sec.

The properties of the half space are based approximately upon the properties of a cohesionless test bed used for model footing tests. For convenience, Ramberg-Osgood equations were used to describe the stress-strain properties of the linear model as well as those of the nonlinear models of the half space. The low amplitude shear modulus in each model is 700250 psf (4860 psi). To give linear stress-strain curves under the stresses encountered, the Ramberg-Osgood parameters, R, α, C_1 and $\tilde{\gamma}_y$ were selected as 3, 0.1, 0.8, and 5000 psf (34.7 psi), respectively. For the nonlinear models these parameters were assigned values of 3, 1, 0.8, and 150 psf (1.04 psi), respectively. These values

of R, α and C_1 have been found to give shearing stress-shearing strain curves which model the behavior of sands over a broad range of stress (Richart, 1975). The values of τ_y and C_1 give the half space a shearing strength of 188 psf (1.31 psi). The slip stress was assigned a value of 140 psf, small enough to demonstrate the effects of slip yet sufficient to permit a reversal in the angular displacement of the disk during the analyzed period of time.

The impulse consists of the positive half cycle of a sine wave having an amplitude equal to 30 ft-lb. and a duration of 0.00167 sec. The analysis was carried out over a time span of 0.0058 sec, and using a Fortran G-level compiler and an Amdahl 470 V/6 computer, approximately 346 seconds of CPU time were needed to solve each example.

b. Response of The Disk--The angular velocity of the disk vs. time is presented in Fig. 6.15 along with the applied torque. There are significant differences between the results from the nonlinear inelastic models and the linear elastic model. The positive velocities from the nonlinear models have larger amplitudes and longer durations, and the negative velocities have lesser amplitudes than the corresponding

velocities from the linear model. The differences between the results from the two nonlinear models are small. This is because the difference between the shearing strength of the medium and the slip-stress is fairly small.

To give greater insight into the response of the disk, the angular velocity of the disk was integrated with respect to time giving the angular displacement of the disk, also shown in Fig. 6.15. The peaks of the angular displacements from the nonlinear models are greater and occur at a later time than those from the linear model. The angular displacements from the nonlinear models are positive throughout the analysis, whereas those from the linear model become negative.

Since the applied moment and the mass moment of inertia of the disk are the same in each example, differences in the responses of the disk amongst the various models are due entirely to differences amongst the resultant moments of the distributions of shearing stress along the interface. This distribution depends primarily on the properties of the half space.

Plots of the average stress vs. average strain from a subcell are presented for the linear and nonlinear inelastic cases in Fig. 6.16 and 6.17 for each of the coordinate directions. As shown in Fig. 6.18 these

curves were obtained from a subcell located near the edge of the disk, a region where deformation is significant. The slope of the linear curve for the radial direction is within 9 percent of the low amplitude shear modulus whereas that in the z-direction is within 3 percent. These differences are caused by approximations in the numerical method and by approximations in the techniques used to evaluate the average stresses and strains for the subcells. Results improve with increases in the fineness of the grid.

The stress-strain curves for the nonlinear model are highly nonlinear and hysteretic and similar results are obtained from the slip model. The initial loading and the unloading slopes are within 4 percent of the low amplitude shear modulus. Each curve, however, is characterized by indistinct reversals of stress and the curve for the radial direction is more hysteretic than it should be for the stress level reached. This behavior is thought to be due to the specific approximations associated with the nonlinear model, in addition to the approximations of the linear model.

At lower levels of nonlinearity, stress-strain curves have been found to improve considerably giving distinct reversals with increases in the fineness of the grid. It is also important to note that the values of

the moduli used in computations are obtained from the Ramberg-Osgood equations and are not equal to the slopes of the stress-strain curves from the subcells where these slopes are clearly incorrect. In Fig. 6.19, which gives the energy ratio vs. time, it may be observed that energy and work balance quite well for all models.

In order to demonstrate the effect of the properties of the half space on the distribution of τ_z-stresses along the interface, this distribution is shown in Fig. 6.20 through 6.23 for several times in the transient for the various models. Figures 6.20 and 6.22 give results from the portion of the cycle in which the disk loads the half space. As shown in Fig. 6.20, during this period, the buildup in the τ_z-stress distribution for the linear elastic model takes place without a change in shape. The maximum stress is developed at all radii simultaneously and near the edge of the disk the maximum stress is very large.

As shown in Fig. 6.22, the buildup in the τ_z-stress distribution for the nonlinear model does involve a change in shape. As time increases, stresses at the edge of the disk approach a limiting value while stresses near the center continue to increase. This happens because, at the edge, stresses are relatively large, and consequently, the degree of nonlinearity is

high. The corresponding reduction in shearing rigidity prevents large increases in stress with increases in the angular displacement of the disk. Likewise, because of this stress-limiting phenomena, the stresses at the edge of the disk are very much smaller in the nonlinear case than those in the linear case. Near the center of the disk less displacement is imposed on the half space than near the edge. Thus, near the center, stresses are lower, the material is in a more elastic, rigid state, and increases in the angular displacement are accompanied by reasonably proportional increases in stress.

As shown in Fig. 6.22, behavior when allowing slip at the interface is similar to that when slip is not allowed except that stresses at the interface are limited by the slip-stress. This limit leads to the development of zones of constant stress within the stress distribution at the locations at which the slip has occurred.

Figures 6.21 and 6.23 give the stress distributions along the interface for each model for various times during the portion of the transient in which the disk unloads and then reloads the half space. For the elastic case, there is no significant change in the shape of the distribution with time. All radii develop zero stresses as well as the maximum reverse loading

stresses simultaneously. As shown in Fig. 6.23, in the nonlinear case, unloading takes place at the edge of the disk first. During unloading, oscillations appear in these distributions. These oscillations develop because the strains of all the subcells do not reverse simultaneously. As the number of reversals which take place decreases with time, these oscillations decrease as shown in Fig. 6.23. The particle velocities of the half space are somewhat sensitive to these oscillations but the motion of the disk and the resultant moment at the interface are not.

During unloading, stresses develop a value of zero at the edge of the disk first. Since, at this location, the half space had undergone the greatest amount of inelastic deformation, much less reverse rotation of the disk is needed to unload this region than to unload the inner zones. For these "elastic" regions to unload the disk must return to approximately its original undisplaced state. As shown in Fig. 6.23, during unloading, the stress distributions when slip is allowed along the interface, are similar to those when slip is not allowed, however, the minor oscillations in the distributions are smaller.

The resultant moment of the distribution of stresses along the interface and the angular displacement of the disk vs. time are given in Fig. 6.24 for

each of the three models. Large negative and positive moments are developed in the linear elastic model. These large moments are caused primarily by the large stresses which act at the edge of the disk. Because the half space develops large moments which resist the motion of the disk, as shown in Fig. 6.24, the motion of the disk is reversed very rapidly following the impulse. In addition, because a large amount of elastic strain energy is stored within the half space when the disk is at its maximum angular displacement, the disk develops a very large negative angular velocity as shown in Fig. 6.15. Assuming that the angular displacement at which the resultant moment is zero (t = 0.0044 sec in Fig. 6.24) defines the equilibrium position of the disk, it is clear from Fig. 6.24 that this equilibrium position does not change significantly.

As shown in Fig. 6.24, the resultant moments in the nonlinear cases are similar and, therefore, so are the responses of the disk in these cases. These moments do not develop to values as large as those in the elastic model because the τ_z-stresses which develop along the interface are much less in the nonlinear model. As a result the nonlinear half space with or without slip does not have the capability to resist the motion of the disk which the linear half space does.

This is why, as shown in Fig. 6.24, in the nonlinear cases, the disk rotates to a greater maximum angular displacement and why the reversal of the rotation takes place at a later time than in the linear case. Assuming that the angular displacement of the disk for which the resultant moment is equal to zero (t = 0.0057 sec in Fig. 6.24) corresponds roughly to the equilibrium position of the disk, it is clear that during the transient motion, the equilibrium positions have changed considerably in the nonlinear models. Because of the lower magnitudes of the negative angular velocities of the disk at these equilibrium positions, very little changes are expected in these positions during the remainders of the transient motions. Therefore, the disk has undergone a large amount of permanent angular displacement. This permanent angular displacement is caused by inelastic deformation of the half space and, in the slip model, also by slip along the interface.

While the effect of slip relative to nonlinearity has not been large in this example it is of interest to study the phenomena of slip. The development of slip along the interface is illustrated in Fig. 6.25. In this figure, the displacement of the surface of the half space, and the simultaneous displacement of the disk vs. radius are presented for two times during

the transient. The later time corresponds to the time at which the stress distribution along the interface is near its maximum state. Slip, at a given radius, is the difference between the displacements of the disk and of the half space at this radius. As shown in Fig. 6.25, slip initially develops at the outer edge of the footing where stresses are highest, and migrates inwards along the interface as slip-stresses continue to develop in this direction. During slip, the progression of the velocity distribution of the half space along the interface is fairly complex. This is a consequence of the development of τ_r-stresses at the interface and interactions between the slipping zones. Because of this complex velocity distribution, as shown in Fig. 6.25, as time increases, slip develops further at some of the inner nodes along the interface than at the outer node.

c. Response of the Half Space--In order to study the response of the half space to the motion of the disk, the particle velocity of the half space vs. time is plotted in Fig. 6.26 for a point within the half space for each of the models. As shown to scale in Fig. 6.18, this point is located at a depth of 0.36 ft and a radius of 0.67 ft. The velocities of the edge of

the disk from the nonlinear and linear models are also shown in Fig. 6.26 as a reference. This velocity from the slip model is not plotted because of its similarity to that from the nonlinear model in which slip is not included. The particle velocity in the half space of the slip model is not as smooth as that of the no-slip nonlinear model. This is because the development of slip at a node causes abrupt changes in the particle velocity at the node which are transmitted throughout the half space. After approximately 0.0035 sec, minor erratic behavior develops in the particle velocities from both nonlinear models. This behavior was thought to be caused by the abrupt non-simultaneous changes in shear moduli induced by strain reversals in the subcells.

As shown in Fig. 6.26, the initial peak of the particle velocity within the half space in the linear case is much greater than those in the nonlinear cases. The values of all the dependent variables from the nonlinear models are smaller within the half space than those from the linear model. This is demonstrated in Figs. 6.27, 6.28, and 6.29, in which are presented, for a given time, the curves of the dependent variables vs. distance from the outer node of the interface along a

line at an angle of 45° relative to the horizontal (see Fig. 6.18).

As shown in Fig. 6.26, for the elastic model, the particle velocity at a point within the half space is reasonably similar in shape to the corresponding velocity of the edge of the disk. This is not the case for the nonlinear models.

The effects of the stress-strain properties of the half space on the disturbance within the half space are similar to the effects of these properties on the disturbance within a medium under one-dimensional conditions (see Section D.2.b.). Geometry, however, is an additional complicating factor under two-dimensional conditions.

As shown in Figs. 6.26 and 6.27, 6.28, and 6.29, the effect of slip on the disturbance within the half space is a slight change in the amplitude and shape of the disturbance. Slip affects the nature of a disturbance by dissipating energy along the interface, thus, affecting the amount of energy, and the levels of stress and nonlinearity within the half space.

d. Energy Considerations--The behavior of the system may be viewed in terms of the distribution of energy. During the transient motion, energy is

distributed between the disk and the half space and energy is also distributed amongst several forms within the half space. These distributions depend upon the properties of the half space. To demonstrate the effect of these properties on the distribution of energy between the disk and the half space, various energies are given in Table 6.1 for each of the models at a time when the disk in the linear model is at its maximum angular displacement. At this time the work done on the disk by the applied moment is approximately the same for each of the models. In the linear elastic model, however, the disk has negligible kinetic energy and almost all work done on the disk is stored as energy within the half space. In each of the nonlinear models, in which the disk continues to rotate, the disk has significant kinetic energy and the half space has approximately 23 percent less energy than that of the linear model. The least amount of energy is introduced into the half space of the nonlinear model in which slip is allowed and in this model the disk has the greatest amount of kinetic energy.

The effects of the properties of the half space, on the distribution of energy within the half space, are similar to the effects of the properties of a medium, on

the distribution of energy within the medium under one-dimensional conditions (see Section D.2.c).

Table 6.1: Various Works and Energies of Disk-Half Space System for Each Numerical Model. Time = 0.00264 Sec.

	Linear Elastic	Nonlinear Inelastic	Nonlinear Inelastic with Slip
Work done on Disk (ft-lb)	0.282×10^{-2}	0.289×10^{-2}	0.289×10^{-2}
Kinetic Energy of Disk (ft-lb)	0.72×10^{-6}	0.58×10^{-3}	0.66×10^{-3}
Work done on Half Space (ft-lb)	0.282×10^{-2}	0.231×10^{-2}	0.223×10^{-2}

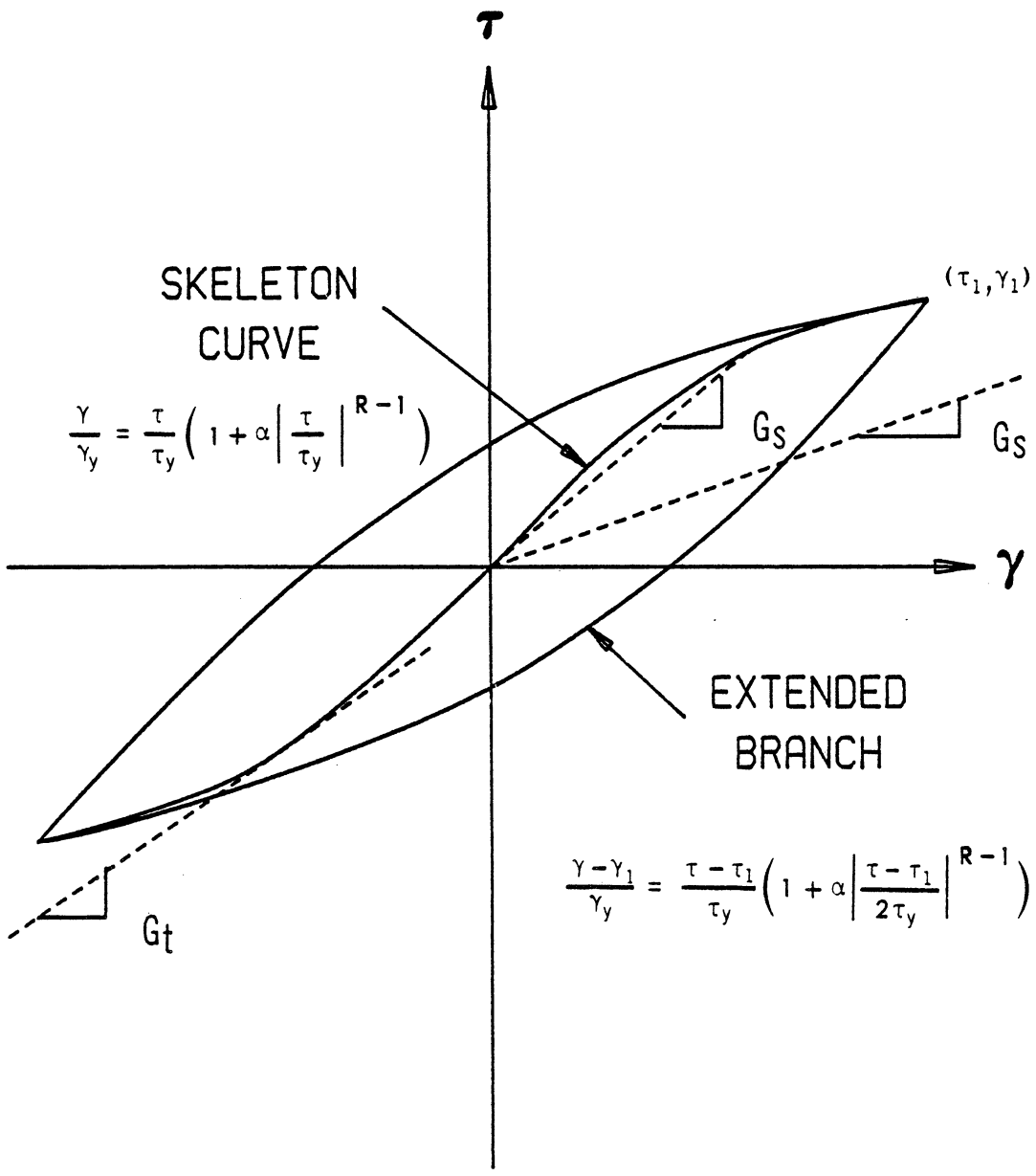

Fig. 6.1: Ramberg-Osgood Shearing Stress-Strain Curves.

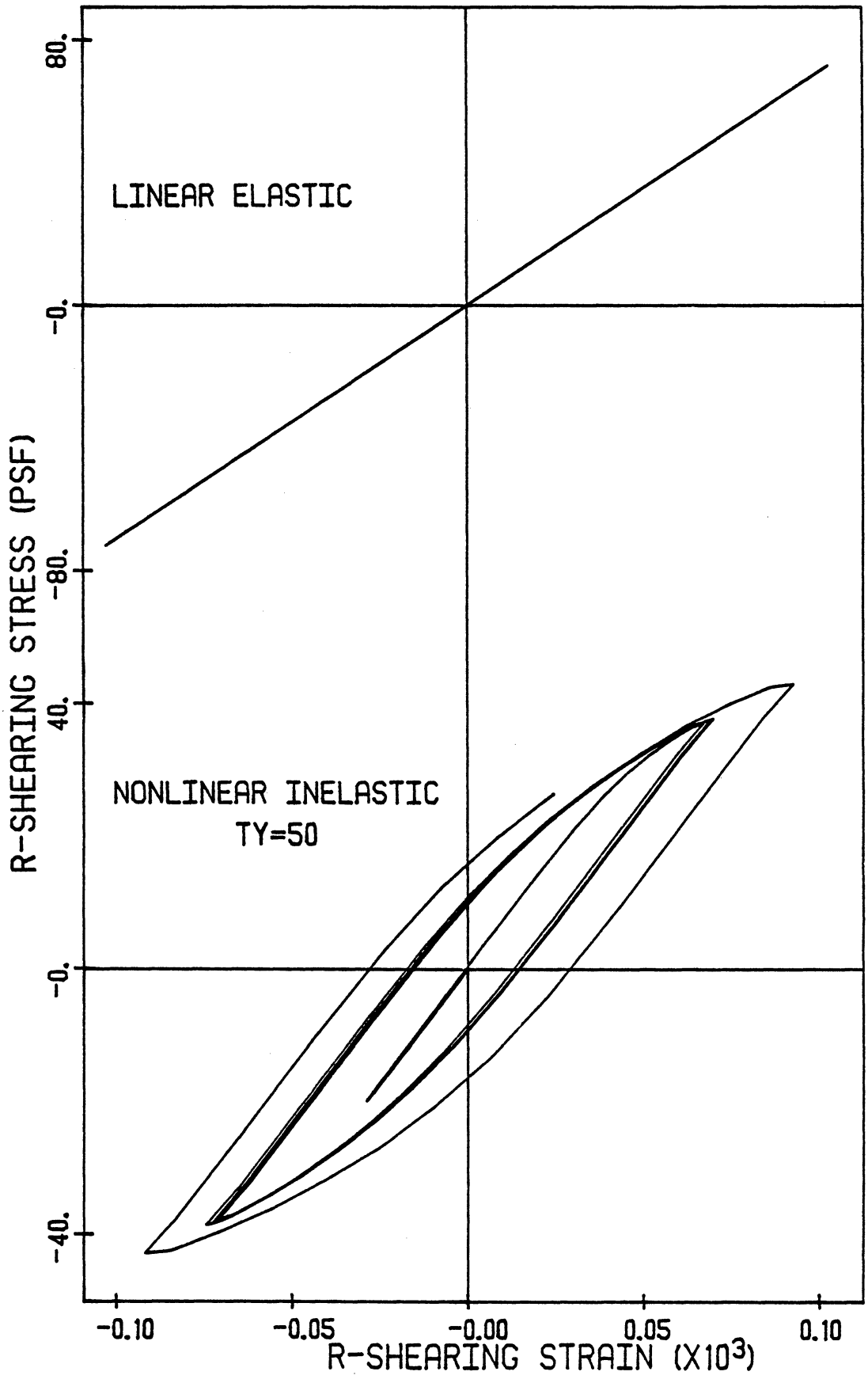

Fig. 6.2: Radial Wave Propagation: Shearing Stress-Strain Curves from Subcells Located at r = 1000.75 ft.

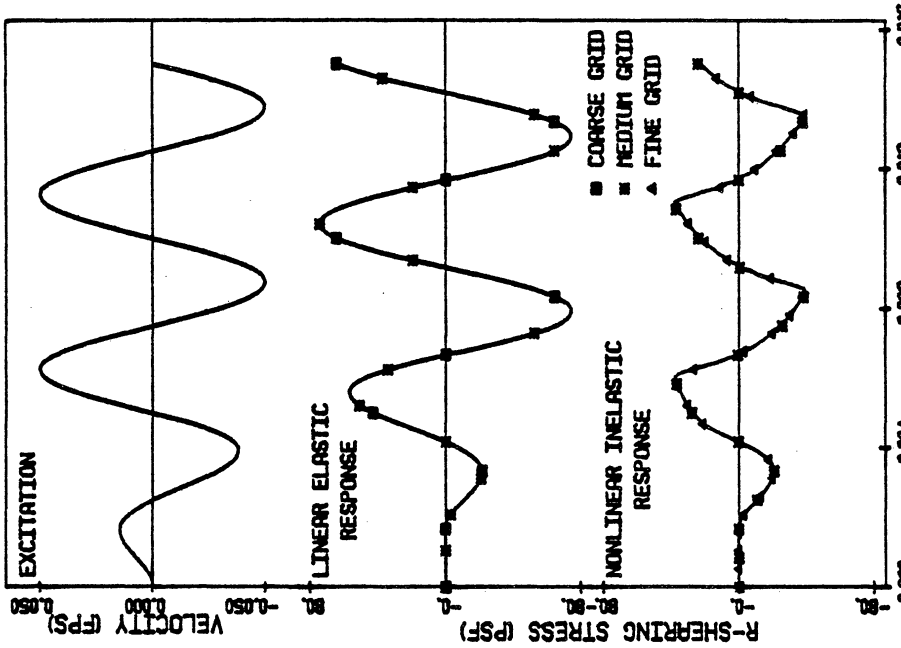

Fig. 6.4: Radial Wave Propagation: Particle Velocity and τ_r-Stress vs. Time at r = 1000.78 ft. Not All Points Shown.

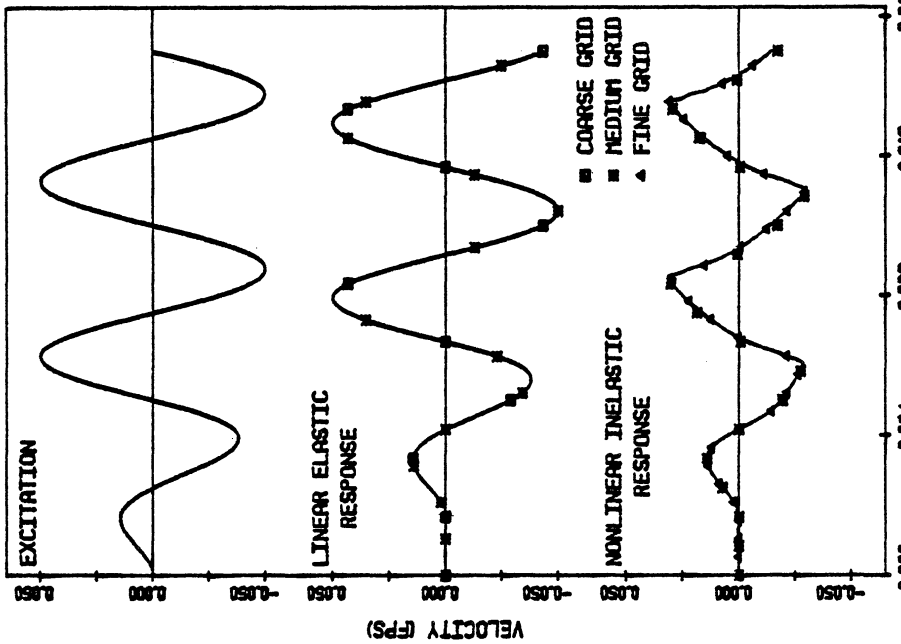

Fig. 6.3: Radial Wave Propagation: Particle Velocity vs. Time at r = 1000.78 ft. Not All Points Shown.

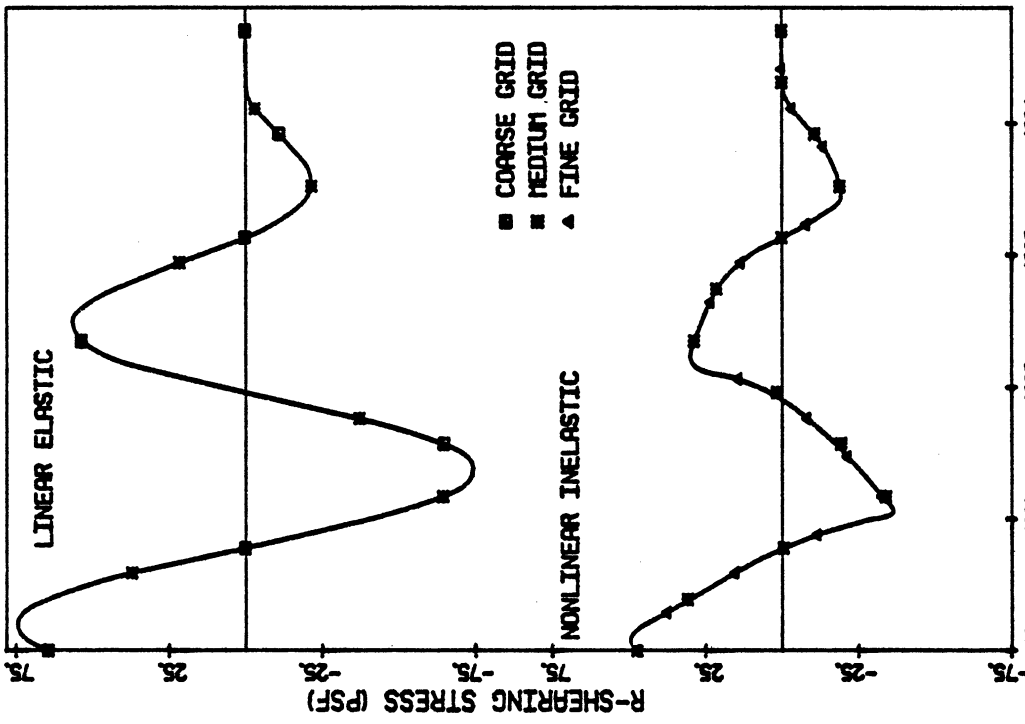

Fig. 6.6: Radial Wave Propagation: τ_r-Stress vs. r at Time of 0.00916 sec. Not All Points Shown.

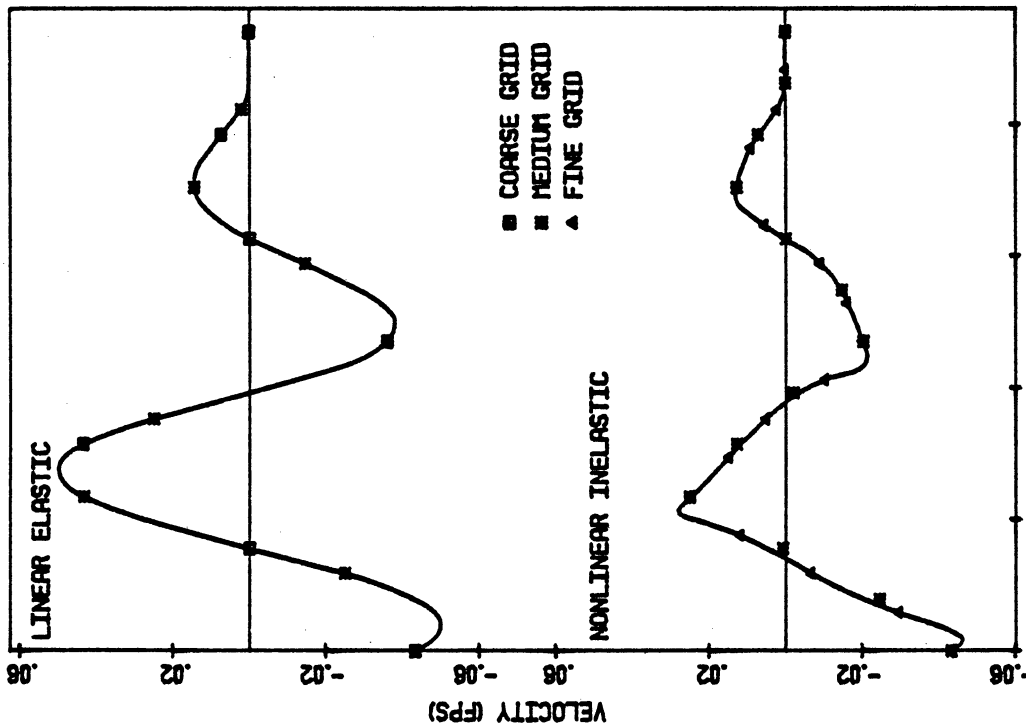

Fig. 6.5: Radial Wave Propagation: Particle Velocity vs. r at Time of 0.00916 sec. Not All Points Shown.

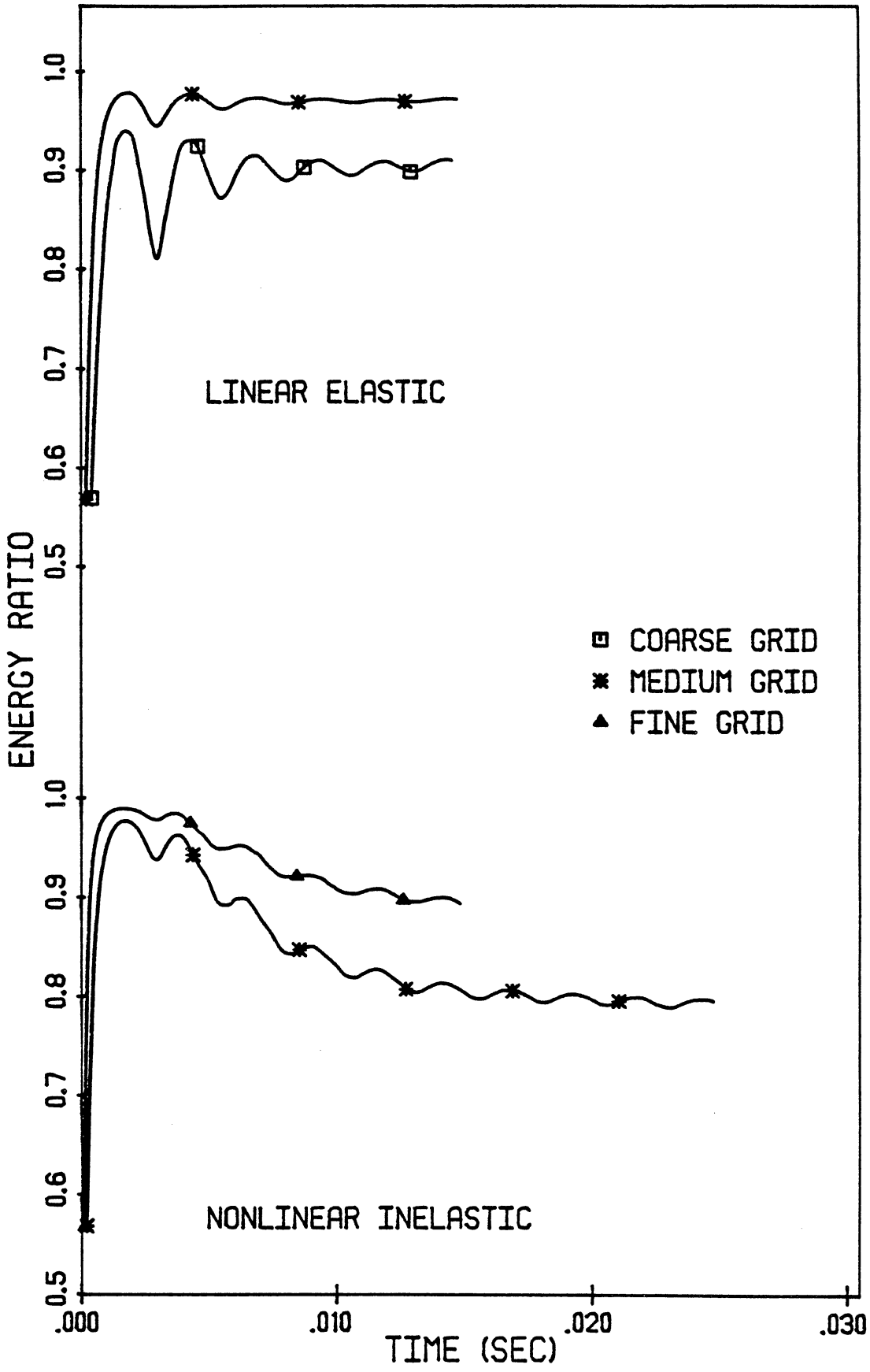

Fig. 6.7: Radial Wave Propagation: Energy Ratio vs. Time. Not All Points Shown.

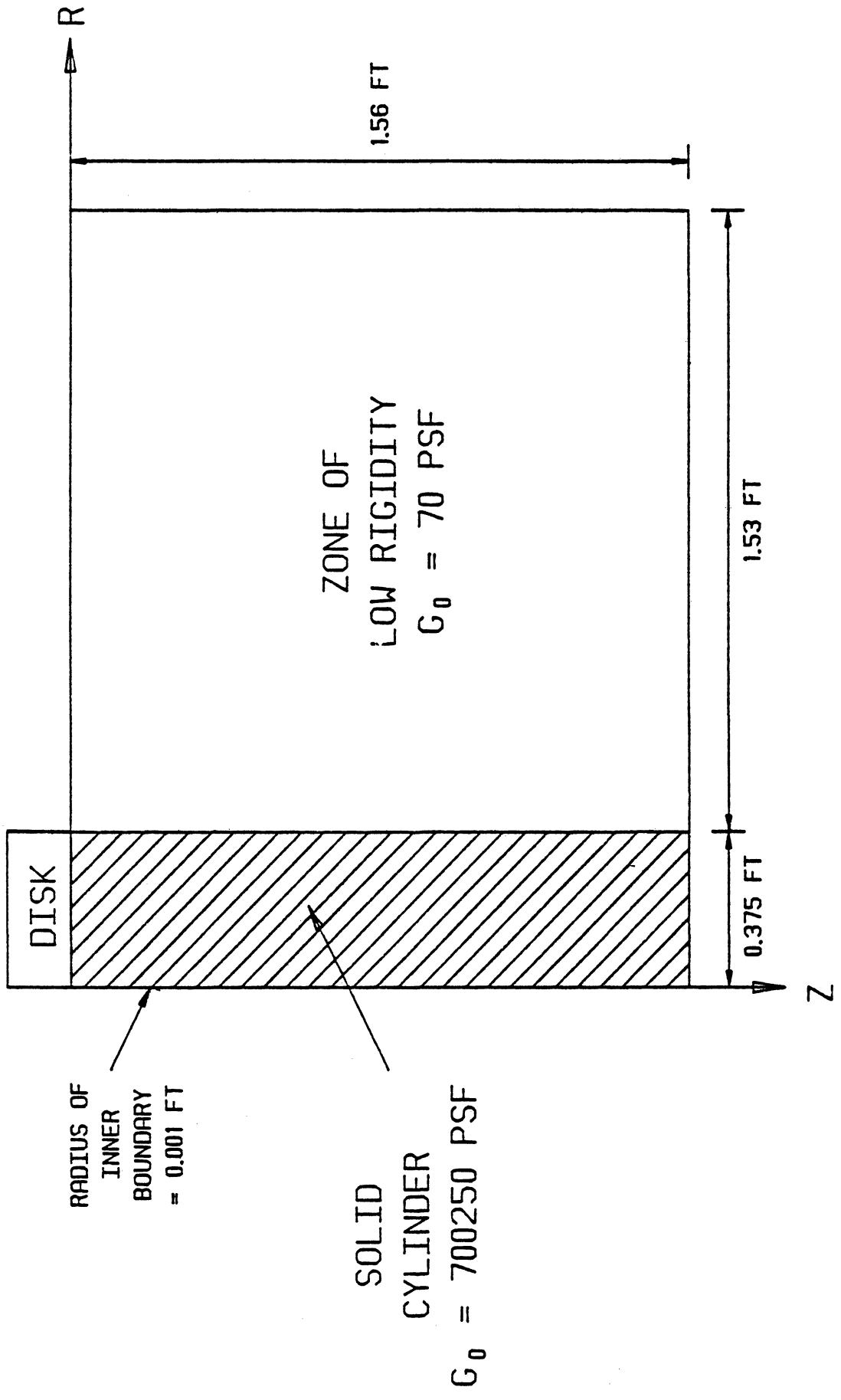

Fig. 6.8: Divisions of Grid Used to Model Wave Propagation Along Solid Cylinder.

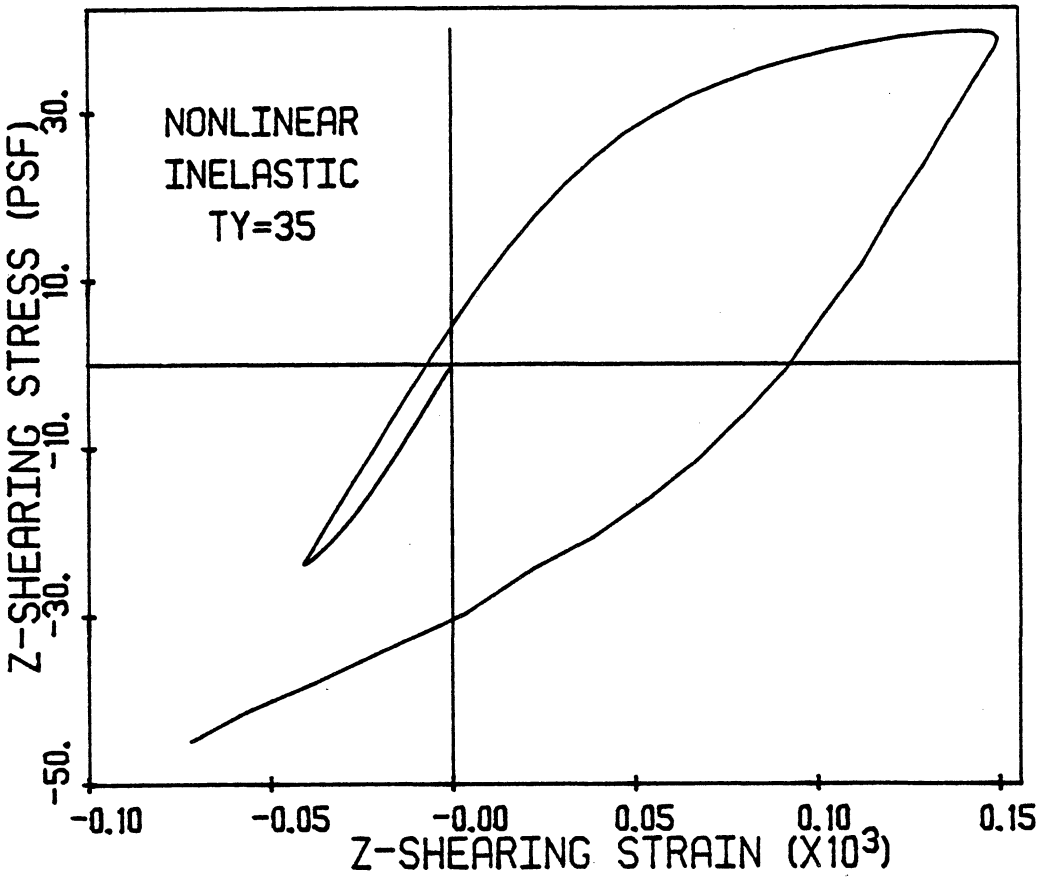

Fig. 6.9: Longitudinal Wave Propagation: Shearing Stress-Strain Curves in Solid Cylinder from Subcell at r = 0.288 ft and z = 0.0288 ft.

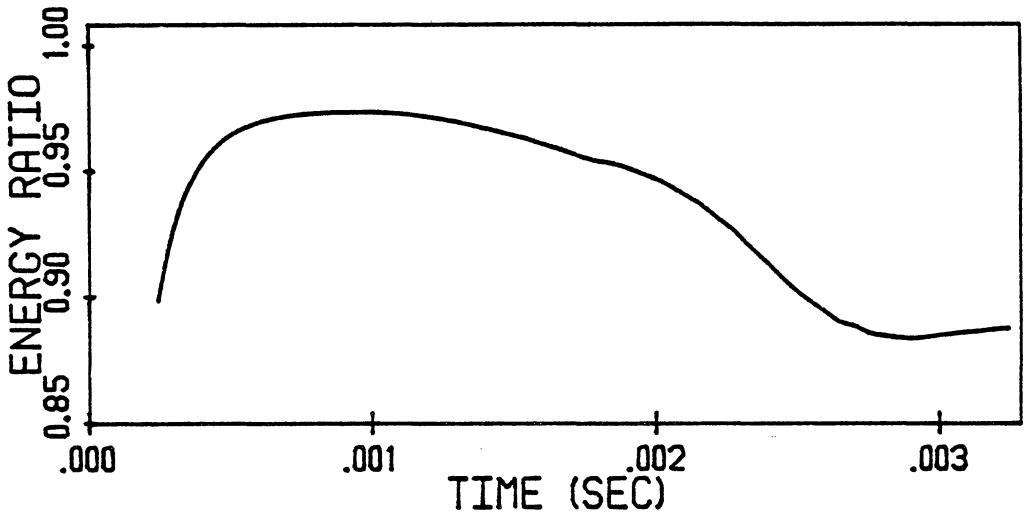

Fig. 6.10: Longitudinal Wave Propagation: Energy Ratio vs. Time.

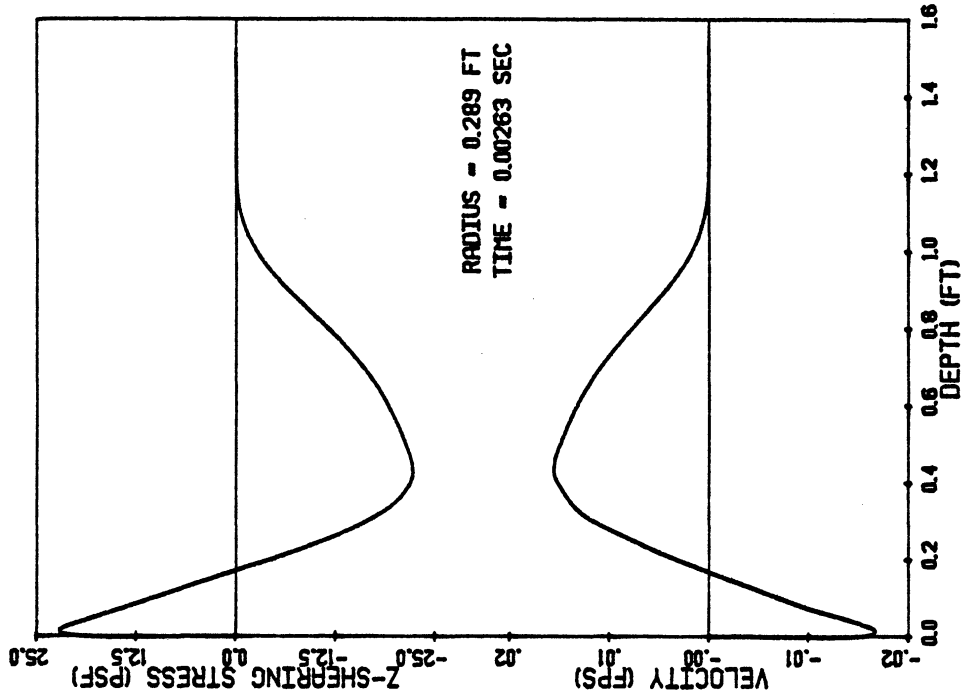

Fig. 6.12: Longitudinal Wave Propagation: τ_z-Stress and Particle Velocity vs. z at r = 0.289 ft and at Time of 0.00263 sec.

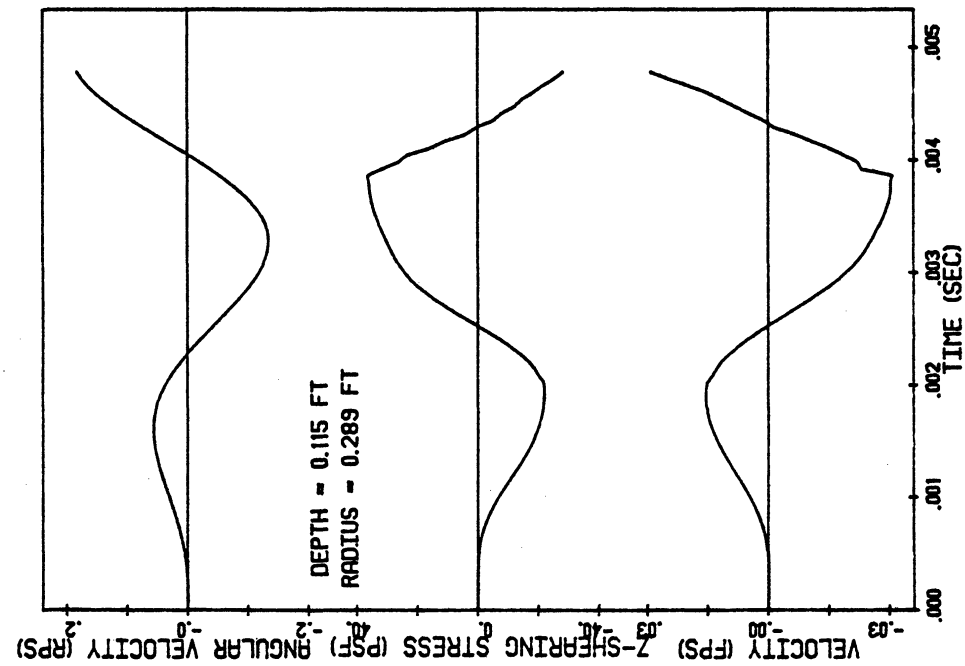

Fig. 6.11: Longitudinal Wave Propagation: Angular Velocity of Disk, and τ_z-Stress and Particle Velocity in Solid Cylinder at z = 0.115 ft and r = 0.289 ft vs. Time.

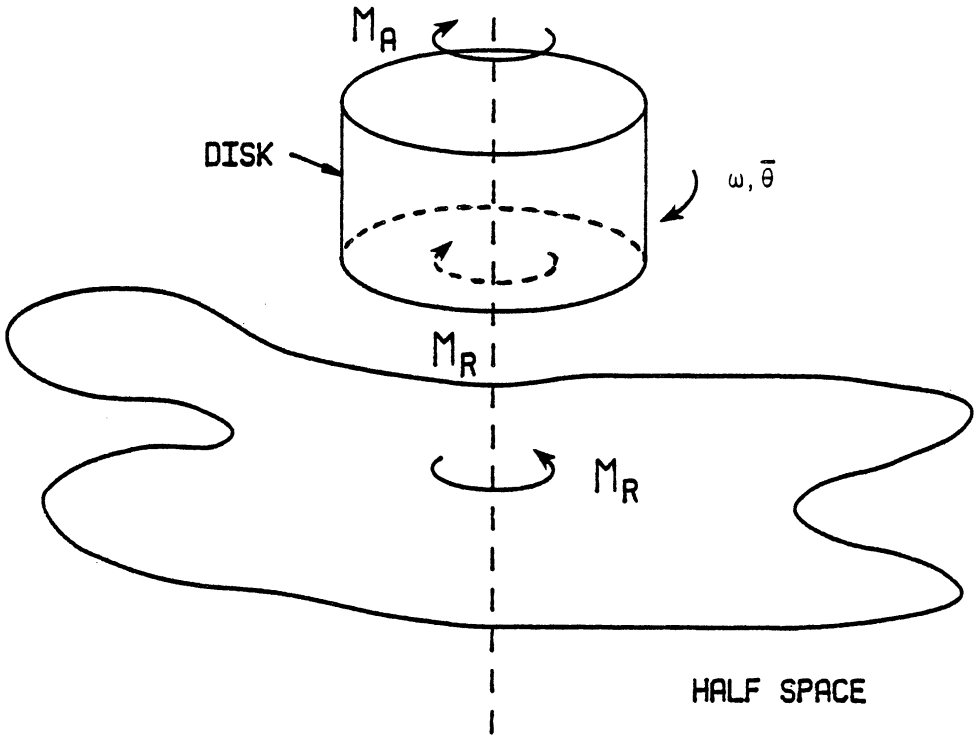

Fig. 6.13: Schematic Diagram of Disk and Half Space Showing Positive Moments and Motions.

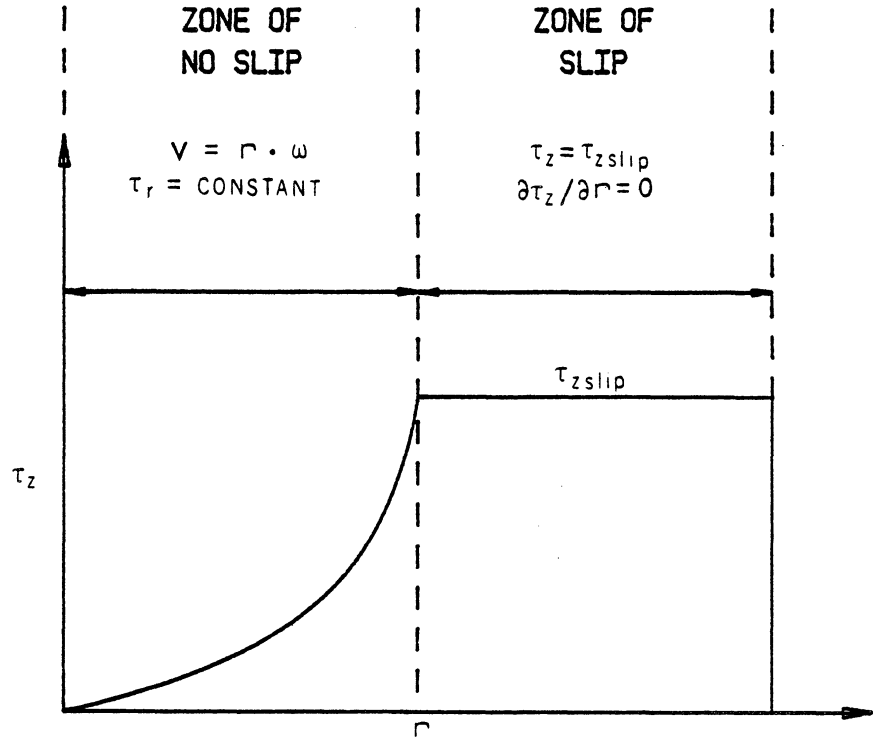

Fig. 6.14: Typical τ_z-Stress Distribution Developed Along Interface with Slip.

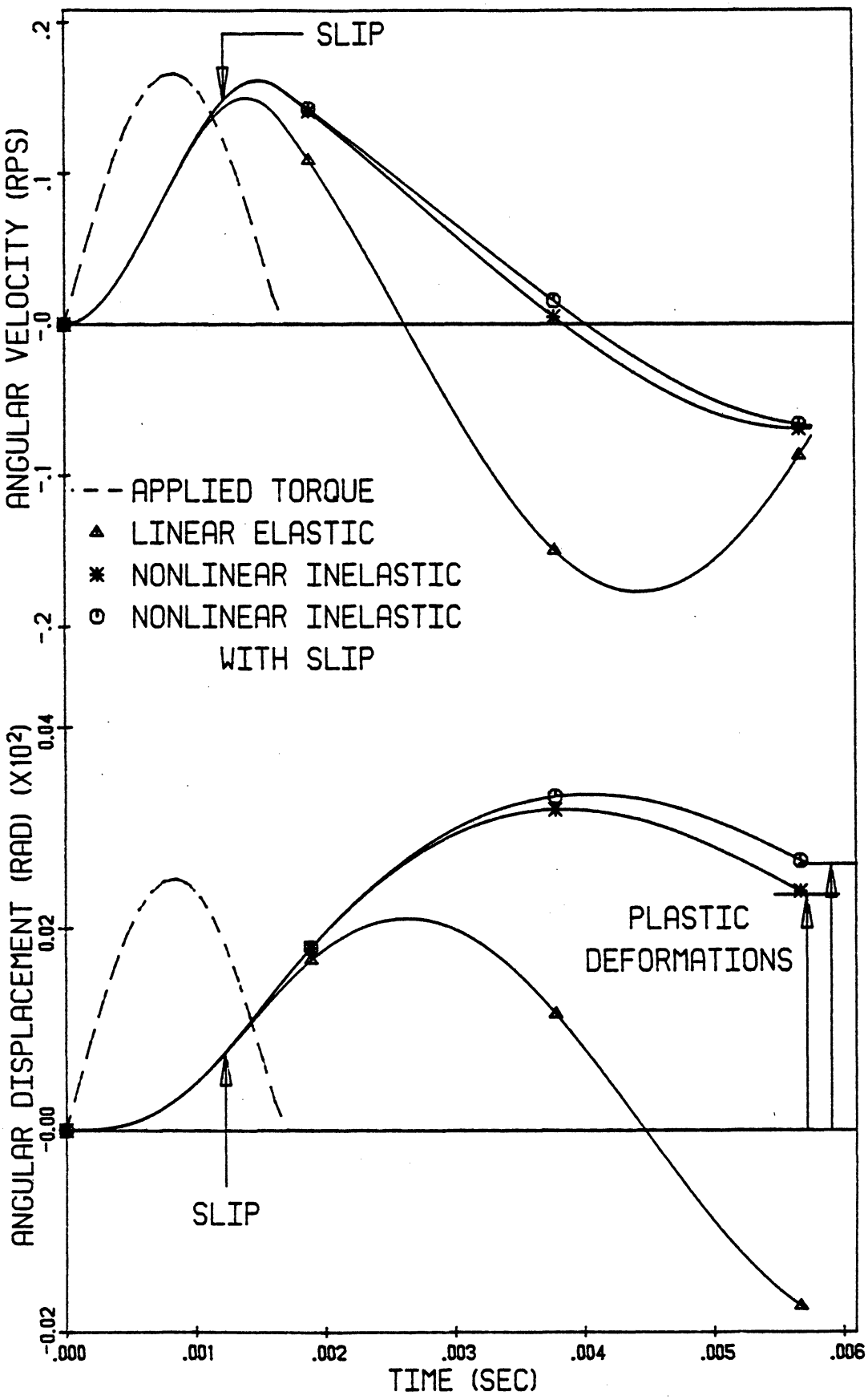

Fig. 6.15: Problem of Disk on Half Space: Angular Velocities and Angular Displacements of Disk vs. Time. Not All Points Shown.

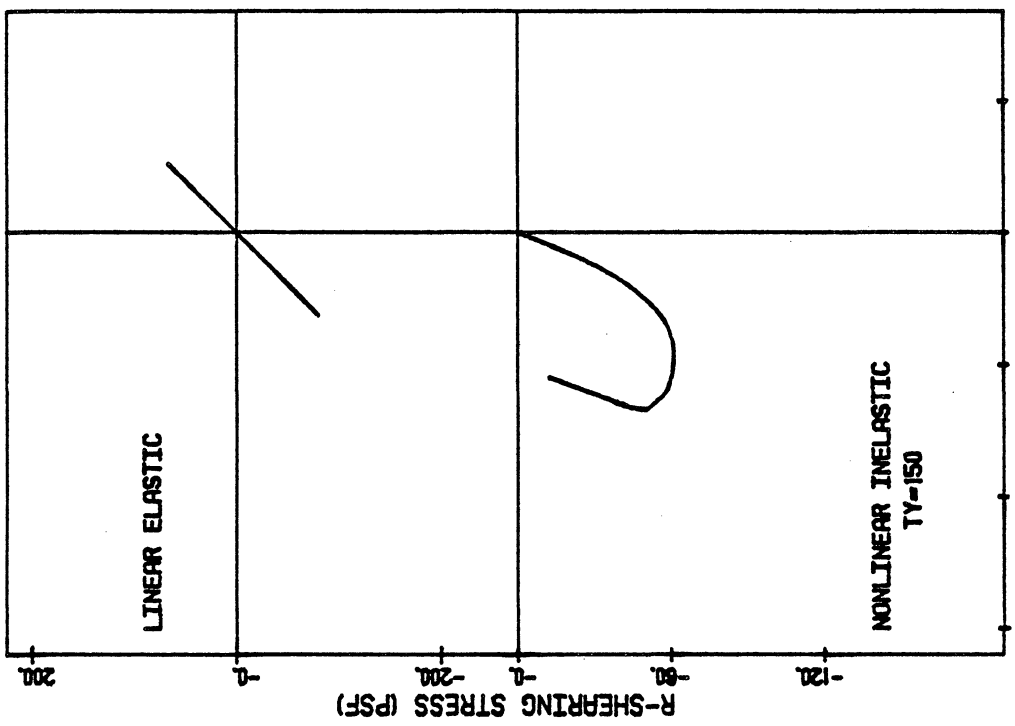

Fig. 6.17: Problem of Disk on Half Space: τ_r-Stress vs. γ_r-Strain from Subcell at r = 0.267 ft and z = 0.044 ft (See Fig. 6.18).

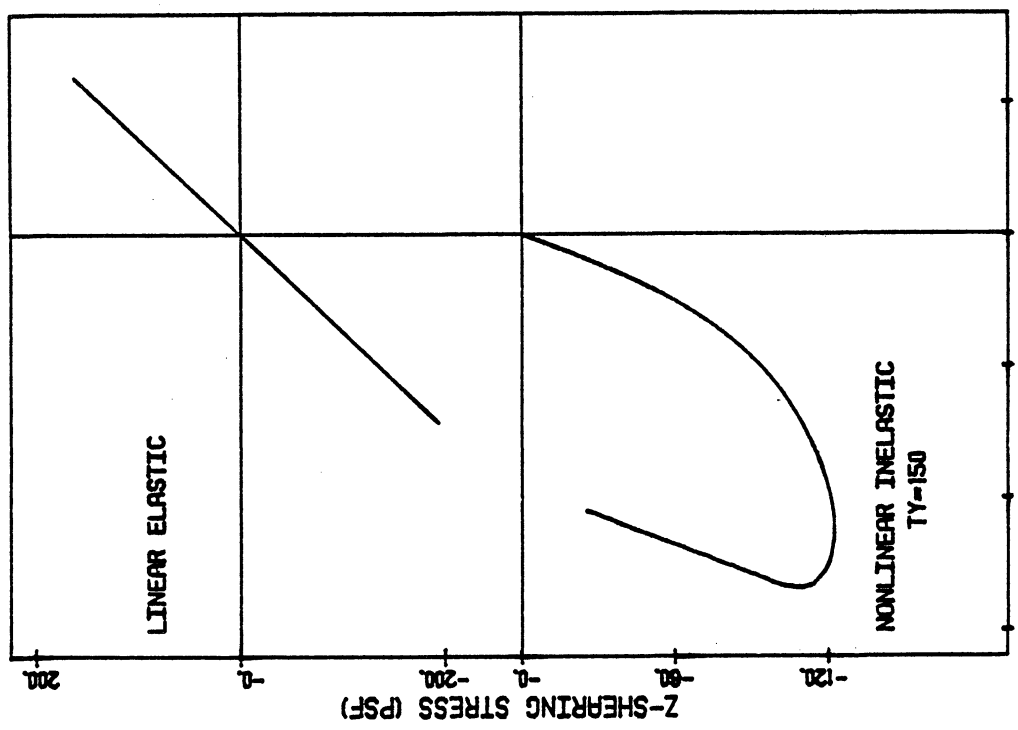

Fig. 6.16: Problem of Disk on Half Space: τ_z-Stress vs. γ_z-Strain from Subcell at r = 0.267 ft and z = 0.044 ft (See Fig. 6.18).

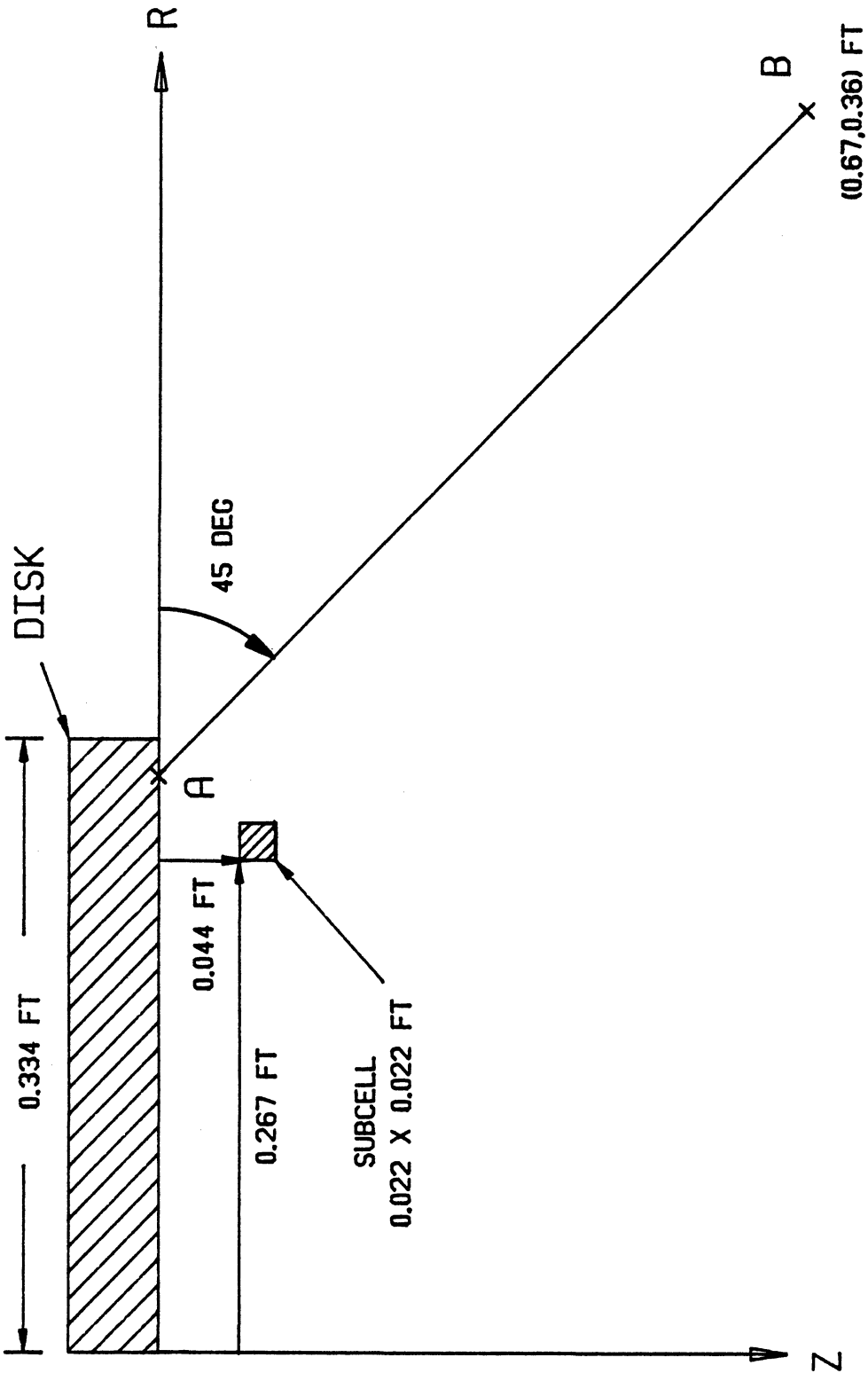

Fig. 6.18: Schematic, Scale Diagram of Region near Disk Showing Subcell from which Stress-Strain Curves were Obtained and Line AB along which Dependent Variables were Obtained.

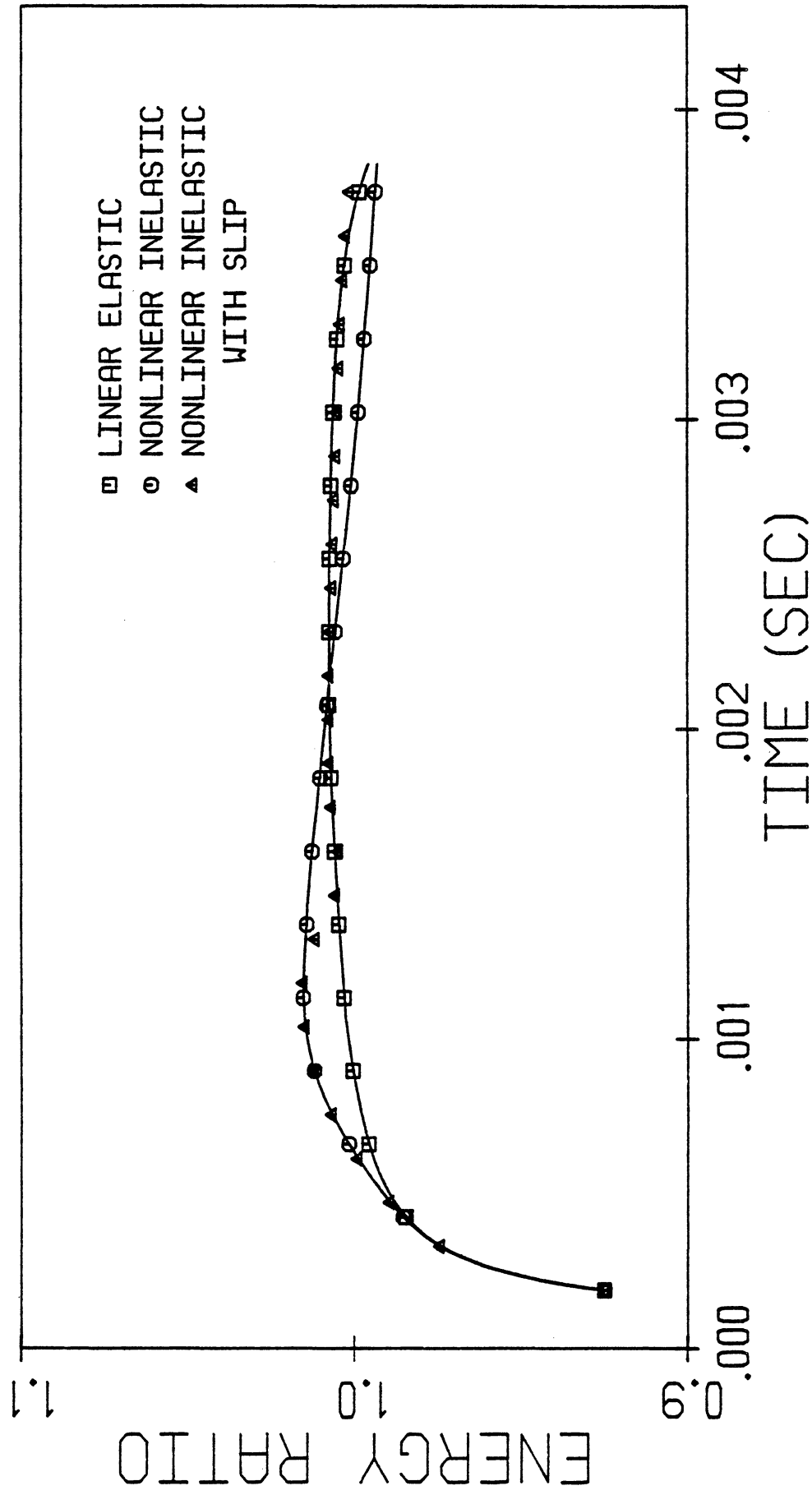

Fig. 6.19: Problem of Disk on Half Space: Energy Ratio vs. Time. Not All Points Shown.

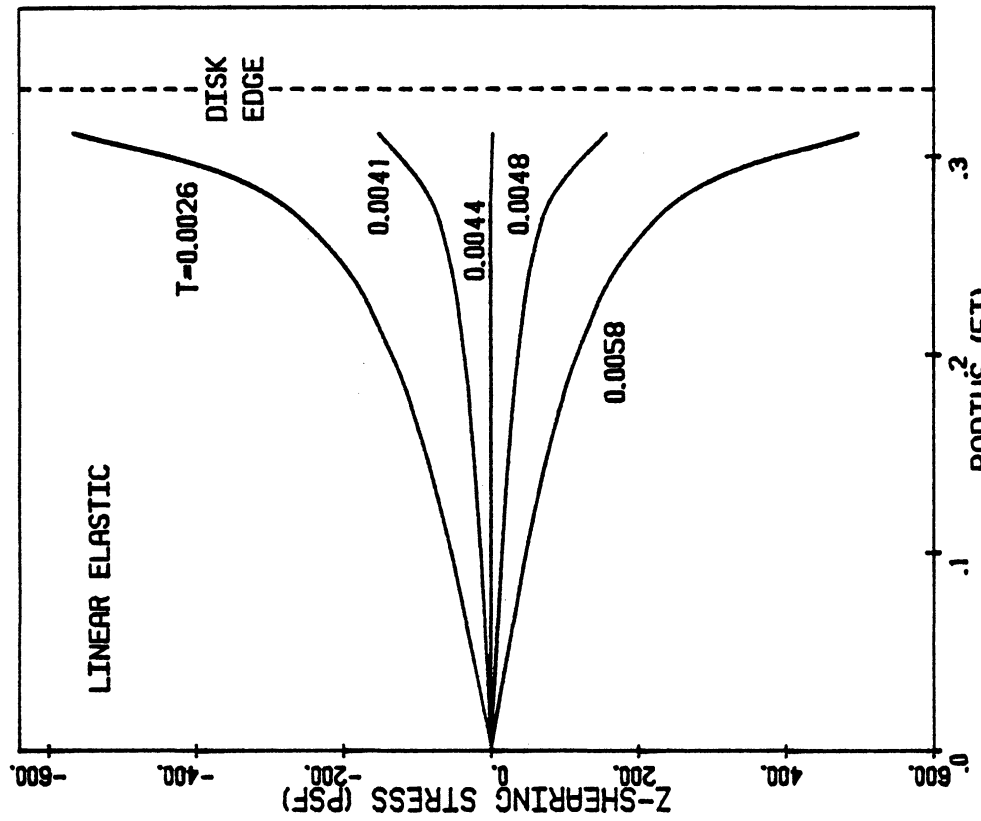

Fig. 6.21: Problem of Disk on Half Space: τ_z-Stress vs. r Along Interface Developed in Elastic Model During the Unloading of the Half Space.

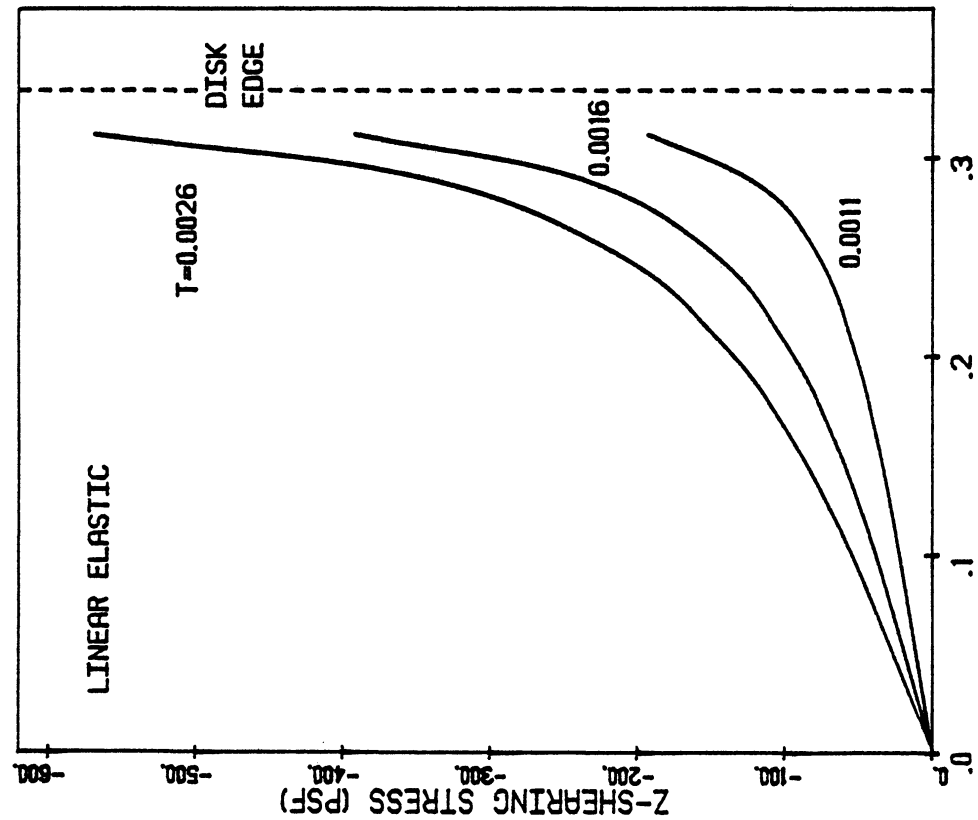

Fig. 6.20: Problem of Disk on Half Space: τ_z-Stress vs. r along Interface Developed in Elastic Model during the Loading of the Half Space.

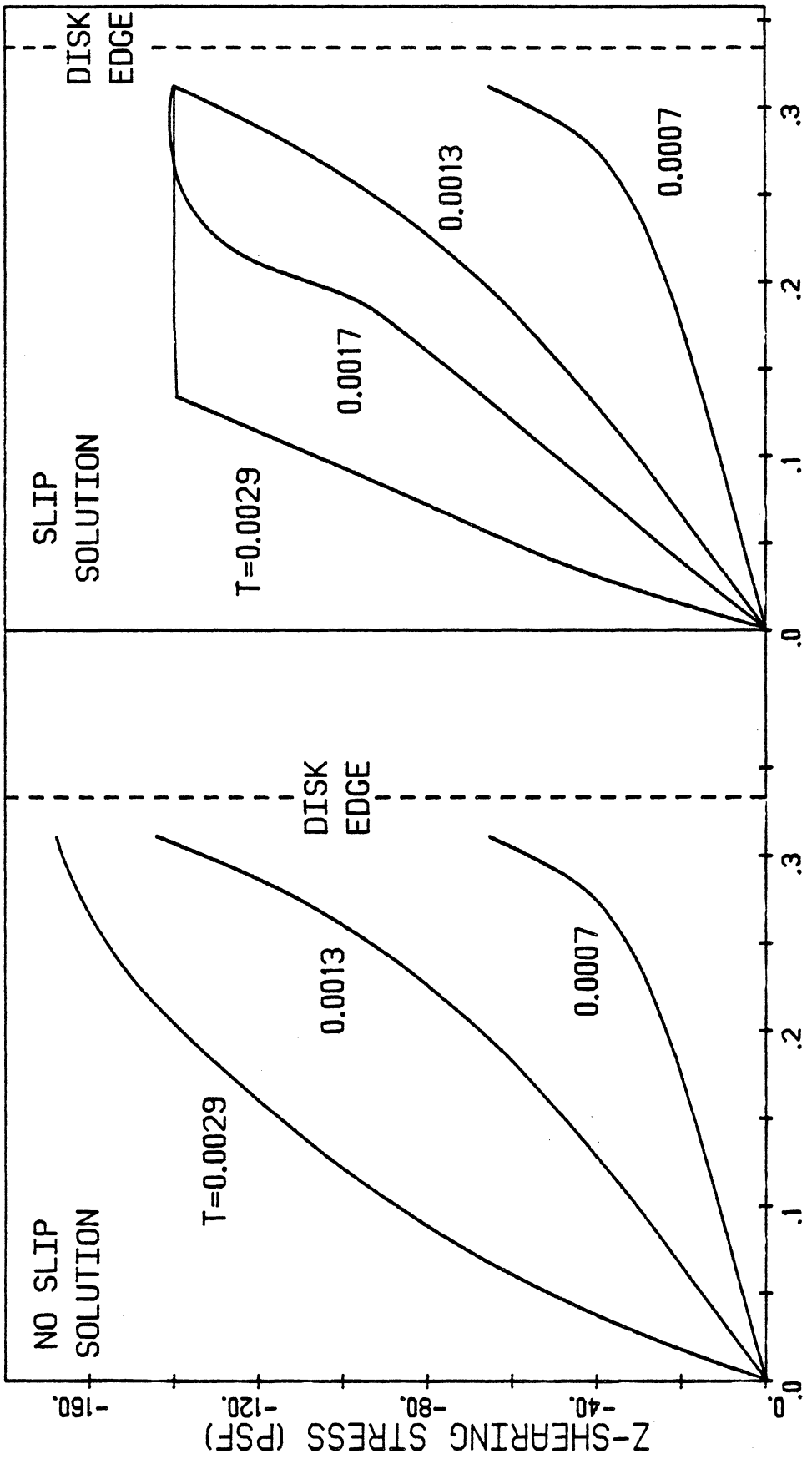

Fig. 6.22: Problem of Disk on Half Space: τ_z-Stress vs. r Along Interface Developed in Nonlinear Models During the Loading of the Half Space.

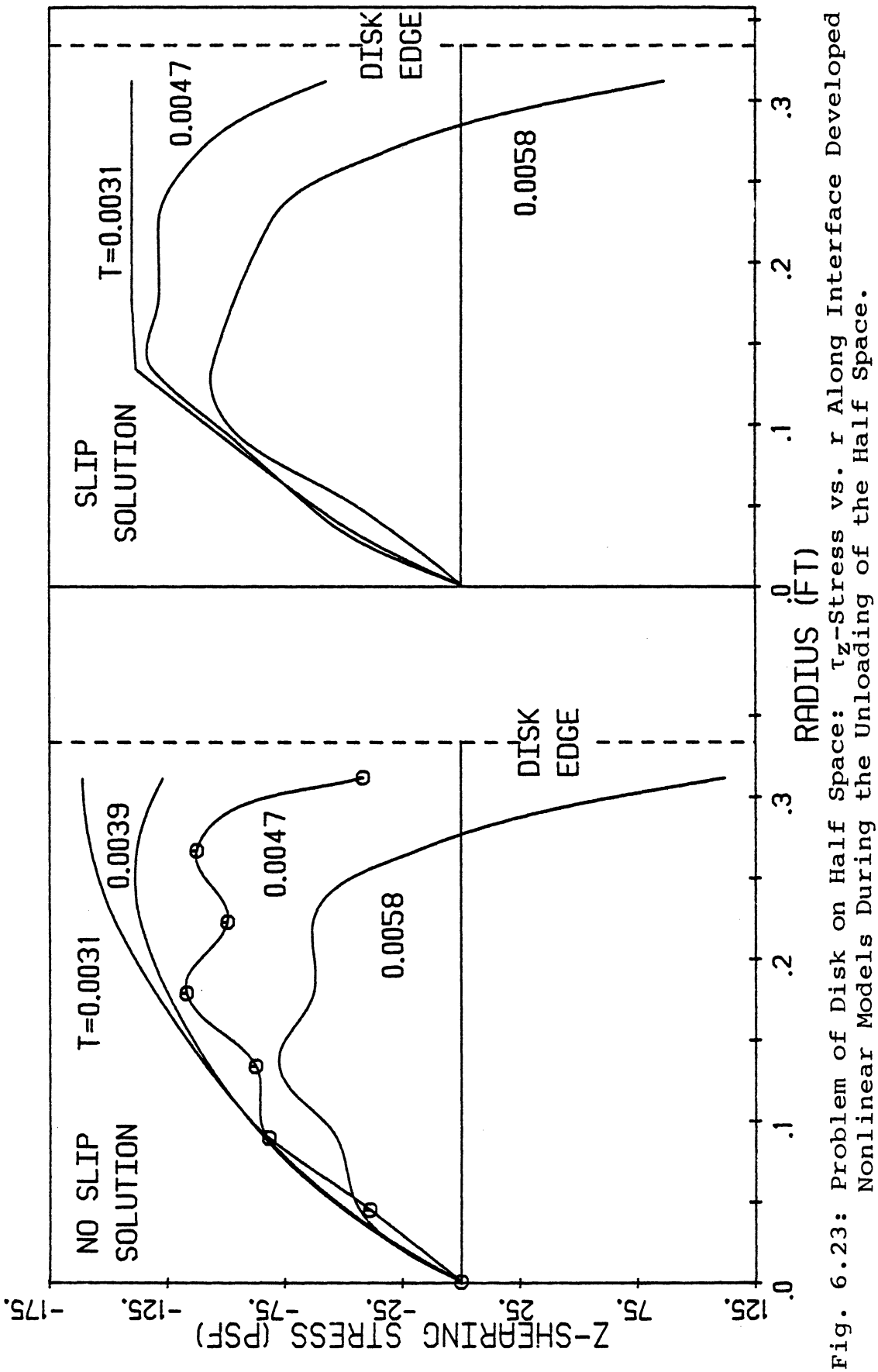

Fig. 6.23: Problem of Disk on Half Space: τ_z-Stress vs. r Along Interface Developed in Nonlinear Models During the Unloading of the Half Space.

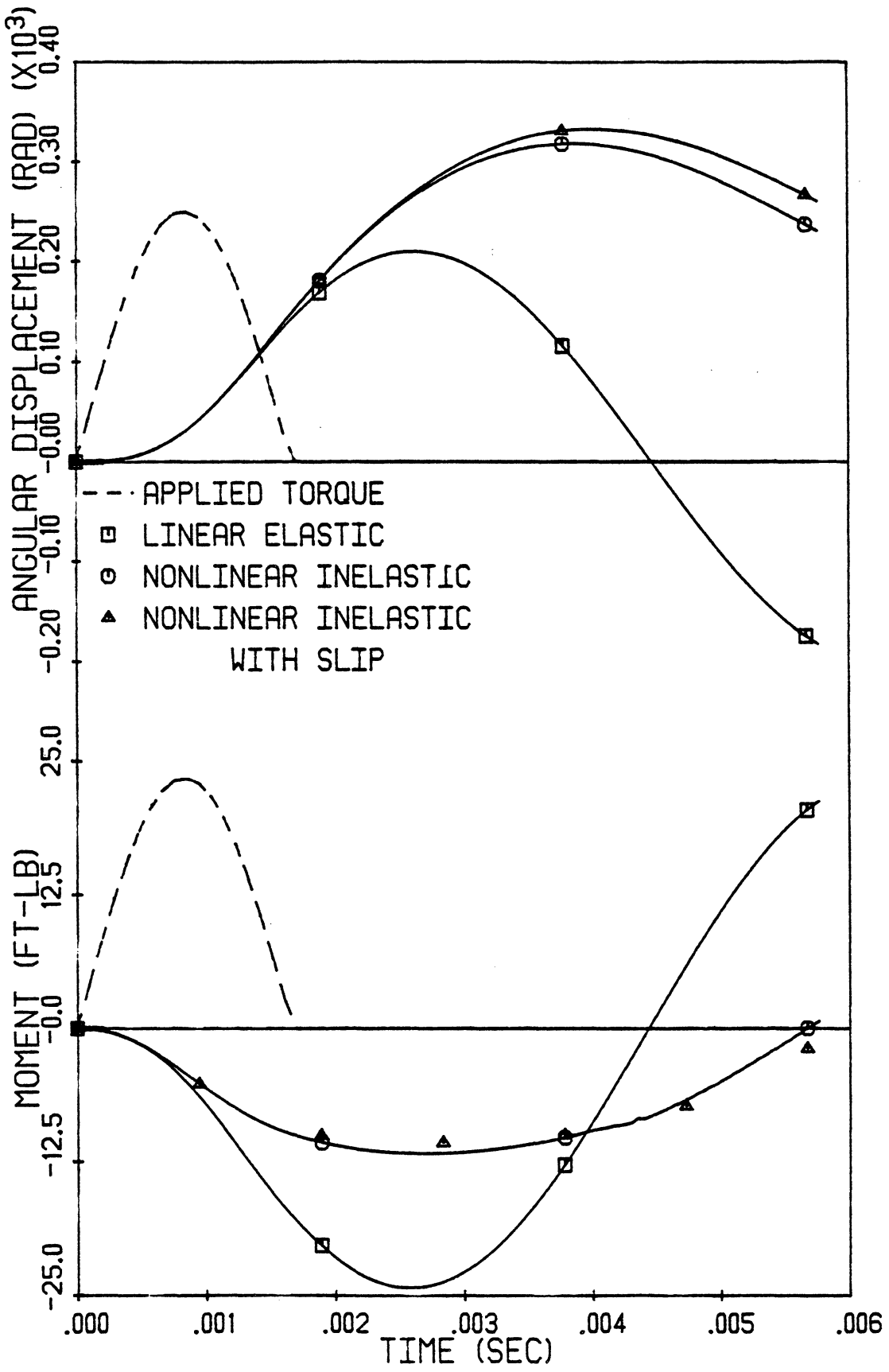

Fig. 6.24: Problem of Disk on Half Space: Angular Displacement of Disk and Resultant Moment at Interface vs. Time. Not All Points Shown.

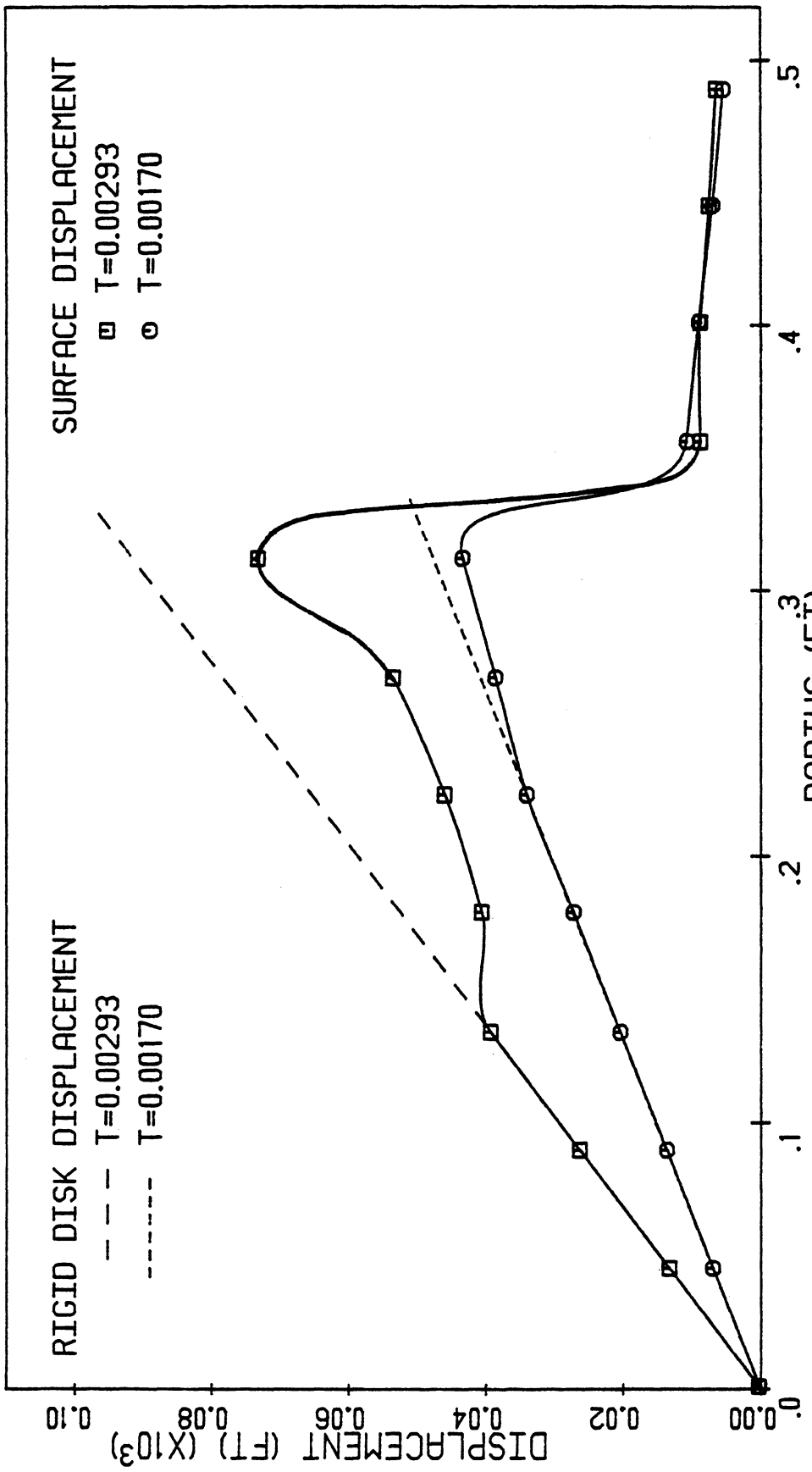

Fig. 6.25: Problem of Disk on Half Space: Displacement of Disk and Half Space Along Surface of Half Space vs. Radius at Indicated Times.

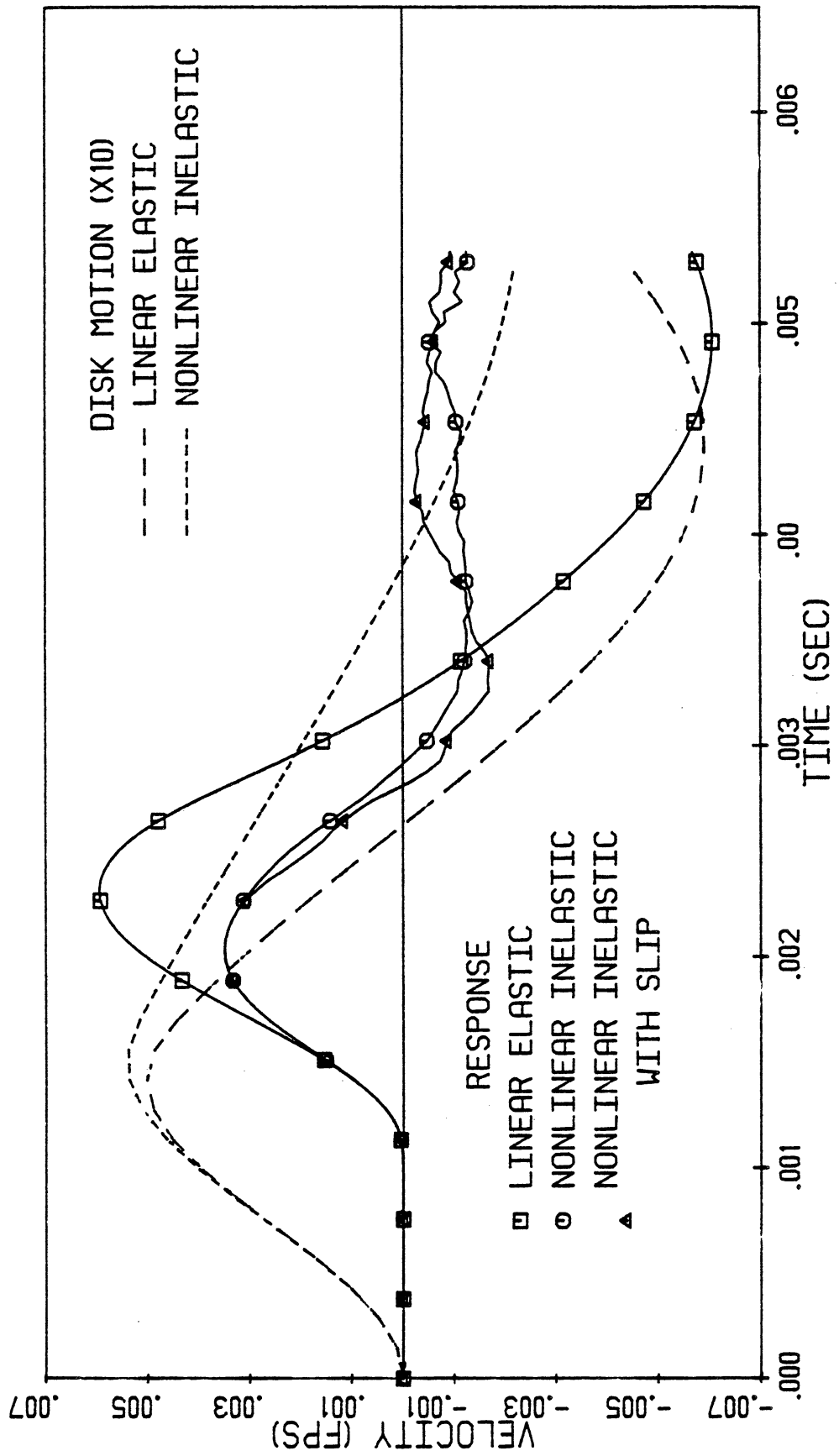

Fig. 6.26: Problem of Disk on Half Space: Particle Velocities within Half Space at r = 0.67 ft and z = 0.36 ft (See Fig. 6.18) and Velocities of Edge of Disk vs. Time. Not All Points Shown.

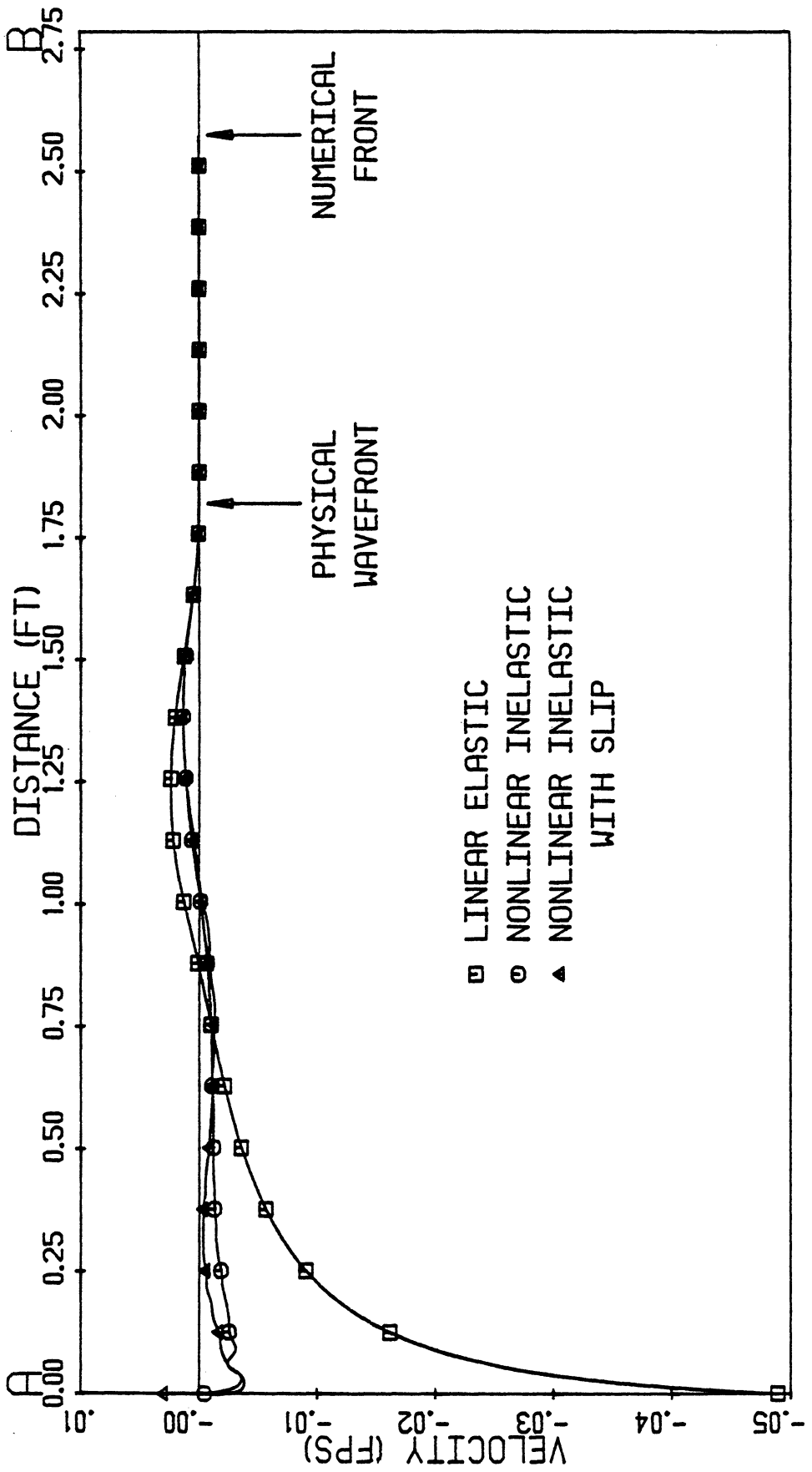

Fig. 6.27: Problem of Disk on Half Space: Particle Velocities vs. Distance Along Line AB Within Half Space (See Fig. 6.18) at Time of 0.00387 sec. Not All Points Shown.

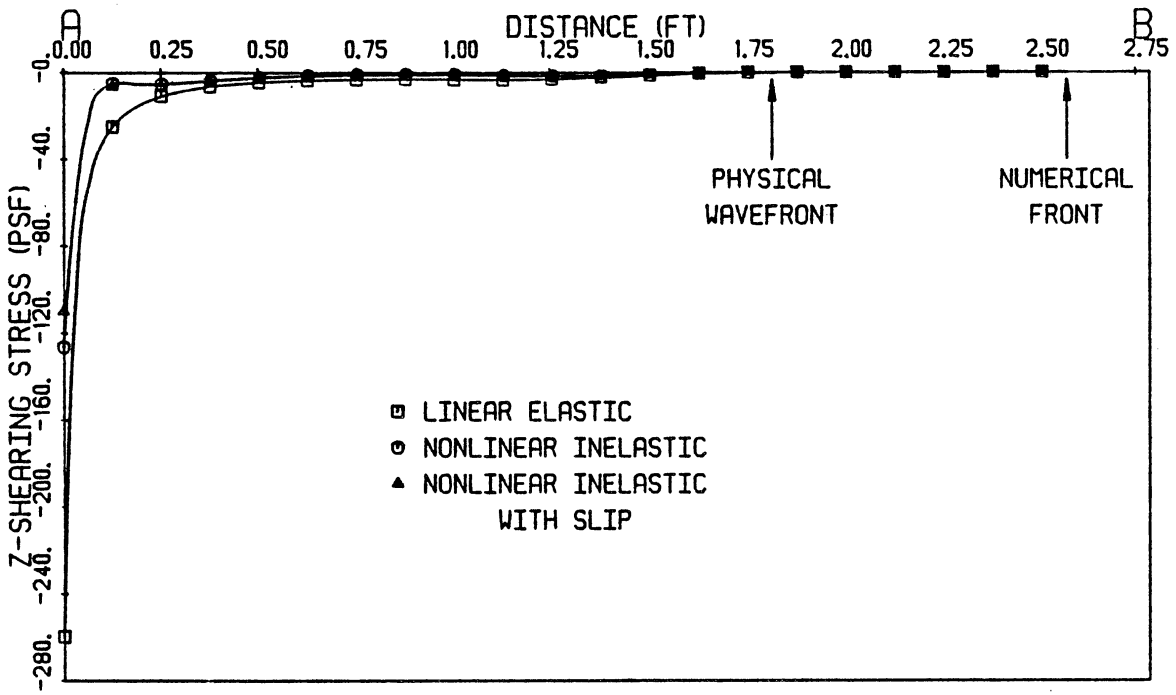

Fig. 6.28: Problem of Disk on Half Space: τ_z-Stress vs. Distance Along Line AB Within Half Space (See Fig. 6.18) at Time of 0.00387 sec. Not All Points Shown.

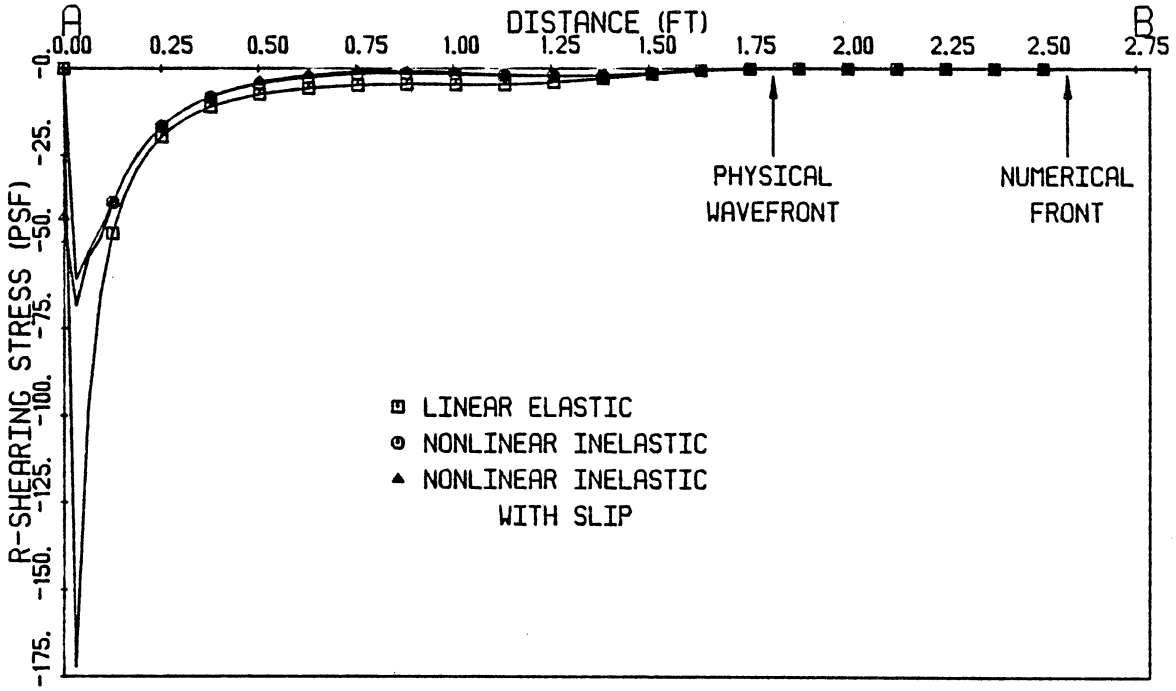

Fig. 6.29: Problem of Disk on Half Space: τ_r-Stress vs. Distance Along Line AB Within Half Space (See Fig. 6.18) at Time of 0.00387 sec. Not All Points Shown.

CHAPTER VII

TEST OBJECTIVES AND TEST EQUIPMENT

A. Introduction

An experiment was conducted in order to provide a comparison with the nonlinear numerical analysis. The arrangement of this experiment is shown schematically in Fig. 7.1. In this experiment a rigid model footing resting on the horizontal surface of a granular test bed was excited torsionally and in response, the footing rotated. This rotation was resisted by the inertia of the footing and by shearing stresses which developed within the test bed along the interface between the footing and the test bed. The rotation of the footing generated axisymmetric disturbances which propagated into the test bed. Information obtained from these tests included the history of the applied torque, the angular velocity of the footing and particle velocities within the test bed at selected locations.

In these tests attention was directed towards developing high amplitudes of shearing strain to emphasize the influence of nonlinear inelasticity. The

strain amplitudes developed were on the order of 0.25 percent or larger. Such strains are often encountered in earthquake motions and can be developed in the neighborhood of nuclear explosions (Woods, 1978).

Tests were also conducted to determine the properties of the test bed which influence dynamic response. These properties, needed primarily for the numerical models of the tests, include the mass density, the dynamic shear modulus, and the shearing strength.

In this chapter the objectives of the various tests and the design of testing equipment are discussed. A list of major equipment used in the tests is given in Appendix II along with with the manufacturers and model numbers of the equipment. In Chapter VIII the procedures for performing all tests are described and the results from these tests are presented in Chapter IX.

B. Granular Test Bed

An ideal test bed is one which is uniform in density, elastic shearing rigidity and shearing strength and has adequate rigidity and strength. If the test bed is uniform, then numerical modeling of the test is simplified and the degree of repeatibility in testing is greater. The strength and stiffness of the bed must be

sufficient to develop dynamic motions within the bed which are measured easily. In addition, to obtain consistent results from tests, it is important that the test bed may be reconstituted easily to its original undisturbed state.

A facility designed to provide a test bed which meets these objectives is described in the following sections. Procedures taken to prepare the test bed correctly are given in Chapter VIII.

1. Quicksand Tank

A quicksand tank, constructed and described by Chon (1977), is shown in Figs. 7.2 and 7.3. The tank contains a uniform, fine, cohesionless Muskegon Dune Sand which simulated a nonlinear inelastic half space for model footing tests. For this quartz sand, the uniformity coefficient was 1.5 and the maximum and minimum void ratios were 0.78 and 0.55, respectively.

Water is introduced at the base of this tank through a manifold as shown in Fig. 7.3 and flows upward through a filter and the sand bed. As the rate of flow is increased the sand loses its shearing strength and becomes "liquefied." Upon reducing the rate of the flow the sand is deposited. Thus, prior to each test it is

possible to reconstitute the sand bed, starting with this liquefaction procedure.

Because density, elastic, rigidity, and shearing strength are functions of void ratio, the sand must be deposited with a reasonably uniform void ratio. This requires a flow which is distributed uniformly within the tank and the component which governs the distribution of this flow is the manifold.

2. Surcharge Pressure System

Since the elastic moduli and shearing strength of cohesionless soils depend upon the value of confining pressure, as well as on void ratio, under simple gravity loading these properties vary in magnitude from zero at the surface to finite values within the sand bed. In order to improve the uniformity of these properties a uniform surcharge pressure was provided at the surface by a pressure bag system. A detailed discussion of the construction, installation and maintenance of this system is given in Appendix III.

C. Model Footing

To simulate effectively the mathematical problem of the torsional response of a rigid footing on a deformable half space, the footing must be rigid relative to the test bed. Also the applied loading must be a pure

torque about the vertical centerline of the footing and the response a pure rotation. The base of the footing must be of sufficient area to develop a reasonable distribution of stresses along the interface despite minor variations in soil conditions, yet small enough for the test bed to model adequately a half space. To develop uniformity of the elastic rigidity and strength of the test bed beneath the footing, it was important that the contact pressure of the footing be equal to the surcharge pressure. It was also of interest to design the footing to undergo significant motions prior to the arrival time of reflections from the wall of the quicksand tank. At this time the assumption of half space behavior is no longer valid (Drnevich, et al, 1966). Also, the practical considerations of handling and compatibility with the surcharge pressure system were included in the design objectives.

In the following sections the design and construction of a footing which satisfies reasonably these objectives is discussed. A measuring system designed to sense and display the applied loading and the motion of the footing is also discussed.

1. Mechanical Design and Construction of Footing Assembly

a. Principle of Operation--The entire footing assembly is shown in Fig. 7.4 and a detailed cross section of this assembly is given in Fig. 7.5. An impulse device, consisting of a double-headed, freely-rotating hammer arm and a lower target arm, was attached to the top of the footing. An impulse was delivered to the footing by rotating the hammer arm into this target arm. To assure proper functioning of the device, considerable care was taken during machining, balancing, and assembly.

b. Impulse System--The hammer arm carried two hammer heads, one attached to each end. Each hammer weighed 2.23 lb, and was carefully machined and balanced and bolted tightly to the arm. Pins were driven through the arm and hammers for additional security against slip. A centered shaft, which defined the axis about which the arm rotated, was welded perpendicular to the arm.

The target arm supported two target heads upon which the hammers impacted. These target heads were built up from balanced 1/4 inch thick plates firmly secured to the target arm by bolts and pins as shown in Fig. 7.6. For a distributed impact, the impact surfaces

were machined at an angle relative to the length of the arm. Two balanced 8 pound weights were attached to the target arm at equal distances from the center. These weights modified the arm motion and provided a more desirable load-time impulse to the footing.

As shown in Figs. 7.5 and 7.7, the shaft of the hammer arm rotated in a bronze bushing which also provided vertical support to the arm. The bushing was carefully reamed to give a clearance of approximately 0.001 inch allowing free rotation of the shaft with a minimum of free play. The housing of the bushing was suspended by two diametrically opposed conically-tipped bolts. These bolts were threaded horizontally into a centrally located pipe welded perpendicularly to the target arm. Adjustment of these bolts permitted lateral positioning of the hammer arm in a direction perpendicular to the length of the target arm.

c. Footing--The footing was constructed from steel for high rigidity relative to the test bed. As shown in Fig. 7.5, the main body consisted of two thick horizontal circular plates separated by a large outer and a smaller inner cylinder. These components were machined carefully to insure perpendicularity between the plates and the cylinders, concentricity of the

components, and a plane mounting platform for the velocity transducers. Holes for mounting the velocity transducers and the load cell were located precisely, drilled, and tapped. Then, these components were assembled by welding. The base and the mounting surface for the load cell were machined flat and perpendicular to the vertical centerline. This order of fabrication minimized distortions induced by welding.

To improve coupling with the test bed a layer of sand was epoxied to the base. Dry sand from the test bed was deposited carefully on a thin uniform coating of epoxy cement spread on the base. After 24 hours excess sand was swept off leaving a one-grain thick well-bonded layer of sand on the bearing surface.

d. Load Cell--The mechanical functions of the load cell, shown in Fig. 7.8, were to transmit torsional pulses between the target arm and the upper plate of the footing and to serve as a mount for strain gages. For the transmission of pure torque, the distribution of shearing stresses along the mounting surfaces of the load cell must be uniform. This requires uniform contact pressures; therefore, thick mounting flanges (see Fig. 7.5) were selected for the load cell to prevent localized distortion under bolting loads. Following

assembly by welding, the mounting faces of the load cell were machined flat and perpendicular to the axis of the cylinder.

To improve transmission of energy through the load cell, the joints were designed to prevent slip. For this, the shearing resistance of the joint derived from the clamping force of the fasteners must exceed greatly the expected maximum shearing force. Thus, in addition to the steps taken to insure the transmission of pure torque, to prevent slip, a sufficient number of correctly sized and torqued bolts were needed.

Prior to assembly, the mounting surfaces of the load cell were degreased thoroughly and cleaned. The load cell was attached by torquing sequentially the attachment bolts in small increments to prevent distortion of the flanges and plate.

As a mount for strain gages, the load cell must develop strains large enough to provide adequate output from the strain gages. Localized flexibility was obtained in the gage region by increasing the inside diameter to reduce the thickness of the cylinder wall. The minimum wall thickness was limited by torsional buckling and plastic deformation. A transition radius was machined at the boundaries of this zone to prevent stress concentrations. Then the outer surface of the

cylinder was machined smooth and polished to provide a good surface on which to mount the strain gages.

e. Velocity Transducers--Two balanced, horizontal velocity transducers were mounted transversely to the underside of the upper plate of the footing as shown in Fig. 7.9. These transducers were placed in a diametrically opposed arrangement and each was located 4.97 inches from the vertical centerline. This arrangement permitted the sensing of pure rotation The transducers were oriented precisely by matching alignment marks scribed on the mounting frame of each transducer and the upper plate of the footing. It was necessary to insert shims between the mounting frames and the upper plate in order to develop sufficient tightness of the mounting studs with the transducers oriented correctly.

f. Properties of the Footing--With all equipment in place the footing weighed approximately 97 lbs resulting in an average contact pressure of 1.95 psi. The mass moment of inertia of the footing about its vertical centerline and below the midpoint of the load cell, at which the applied torque is known, was needed for the numerical model of the experiment. Neglecting the contributions of the bolts, the

constriction of the load cell, all welds, and the strain gages, and with two vertical velocity transducers attached to the footing this quantity is equal to 0.155 slugs-ft^2. Without these transducers this quantity is equal to 0.145 slugs-ft^2.

2. Measuring System

The measuring system, used to measure simultaneously the loads applied to the footing and the motion of the footing, consisted of load cells and velocity transducers to sense these quantities and various components to display and record permanently information sensed. The possible components of load and motion are shown in the diagram of Fig. 7.10. Only M_z and $\ddot{\Theta}_z$ are desired for pure torsional moments. The unwanted components may be developed because of the mechanical imprecision and imbalance of the footing, and testing environmental influences.

a. Load Cells--Load components were sensed by strain gages mounted on the load cell. These gages were arranged to sense M_x, M_y, and M_z independently. Forces and moments at the level of the load cell originate from one of the flanges of the load cell. The forces, F_x and F_y, (see Fig. 7.10) at either of these locations cause M_y and M_x at the level of the load cell.

Thus by sensing M_x and M_y, generally, F_y and F_x may be sensed. The force F_z was assumed to be small and gages were not placed to detect this component.

The three load cells were designed to meet several objectives: adequate sensitivity, durability, insensitivity to other loading components and temperature compensation. The torsional load cell consisted of four Micro-Measurement EA-06-250BK-10C gages spaced equally around the circumference of the load cell and each mounted at 45 degree angles with the vertical as shown in Fig. 7.11(a). With this arrangement the gages sensed the principal strains associated with a pure torque (see Fig. 7.11(b)). For sensitivity, the bridge circuit was connected such that the voltage responses of the gages were cumulative. An inspection of Fig. 7.11 reveals that this circuit was unresponsive to force along the z-axis, bending in the x-z and y-z planes, and to temperature changes.

Because the load cells used to measure bending were identical except in position, only the load cell used to measure bending in the x-z plane is discussed. Two diametrically opposed Micro-Measurements EA-06-250BK-10C gages, oriented vertically, were positioned along the x-axis and shown in Fig. 7.12(a). These gages sensed the principal strains associated with

bending in the x-z plane (see Fig. 7.12(b)). In Fig. 7.12, it may be seen that the responses of the gages were cumulative and that the gage circuit was insensitive to bending in the y-z plane, torque about the z-axis, force in the z-direction, and temperature changes.

All gages were cemented to the load cell in accordance with instructions from Micro-Measurements. In order to provide durability, the assembly was completed by covering all gages with an elastic protective compound also manufactured by Micro-Measurements. For a detailed discussion of applicable theory of strain gages the reader is referred to the text by Dally (1978).

The equipment and circuitry needed to display information from the load cells are shown in Fig. 7.13 and 7.14. A preamplifier and power suppy were used to supply the excitation voltage to the bridge circuits, to amplify the output from these circuits and to provide resistance to these circuits as needed. The preamplifier provided variable amplification and the capability to balance the resistance and the capacitance of the bridge circuits. The cables of these circuits were collected conveniently at a junction box. A storage oscilloscope provided additional amplification and a

means of displaying information from the load cells. An oscilloscope camera was used to obtain a permanent record of the information displayed.

b. Velocity Transducers--As shown in Fig. 9.15, pairs of velocity transducers in various positions and orientations were used to detect the components of unwanted motion of the footing. The equipment and circuitry needed to display information from all velocity transducers attached to the footing are shown in Fig. 7.15.

c. Pre-Impact Triggering System--The equipment and circuitry needed to trigger the sweep of the oscilloscope are shown in Fig. 7.16. The hammer and target arms functioned as a switch in the triggering circuit. As shown in Fig. 7.7, these arms were isolated electrically from one another by an insulating cylinder which separated the bronze bearing from its housing. Electric contact between the hammer and target heads closed the circuit. An electronic triggering circuit was included to shorten the rise time for the buildup to triggering voltage (Woods, 1978).

To capture a complete record of transient signals, it was necessary to effect triggering prior to impact. For this purpose a brass rod (Fig. 7.17) with a

weak spring extending from one end was slip-fitted into a hole machined perpendicular to the face of the hammer head. A lateral set screw permitted this rod to be locked into an adjustable position. For effective pre-impact triggering the rod was secured with the spring protruding slightly from the impact face of the hammer as shown in Fig. 7.17(b). By varying the length of protrusion it was possible to vary the time delay between triggering and impact.

D. System for Measuring Particle Velocities within Test Bed

1. Sensing System

Horiziontal velocity transducers, waterproofed with silicon sealant (for operation in a moist environment), were used to sense the particle velocities within the test bed. These transducers were suspended in the sand at preselected locations during the preparation of the test bed.

A suspending system, conceived by Ben Bourland, consisted of a track, two adjustable frames and two adjustable rods. As shown in Fig. 7.18, the tracks bridged the outer frame of the quicksand tank. Four clamping screws permitted each frame to be locked into any position along the track. The rods from which the

transducers were suspended were made from aluminum. The 3/8 inch diameter of each rod was large enough to prevent significant flexing during the preparation of the test bed, yet sufficiently small to avoid excessive disturbance to the sand. Each rod was oriented vertically by a 2 inch long guide fixed to each frame and a slip-fit permitted vertical and rotational movement. A horizontal, plastic-tipped, clamping screw allowed each rod to be locked into position without damage. By locking each rod, the position of each transducer was fixed.

Each suspending rod was designed to be removed after the test bed had been prepared, leaving each transducer oriented properly in the desired location. As shown in Fig. 7.19, each of the three feet long rods consisted of two basic components: an inner solid steel rod and an outer aluminum tube. The tube was threaded very loosely into an aluminum ring fixed to the transducer. Twisting a locking knob to advance the rod relative to the tube, placed the tube in tension. This locked the threaded connection of the tube and the ring and, consequently, the orientation of the transducer. Retraction of the rod loosened the connection and permitted the free removal of the suspending rod.

In order to improve coupling with the sand bed a layer of dry test sand was cemented to the surfaces of the transducers.

2. Recording System

Equipment and circuitry, used to display information sensed by the velocity transducers within the test bed, are shown in Fig. 7.20. This information was displayed along with the information sensed at the footing. A photograph showing the entire measuring system used in the dynamic model footing tests, excluding transducers, is presented in Fig. 7.21.

In most of the dynamic footing tests, signals from the transducers located within the test bed were clouded with a high frequency noise of unknown origin. This noise, which impaired the ability of the oscilloscope to display information, was eliminated from the output of these transducers by the use of low pass filters. These filters had nominal cutoff frequencies of approximately 1500 Hz and were designed and constructed by Lou North.

E. Equipment for Tests Related to Dynamic Model Footing Tests

The following sections describe equipment needed to perform tests which were conducted in preparation for the dynamic model footing tests.

1. Calibration of Load Cells

In the calibration of an elastic load cell, the linear relationship between the applied load and electric signal developed is established. Each load cell was calibrated statically by applying a sequence of static moments about an axis of interest and measuring the voltage response of the load cell.

As shown in Fig. 7.22, a pair of horizontally opposed forces directed perpendicular to the length of the target arm of the footing was used to provide a static torque about the vertical centerline of the footing. These forces were generated by two sets of balanced weights, each of which was suspended vertically by a hanger. Each force was applied to each adjustable eye bolt attached to each end of the target arm and each force was directed by an adjustable pulley.

To apply a static moment about the y-axis, an arm was constructed which attached to the center of the target arm and extended horizontally in a direction perpendicular to the length of the target arm. Load was developed by suspending vertically a series of weights from the outer end of this additional arm. Bending moments were applied about the x-axis by suspending vertically a series of weights from either end of the target arm.

The measuring systems used for calibrations were identical to those used to measure loads in the dynamic footing tests and are shown in Figs. 7.13 and 7.14.

2. Calibrations of Velocity Transducers

In the calibration of a velocity transducer, a linear relationship between the velocity of the transducer and the electric signal developed is obtained for applicable ranges of frequencies and displacement amplitudes. In order to calibrate a velocity transducer, a sinusoidally varying displacement of known amplitude and frequency was imposed on the transducer. The voltage response of the transducer was measured and the procedure was repeated for the relevant ranges of frequencies and amplitudes.

The equipment and circuitry shown in Fig. 7.23 was used in calibrating the transducers. Harmonic displacements in either the horizontal or vertical mode were imposed by the vibration exciter. The oscillator provided a harmonic signal for the vibration exciter which was amplified to a level needed to drive the exciter. The frequency of this motion was controlled by the oscillator and the amplitude was controlled by the amplifier and the field coil. Power was provided by the power supply. Accurate measurements of frequency were

obtained using a period counter. The displacement of the velocity transducer was detected with an optical displacement transducer. Outputs from the displacement and the velocity transducers were displayed using ac voltmeters for accuracy, and an oscilloscope to allow inspection of the waveform. In order to reduce high and low frequency noise appearing at the output of the displacement transducer, the signal from this transducer was filtered.

3. Filter Tests

The filters discussed in Sections D.2 and E.2 modify the amplitudes and phases of signals to a degree which depends on frequency and amplitude. To correct for this effect it was necessary to obtain experimentally the modifying characteristics of each filter. Only the effect on the amplitude of a signal was needed for the filter discussed in Section E.2.

To determine the manner in which a filter affected the amplitude of a signal, a sinusoidal signal of known frequency and amplitude was applied to the input terminal of the filter. The voltage was measured at the output terminal. The ratio between the rms value of the output and input voltages gives the amplification of the signal at the selected frequency and amplitude.

To determine the manner in which phase was affected by a filter the time shift between the waveforms of the input and output signals was measured. These tests were repeated over relevant ranges of frequency and amplitude.

The equipment and the circuitry used to obtain the characteristics of the filters are shown in Fig. 7.24. The harmonic signal was provided by a function generator which permitted control of the frequency and the amplitude of the signal. An oscilloscope camera was used to acquire permanent records of the displayed waveforms from which phase shift characteristics were obtained. The functions of the remaining equipment shown in Fig. 7.24 were as described in Section 2.

4. Preliminary Dynamic Model Footing Tests

The horizontal angle between the target and hammer arms at contact and the resilience of the impacting surfaces of the hammer heads influenced the nature of the load applied to the footing and thus the response of the footing. The horizontal angle affected principally the distribution of impact energy between the two ends of the target arms. This angle was adjusted by repositioning the bearing which supported the hammer shaft and by sanding lightly the impact faces

of the target heads. The resilience of the impacting surfaces, which was varied by attaching gum rubber pads having various thicknesses to each of these surfaces (see Fig. 7.17 (b)), affected primarily the character of an impact.

Prior to performing the model footing tests in the quicksand tank, a number of preliminary tests were conducted in a small pan containing sand from the test bed. The corresponding test set up is shown in Fig. 7.4. These tests were performed to adjust the horizontal angle between the hammer and target arms to obtain the best performance from the footing and to determine the optimum resilience of the impacting surfaces. In addition the unwanted components of load and motion were measured.

The electronic measuring equipment used in these tests was identical to that used in the footing tests conducted in the quicksand tank.

F. Equipment for Dynamic Model Footing Tests

1. Accessories to Surcharge Pressure System

The clamping method used to seal the air bags along edges, described in Appendix III, restrained the deformation of the air bags locally. As a result a large annular zone surrounding the base of the footing

remained unconfined. To reduce the width of this region, an eight inch diameter tire tube with a separate line for air pressure was located beneath the underside of the central air bag. As shown in Fig. 7.25, this tube was positioned concentrically with the central access hole. A cylindrical guard constructed from sheet metal was attached to the lower clamping ring to prevent the expansion of the inner tube towards the footing. With this arrangement, surcharge pressure was applied to within 1/2 inch of the edge of the footing.

2. System for Leveling of Test Area

In order to provide a level base for the footing and to promote a favorable distribution of contact pressure the surface of the test bed exposed by the central access hole was leveled prior to the placement of the footing. A scraping device, shown fully assembled in Fig. 7.26, was constructed for this purpose. The device consisted of a knife-edged straight blade attached to an aluminum rod three feet in length. This device was capable of sweeping out a plane horizontal circle slightly larger in area than the base of the footing. The rod defined the axis about which the blade rotated. The angle between the blade and the rod was adjustable. The rod was guided by lower and upper

slip-fit guides which were attached to the track-frame system. A clamping screw, used to lock the position of the rod, was threaded into the upper guide.

As shown in Fig. 7.26, the upper guide was housed in the inner race of a ball bearing and the outer race of this bearing was housed in a large diameter threaded coupling. This assembly, conceived by Ben Bourland, permitted the rotation of the locked rod and the fine adjustment of the scraped plane in the vertical direction.

3. System for Placing Footing

In order to develop uniform contact with the level surface of the sand the base of the footing must be placed horizontally. In addition, to position the footing correctly relative to the velocity transducers within the half space, the footing must be centered properly on the centerline of the test bed. As shown in Fig. 7.27, a suspending system consisting of three cables was assembled to place the footing properly. Each cable was attached to an inverted eye bolt which was supported by the track-frame system. To lower the footing, the eye bolt was lowered by turning its retaining nut. Each cable of the system was adjustable in length thus permitting leveling of the footing. The

lateral positioning capability provided by the track-frame system allowed the centering of the footing.

4. Frame for Controlling Impact

In order to excite the footing with repeatable purely torsional impacts, it was necessary to devise a means to control the impulses. An inverted T-frame was constructed for this purpose and, as shown in Fig. 7.28, this frame was suspended above the footing from the track-frame system. At each end of the hammer arm a spring from a matched set was connected between the arm and the appropriate end of the T-frame. The attachment points of the springs to the T-frame were triaxially adjustable thus permitting the alignment of each spring and variable pretensioning.

Energy for the impact was derived from tension in the springs developed by separating the hammer arm from the target arm. The extent of the separation at the release of the hammer determined the energy and the character of the applied torque.

G. Equipment for Evaluation of Properties of Test Bed

1. Density, Void Ratio

The density and the void ratio of the test bed were determined by analyzing samples obtained from drive cylinders which were suspended within the test bed

during liquefaction. These newly machined cylinders were thin-walled, 3 7/8 inches in inside diameter, and 4 inches in depth. As shown in Fig. 7.29, the cylinders were suspended vertically by strings from a horizontal pipe which spanned the platform opening of the quicksand tank.

2. Low Amplitude Shear Modulus

Torsional seismic crosshole tests were conducted within the test bed to determine shear wave velocities. From these, the low amplitude shear moduli of the test bed were calculated. In this test a torsional disturbance was introduced into the test bed. A shear wave propagated from this disturbance and the velocity at which this wave propagated was measured.

The equipment needed to conduct a torsional seismic crosshole test included a torsional source which generated shear waves and a measuring system for obtaining shear wave velocities.

a. Torsional Source--The principal wave generated within the test bed by the torsional source was a horizontally polarized shear wave in which the particle motions were horizontal. This disturbance was similar to that developed in the dynamic footing tests and the purity of this disturbance facilitated data

analysis. Because vertical penetration of the source during testing was minimized, the torsional source also gave good depth control.

The entire test set up is shown schematically in Fig. 7.30. Torsional disturbances were generated by a torsional hammer, suggested by Woods. This device, shown in Fig. 7.31, is basically the same impacting device which was used to excite the footing in the dynamic footing tests (Sections C.1.a and C.1.b). As applied to the seismic crosshole test, this device was in an earlier stage of development than for the footing tests. Hardwood bearings were used to guide the shaft of the hammer arm rather than the bronze bearing used in the footing. While adequate for the cross hole test, these wooden bearings did not provide the precision necessary to conduct high quality dynamic footing tests.

Disturbances generated by the torsional hammer traveled down a straight 8 foot long, 1 inch diameter, steel pipe coupled tightly to the bottom of this device. A straight, thin-walled, concentric Shelby tube, 14 inches in length and two inches in diameter was threaded tightly to the end of this pipe. The Shelby tube coupled the disturbance into the test bed. To improve the coupling a layer of sand was cemented to the surface of the Shelby tube.

To minimize the introduction of non-torsional disturbances into the sand by lateral sway of the source during a test, a wooden guide, conceived by Don Hutchings, was constructed for the source. This guide, shown in testing position in Fig. 7.32, consisted of two wooden bearings with which to align the source. Clearances in each bearing were adjustable to permit corrections for wear. The upper bearing was also adjustable in height. This feature provided maximum lateral stability to the source by allowing the largest possible spacing between the bearings to be used for testing at any given depth.

b. System for Measuring Shear Wave Velocity--To determine the shear wave velocity, a measuring system capable of sensing the disturbance within the test bed and recording permanently the information sensed was needed. As shown in Fig. 7.30, two horizontal velocity transducers were placed at the depth of the tip of the Shelby tube and in line with the Shelby tube to sense the disturbance. The spacing between the transducers was about 20 inches and this arrangement spanned the zone of interest. To maximize the response of each transducer to the radiating wavefield, each transducer was oriented transversely to

the horizontal radius extending from the Shelby tube and intersecting the transducer.

In order to position the source and the transducers within the test bed it was necessary to gain access to the surface of the sand. As shown in Fig. 7.33, access was provided by three plastic pipes each 1 foot in length and 3 to 4 inches in diameter. These pipes were placed through the covers of the surcharge pressure system to the surface of the sand. The outer pipes were wedged between air bags and a light frame, shown in Fig. 7.33, was needed to maintain these pipes in position under pressure from the air bags.

The suspending rods, shown in Fig. 7.19 were used to place and orient the transducers at depth in the boreholes. In order to improve coupling with the sand a layer of sand was cemented to the surfaces of these transducers.

The components of the recording system and the connecting circuitry needed in the torsional seismic crosshole tests are shown in Fig. 7.30. An oscilloscope camera was also used. The triggering system was as described in Section C.2.c except that the pre-impact triggering device was not used.

3. Shearing Strength

The shearing strength of the sand at the surface of the test bed was determined by conducting a static torsional loading test on the model footing in its dynamic testing environment. In this test a static torque was applied incrementally to the footing and the resulting angular displacement of the footing was measured. By loading the footing to a level approaching failure it was possible to obtain an estimate of this shearing strength.

Only the torsional loading system and the system for measuring the angular displacements of the footing were different from those used in the dynamic footing tests.

a. Loading System--A torque was applied statically to the footing by imposing equal but opposite horizontal forces at the end of each target arm. These forces were directed perpendicular to the length of the target arm. As shown in Fig. 7.34, this force system was developed by suspending vertically at each end of the target arm a hanger supporting a matched set of weights. Adjustable pulleys, rigidly attached near each end of the target arm to the I-beams of the surcharge pressure system, were used to direct these forces.

b. System for Measuring Angular Displacements--To obtain the angular displacement of the footing about its vertical centerline, the transverse displacement of the footing was measured at two locations. A diametrically opposed arrangement of two horizontally oriented dial gages centered on the centerline of the footing was used for these measurements. In order to extend the radius of the measurement for greater sensitivity two horizontal arms, one for each gage and each directed radially, were attached to the underside of the upper plate of the footing.

A third gage was mounted in order to detect unwanted lateral translation of the centerline of the footing. The sensing arm of this gage was positioned against the upper flange of the load cell in an orientation directed horizontally towards the centerline of the footing.

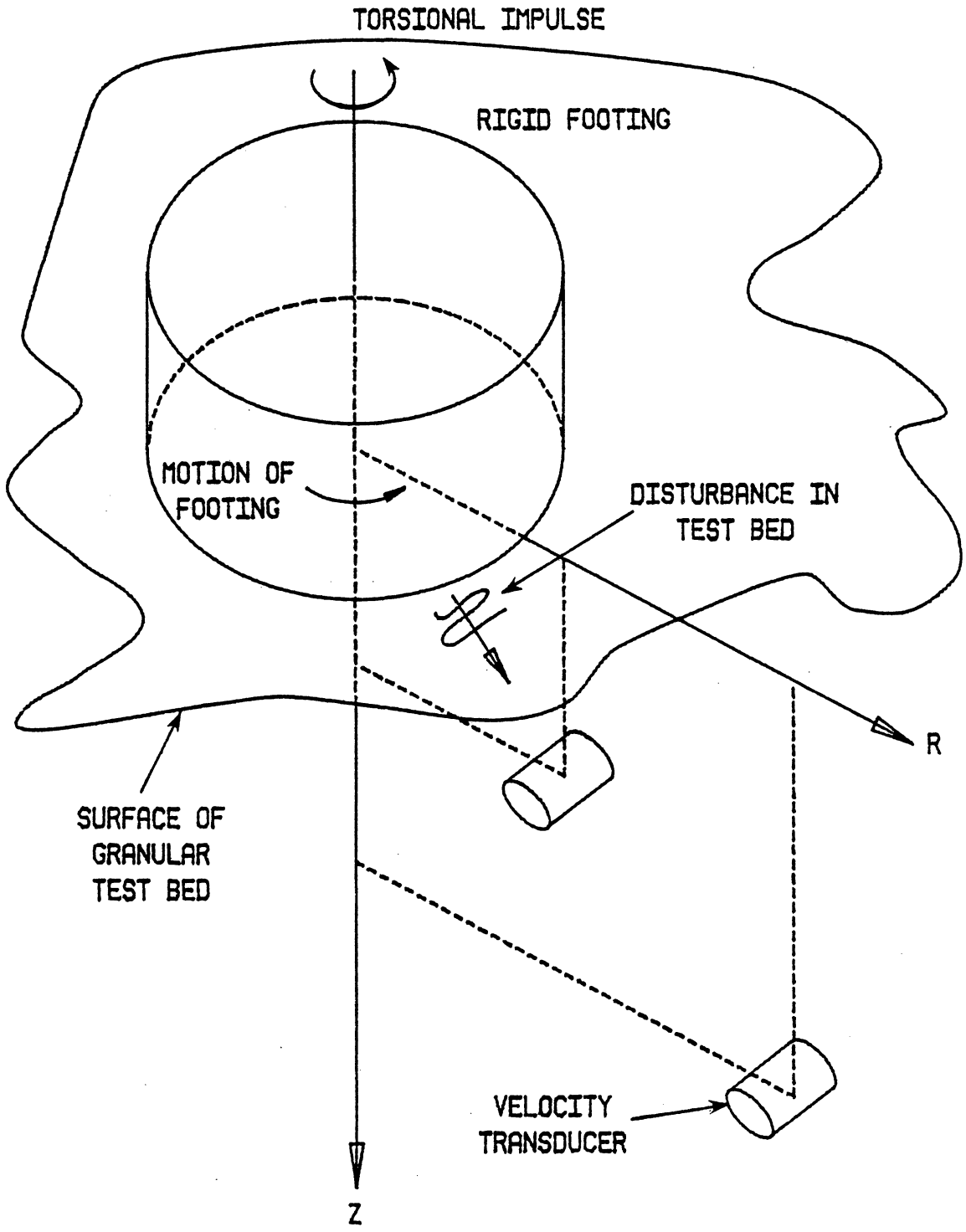

Fig. 7.1: Schematic Diagram of Experiment.

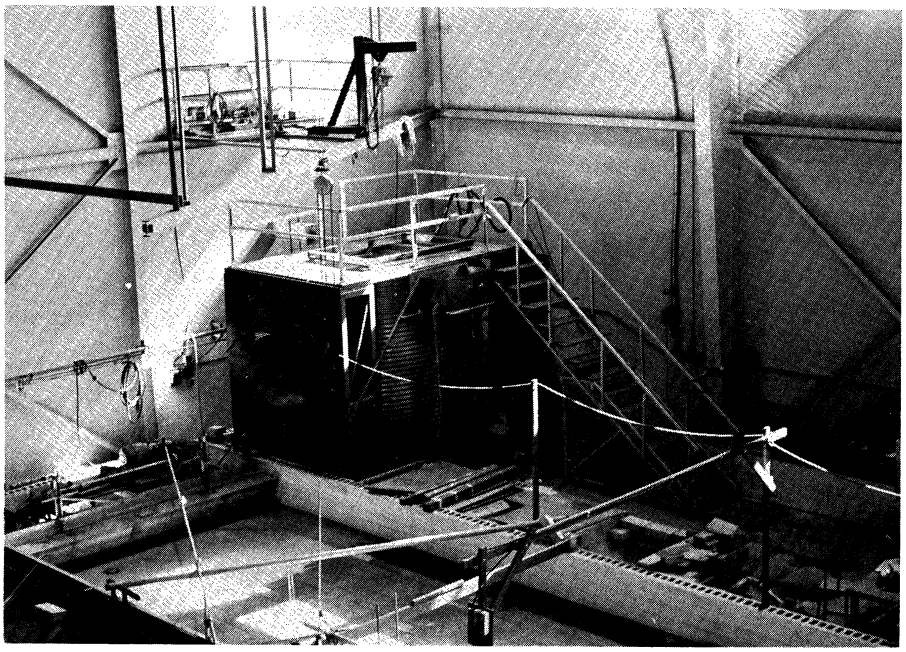

Fig. 7.2: Quicksand Tank.

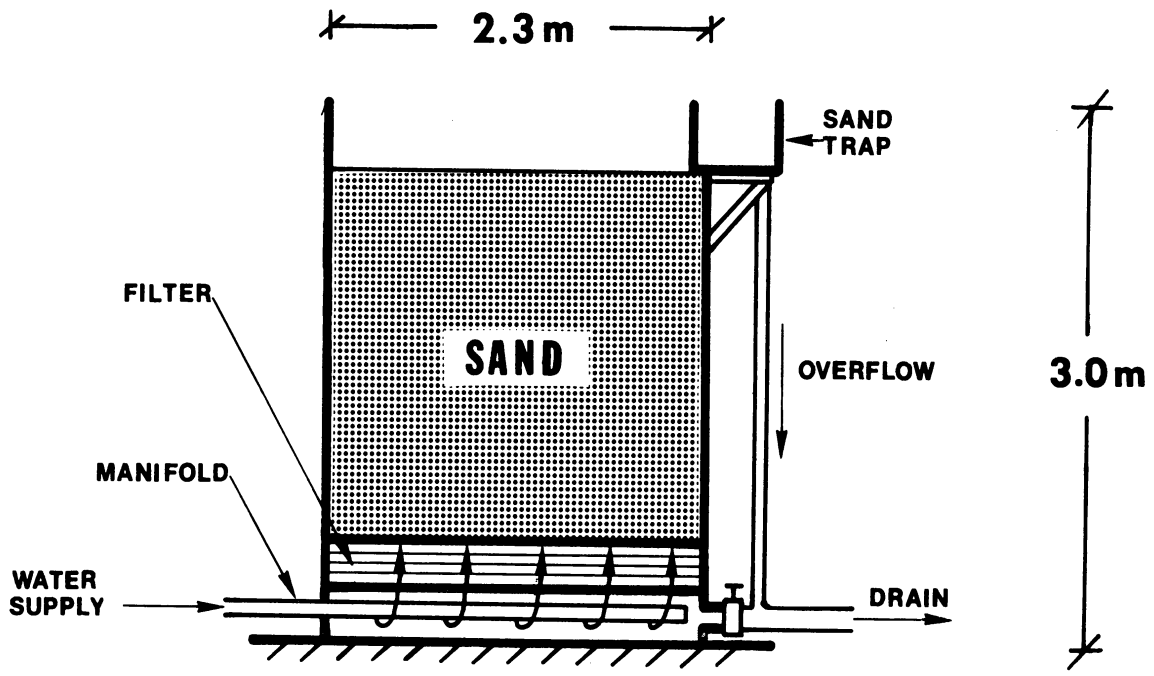

Fig. 7.3: Schematic Diagram of Quicksand Tank.

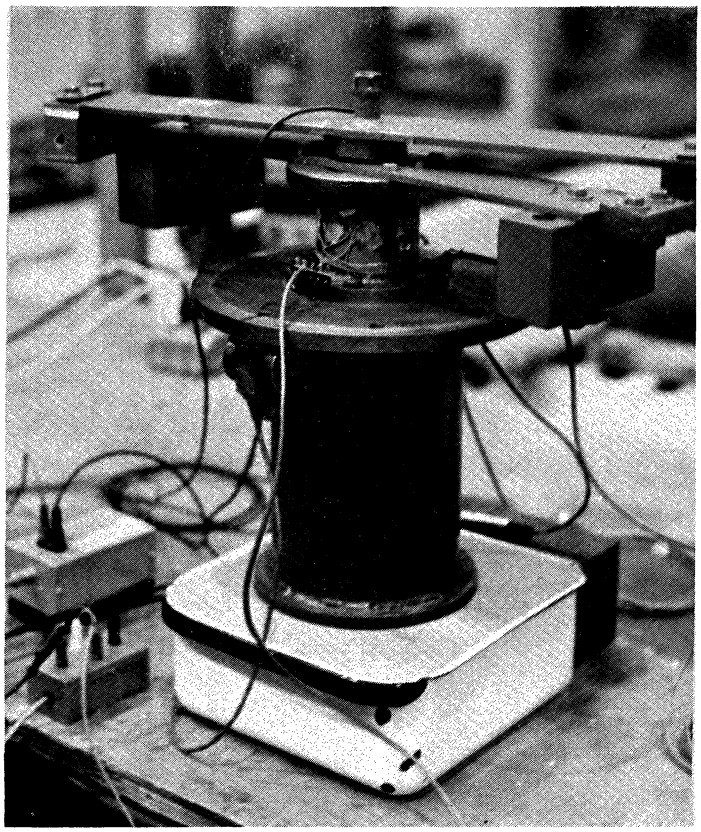

Fig. 7.4: Fully Assembled Footing on Small Scale Test Bed.

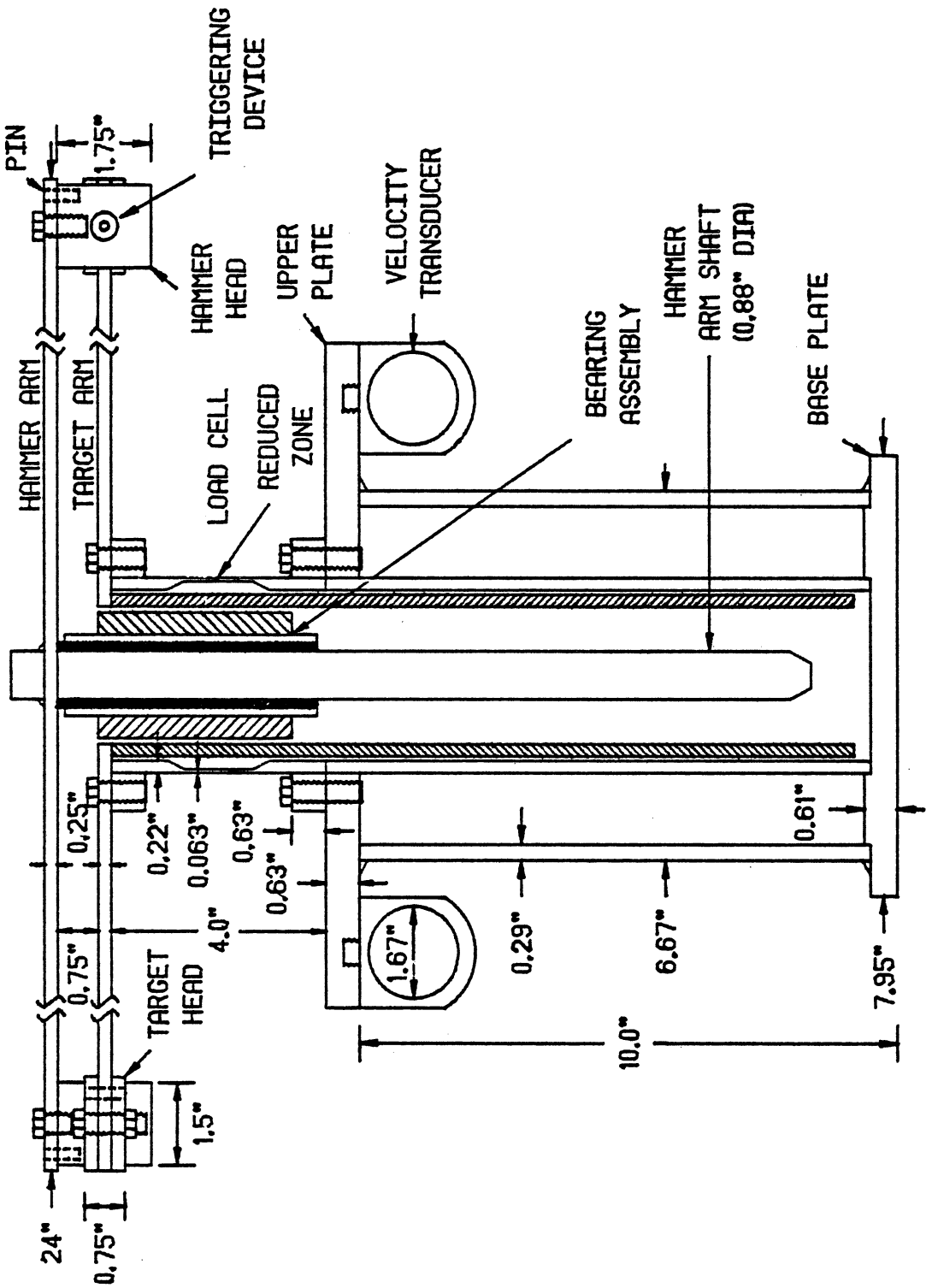

Fig. 7.5: Cross Section of Assembled Footing and Impacting Device.

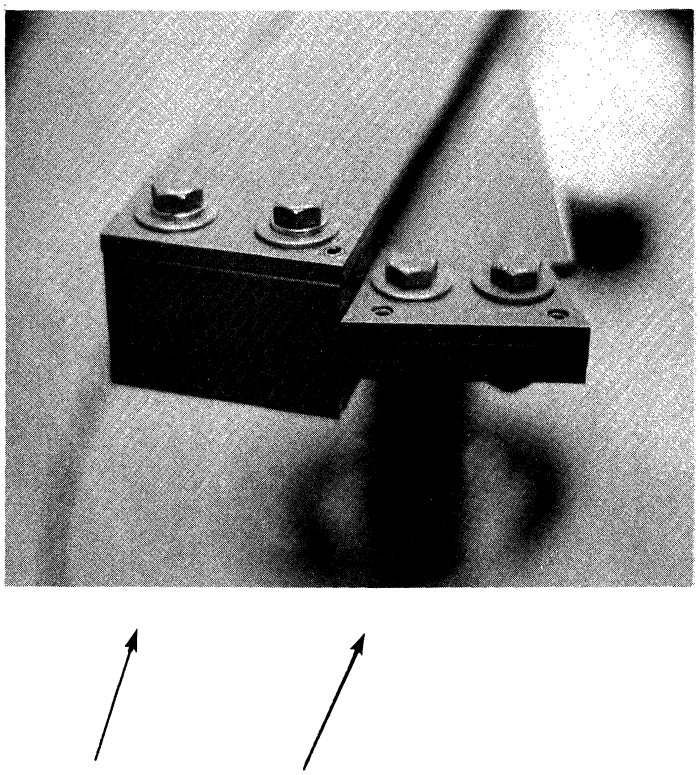

Fig. 7.6: Hammer and Target Heads at Contact.

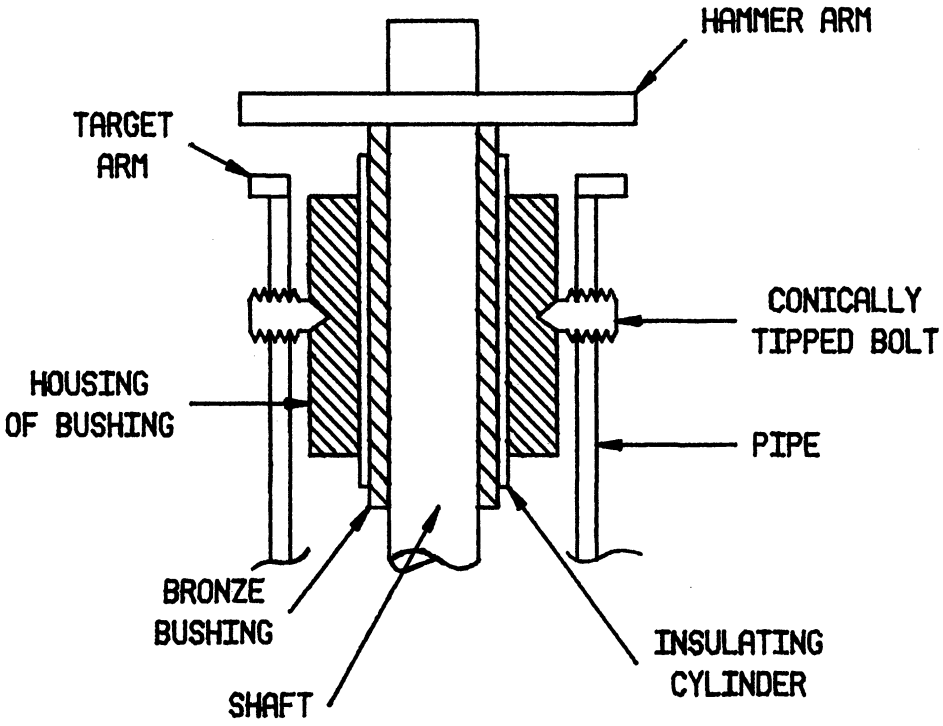

Fig. 7.7: Cross Section of Bronze Bushing Assembly. Long Axis of Target Arm is Perpendicular to Plane of Diagram.

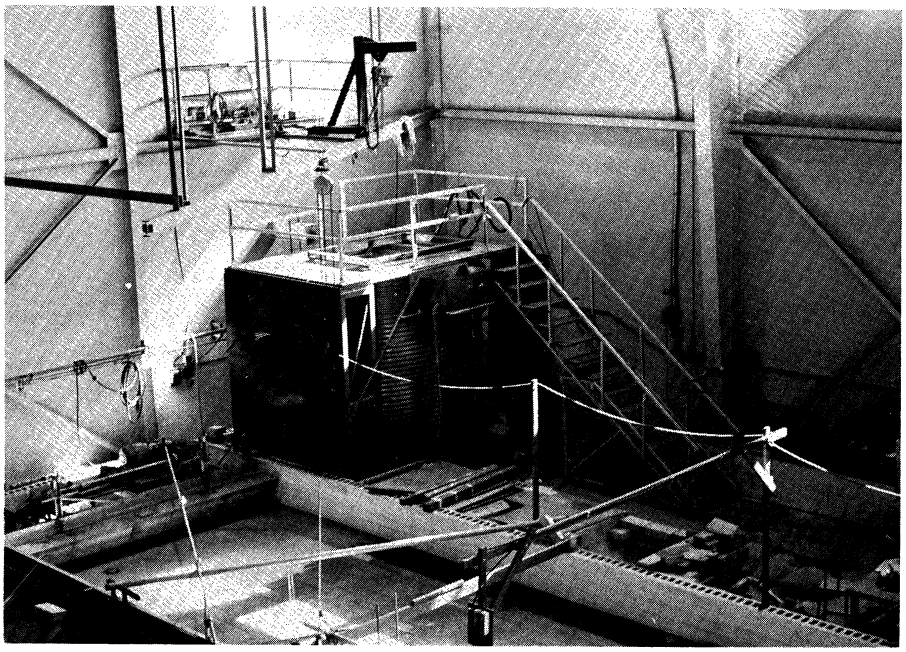

Fig. 7.2: Quicksand Tank.

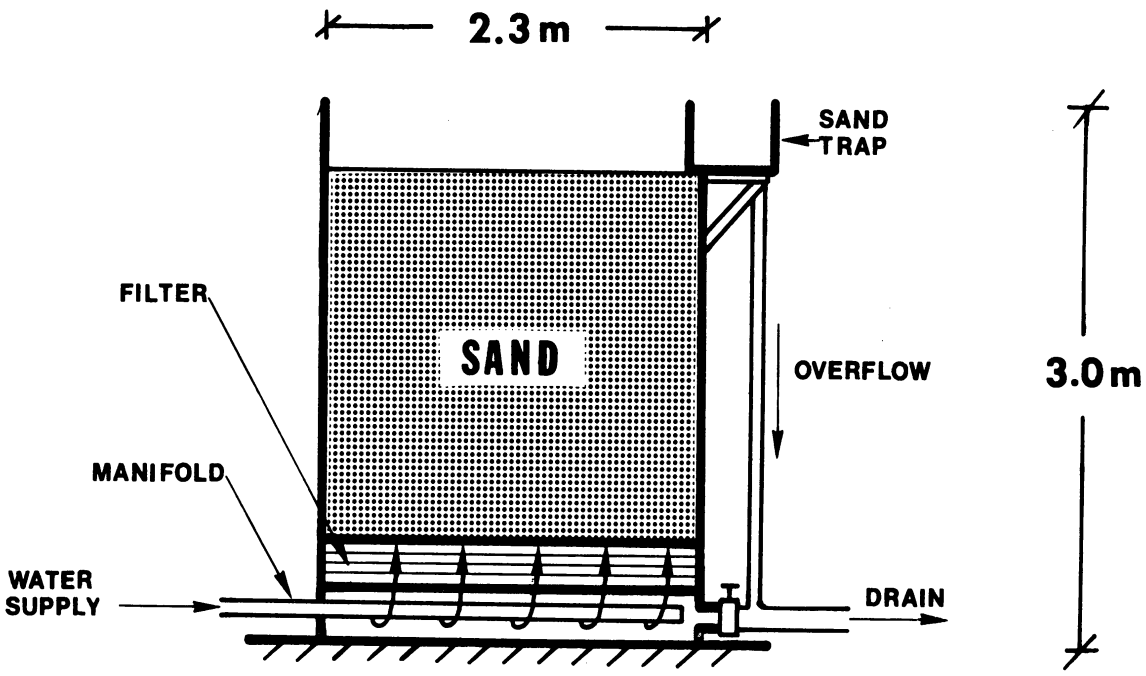

Fig. 7.3: Schematic Diagram of Quicksand Tank.

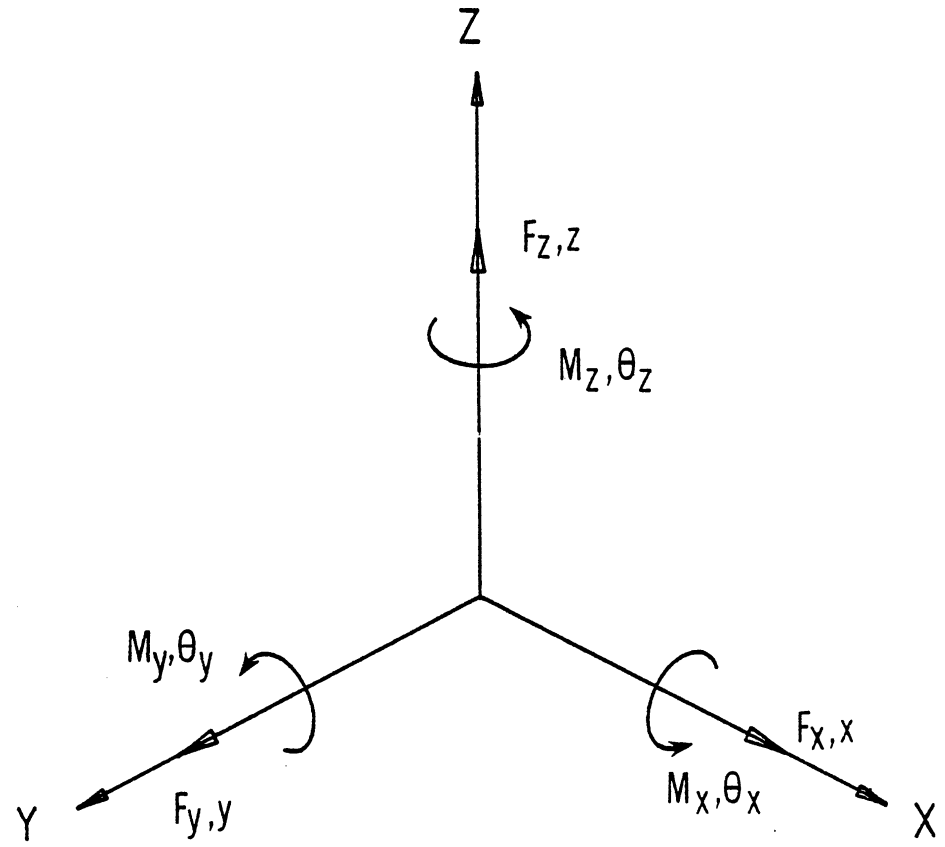

Fig. 7.10: Possible Components of Load and Motion: x, y, z = Translational Components, θ_x, θ_y, θ_z = Rotational Components, F_x, F_y, F_z = Force Components and M_x, M_y, M_z = Moment Components.

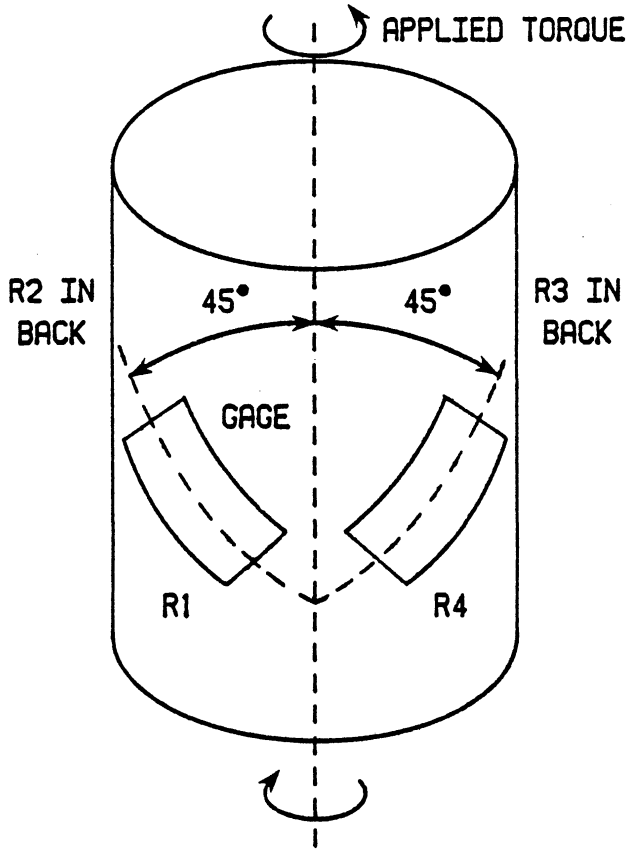

(a) Arrangement of Gages

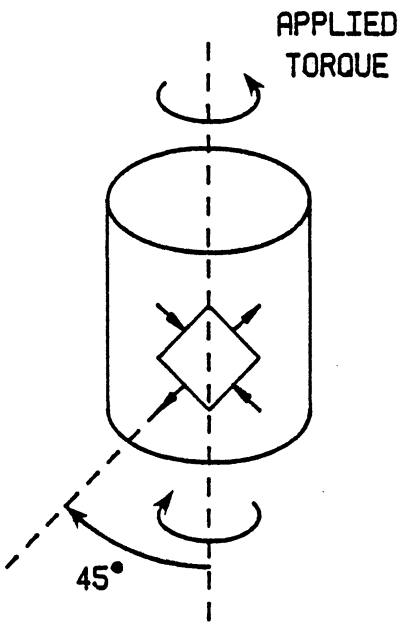

(b) Principal State of Strain in Cylinder Subjected to Pure Torque

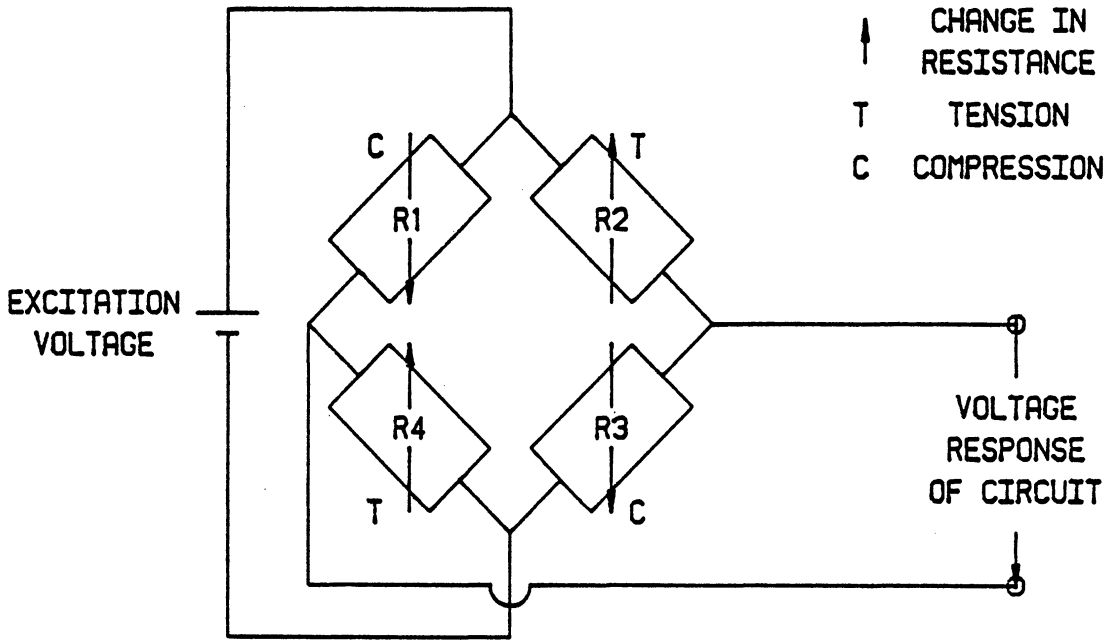

(c) Bridge Circuit Indicating Response of Gages and Circuit to Loading Shown in Fig. 7.11(a).

Fig. 7.11: Aspects of Torsional Load Cell.

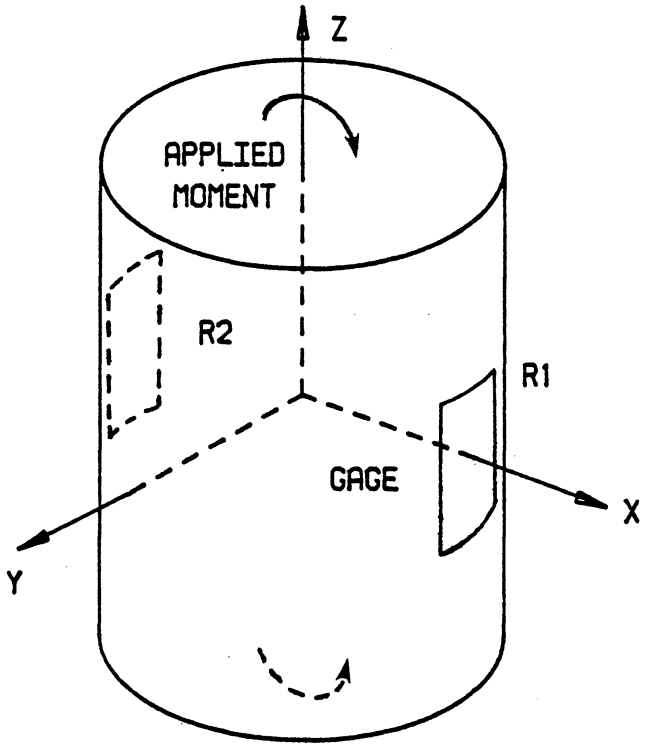

(a) Arrangement of Gages.

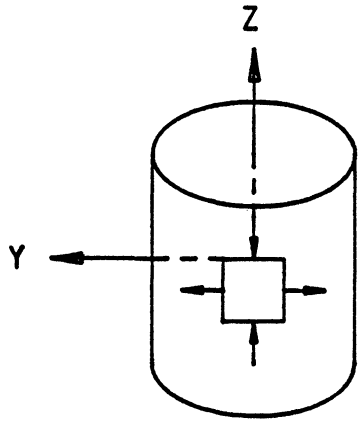

(b) Principal State of Strain Associated with Bending in x-z Plane.

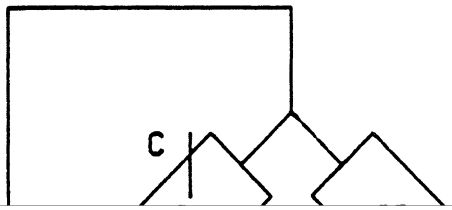

CHANGE IN RESISTANCE

T TENSION

C COMPRESSION

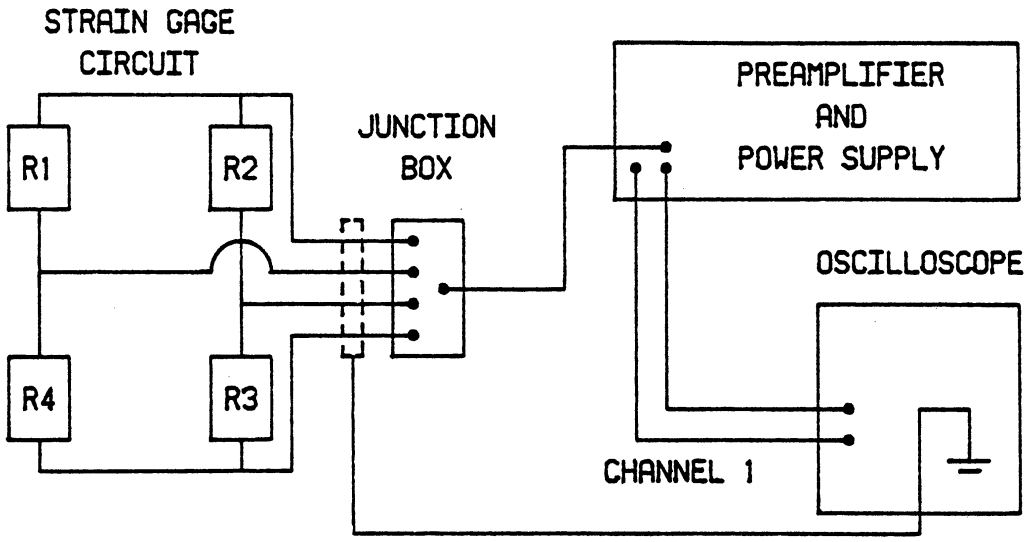

Fig. 7.13: Torsion Measuring System.

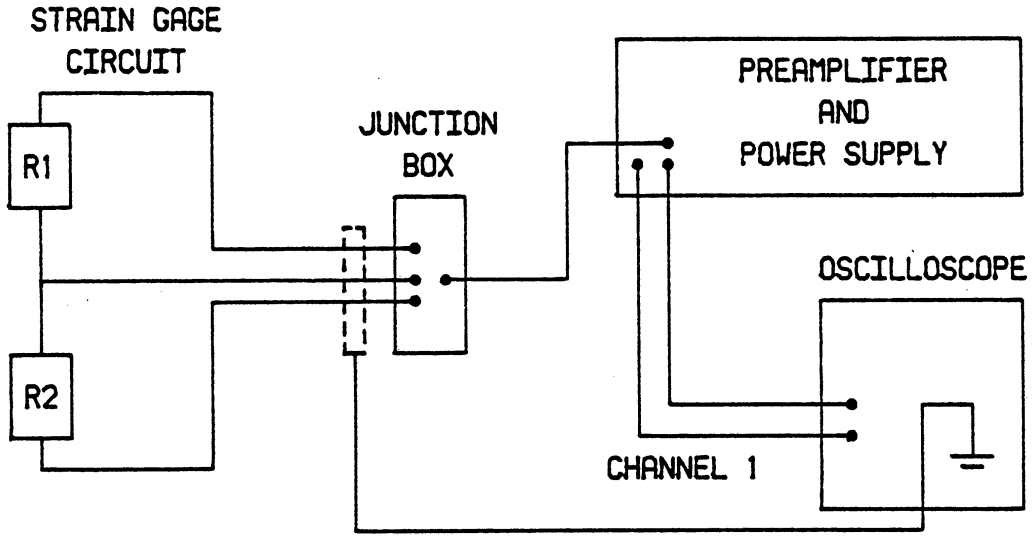

Fig. 7.14: Bending Measuring System.

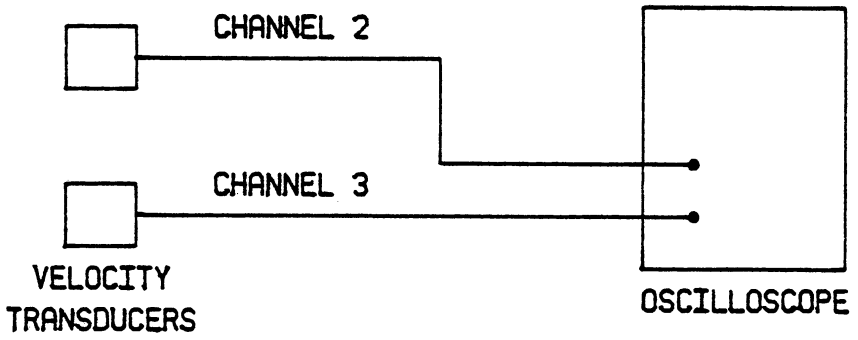

Fig. 7.15: System for Measuring Velocities of Footing.

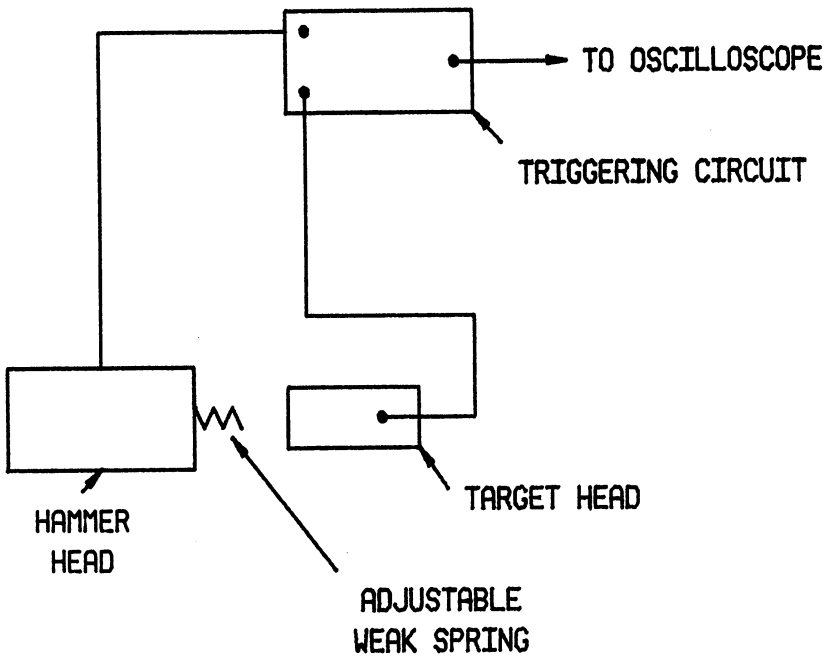

Fig. 7.16: Components and Circuitry of Pre-Impact Triggering System.

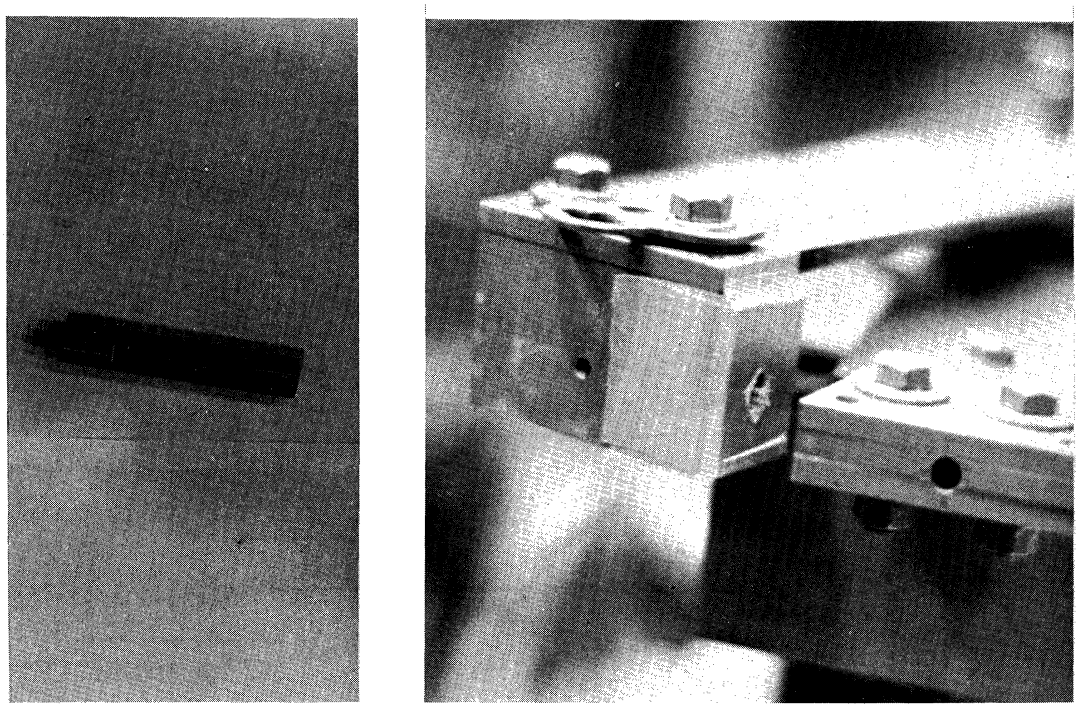

(a) Brass Rod with Spring.

(b) Brass Rod Positioned in Hammer Head.

Fig. 7.17: Components of Pre-Impact Triggering System.

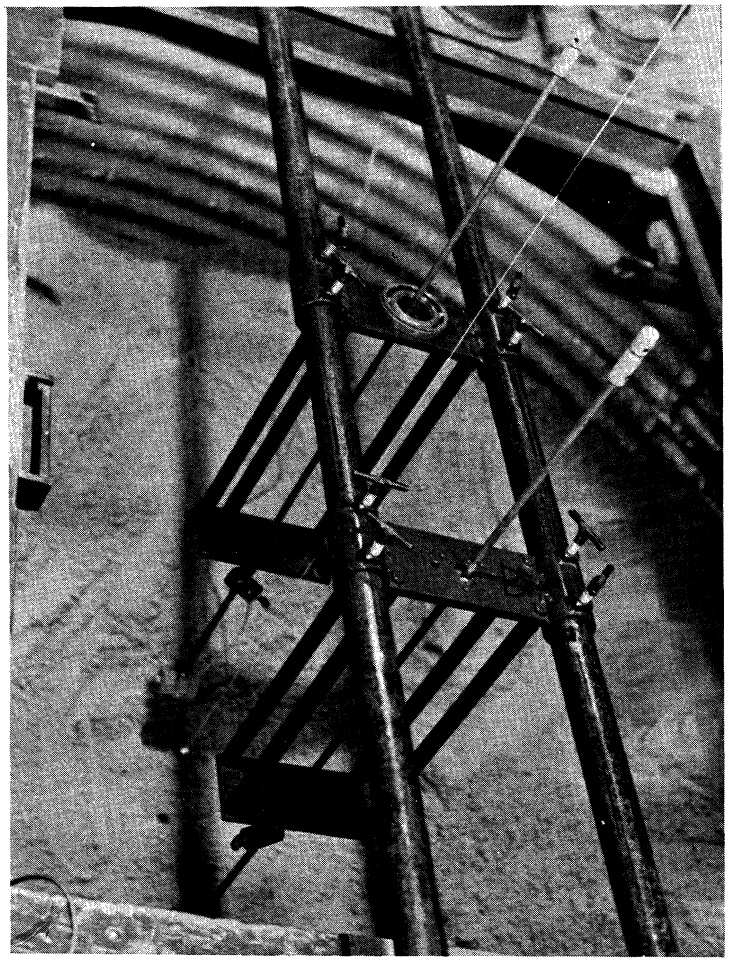

Fig. 7.18: System for Suspending Velocity Transducers within Test Bed.

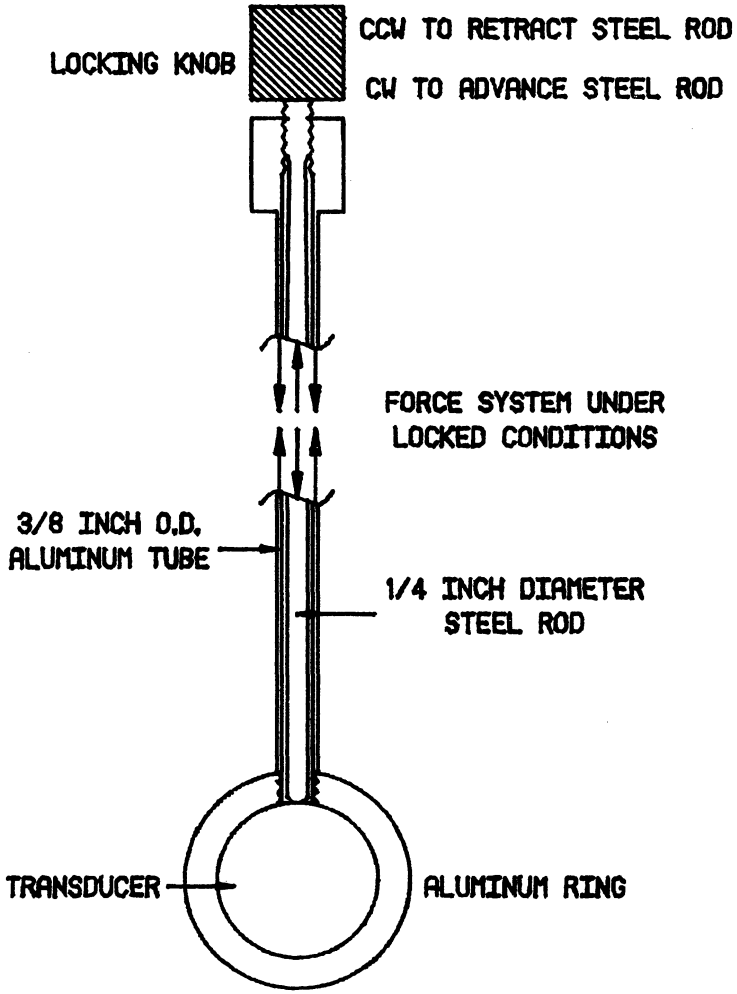

Fig. 7.19: Velocity Transducer and Suspending Rod.

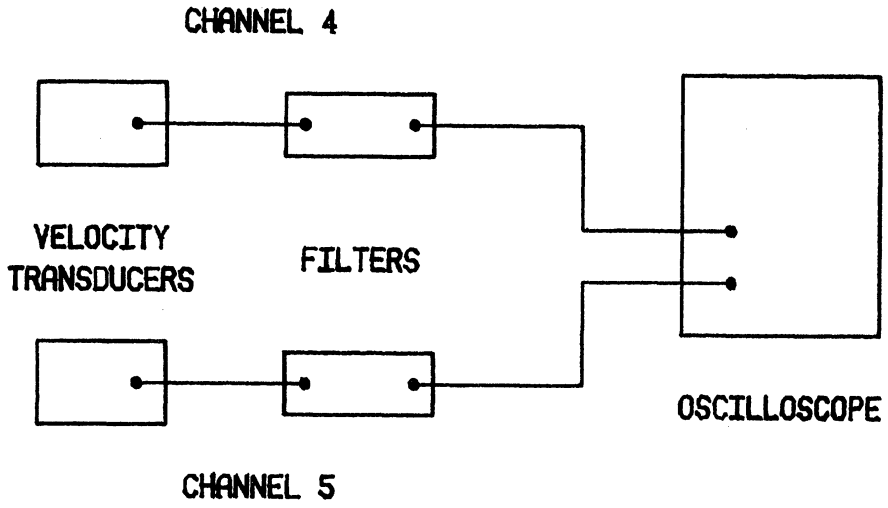

Fig. 7.20: System for Measuring Particle Velocities within Half Space.

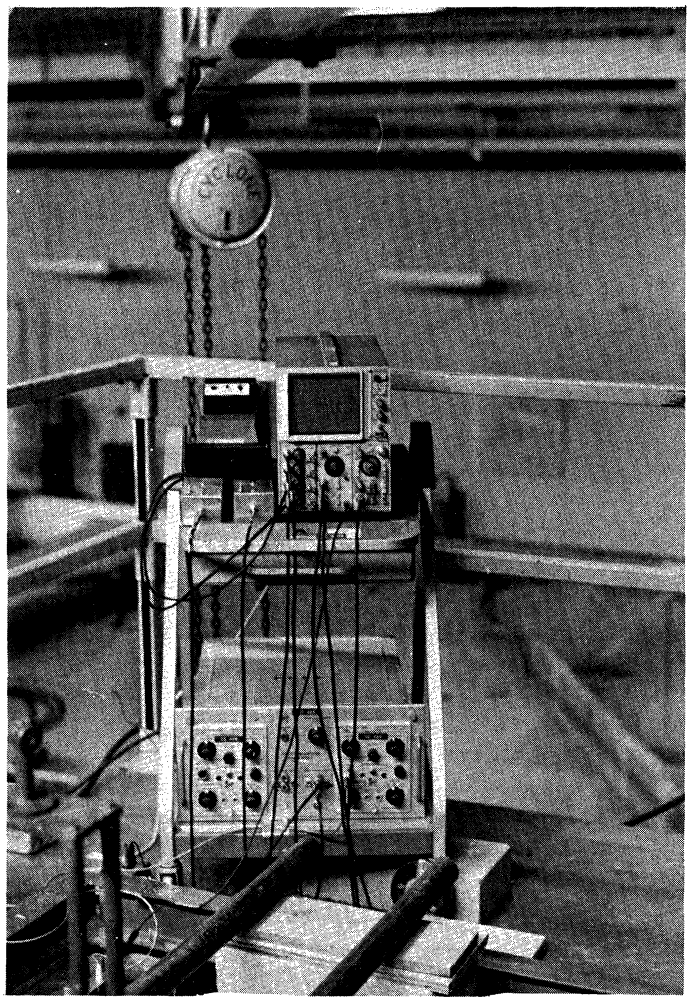

Fig. 7.21: Components of Measuring System Used for Dynamic Model Footing Tests.

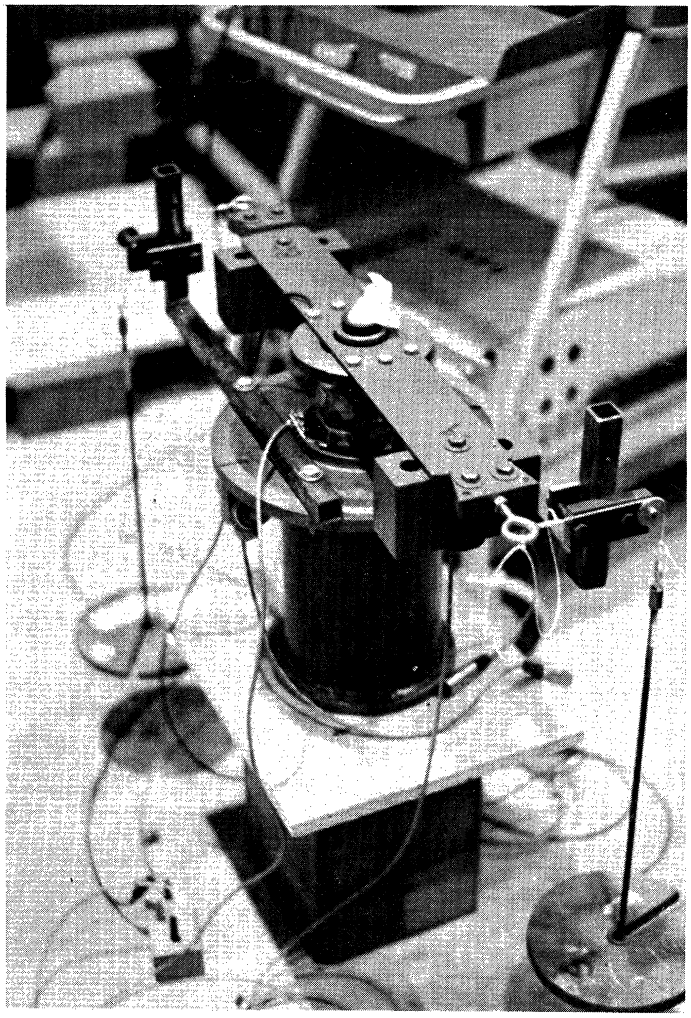

Fig. 7.22: Loading System Used for Calibration of Torsional Load Cell.

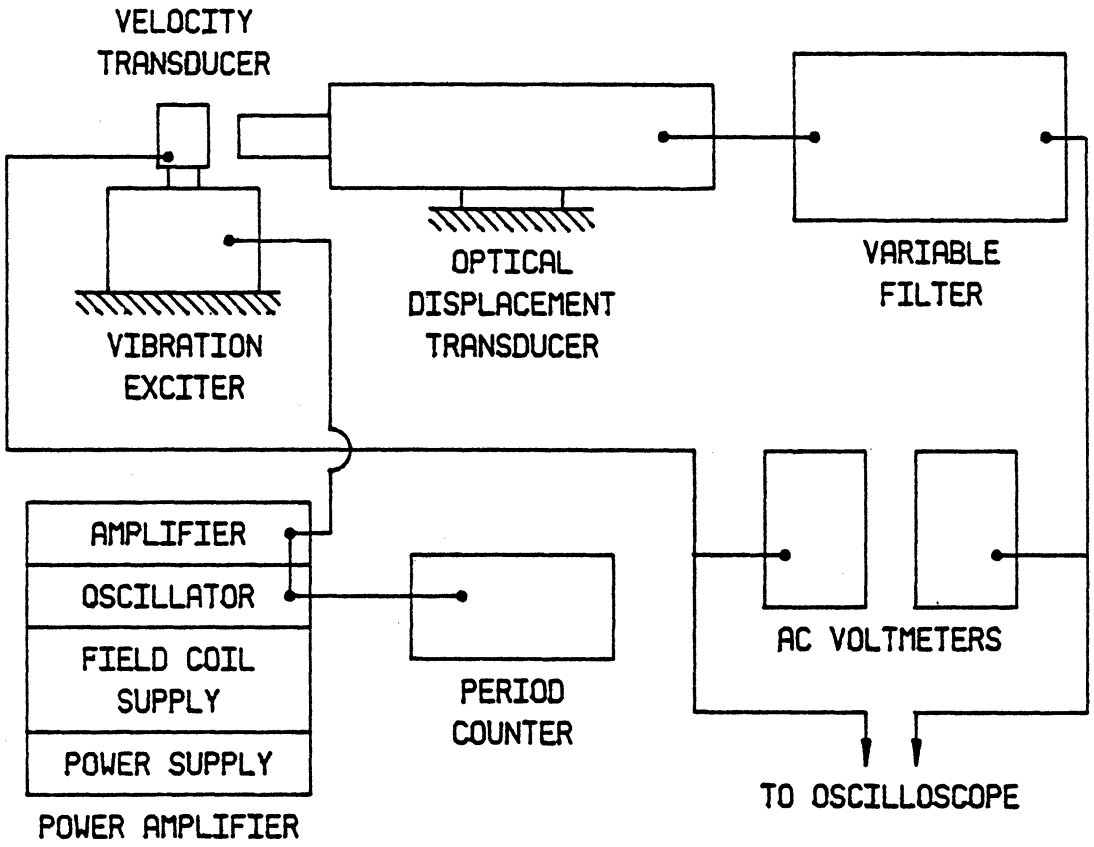

Fig. 7.23: Equipment and Circuitry Used for Calibrations of Velocity Transducers.

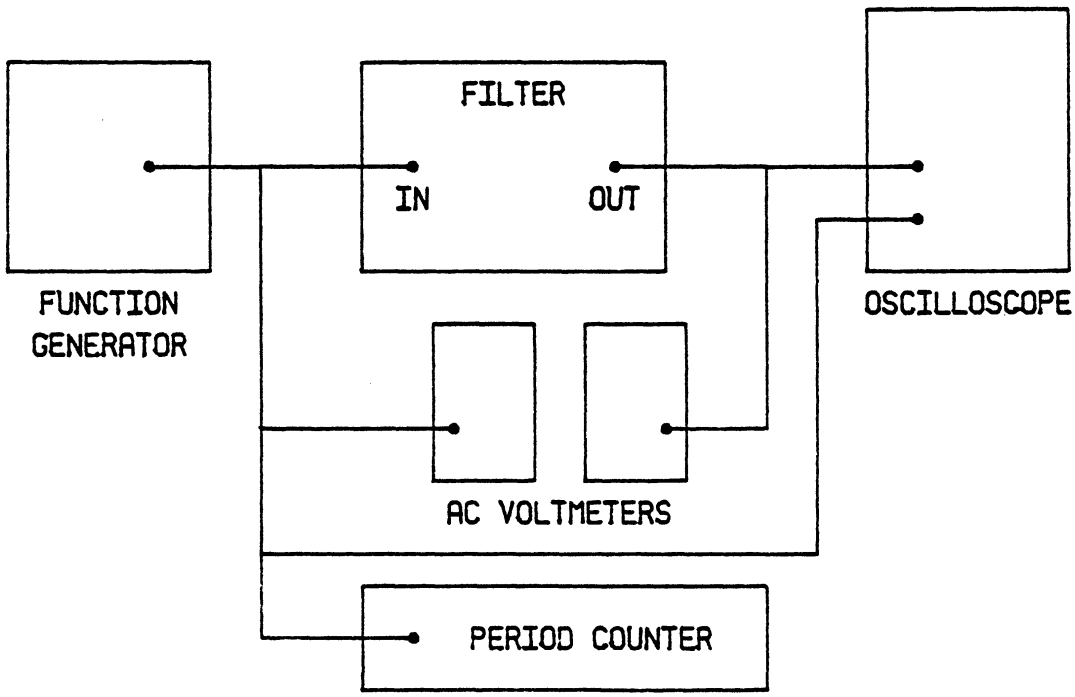

Fig. 7.24: Equipment and Circuitry Used for Filter Tests.

Fig. 7.25: Inner Tube Surrounding Central Access Hole.

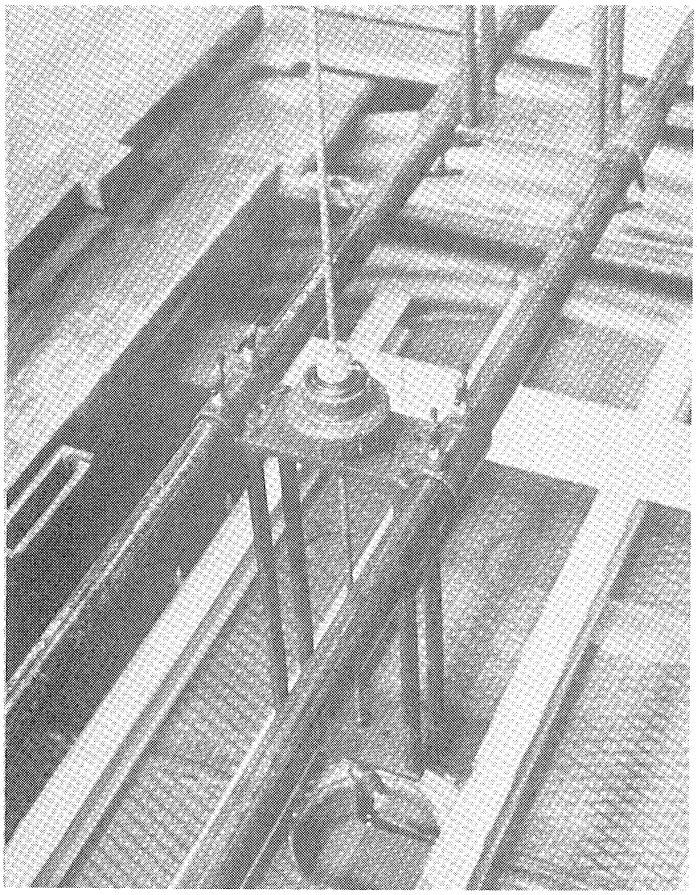

Fig. 7.26: Device Used for Scraping Test Area.

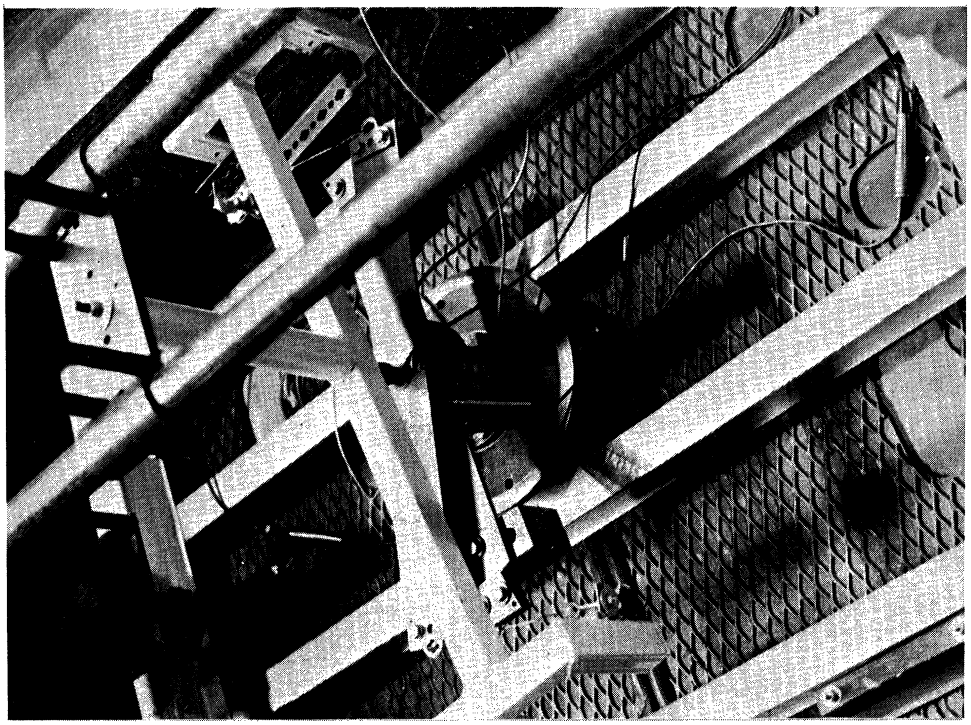

Fig. 7.28: Frame for Controlling Impact.

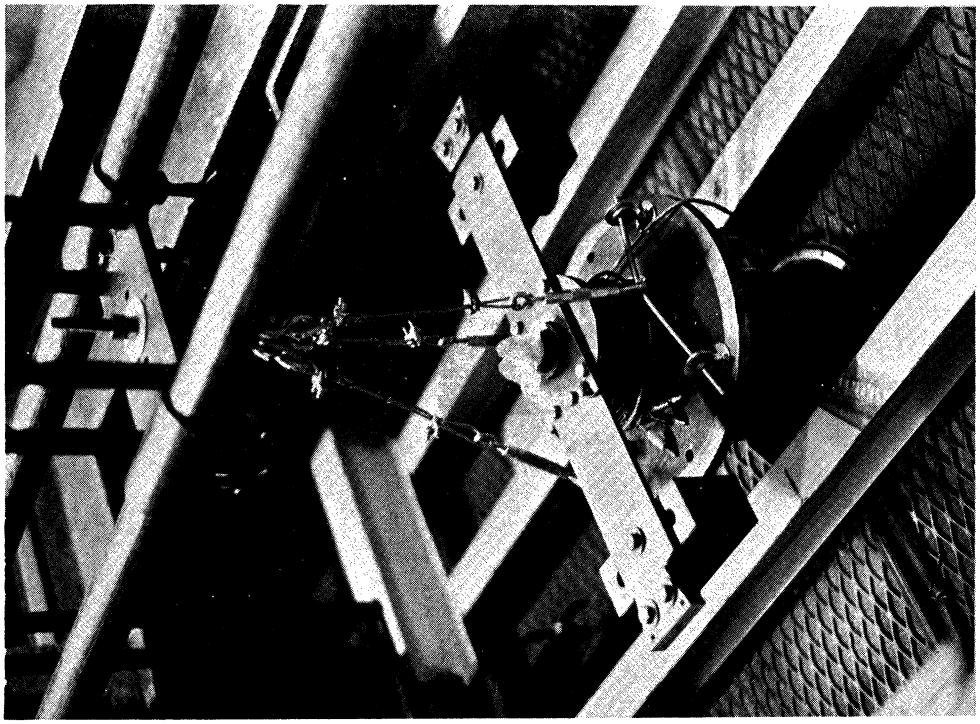

Fig. 7.27: System for Suspending Footing.

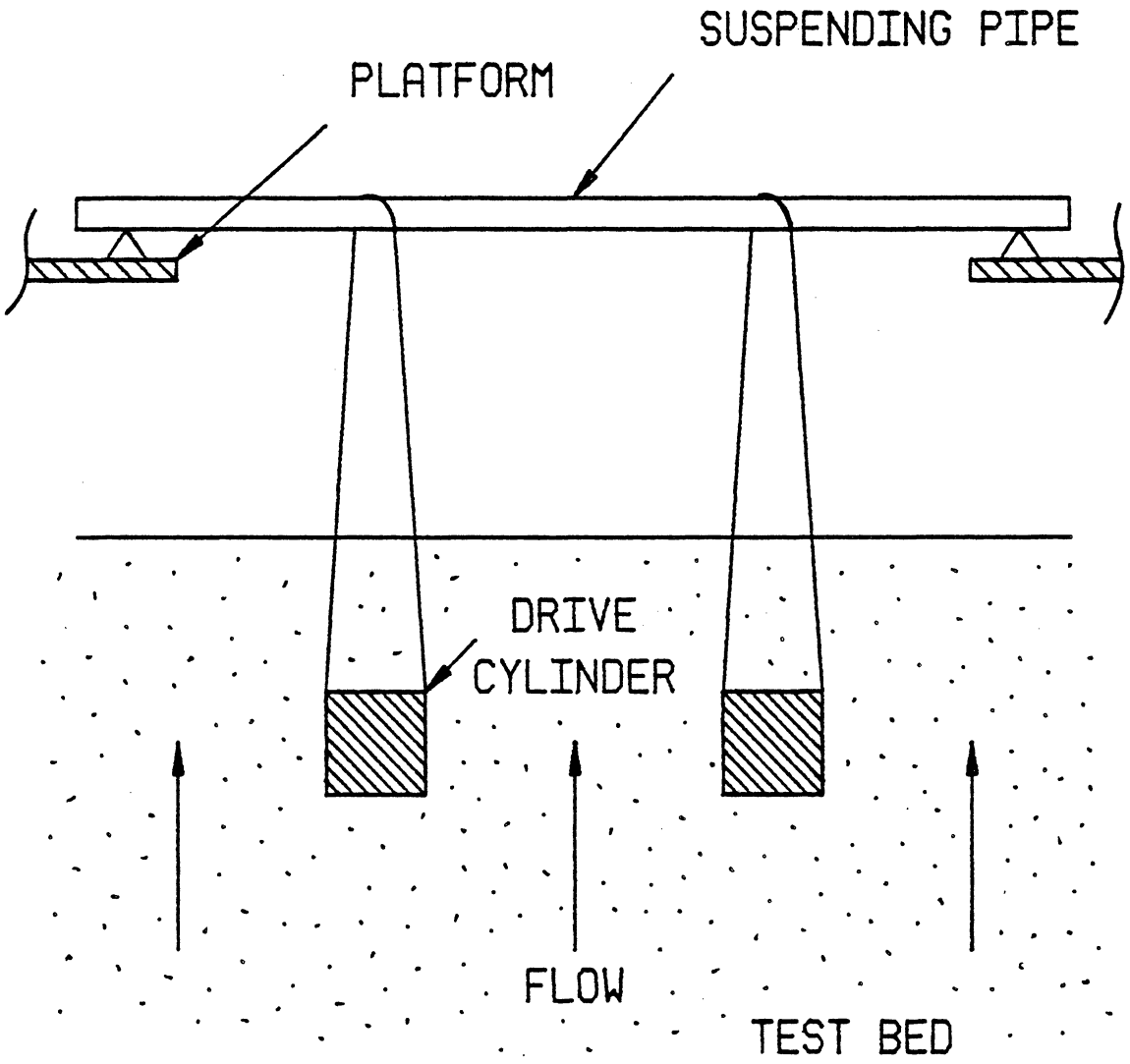

Fig. 7.29: Schematic Diagram of Set up for Density and Void Ratio Tests Conducted in Quicksand Tank.

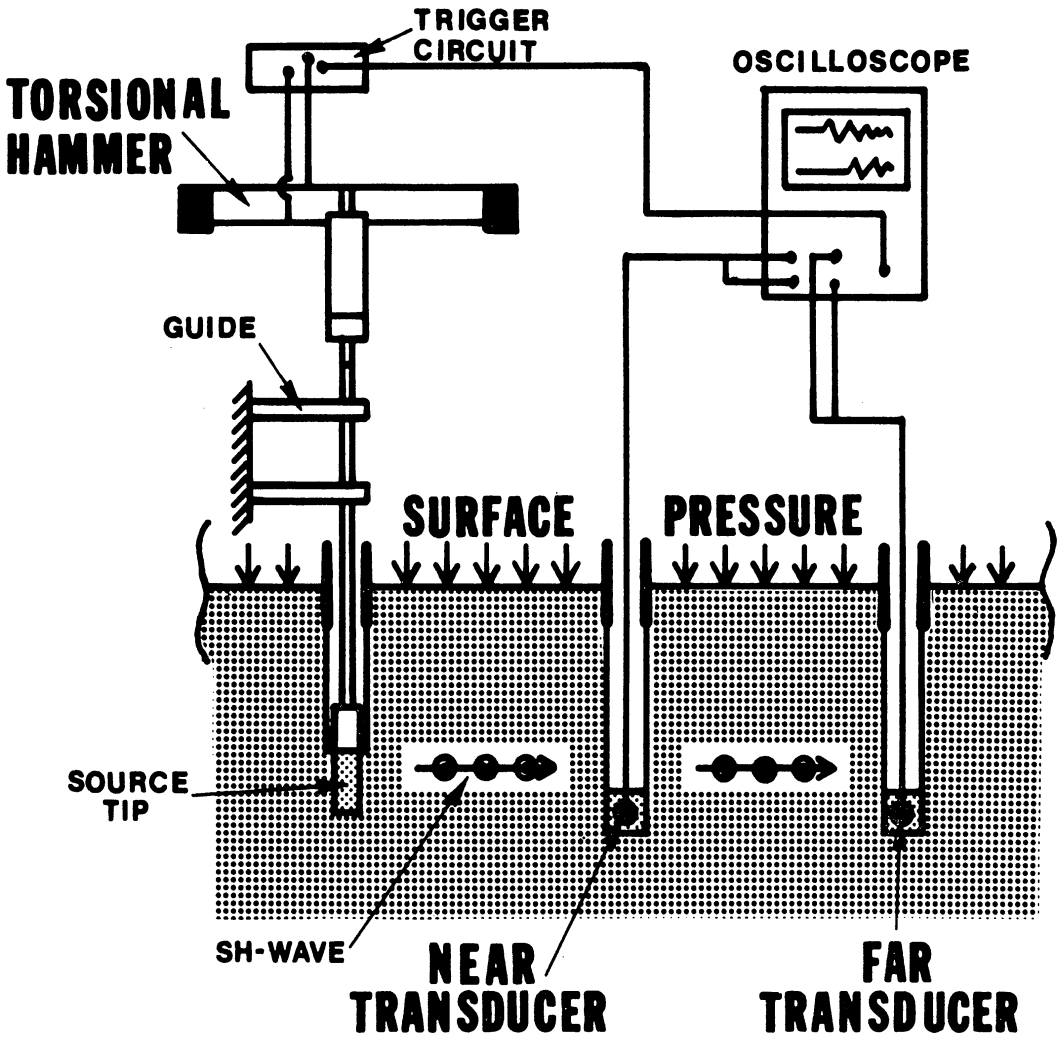

Fig. 7.30: Schematic Diagram of Set Up for Torsional Seismic Crosshole Tests Conducted in Quicksand Tank.

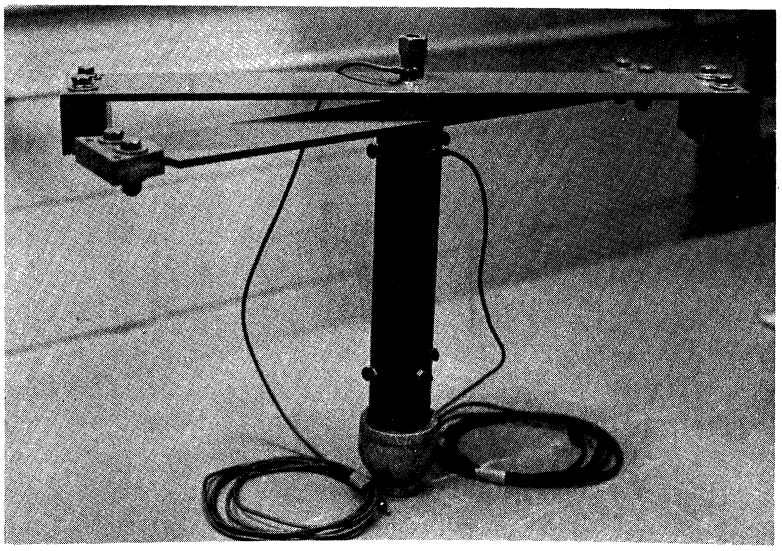

Fig. 7.31: Torsional Hammer Used for Torsional Seismic Crosshole Tests.

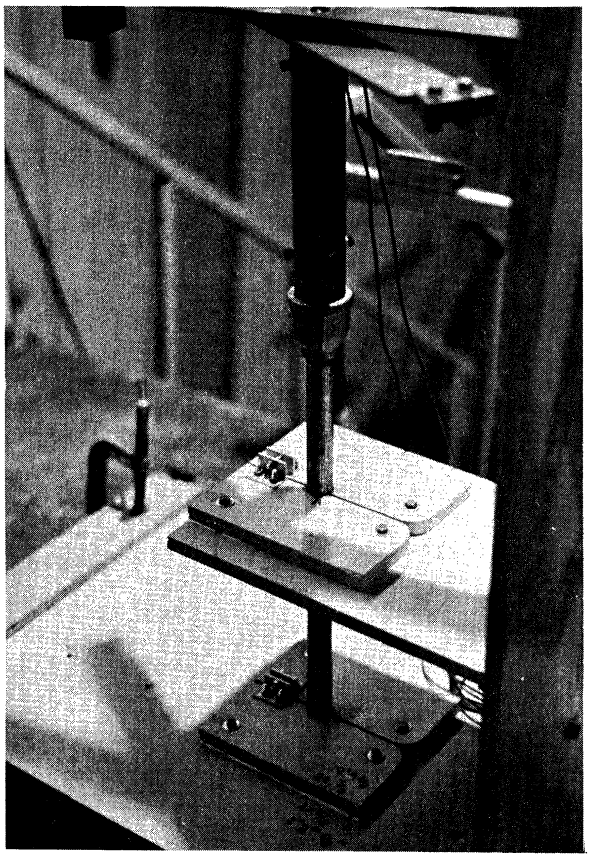

Fig. 7.32: Guide for Torsional Source.

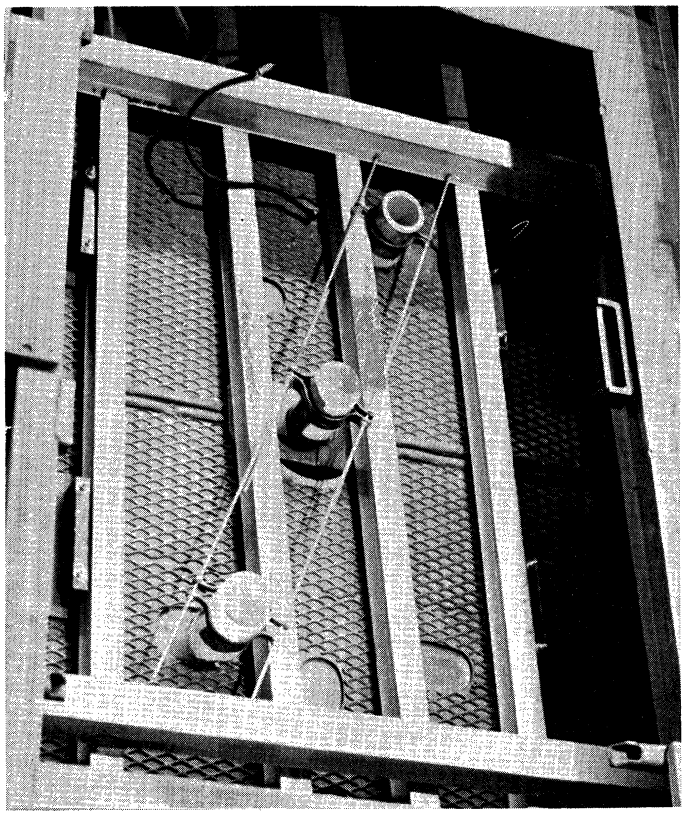

Fig. 7.33: Surcharge Pressure System as Adapted for Torsional Seismic Crosshole Test.

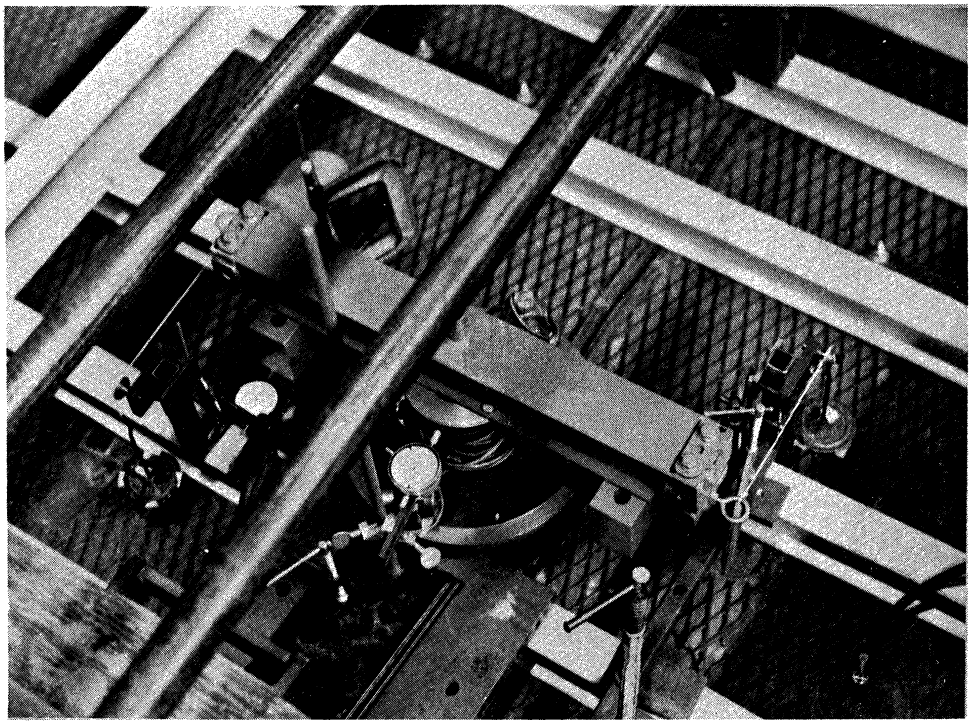

Fig. 7.34: Equipment Set Up for Static Torsional Loading Test.

CHAPTER VIII

TEST PROCEDURES

A. Introduction

In this chapter, the procedures which were used to carry out each test are described. These procedures include preparation of the test bed, evaluation of the properties of the test bed, and those related to the dynamic model footing tests. Techniques of processing data obtained from various tests are also presented.

B. Preparation of Test Bed

During the preparation of the test bed the rate of upward flow through quicksand tank was slowly changed by increments to allow equilibrium to develop at each flow level. This was done to maintain uniform flow conditions needed to provide a test bed having a uniform void ratio. For repeatability in the preparation of the test bed, it was necessary to establish a set preparation procedure. This involved finding the optimum maximum flow rate, the time needed to develop this flow rate, and the time needed to stop the flow. After each preparation, the overall void ratio of the test bed was

checked for consistency by measuring the depth to the sand surface of all corners and midedges of the rectangular platform opening of the quicksand tank.

C. Evaluation of Properties of Test Bed

1. Density, Void Ratio

The in-situ density was obtained by suspending leveled drive cylinders within the liquefied test bed at the locations shown in Fig. 8.1. The flow was allowed to reach a state of equilibrium with these cylinders in place, after which the flow rate was reduced and reversed. After the tank had been drained, the suspending lines were cut and the soil surrounding the drive cylinders was excavated very carefully to expose each buried cylinder. Each cylinder was supported carefully by hand and a thin wire was looped around the soil beneath the base of each cylinder. To separate the cylinder and its contents from the supporting soil, the loop was contracted slowly using a sawing action. Following separation the sample was quickly, but very carefully, trimmed and placed into a reasonably airtight container. Weights and water contents were taken immediately.

2. Low Amplitude Shear Modulus

a. Test Procedures--The shear wave velocities within the test bed were evaluated by torsional seismic cross hole tests for a sequence of surcharge pressures. The test bed was first prepared by liquefaction, then the surcharge pressure system was installed as described in Appendix III.

At each testing depth crosshole tests were conducted for each pressure of the selected sequence of surcharge pressures. To maintain consistent water contents, prior to preparing for tests at each depth, the water level within the tank was raised slowly to the depth at which the preceding test was conducted, and then drained, leaving the sand in a partially saturated state.

Immediately following drainage, the boreholes for the transducers were augered vertically to depth using a three inch diameter hand auger. In order to develop adequate coupling between the Shelby tube (See Chapter VII, Section G.2.a) and the sand a precise borehole of minimum diameter was needed for the source. Such a borehole was excavated by use of the fully assembled source appropriately positioned in its guide. This excavation was taken to a depth which provided a six

inch embedment of the Shelby tube. In order to determine accurately the spacings between boreholes, plumblines were lowered to the center of the base of each borehole. Spacing measurements were then made at the surface between these centered plumblines.

The transducers were checked for identical polarity of response and the suspending rods were attached to the transducers. To enable the alignment of each transducer from the surface, a straight rod was clamped perpendicular to each suspending rod and in a direction parallel to the sensing axis of the transducer. Taut horizontal strings intersecting the centerlines of the boreholes functioned as alignment references along the surface. The alignment of each transducer centered in the base of each borehole was carried out by squaring the clamped alignment rod with the taut string. Then, to improve the coupling between the transducers and the test bed, the boreholes were refilled partially with sand to bury the transducers. The added sand was tamped lightly from the surface using a long, flat-ended rod.

The entire source assembly was relocated above the appropriate borehole and the guide for the source was firmly clamped to its support. To minimize the sensing of compressional waves, the target arm was

oriented in the direction of the transducers and then the source was forced carefully to the testing depth.

To begin testing, the surcharge pressure was slowly brought to the desired level. Throughout testing, each change in the surcharge pressure was followed by a 15 minute time delay to permit readjustment of the soil grains to the new load. After this period, the pressure in each air bag was rechecked. To conduct a test, a torsional impact was delivered manually with an amplitude large enough to give an adequate signal-to-noise ratio in the voltage response of the transducers yet insufficient to cause excessive disturbance to the soil. Tests were conducted using various settings of the oscilloscope, and records thought to be useful in the reduction of data were photographed for later analysis. This procedure was carried out for each surcharge pressure.

b. Data Reduction--To obtain the reported results, it was assumed that the shear waves traveled along horizontal paths between the two transducers. The shear wave velocity was computed by dividing the spacing between the transducers by the travel time of the disturbance between the transducers as determined from test records. As illustrated in Fig. 8.2, this travel

time is the difference in time between common points on the waveforms obtained from each transducer. For greatest accuracy, most computations were based upon records obtained at the maximum sweep rate. Records obtained at low sweep rates were generally used to assist in interpretations.

Reflections from the surface of the test bed and compression waves caused random shifts in the peaks of the waveforms. To reduce the effects of these shifts, wave velocities were obtained for as many distinct wave-points from a given pair of records as possible prior to the arrival time of reflections from the walls of the quicksand tank. The shear wave velocity reported for a particular surcharge pressure-depth combination was the average of all of the velocities obtained for this combination.

3. Shearing Strength

To determine the shearing strength at the surface of the test bed by a static torsional loading test, the test bed was prepared, the surcharge system was installed, and the footing was placed in the manner described for the dynamic footing tests. The loading and displacement measuring systems were attached to the I-beam grid. During preliminary testing this grid was

found to displace significantly in response to changes in the surcharge pressure. Therefore, to maintain the alignments of the loading and measuring systems it was important to apply the test pressures to the air bags immediately prior to carrying out alignment procedures. Then, the dial gages, the pulleys, and the eyebolts attached to the target arms were adjusted or aligned to give the desired arrangement of gages and system of forces. The distance between the forces of this system was measured.

Prior to testing, the water level within the quicksand tank was raised slowly to the surface of the sand and then the tank was drained. In order to minimize disturbances to the gages, it was necessary to avoid excessive contact with the grid. For this purpose, the track-frame system was adapted to support the investigator during testing. With this system in position the pressures in the air bags were rechecked and all gages were zeroed. Load was applied incrementally by placing simultaneously on each hanger a matched weight from each of the balanced sets. To permit the sand grains to readjust to a new load, a time delay of several minutes was imposed between loads. Loading was carried out to a level at which nearly unrestrained

rotation occurred, a condition indicated by large responses and rates of responses of the dial gages.

D. Tests Related to Dynamic Model Footing Tests

In the following sections, procedures are given for tests which were conducted in a separate lab in preparation for the dynamic model footing tests. In each of the tests, the appropriate electronic instruments were warmed up for one hour prior to testing.

1. Calibrations of Load Cells

Calibrations of each load cell were similar, and with noted exceptions the following procedure applied generally. The footing was leveled and appropriate loading systems were assembled. For the calibration of the torsional load cell, the components of the loading system including the pulleys, the supporting arms of the pulleys, and the eyebolts attached to the target arm were adjusted or aligned to give the desired system of forces. Then the lengths of appropriate moment arms were measured.

The required electronic equipment was connected using the same cables which were to be used for the dynamic footing tests. The preamplifier was set to an amplification of 50 microstrain/div, the maximum sensitivity for which the preamplifier operated in the

linear range for the loading ranges of interest. With the footing fully unloaded, the capacitance and resistance of the bridge circuit of the load cell were balanced. The calibration was carried out by applying incrementally and then removing the weights from a selected sequence of weights. The calibration of the torsional load cell required the simultaneous application or removal of two matched weights from two matched sets of a selected sequence of weights. At each loading level, the voltage response of the load cell was recorded.

2. Filter Tests

The variable filter was set at preselected upper and lower cutoff frequencies. Each filter was tested using the procedure described in Chapter VII, Section E.3. In addition, the display of the oscilloscope was photographed when testing filters for which phase shift characteristics were needed.

3. Calibrations of Velocity Transducers

To insure that the variable filter performed as originally set, the characteristics of this filter were spot checked at several frequencies and amplitudes. The connecting cables used with the velocity transducers were those which were to be used in the dynamic footing

tests. All structural bolts of importance were checked for tightness.

A static calibration factor of the Optron was needed to analyze the data. This factor was obtained by imposing a static displacement on the Optron relative to the target and measuring the voltage response of the Optron. This procedure was repeated over a range of displacements. The dynamic calibration was then carried out as described in Chapter VII, Section E.2. The voltage waveforms from the Optron and velocity transducers were inspected, and if found acceptable, the rms values of these waveforms were recorded.

4. Preliminary Dynamic Model Footing Tests

First, preliminary dynamic model footing tests were conducted to obtain the optimum rotational response of the footing. For this the horizontal angle between the hammer and target arms was adjusted. To determine the effect of an adjustment, an impact was delivered manually at a selected amplitude and the responses of the velocity transducers mounted on the footing were displayed. These responses were inspected and served as the basis for readjustments of this angle. This procedure was repeated until improvements were no longer observed. To further improve response, the resilience

of the impacting surfaces of the hammer heads was changed until, again, improvements were no longer observed.

Then the magnitudes of the unwanted components of load and motion were checked. To measure related components simultaneously appropriate load cells were connected to the measuring circuitry, and appropriate arrangements of the velocity transducers were assembled on the footing. Dynamic footing tests were conducted and the excitation and response were recorded. The footing was adjusted as needed.

E. Dynamic Model Footing Tests

Preparations for the dynamic model footing tests, and procedures for performing these tests and for processing results from these tests are described in the following sections.

1. Placement of Velocity Transducers Within Test Bed

Velocity transducers were placed within the test bed by first excavating a trench of sufficient dimensions to expose the sites of these transducers. Then the vertical centerline of the test bed was determined using a plumbline. The system for suspending the transducers within the test bed (see Fig. 7.18) was aligned,

leveled and centered on the test centerline. The velocity transducers were positioned carefully at the correct depths and horizontal radii from the centerline of the test bed. Each transducer was oriented with its sensing axis perpendicular to its horizontal radius. All fasteners and clamps were rechecked, as were all measurements, and the trench was refilled carefully with the excavated sand, avoiding disturbances to the transducers and the supporting frame.

The test bed was liquefied, and after draining the tank partially, with the suspending system as shown in Fig. 8.3, the rods suspending the transducers were unclamped from the suspending frame and unlocked from the transducers. Each rod was unscrewed carefully from each transducer ring and removed carefully from the soil, minimizing disturbances. The remaining holes were refilled with sand.

In order to maintain the reference used to place the transducers, prior to disassembly, the position of the track-frame system and the relative positions of all its components were marked. This permitted the reassembly of the system to its original state. Following the disassembly of this system the surcharge pressure system was installed as described in Appendix III.

2. Leveling of Test Area

The test area exposed by the central access hole was leveled using the track-frame system adapted to support the scraper as shown in Fig. 7.26. The edge of the scraping blade was adjusted to sweep out a plane surface on rotation. After shimming the track ends to give a horizontal scraped plane and aligning the axis of rotation of the scraper with the centerline of the test bed the blade was lowered to the surface of the sand. In order to prevent excessive disturbance to the sand caused by scraping, the water in the tank was raised to a level sufficient to eliminate capillary tension at the surface. Scraping was carried out by repeated careful rotation of the blade and fine lowering of the blade until sand had been collected over the entire length of the blade. Then the water level was lowered slightly to allow capillary tension to redevelop, and using a putty knife, sand clinging to the blade was removed carefully. This procedure was repeated until the entire test area was horizontal at the desired level. During this process a mound of unleveled soil surrounding the scraped area developed. With the soil under the influence of capillary tension, this mound was removed carefully using a putty knife.

3. Placement of Footing

Prior to placing the footing, all assembly bolts of the footing were checked for proper torque and the velocity transducers were checked for tightness and orientation. Preliminary torsional impact tests were conducted to verify the satisfactory operation of the footing.

With the track-frame system appropriately assembled and positioned and with the footing suspended above the central access hole as shown in Fig. 7.27, the suspending cables were adjusted to level the footing. Using centralizing marks made on the I-beams during the installation of the surcharge pressure system, the footing was also centered on the centerline of the test bed. Then the footing was lowered slowly to the sand surface. During this process, the levelness and central alignment of the footing were frequently rechecked and readjusted as needed. After placing the footing, the pressure in the air bags was brought slowly up to test pressure.

4. Installation of Frame for Controlling Impact

The frame needed to control the impact delivered to the footing was installed as shown in Fig. 7.28. Large changes in surcharge pressure caused relative

displacements between the footing and this frame. These displacements affected the alignment of the springs attached between this frame and the hammer heads of the footing. In order to minimize misalignments, the pressure in the air bags was checked, and if necessary, brought to test level before alignment procedures were carried out. With the springs equidistant from the centerline of the footing, each spring was aligned properly and then adjusted equally to provide a very small pretension.

5. Connection of Electronic Components

The electronic components needed for the dynamic model footing tests were connected and cables leading from the footing were routed so as not to exert significant restraining forces on the footing during its motion.

6. Miscellaneous Procedures

Immediately prior to conducting the model footing tests, the water level in the quicksand tank was raised slowly above the surface of the sand, and then the tank was drained. Pressures within all air bags were checked and corrected if necessary. The depth of the upper plate of the footing relative to the track-frame system was measured carefully at several locations

as a reference from which to detect settlement of the footing. The drive springs attached to the hammer head were rechecked for equality in the pretension, and the pre-impact triggering device was adjusted to insure an adequate recording lead time preceding impact. All oscilloscope settings were checked after which the bridge circuit of the load cell was balanced.

7. Dynamic Model Footing Tests

Dynamic model footing tests were performed by separating the hammer heads from the target heads by a preselected distance and then releasing the hammer. The information sensed during the resulting transient motion was displayed on the oscilloscope, and if judged to be adequate, this display was photographed for later analysis. Throughout scheduled testing, the levelness and permanent settlement of the footing were checked carefully.

8. Measurement of Positions of Velocity Transducers within Test Bed

The positions of the velocity transducers within the test bed relative to the base of the footing were measured accurately following the completion of testing. To obtain these measurements, the entire installation, excluding the transducers within the test bed, was

disassembled carefully, avoiding disturbances to the soil. Using the references marked during preparations for the tests, the track-frame system was reconstructed to its original pretest state. The sand surrounding the buried transducers was excavated carefully to expose these transducers and the depth, radial position and orientation of these transducers were remeasured.

9. Processing of Recorded Data

In order to process recorded information, first records were digitized and using appropriate calibration factors, the digitized records were converted to applied torque- and velocity-time histories. To facilitate processing, all digitized records were redefined on time scales having common increments by using linear interpolation. The two records giving the transverse velocities of the footing were converted to angular velocity records and then averaged.

Records giving filtered information needed additional processing to correct for the magnifications and phase shifts introduced by the filters. Techniques of Fourier analysis were applied to correct these records. As shown in Fig. 8.4, such a record was inverted and reversed to give a fictitious, odd periodic function having a period equal to twice the length of the record.

This function was decomposed into Fourier sine components using the following equations:

$$f(t) \cong \sum_{n=1}^{N} b_n \sin \frac{n\pi t}{T'} \qquad 7.1(a)$$

$$b_n = \frac{2}{T'} \int_0^{T'} f(t) \sin \frac{n\pi t}{T'} \, dt \qquad 7.1(b)$$

where f(t) = the approximate representation of the function

T' = the length of the record

n = the number of cycles of the n^{th} Fourier component contained in one period of the fictitious function

N = Maximum n used for the approximation

Integrations were carried out numerically using the trapezoidal rule, and for each record so processed, the quality of the Fourier approximation was tested by comparing the reconstructed unprocessed record with the original record.

The phase shift and amplification characteristics of the filters, which were obtained experimentally for discrete values of frequency, were represented as continuous functions of frequency in a piecewise linear fashion. Each Fourier component of each fictitious function, was phase shifted and amplified an amount determined by the frequency of the component and

the characteristics of the relevant filter. Then these modified components were added giving the final processed record.

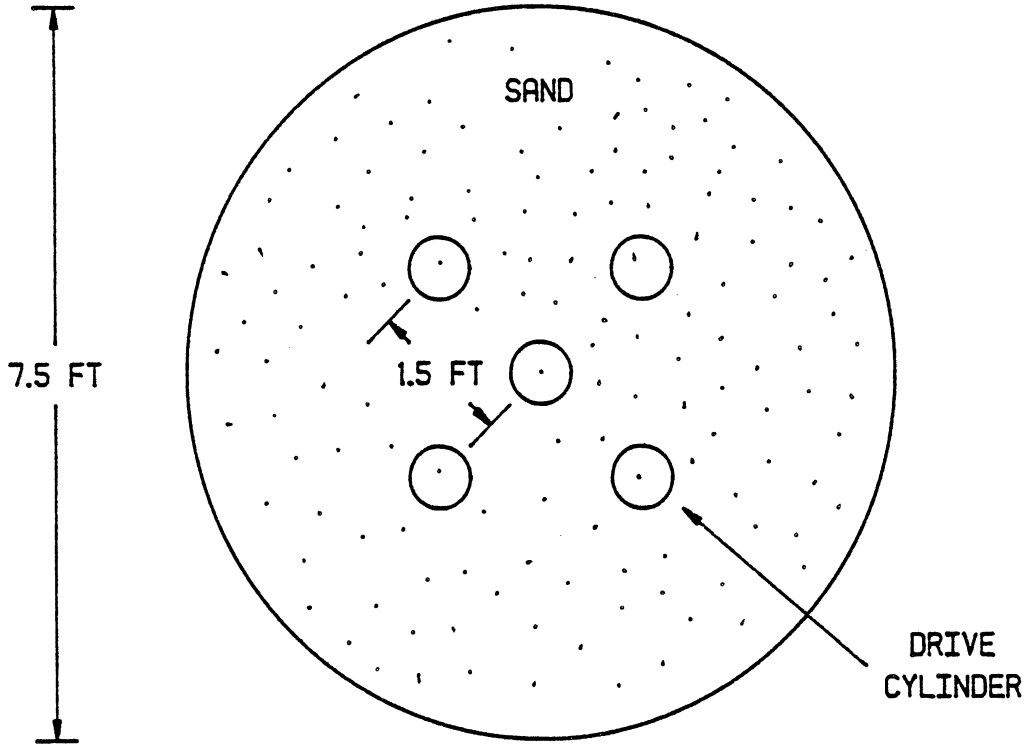

Fig. 8.1: Plan View of Quicksand Tank Showing Locations of Drive Cylinders.

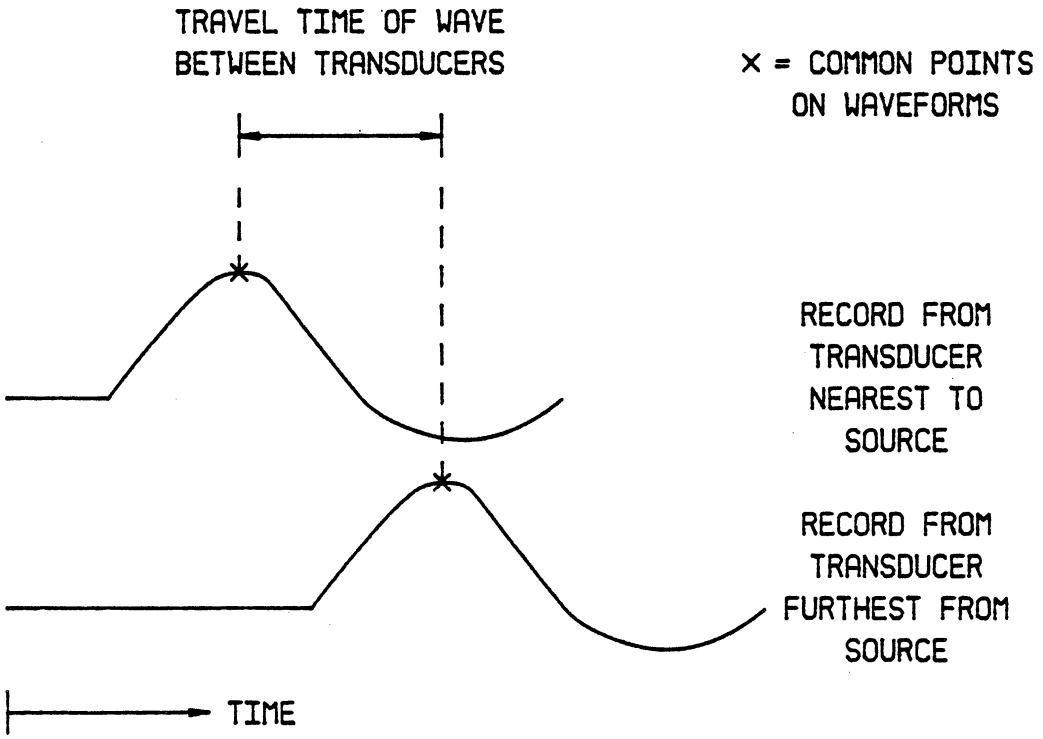

Fig. 8.2: Schematic Diagram of Records from a Torsional Seismic Crosshole Test.

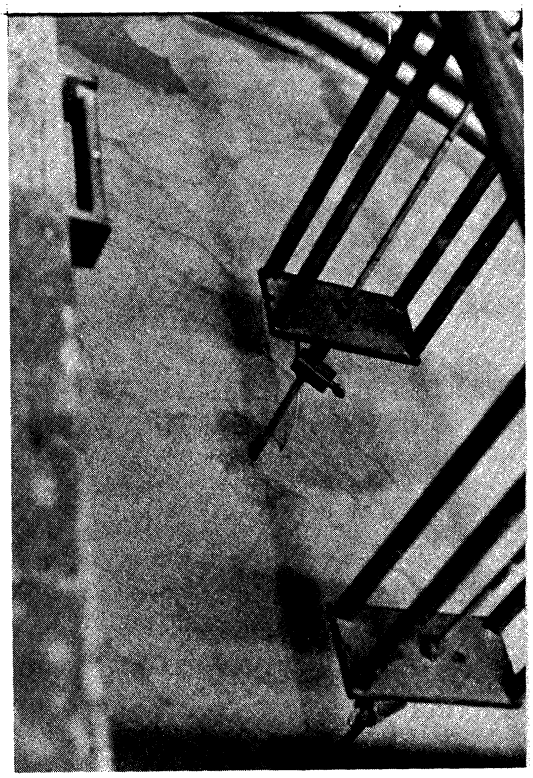

Fig. 8.3: Velocity Transducers Suspended within Test Bed Following Drainage of Tank.

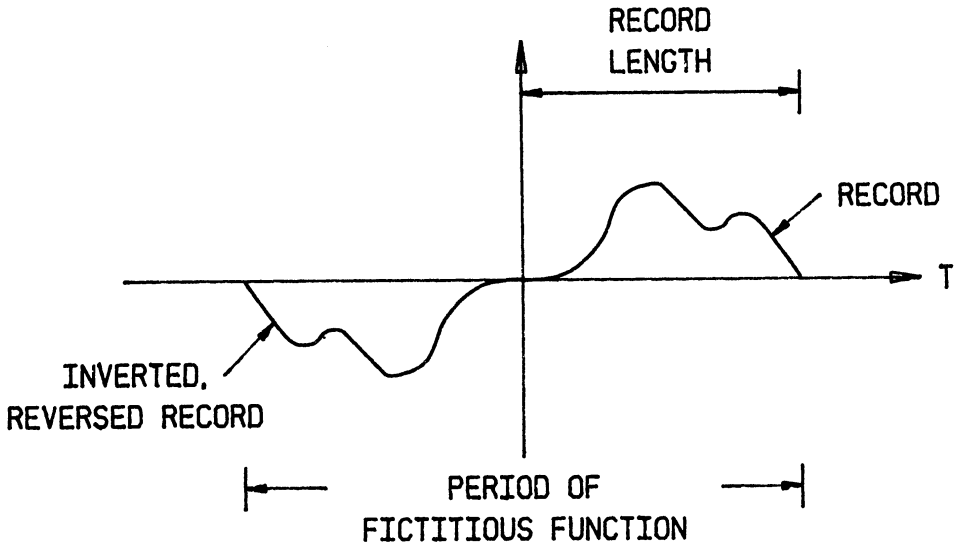

Fig. 8.4: Fictitious Odd Periodic Function Based on Velocity Record.

CHAPTER IX

EXPERIMENTAL RESULTS, SAMPLE CALCULATIONS AND DISCUSSIONS

A. Introduction

In this chapter, experimental results and sample calculations are presented and discussed.

B. Properties of Test Bed

1. Density, Void Ratio

The density and the void ratio of the test bed, as well as other related properties, were based upon results from 6 tests, in which a total of 12 drive cylinders were suspended within the test bed. These tests were conducted only after a repeatable technique of preparing the test bed had been developed and proficiency at sampling had been achieved. Because of difficulties in obtaining samples at greater depth, cylinders were suspended only at depths of 6 and 12 inches. It is, however, the properties near the surface which have the greatest effect on the dynamic response of a shallow footing.

Test results, presented as averages in Table 9.1, covered a broad range. Relative densities varied from 4.3 to 60.9% and from 21.7 to 65.2% at depths of 6 and 12 inches, respectively. One source of this scatter was nonuniformity in the void ratio of the test bed caused by sand currents and boils which developed during the preparation of the test bed. These disturbances were most intense directly above the inlet of the manifold and the lowest values of relative density were found directly above the opposite end of the manifold. Thus, this nonuniformity in the flow was believed to have been caused primarily by the manner in which the manifold distributed flow.

A second major factor causing scatter in the results and giving an apparent nonuniformity was thought to be the sampling process. The process used can cause nonuniformities within as well as amongst the samples. These nonuniformities develop as a result of the tilting of cylinders and friction along the walls of the cylinders. During liquefaction, the flow within a tilted cylinder is nonuniform leading to nonuniform void ratios within the cylinder. During deposition, friction along the wall of a cylinder restrains the displacements of particles near the wall but not near the center line.

The overall volume of the test bed, as indicated by the average height of the surface of the sand measured after each preparation, was quite consistent. Amongst the 6 tests conducted, this height was found to vary by no more than 1/4 inch.

The observed nonuniformities of the test bed, whether real or apparent, did not appear to have a large adverse effect on the quality or repeatability of dynamic model footing tests.

2. Low Amplitude Shear Moduli

a. Results from Tests -- The shear wave velocities within the test bed were obtained by conducting torsional seismic crosshole tests for the following sequence of surcharge pressures: 5, 4, 3, 2, 1, 2, 3, 4, and 5 psi at depths of .5, 1, 2, 3, 4, and 5 feet.

A selection of records from tests conducted at each depth for the surcharge pressures of 1, 3, and 5 psi is given in Figs. 9.1 (a), (b), and (c). In each of these records, the upper and lower traces give the responses of the transducer nearest to and furthest from the source, respectively. In Figs. 9.2 (a) and (b) are given examples of records obtained at a slower sweep rate than those of Fig. 9.1. In each of the records in

Fig. 9.2, traces 1 and 3 give records for one impact, and traces 2 and 4 give records for a second, successive, impact: a format which shows the reproducibility of results from the tests. The times at which the high amplitude portions of the records from the near and far transducers begin to differ in Fig. 9.2 (a) and (b) correlate with the arrival times of reflections from the wall of the quicksand tank.

As shown in Figs. 9.1 and 9.2, in most tests the response of the far transducer was similar to that of the near transducer. In some tests, however, there was a significant loss of high frequency information between the two transducers. This loss was most pronounced at low surcharge pressures and shallow depths. Thus this loss was believed to have been caused by the inability of the granular test bed to transmit high frequency disturbances at low levels of confining pressure. An extreme example of this behavior is given by the record in Fig. 9.1 (a) for the depth of 2 feet. Because the loss of information in this test was so large it was necessary to use a record obtained at a low sweep rate (Fig. 9.2 (a)) for assistance in interpretation.

In some tests, particularly these conducted at shallower depths, an initial low amplitude disturbance appeared in the record from the far transducer but not

in that from the near transducer. This disturbance, pointed out in Fig. 9.1 (b) in the records obtained from the depth of .5 feet, was thought to be caused primarily by reflections from the surface of the test bed and compression waves.

b. Reduction of Data -- To demonstrate the reduction of data, the results obtained from the records shown in Fig. 9.3 are presented in Table 9.2. As shown in Fig. 9.3, the wavepoints which were used to obtain results were the distinct peaks and troughs of the waveforms.

c. Results from Analysis -- Results from the entire analysis, along with statistical information are given in Table 9.3. Selected statistical results, taken from Table 9.3 are presented in Table 9.4 which gives, for each depth, the maximum and average ranges of shear wave velocities as percentages of the average shear wave velocities. These percentages are not large indicating that the technique used to obtain the reported average shear wave velocities was acceptable.

The total time of testing at a single depth was approximately 12 hours. Over this period of time, drainage, evaporation and the continual readjustments of grains to the surcharge pressures caused changes in the

elastic properties of the test bed. Table 9.5, which gives the profiles of shear wave velocity under the initial and final surcharge pressures, both 5 psi, shows that for each depth, the difference between the shear wave velocities in these two states was small. Thus, over the span of 12 hours the changes in the elastic properties of the test bed were small.

The curves of shear wave velocity vs. depth are presented in Fig. 9.4 for the pressures of the increasing portion of the sequence of surcharge pressures. Increases in the surcharge pressure caused increases in the shear wave velocity at all depths, however, these increases were largest near the upper surface of the test bed.

Waves refract toward zones of higher wave speed. In order to estimate the amount of refraction within the test bed to determine whether the curves in Fig. 9.4 needed to be corrected for this effect a simple method presented by Dobrin (1961) was used. This method assumes a linear variation in wave velocity with depth and gives circular ray paths. Based upon a bilinear approximation of the curve of shear wave velocity vs. depth for the surcharge pressure of 5 psi, refraction in the upward direction was found to be less than 3/4 inch, and therefore was neglected.

d. Theoretical Explanation of Results -- In a mass of cohesionless soil having a reasonably uniform void ratio, the shear wave velocity is primarily a function of the confining pressure. Therefore, the behavior observed in Fig. 9.4 may be accounted for largely in terms of the distribution of confining pressure within the test bed. An empirical expression giving the shear wave velocity as a function of void ratio and confining pressure, in a round-grained, cohesionless sand, in which the void ratio is less than 0.8, is given below as (Richart, Hall and Woods, 1970)

$$V_s\,(fps) = (170 - 78.2\,e)\,\bar{\sigma}_o^{\,.25}\,(psf) \qquad (9.1)$$

To explain the curves in Fig. 9.4, each of two simplified models describing one dimensional distributions of vertical stress were used to estimate the distribution of confining stress within the test bed. Each distribution of confining pressure was then introduced into Eq. (9.1) to obtain theoretical curves of shear wave velocity vs. depth for comparison with the experimental profiles.

In the first model, vertical stress is developed by combined gravity and surcharge loadings and the

corresponding distribution of confining pressure is given as

$$\bar{\sigma}_o = \left(\frac{1+2K}{3}\right)(\gamma z + p) \tag{9.2}$$

where p is the surcharge pressure, γ is the unit weight of the soil and K is the ratio of the lateral to the vertical normal stresses. In the second model, formulated by Terzaghi (1943), and suggested by Richart, the medium in which the stresses are developed is bounded laterally by the rigid wall of a cylinder having radius, R. In addition to gravity and surcharge loadings, this model takes into account shearing stresses developed along the wall in response to gravity and surcharge loadings. The magnitudes of these shearing stresses are determined by the Mohr-Coulomb failure theory and the local normal stresses acting on the wall. The distribution of vertical stress given by this theory for arching in a cohesionless soil is

$$\bar{\sigma}_v = \frac{R\gamma}{2K\tan\bar{\phi}}\left(1 - \epsilon^{-(2Kz/R)\tan\bar{\phi}}\right) + p\,\epsilon^{-(2Kz/R)\tan\bar{\phi}} \tag{9.3}$$

where $\bar{\phi}$ is the angle of internal friction of the soil and $\bar{\sigma}_v$ is the effective vertical stress. The confining pressure is related to $\bar{\sigma}_v$ by

$$\bar{\sigma}_o = \left(\frac{1+2K}{3}\right)\bar{\sigma}_v \qquad (9.4)$$

Relevant values of the properties of the test bed which were obtained experimentally include γ = 102.15 lb/ft3, e = 0.69 and $\bar{\Phi}$ = 32.5. The value of was based upon a series of drained triaxial tests. The value of K was assumed to be 0.4, the value used by Chon (1977) for the test bed at a relative density of 76%. Results were found to be insensitive qualitatively to a variation of K over a typical range: 0.4 to 0.6 in a cohesionless soil under at rest conditions.

The curves of shear wave velocity vs. depth based upon the two assumed stress distributions are shown in Figs. 9.5 and 9.6 for the surcharge pressures of 0, 1 and 5 psi, along with test results for the surcharge pressures of 1 and 5 psi. As shown in Fig. 9.5, the theoretical profiles based upon the Eq. (9.2) do not give good agreement with the experimental profiles. Shear wave velocities and normal stresses (Eq. 9.1) are overestimated at depth and underestimated near the upper surface of the test bed. As shown in

Fig. 9.6, the theoetical profiles based upon the stress distribution given by Eq. (9.3) give improved agreement with experimental profiles. Nevertheless, for the surcharge pressures of 1 and 5 psi, shear wave velocities are underestimated near the upper surface of the test bed and for the surcharge pressure of 5 psi, shear wave velocities are overestimated at depth.

In view of Eq. (9.1), the curves in Fig. 9.6 imply that, at least for the surcharge pressure of 5 psi, confining pressures near the surface of the test bed are underestimated and at depth, overestimated. Near the center of the upper surface of the test bed, where conditions are approximately one-dimensional, vertical stresses were believed to have been within the bounds given by the two theories. Thus differences between theoretical and experimental results at this location were believed to have been caused by underestimates of lateral stress.

Lateral stresses developed within the test bed depend on the lateral displacements of the flexible wall of the quicksand tank. Lateral displacements occurred because the upward load from the surcharge pressure was transmitted eccentrically to the wall of the tank and because this corrugated wall stretched in the vertical direction when the surcharge pressure was applied. The

lateral stress and the shear wave velocity which develop at a level within the test bed during the application of a given vertical stress will be larger if the tank contracts and smaller if the tank expands than if the wall remains rigid.

Using a dial indicater, the lateral displacements of the wall of the quicksand tank were measured along the West side of the wall during the crosshole tests. These rough measurements were obtained at both the crests and troughs of the corrugations. The net lateral displacements of the wall, estimated from these measurements, are given in Table 9.6 as a function of depth for the surcharge pressure of 5 psi. Above a depth of approximately 19 inches, the tank contracted. As argued, theory would be expected to underestimate shear wave velocity above this depth and as shown in Fig. 9.6, this does happen.

The larger lateral stresses associated with contraction also allow larger shearing stresses to develop along the wall near the surface of the test bed. This factor further restricts the effects of surcharge pressure to locations near the surface of the test bed. Neglecting this factor contributes to overestimates of the confining pressure and the shear wave velocity at depth.

e. Application of Results -- The experimental curves of shear wave velocity vs. depth were used to select the surcharge pressure which provided a test bed having the most favorable characteristics for the dynamic model footing tests (See Chapter VII, Section B). From an examination of Fig. 9.4, it was judged that the surcharge pressure of 2 psi gave the best soil properties, and this value was used for the footing tests.

3. Shearing Strength

a. Results from Test -- The results from the static torsional loading test are plotted in Fig. 9.7. This figure shows the moment applied to the footing vs. the angular displacement of the footing. The angular displacement was obtained by averaging the values of angular displacement obtained from each of th two transverse dial gages.

Two measures of the quality of such a test are the percentage difference between the readings of the two transverse displacement gages and the ratio between the average transverse displacement and the lateral displacement of the centerline of the footing. A small percentage difference and a large ratio indicate a high degree of pure rotation. The value of the percentage

difference at the maximum angle of rotation is 11 percent and that of the ratio is 67. The maximum torque obtained from the torsional loading test is 11.73 ft-lb.

b. Results from Analysis -- Given an applied moment and assuming a shape for the distribution of shearing stresses along the base of the footing, the amplitude of this shape may be computed using Eq. (4.32). This equation relates a distribution of shearing stresses to its resultant moment. To determine the shearing strength of the test bed at the surface, τ_{zm}, a uniform distribution of shearing stress (See Fig. 9.8) was assumed to be resisting the maximum experimentally applied moment, M_{max}. This distribution represents a fully plastic state and its amplitude, which is the shearing strength, may be evaluated from Eq. (4.32) giving

$$\tau_{zm} = \frac{3 M_{max}}{2\pi \bar{r}_o^3} \tag{9.6}$$

Substituting measured values for M_{max} and $\bar{r}_o$ into Eq. (9.6) gives $\tau_{zm} \cong 150$ psf (1.04 psi).

c. Discussion of Results -- This method for obtaining τ_{zm} is a approximate for a number of reasons. The assumption of a uniform distribution of shearing

stress at the maximum moment assumes a uniform distribution of contact pressure along the base of the footing and fully unrestrained rotation of the footing. Because, in this test, an unconfined ring approximately 1/2 inch in width surrounded the edge of the footing, the capacity of the sand to withstand normal stress was reduced in this zone. As a result, the contact pressure and shearing strength of the test bed were thought to be less at the edge than near the center of the footing. Although approached, a state of unrestrained rotation was not developed in the torsional loading test. Theoretically, the zone of the test bed near the center of the footing is the last zone to develop its shearing strength under rotation of the footing. Thus, if this rotation is less than maximum, full shearing resistance is not developed in this zone.

A probable distribution of shearing stress which takes these factors into account is sketched in Fig. 9.8 using a dashed line. By assuming a uniform distribution, the shearing strength of the test bed has been overestimated at the edge of the footing and underestimated elsewhere. In view of the small size of the unconfined gap and the close approach to unrestrained rotation, the degree of these approximations was believed to be small.

The estimate of shearing strength by static means neglects the dynamic effects of strain rate on the shearing strength of the test bed. These effects have been found to be small for dry sands (Richart, 1977) and the partially saturated test sand was assumed to behave similarly.

Despite these approximations, the torsional loading test does offer significant advantages over the readily available alternative of using the Mohr failure criterion in conjunction with results from triaxial tests to predict the shearing strength of the test bed. The torsional loading test simulates closely dynamic testing conditions. The equipment, loading, geometry, and environment of the dynamic footing tests, including the surcharge pressure, water content, and relative density are taken into account. The stressing of the test bed in the dynamic and static tests is similar and little interpretation is required to arrive at the shearing strength. In addition, the torsionsal loading test was considered to be a precisely prepared and conducted test and throughout testing, the geometry of the test bed changed by only very small amounts.

C. Tests Related To Dynamic Model Footing Tests

In the following sections, results and discussions are given for tests which were conducted in preparation for the dynamic model footing tests.

1. Calibrations of Load Cells

a. Calibrations -- Results obtained from the calibrations of the torsional load cell are given in Fig. 9.9. In this figure the applied torque vs. the voltage response of this load cell is plotted. The slight hysteresis present in this curve was believed to be caused by pulley friction. The calibration factor, which is the ratio of the applied moment to the voltage response, was obtained as the slope of a least squares fit to the data. Curves for the bending load cells were not hysteretic and calibration factors for these load cells were obtained directly and are listed in Table 9.7.

b. Supplementary Tests -- Supplementary tests were also conducted. The influence of the movement of various connecting cables on the calibration curves of the load cells was examined. Only the movement of the cables connecting the load cells to the junction box was found to affect the calibration curves and this effect was a zero shift. To obtain accurate

results it was therefore necessary to secure these cables during calibrations and dynamic footing tests.

To interpret properly output from the bending load cells it was necessary to determine the degree to which torsional loading of the footing excited these load cells. This interactive effect was found to be small.

2. Filter Tests

The characteristics of the variable filter were obtained using cutoff frequencies of 20 and 400 Hz. This range permitted the transmission of information of interest while blocking noise effectively. The characteristics of this filter were determined over the range of frequencies of 5 to 500 Hz which included both cutoff frequencies. The smallest voltage amplitude applied to the input of the filter, 40 mV, was limited by the triggering requirements of the period counter. The largest voltage amplitude, 2V, was selected as one which would exceed the maximum voltage generated by the optical displacement transducer during calibrations of the velocity transducers.

In Fig. 9.10, voltage magnification vs. frequency is plotted for the variable filter for each of

the limiting voltage amplitudes. The effects of voltage amplitude were found to be small.

The characteristics of the filters which were used in the dynamic model footing tests were also obtained for the range of voltage amplitudes of 40 mv to 2V. The latter value exceeded the maximum voltage which was expected to be developed by the velocity transducers in the footing tests. The range of frequencies over which characteristics were determined, 10 to 1750 Hz, was chosen to include all frequency components expected in the footing tests. A record used to demonstrate the evaluation of phase shift is given in Fig. 9.11.

In Fig. 9.12, voltage magnification and phase shift vs. frequency are plotted for one of the filters for the limiting voltage amplitudes. These curves indicated that the influence of voltage amplitude was small.

3. Calibrations of Velocity Transducers

The velocity transducers were calibrated over ranges of frequencies and amplitudes as large as 20 to 500 Hz and 0.0005 to 0.005 inches, respectively. Due to power limitations, the larger the amplitude imposed on the transducer, the smaller was the possible upper limit of the frequency range. The low end of the frequency range was determined by the frequency response of the

transducers. The low end of the amplitude range was limited by noise from the displacement transducer.

The calibration factor of a transducer was defined as the voltage response of the transducer per unit velocity. The results from the calibrations of one transducer are presented in Fig. 9.13 in which curves of calibration factor vs. frequency are plotted for several amplitudes. Curves were fitted to the somewhat scattered data by inspection and no trends were observed with amplitude. For each transducer an average calibration factor based on the regions of flat response was reported. If the results from tests conducted on the footing fell beyond the amplitude range of the calibrations, however, the calibration factor for the amplitude closest to the test amplitude was used.

4. Preliminary Dynamic Model Footing Tests

a. Adjustment of Footing -- Selected records from tests carried out to adjust the horizontal angle between the target and hammer arms are presented in Figs. 9.14 (a) and (b). Each photograph in Fig. 9.14 gives the response of the two velocity transducers attached to the footing, caused by a high amplitude impulse delivered to the footing. The response of these velocity transducers would be identical in shape,

amplitude and timing if the footing rotated about its vertical centerline.

The records shown in Fig. 9.14 (a) were obtained using an incompletely adjusted hammer with unpadded faces. These records differ considerably in shape and timing. Records from a similar test in which the hammer was well-adjusted are presented in Fig. 9.14 (b). In these records the shape of the waveforms and the initial timing are in reasonable agreement, however, the amplitudes do not compare well; initial peaks differ by 25%.

The records presented in Fig. 9.14 (c) show the further improvements and changes in response brought about the use of gum rubber pads attached to the impact faces of the hammer. Agreement on the shape and timing is good in these records and the amplitudes of the first peak are within 2% of one another.

b. Unwanted Components of Load and Motion -- Tests were also conducted to estimate the unwanted components of the load and motion, including bending in the y-z and x-z planes, rocking about the x- and y-axes and translation in the x-, y- and z-directions. The components of the motion were measured using the arrangements of transducers shown in Fig. 9.15. Records corresponding to a standard impulse test are given in

Fig. 9.16 (a). In this figure trace 1 gives the response of the torsional load cell and traces 2 and 3 give the responses of the velocity transducers as mounted to detect the rotation of the footing about its vertical centerline. Records from tests in which the amplitude of the impulse was similar to that in Fig. 9.16 (a) are given in Figs. 9.16 (b) and (c). These records show the loads and motions sensed by the arrangements shown in Figs. 9.15 (a) and (b) and are highly erratic. The amplitudes of these records were compared with those obtained from Fig. 9.16 (a). For this the percentages of the peak amplitudes of the unwanted components of load and motion with respect to the corresponding amplitudes of the peaks obtained from Fig. 9.16 (a) were calculated and are presented in Table 9 .8. Clearly, torque about the vertical axis was the dominant loading and rotation about this axis was the dominant response.

D. Dynamic Model Footing Tests

In the following sections, several topics related to the dynamic model footing tests described in the introduction to Chapter VII, are discussed, and the results from these tests are presented.

1. Arrays of Velocity Transducers

Four main dynamic model footing tests, designated G, H, I and J, were conducted. These tests differed primarily in the locations of the two velocity transducers within the test bed. The arrangements of the transducers corresponding to each of the main tests are shown in Fig. 9.17. In test G, the transducers were placed axisymmetrically. For each of tests H, I and J, the two transducers were placed in a linear array at an angle with the horizontal and intersecting the center of the base of the footing. However, to minimize interference with the propagating disturbance, as shown in Fig. 9.17, the transducers in each array line were arranged on opposite sides of the axis of symmetry.

For several reasons, the precise positions of these transducers relative to the base of the footing were unknown prior to testing. The location of the base of the footing depended upon the height of the sand in the test area after deposition and scraping. The initial positions of the transducers were altered by the weight of the soil and negative skin friction acting, after deposition, on the transducers and the suspending rods. Also, the transducers displaced downwards upon separation from the suspending rods. Because of these

factors, the coordinates of the transducers given in Fig. 9.17 were only nominal target values.

The positions of the transducers relative to the base of the footing, as measured carefully following each main test, are given in Table 9.9. These positions were reasonably close to the nominal positions in radius, depth and angular alignment.

2. Effects of Disturbances and Incomplete Seating

a. Discussion--In each of the main tests, a sequence of torsional impulse tests was conducted. These tests were classified as low amplitude tests which did not cause measurable permanent angular displacement of the footing, and high amplitude tests which did. The number of tests conducted in each category is given in Table 9.10.

Because of effects of stress history, void ratio changes, changes in the seating of the footing, and changes in residual stresses, even under identical impulses, the response of the footing will differ amongst the tests conducted in a sequence. In the numerical models of the experiment, these factors were not taken into account; therefore, it is necessary to demonstrate that the collective effect of these factors was small.

Stress history and changes in void ratio cause changes in the shearing stress-strain properties of granular materials. The effects of stress history are discussed by Richart, Hall and Woods, (1970). Changes in void ratio, which may accompany either vibration or the application of shearing stress, cause changes in stress-strain properties by affecting the low amplitude shear modulus and shearing strength of the material.

Residual stresses affect the state of stress within the soil and the buildup of τ_z-stresses along the interface during the motion of the footing. Residual stresses develop within the test bed as a result of slip at the interface and nonlinear inelasticity. To show the effects of slip the displacement of an originally undeformed radius,AB, in the soil at the interface, with and without slip is shown in Fig. 9.18. Without slip the soil along the interface does not deform; therefore, $\tau_r = 0$. Slip however, permits deformations of the type that cause τ_r-stresses. If, at any region undergoing slippage, the τ_z-stresses fall below the shearing strength, slip ceases. When slip ceases, deformations and τ_r-stresses existing at this time are locked in at the interface in this zone until further slip takes place.

To demonstrate the manner in which nonlinear inelasticity causes residual stresses, the condition without slip, shown in Fig. 9.18, is reconsidered. Assuming an undisturbed material, under rotation of the footing, the γ_z-strains and τ_z-stresses, and, therefore, the degree of nonlinear inelasticity along the interface are greater near the edge of the footing than near its center. Because of inelasticity, less reverse rotation of the footing is necessary to relieve the τ_z-stress at the outer edge of the footing than near the center. Since the footing is rigid and can have only one angle of rotation, in returning to a new equilibrium state, residual τ_z-stresses and γ_z-strains, develop along the interface. The distribution of these stresses will be such that equilibrium of moments about the vertical centerline of the footing is satisfied. Under subsequent reloading, the development of the distribution of τ_z-stresses along the interface will differ from that under the initial loading of the undisturbed soil.

Incomplete seating of the footing causes nonuniformities in the distribution of normal stresses along the interface and thus in the properties of the test bed near the interface. Incomplete seating may be caused by angular differences between the plane of the base of the footing and the surface of the test bed, and the

trapping of grains in unstable positions. Motion of the footing causes a repositioning of grains the degree of which depends upon the amplitude of the motion and this repositioning leads to improved seating. These changes, however, change locally the properties of the test bed.

It is difficult to avoid entirely the effects of incomplete seating and disturbances. To seat the footing completely, prior to testing, the interface must be preloaded in torsion. Such preloading, however, introduces the effects of disturbances. In the assembly of the test set-up and during testing, procedures were taken to provide adequate seating while minimizing the effects of disturbances. The test bed was leveled and the footing was placed very carefully to give good seating. The minimum number of tests needed to provide the necessary data were carried out. In addition, a testing program was followed in which the impulses either remained constant or increased in magnitude, thus avoiding excessive preloading.

Testing conditions were thought to be favorable for minimizing disturbances to the void ratio. The apparent cohesion of the test bed, caused by partial saturation, helped reduce densification induced by vibration. Over the span of each major test the accumulated settlement of the footing, which is a measure of

densification, was found to be within 1/32 inch, indicating that densification was small. The footing was also found to remain level during testing.

b. Evaluation of Effects -- To analyze the collective effects of disturbances and incomplete seating, an impulse having an amplitude which had never been exceeded, was delivered to the footing and the records of the loading and motion of the footing were stored. A selected number of unrecorded impulses of similar amplitude were delivered, followed by an impulse in which the results were again recorded. If the effects of incomplete seating and disturbances are large, then the differences between the two recorded responses would be large.

Records from such tests, in which the amplitudes of the impulses were large, are shown in Fig. 9.19. In this figure traces 1, 3 and 5 give the outputs from the load cell and the velocity transducers, respectively, for an initial impulse. Traces 2, 4 and 6 are the corresponding outputs for a final impulse. Figure 9.19 (a) gives the records from a first and second test conducted at a given amplitude. The differences in the degree of seating and the level of disturbance are greater between the first and the second tests conducted

at a given amplitude than between other successive tests conducted at the same amplitude. Thus differences in the response of the footing are expected to be greatest between these two tests. In Fig. 9.19 (a) corresponding records are similar in shape, amplitude and timing. Figure 9.19 (b) gives similar results for a second and a fifth test. The slight shift in the horizontal position between the records for these two tests was caused by differences in the triggering of the sweep. Also, the amplitude of the second impulse was slightly less than that of the fifth and this carried over to the records of the response. These records as well as other similar records indicate that the combined effects of seating and disturbance did not influence excessively the response of the footing.

3. Correction of Filtered Records

Tests were conducted to evaluate the quality of the numerical correction process applied to filtered output. A test was conducted in which information from the torsional load cell and unfiltered information from the velocity transducers within the test bed were recorded. Then a second, similar test was conducted in which the information from the transducers was filtered. The response from the second test was corrected

numerically and then compared with the response from the first test.

The records from such a test are presented in Fig. 9.20. Traces 1 and 2 give the records from the torsional load cell for two consecutive tests and both records are similar in shape, timing, and amplitude. The unfiltered responses of the transducers are given in traces 3 and 5, and the filtered responses in traces 4 and 6.

In Figs. 9.21 (a) and (b), the processed records and the digitized, unfiltered records corresponding to Fig. 9.20 are shown for comparison along with the digitized, unprocessed, filtered records. The Fourier series approximations of the unprocessed, filtered records are also shown as a check. In each figure, there is a small difference between the amplitudes of the processed, filtered curves and unfiltered curves which may be due partially to slight differences between the amplitudes of the impulses. The shape and timing of the processed, filtered curves shown in Figs. 9.21 (a) and (b) are in reasonable agreement with the shape and timing of the unfiltered curves.

4. Unwanted Components of Load and Motion

Tests similar to the tests described in Section C.4.b were conducted to measure the magnitudes of the unwanted bending loads developed under testing conditions in the quicksand tank. Records from such a test are presented in Fig. 9.22. In each photograph in Fig. 9.22, trace 1 gives the output of the indicated load cell and traces 2 and 3 give the outputs of the velocity transducers attached to the footing in the arrangement used to detect rotation about the vertical centerline. From these figures, it is clear that bending moments were an insignificant fraction of the torsional loading.

Unwanted components of motion were not measured for practical reasons. Since these components were found to be small in the preliminary tests and since the control over the preparation and performance of tests in the quicksand tank was much greater than in the preliminary tests, these components of motion were considered to be quite small.

5. Axisymmetry of Wavefield

The numerical model is axisymmetric; thus, for valid comparisons between numerical and experimental responses, experimental results must also be axisymmetric.

Test G was conducted to demonstrate the axisymmetry of the propagating wavefield. As illustrated in Fig. 9.17, in Test G, the transducers were placed symmetrically within the test bed. If the wavefield is axisymmetric then the response at the sites of these transducers will be identical.

A schematic diagram of the set up used in Test G and the records from two high amplitude tests, obtained at different sweep rates, are presented in Figs. 9.23 (c), (a), and (b), respectively. In each of Figs. 9.23 (a) and (b) trace 1 gives the output of the torsional load cell, traces 2 and 3 give the responses of the velocity transducers attached to the footing, and traces 4 and 5 give the unfiltered responses of the velocity transducers within the test bed. Clearly, the responses of the transducers within the test bed are very similar in shape, amplitude and timing.

6. Presentation of Results

a. Motion of Footing -- Records obtained from the dynamic model footing tests, using slow rates of sweep, are given in Figs. 9.24. Traces 1, 2 and 3 in these records give the same information which these traces give in Fig. 9.23 (a) and (b). As shown in Fig. 9.24, the records from the velocity transducers contain

an initial transient and two slowly decaying components having frequencies of approximately 95 and 335 Hz. Peaks corresponding to the 95 Hz component are marked in Fig. 9.24 (a), while peaks of the high frequency component are apparent.

The mode of the motion at the low frequency was one in which the footing and target arm rotated approximately as a unit. The motion at the high frequency involved the motion of the target arm relative to that of the footing.

For further insight into the motion of the footing, the velocity records in Fig. 9.24 (a) were integrated to lead to the curve of the angular displacement of the footing vs. time plotted in Fig. 9.25. The offset of the second rise from the initial angular displacements at a time at which the motion of the footing has decayed, indicates that slip and significant permanent deformation of the test bed had taken place.

b. Response of Test Bed -- The records shown in Figs. 9.23 (a), 9.23 (b), 9.26, and 9.27, give the responses of the transducers within the test bed at the locations shown in Fig. 9.17 as well as the responses of the transducers attached to the footing. Traces 4 and 5 in the records shown in Fig. 9.26 and 9.27 give the

filtered responses of the velocity transducers nearest to and furthest from the footing, respectively. As shown in Figs. 9.20 and 9.21, the most apparent effect of filtering is a time delay. For purposes of inspection, traces 4 and 5 in Figs. 9.26 and 9.27 should be visualized as shifted to the left by approximately 0.5 ms; 1/4 division in Fig. 9.26 and 1/2 division in Fig. 9.27.

In the records shown in Fig. 9.23, 9.26 and 9.27, the initial 13 to 16 ms following the beginning of the transient were reasonably free of reflections from the boundaries of the test bed.

Table 9.1: Selected Properties of Test Bed. Based on $G_s = 2.63$, $e_{min} = 0.55$ and $e_{max} = 0.78$ as Obtained by Chon (1977).

Property	Average (Depth = 6")	Average (Depth = 12")	Overall Average
e	.70	.68	.69
D_r(%)	33.0	45.6	39.3
γ (gm/cm^3)	1.61	1.66	1.64
w (%)	4.34	5.84	5.09
γ_d (gm/cm^3)	1.53	1.57	1.55

Table 9.2: Shear Wave Velocities Determined from Records in Fig. 9.3. Average Shear Wave Velocity = 562 fps. Range = 549 - 582 fps. Range Percentage = 5.9%.

Wavepoint	Number of Divisions Between Common Wavepoints	Shear Wave Velocity (fps)
1	2.84	572
2	2.79	582
3	2.87	566
4	2.91	558
5	2.90	560
6	2.90	560
7	2.96	549
8	2.96	549

Table 9.3: Results from Torsional Seismic Crosshole Tests.

Depth (ft)	Surcharge Pressure (psi)	Shear Wave Velocity (fps)		Range as Percentage of Average Shear Wave Velocity (%)
		Average	Range	
.5	5.05	647	616-677	9.4
.5	4.03	609	580-645	10.7
.5	3.01	559	542-580	6.8
.5	2.02	512	492-540	9.4

Table 9.3: (Continued)

Depth (ft)	Surcharge Pressure (psi)	Shear Wave Velocity (fps) Average	Shear Wave Velocity (fps) Range	Range as Percentage of Average Shear Wave Velocity (%)
3	5.05	484	469-499	6.2
3	3.97	486	478-497	3.9
3	2.97	476	465-487	4.6
3	2.02	464	456-478	4.7
3	1.04	443	433-453	4.5
3	2.02	452	444-462	4.0
3	3.01	464	458-474	3.4
3	4.10	483	473-493	4.1
3	5.10	495	488-505	3.4
4	5.05	493	486-501	3.0
4	3.04	493	481-499	3.7
4	1.04	476	469-491	4.6
4	3.01	485	478-492	2.9
4	5.03	500	489-508	3.8
5	5.05	481	473-491	3.7
5	2.99	482	467-492	5.2
5	1.04	477	461-488	5.7
5	3.01	480	467-488	4.4
5	5.03	489	486-492	1.2

Table 9.4: Maximum and Average Ranges as Percentages of Average Shear Wave Velocities. From Table 9.3.

Depth (ft)	Maximum Percentage (%)	Average Percentage (%)
.5	10.7	8.8
1	9.5	6.6
2	9.7	7.6
3	6.2	4.3
4	4.6	3.6
5	5.7	4.0

Table 9.5: Shear Wave Velocities at Initial and Final Surcharge Pressures (Both 5 psi). From Table 9.3.

Depth (ft)	Shear Wave Velocity (fps)		Percentage Difference Between Initial and Final (%)
	Initial	Final	
.5	647	657	1.5
1	556	582	4.7
2	510	509	.2
3	484	495	2.3
4	493	500	1.4
5	481	489	1.7

Table 9.6: Lateral Displacement of Wall of Quicksand Tank as Function of Depth Beneath Upper Surface of Test Bed. Surcharge Pressure = 5 psi. Positive (+) Indicates Contraction of Tank.

Depth (inches)	Lateral Displacement (inches)
7	+0.010
12.5	+0.005
18	+0.001
22	-0.002
27	-0.002

Table 9.7: Calibration Factors of Load Cells.

Load Cell	Calibration Factor (Ft-lb/volt)
Torsional	67.7
Bending (y - z Plane)	61.9
Bending (x - z Plane)	86.4

Table 9.8: Amplitudes of Unwanted Components of Load or Motion (Figs. 9.16(b) and (c)) Expressed as Percentages of Values of Peaks of Appropriate Torsional Records (Fig. 9.16(a)).

Trace Number and Parameter Measured (Fig. 9.16)	Percentage	
	Arrangement of Fig. 9.15(a)	Arrangement of Fig. 9.15(b)
1 - Load	4.6	3.8
2 - Velocity	6.4	4.1
3 - Velocity	2.1	2.1
4 - Velocity	3.3	2.1
5 - Velocity	3.4	.9

Table 9.9: Nominal and Actual Positions of Velocity Transducers within Test Bed.

Test	Positions of Transducers			
	Depth (Inches)		Radius (Inches)	
	Nominal	Actual	Nominal	Actual
H	12	11 7/8	6	5 7/8
H	24	24	12	11 3/8
I	6	5 7/16	6	5 31/32
I	12	11 13/32	12	11 7/8
J	6	5 19/32	12	11 31/32
J	3	2 1/2	6	5 15/16

Table 9.10: Number of Low and High Amplitude Tests Conducted in Each Major Test.

Test	Number of Low Amplitude Tests	Number of High Amplitude Tests
G	17	19
H	27	9
I	29	7
J	30	12

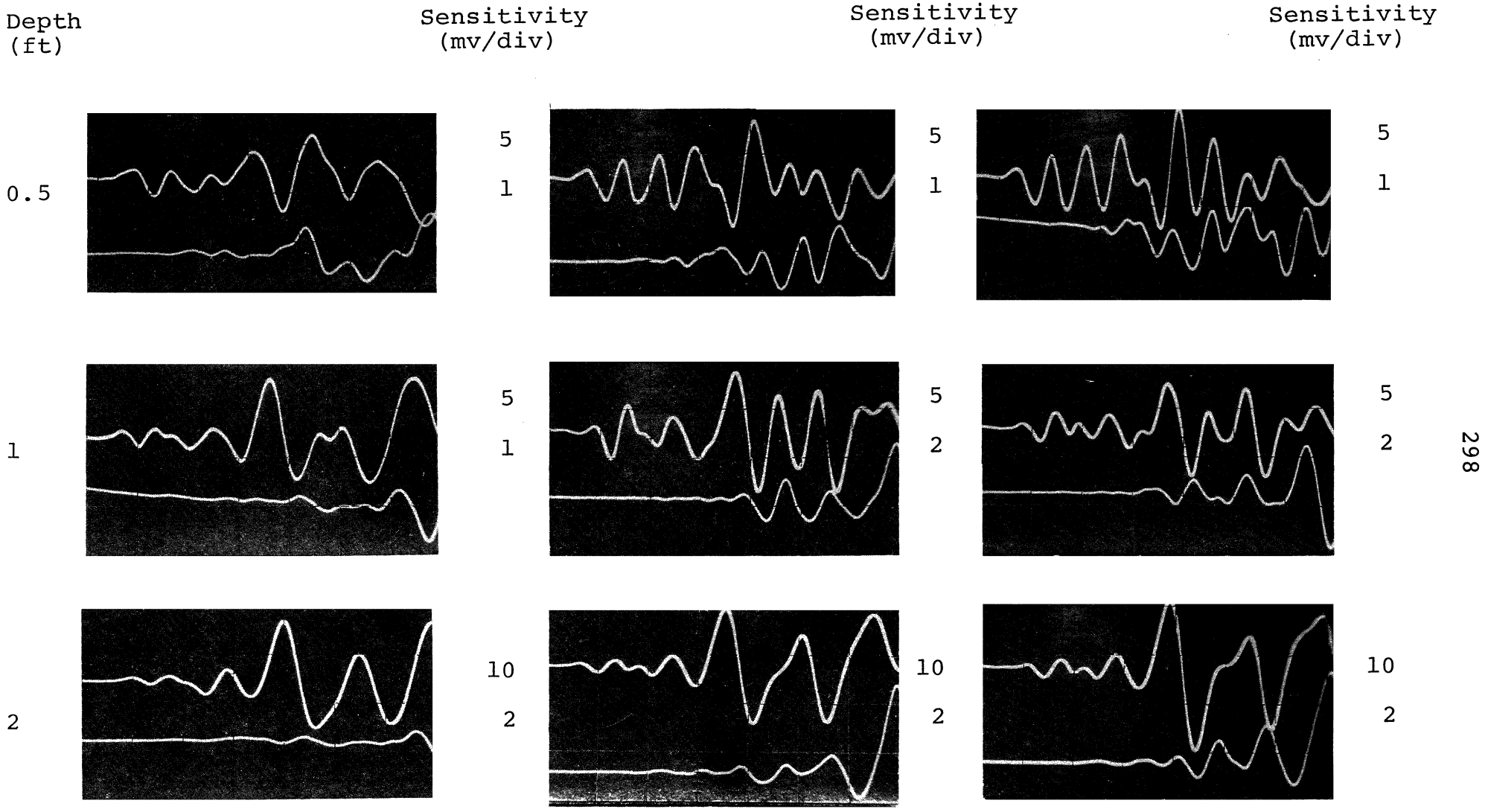

(a) Surcharge Pressure = 1 psi.

(b) Surcharge Pressure = 3 psi.

(c) Surcharge Pressure = 5 psi.

Fig. 9.1: Records from Torsional Seismic Crosshole Test. Sweep Rate = 1 ms/div.

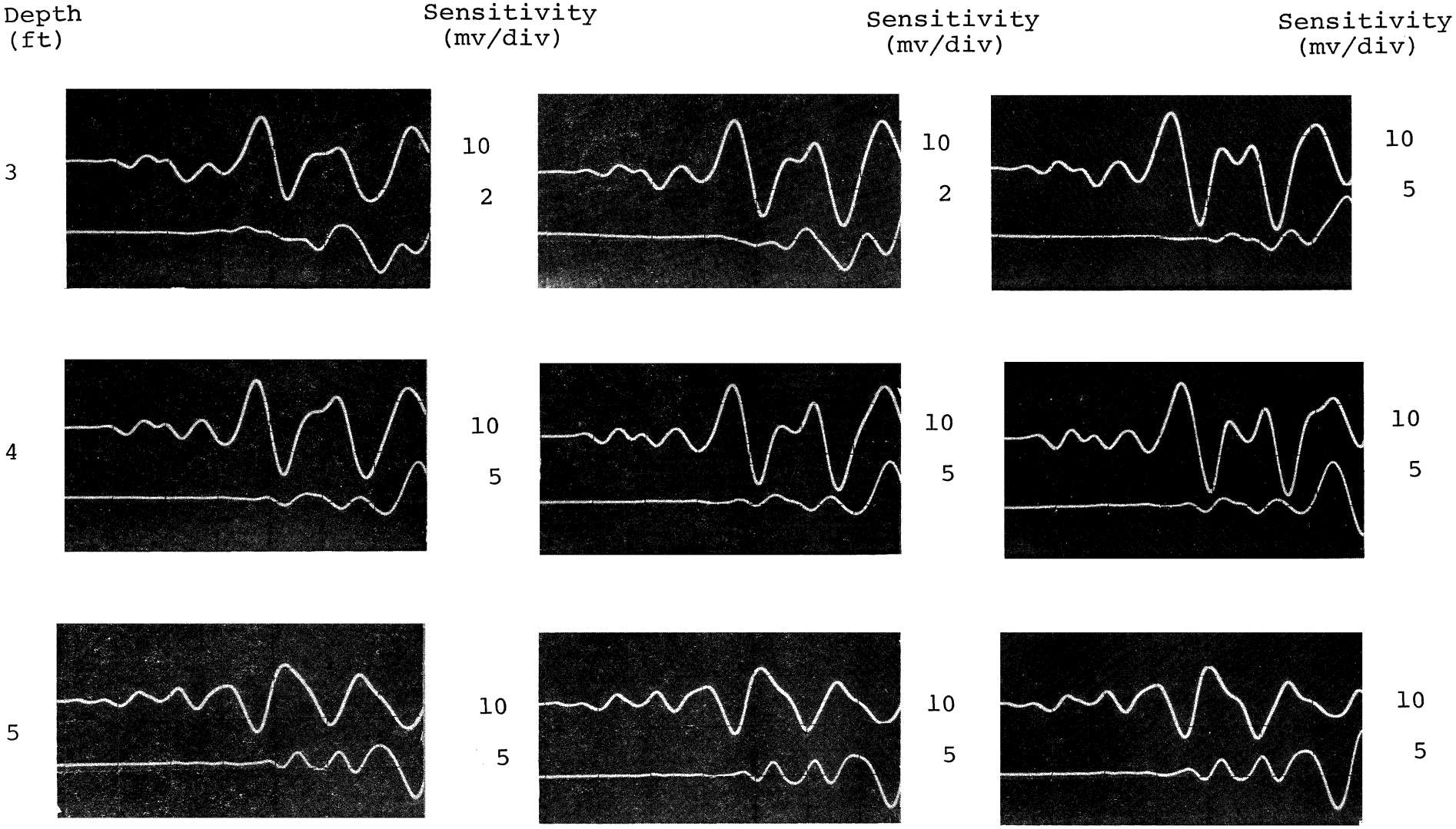

(a) Surcharge Pressure = 1 psi.

(b) Surcharge Pressure = 3 psi.

(c) Surcharge Pressure = 5 psi.

Fig. 9.1: (continued).

(a) Depth = 2 ft,
Sweep Rate =
2 ms/div,
Surcharge
Pressure =
1 psi.

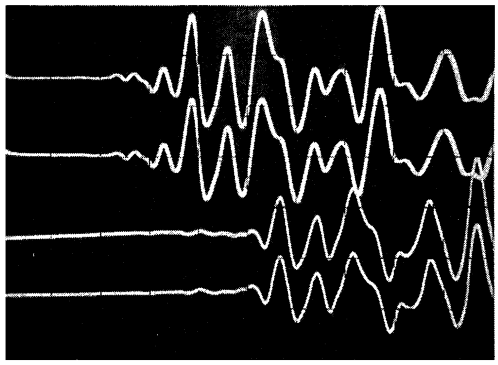

Sensitivity
(mv/div)

10

5

(b) Depth = 5 ft,
Sweep Rate =
2 ms/div,
Surcharge
Pressure =
1 psi.

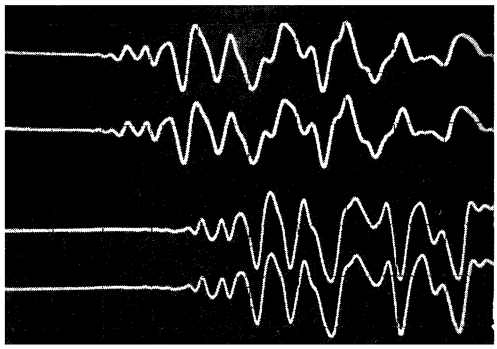

10

5

(c) Depth = 0.5 ft
Sweep Rate =
1 ms/div,
Surcharge
Pressure =
5 psi.

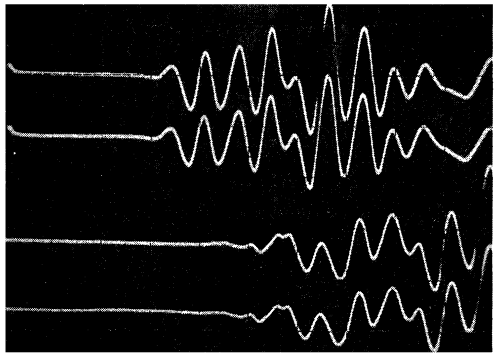

5

1

Fig. 9.2: Records from Torsional Seismic Crosshole Tests.

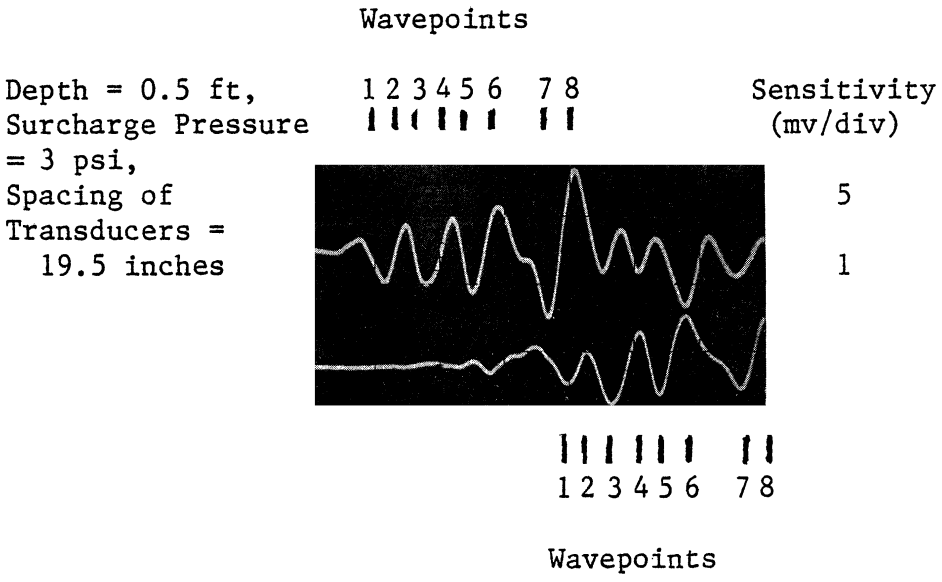

Fig. 9.3: Records from Torsional Seismic Crosshole Test. Sweep Rate = 1 ms/div.

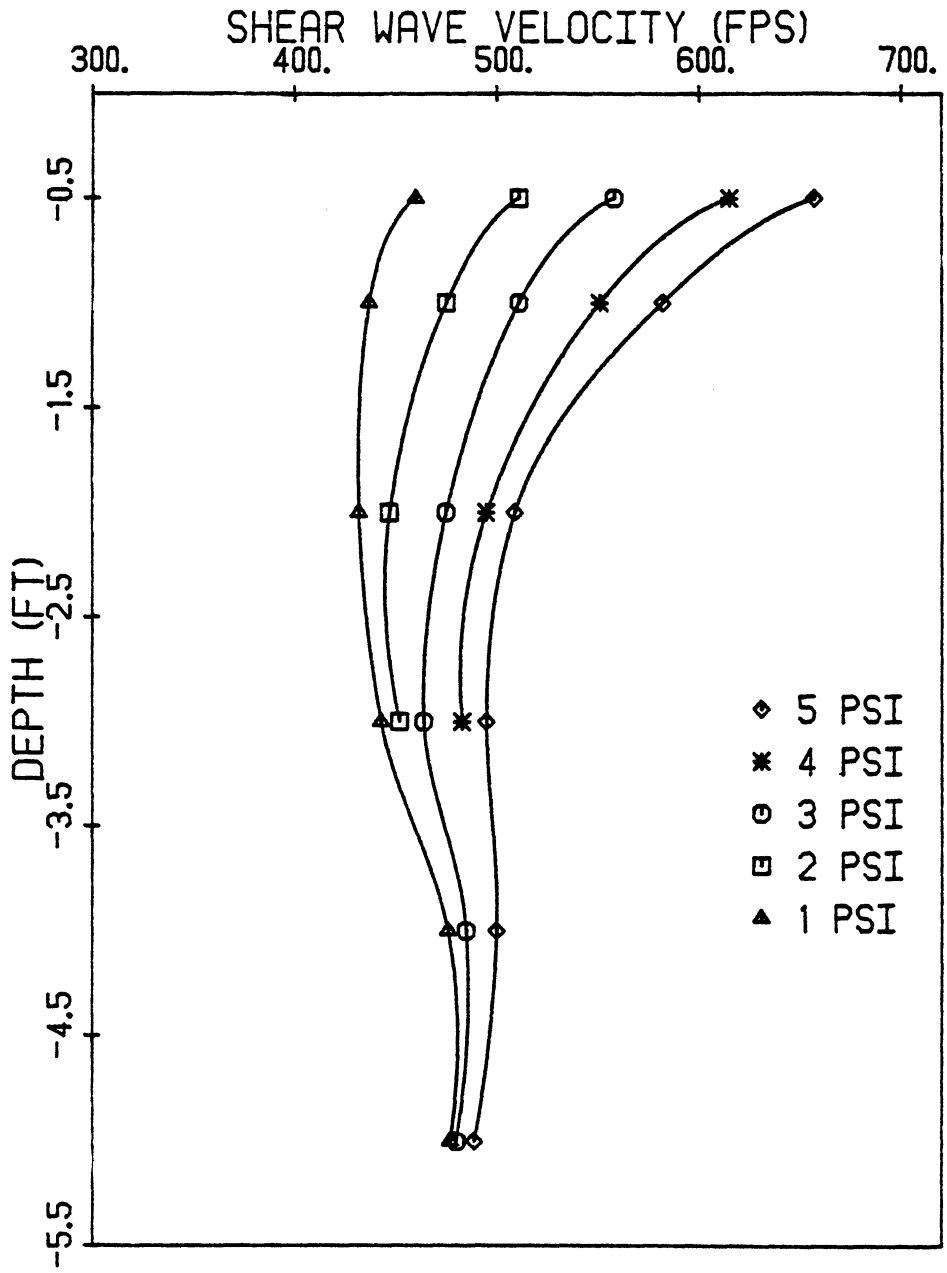

Fig. 9.4: Shear Wave Velocity vs. Depth Obtained from Torsional Seismic Crosshole Test for Increasing Sequence of Surcharge Pressures.

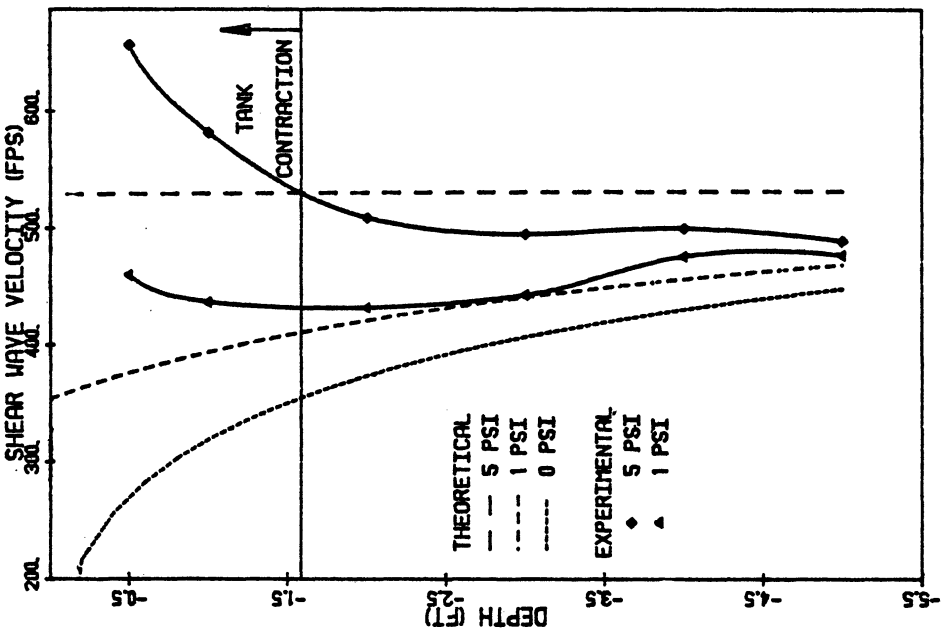

Fig. 9.6: Shear Wave Velocity vs. Depth for Indicated Surcharge Pressures as Obtained by Torsional Seismic Crosshole Test and Theory. Theory Takes Shearing Stresses into Account.

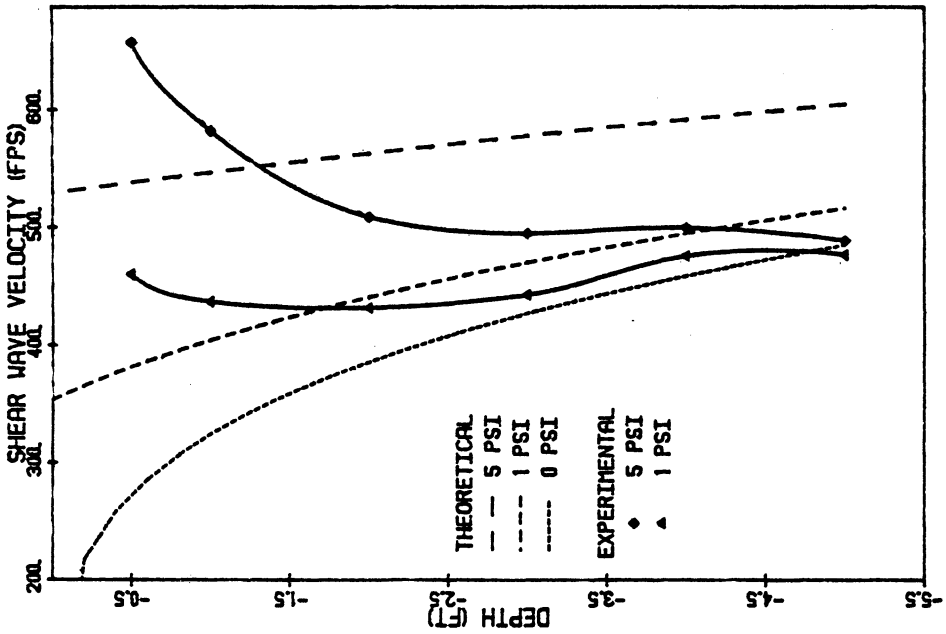

Fig. 9.5: Shear Wave Velocity vs. Depth for Indicated Surcharge Pressures as Obtained by Torsional Seismic Crosshole Test and Theory. Theory Does Not Take Shearing Stresses into Account.

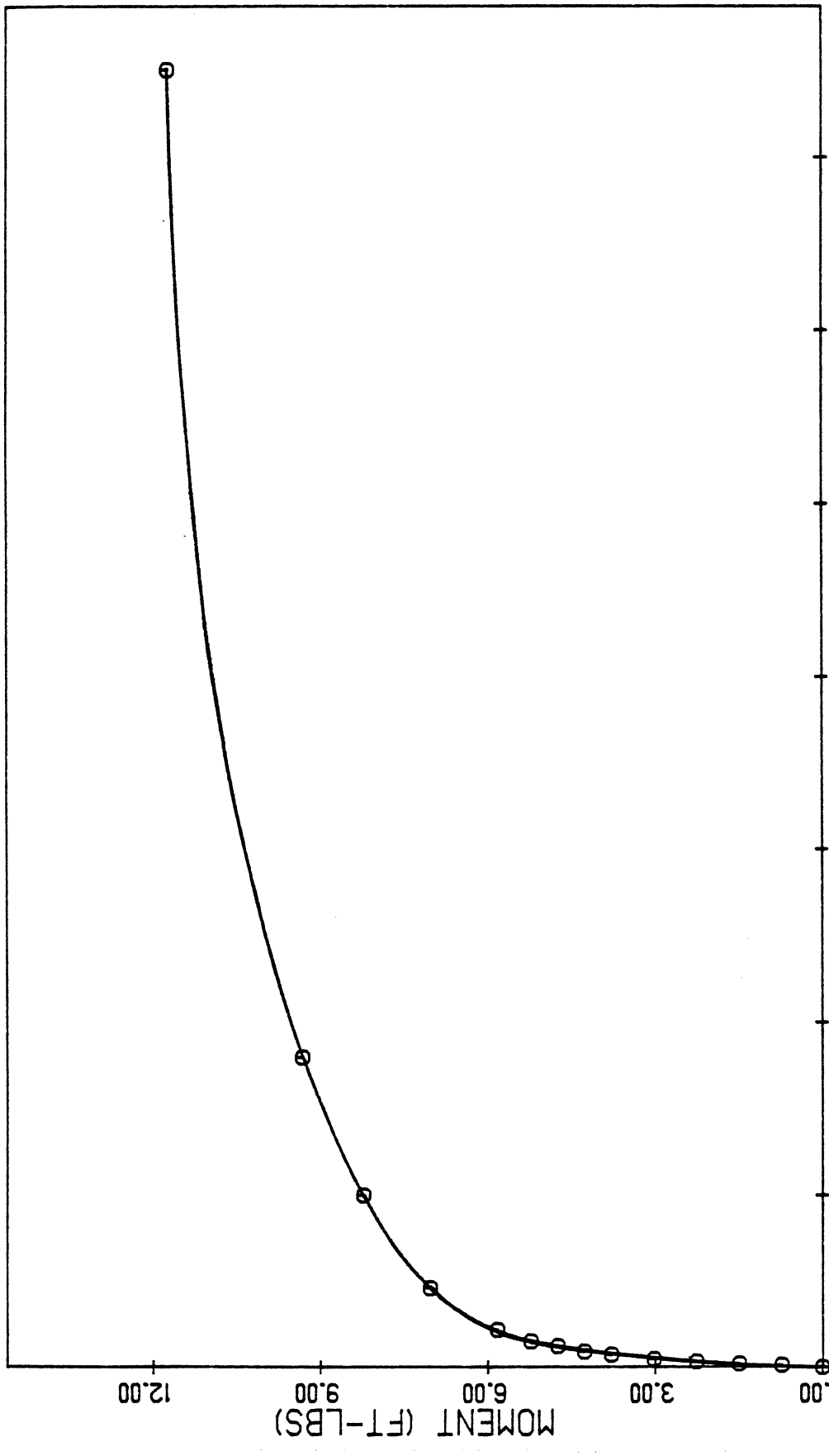

Fig. 9.7: Moment Applied to Footing vs. Angular Displacement of Footing Obtained from Static Torsional Loading Test.

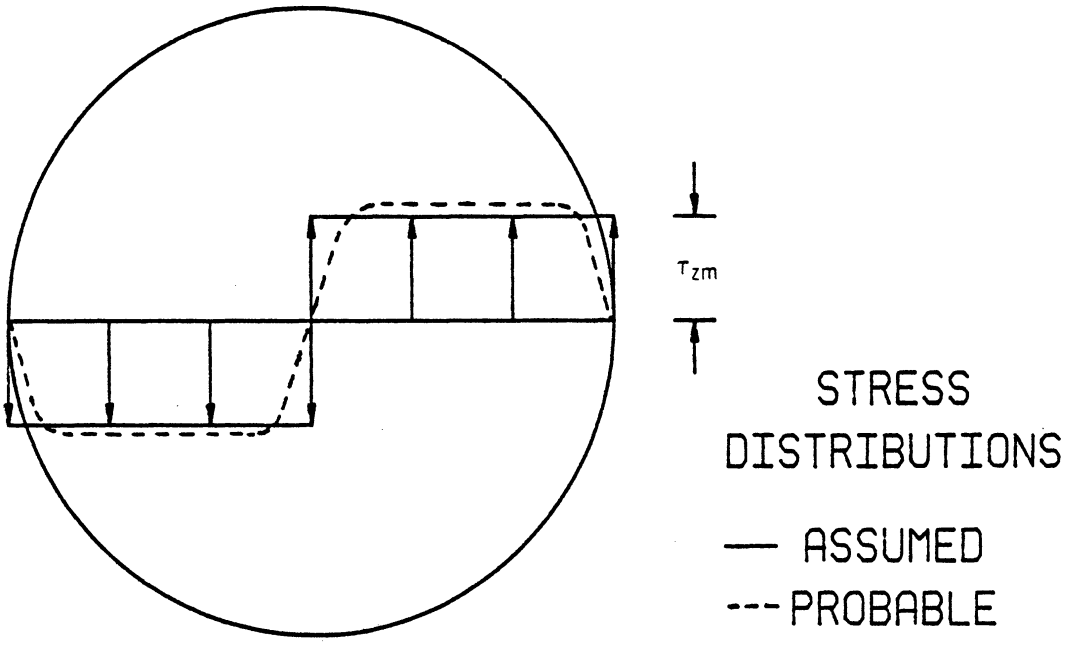

Fig. 9.8: Distribution of Shearing Stresses Developed Along Base of Footing in Static Torsional Loading Test in Response to Maximum Applied Moment.

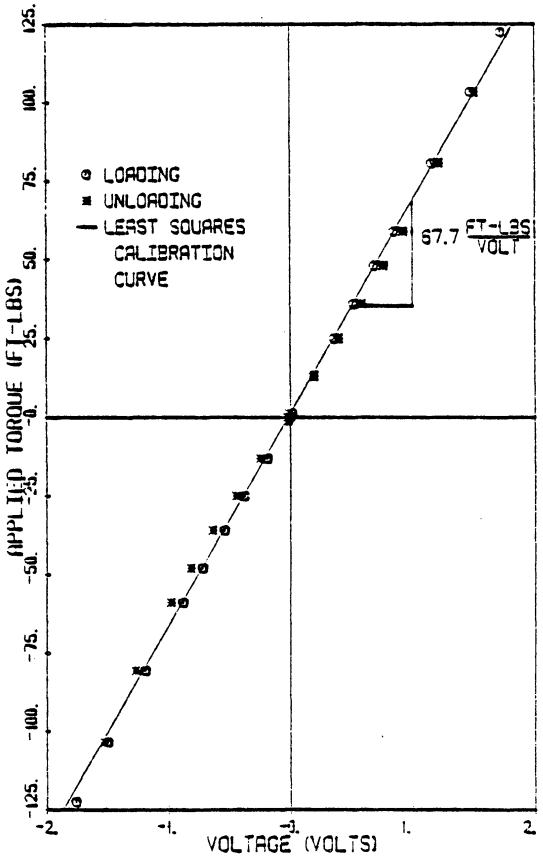

Fig. 9.9: Calibration Curves for Torsional Load Cell.

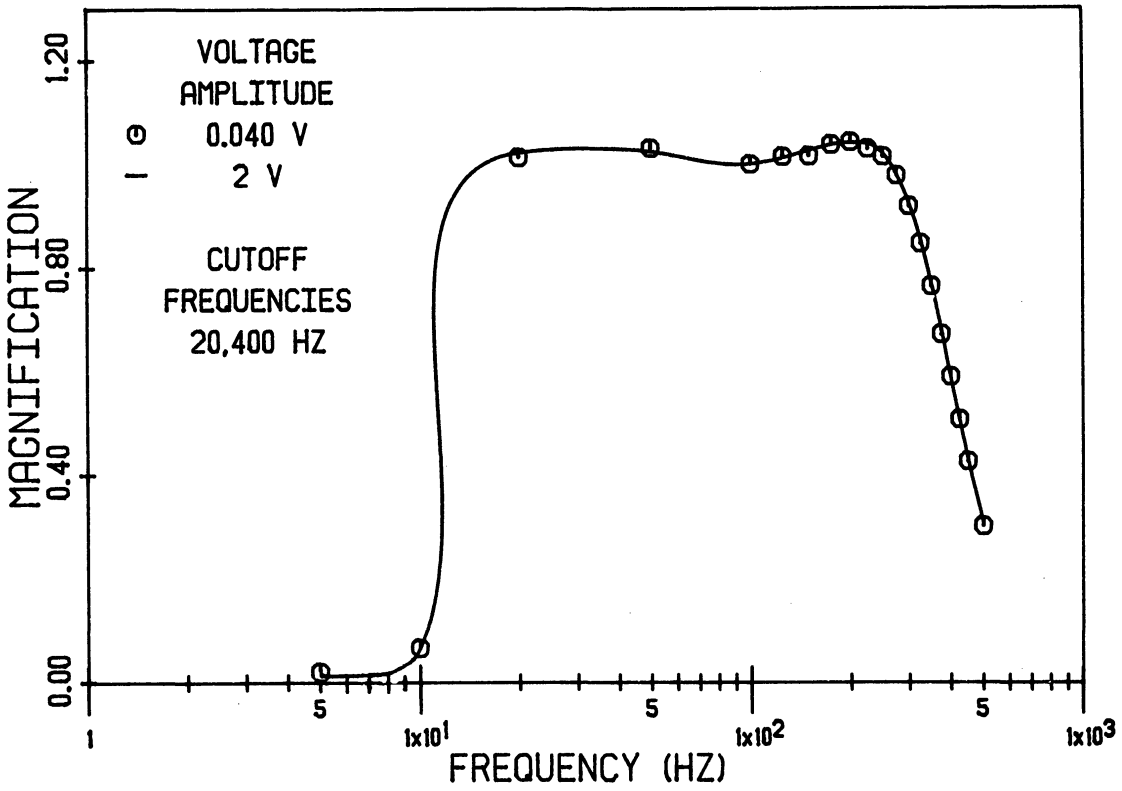

Fig. 9.10: Voltage Magnification vs. Frequency for Two Voltage Amplitudes for Variable Filter.

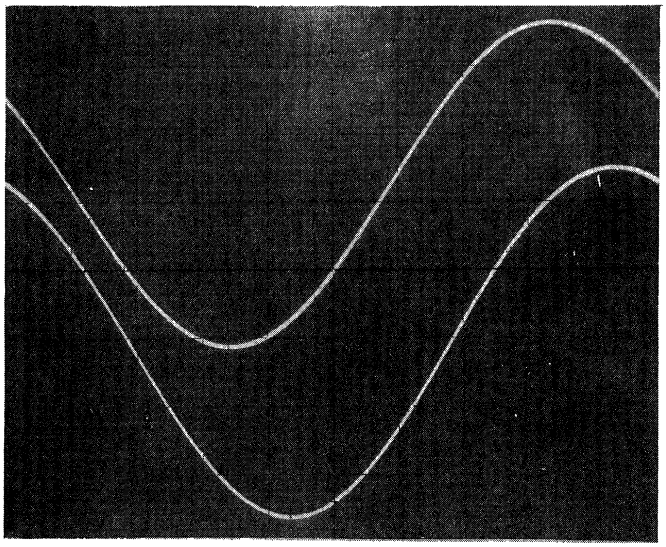

Time Shift = 0.95 div = 0.475 ms

$$\text{Phase Shift} = \frac{(\text{no. div})(\text{sweep rate})}{\text{period of wave}} \times 360$$

$$= 34.2^{o}$$

Fig. 9.11: Record Used to Obtain Phase Shift of Filter. Frequency = 200 Hz, Sweep = 0.5 ms/div.

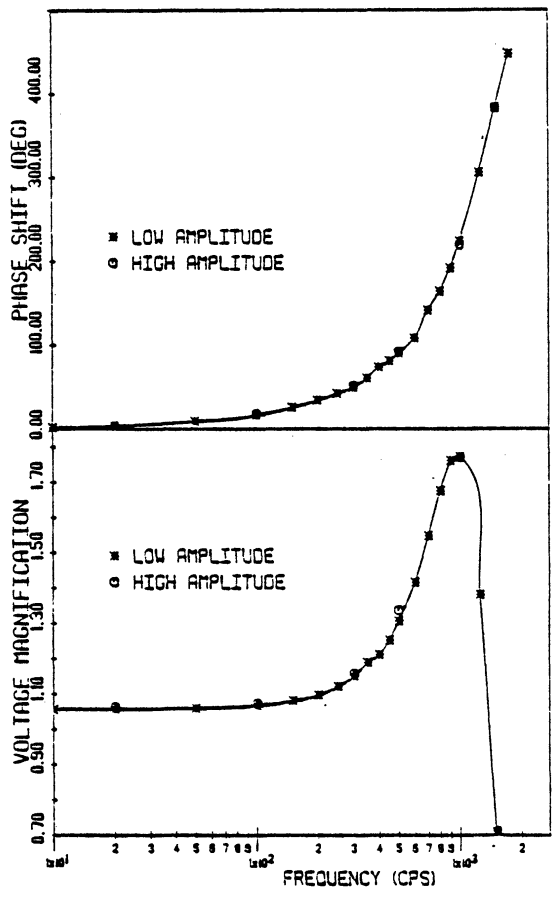

Fig. 9.12: Phase Shift and Voltage Magnification by Filters Used in Dynamic Footing Tests vs. Frequency for Two Voltage Amplitudes: 40 mv and 2 v.

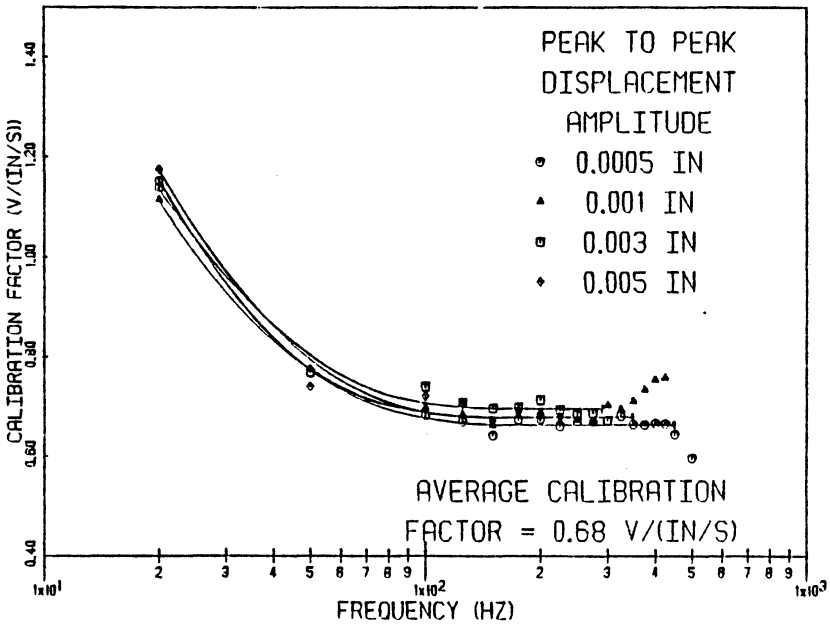

Fig. 9.13: Calibration Factor of Velocity Transducer vs. Frequency at Several Amplitudes.

(a) Unadjusted Hammer, Unpadded Impact Faces.

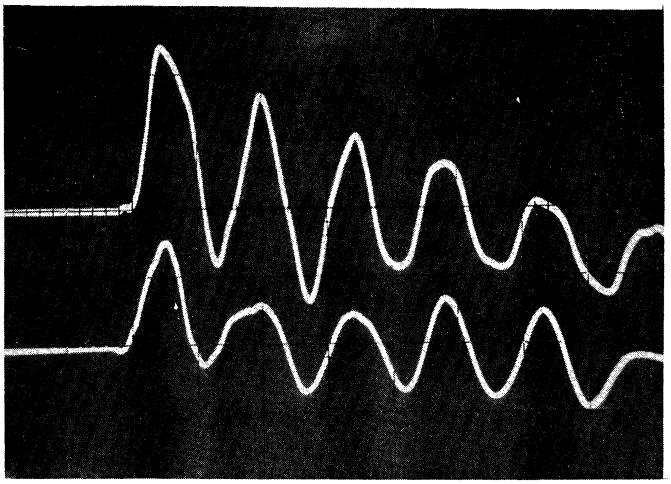

(b) Adjusted Hammer, Unpadded Impact Faces.

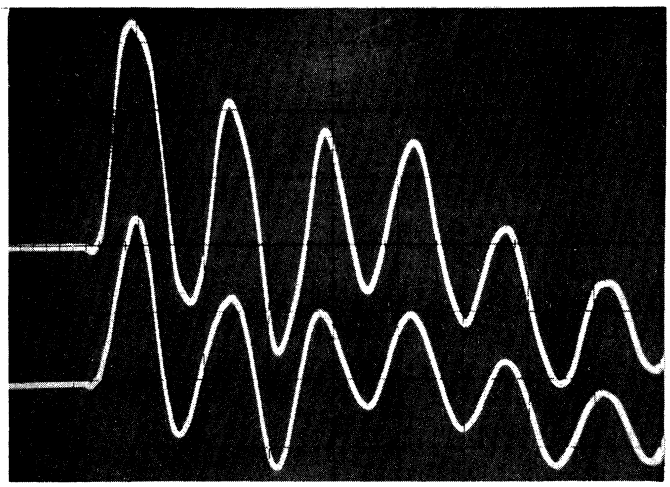

(c) Adjusted Hammer, Padded Impact Faces.

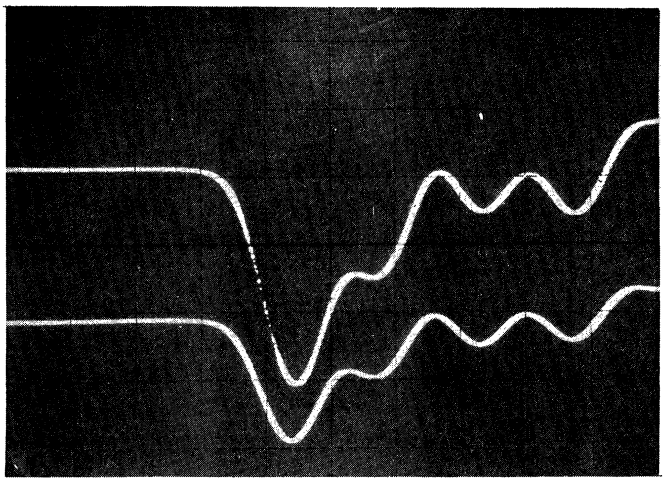

Fig. 9.14: Records from Preliminary Dynamic Model Footing Tests. Sweep = 2 ms/div. Sensitivities: Trace 1 = 0.2 v/div, Trace 2 = 1 v/div. Calibration Factors: Trace 1 = 0.49 v/(in/s), Trace 2 = 1.35 v/(in/s).

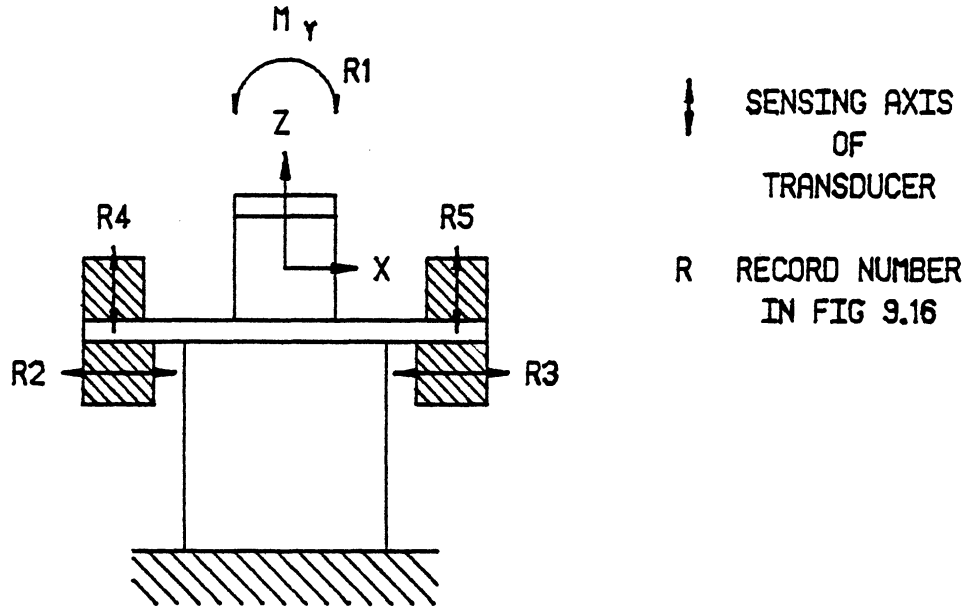

(a) Rocking about y-Axis, Sliding in Direction of x-Axis, and Vertical Motion.

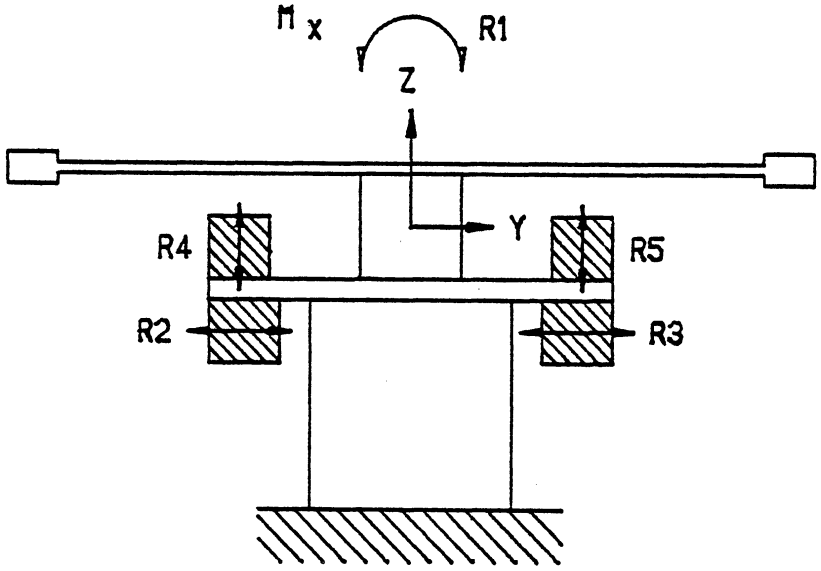

(b) Rocking about x-Axis, Sliding in Direction of y-Axis, and Vertical Motion.

Fig. 9.15: Footing with Transducers Arranged to Measure Indicated Unwanted Components of Motion.

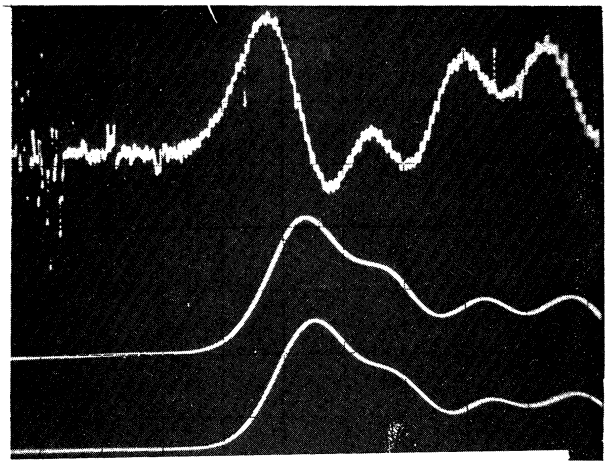

	Sensitivity (v/div)	Calibration Factor
1	0.1	67.7 $\frac{\text{ft-lb}}{\text{volt}}$
2	0.5	1.35 $\frac{\text{volt}}{\text{(in/s)}}$
3	0.2	0.49

(a) Standard Torsional Records.

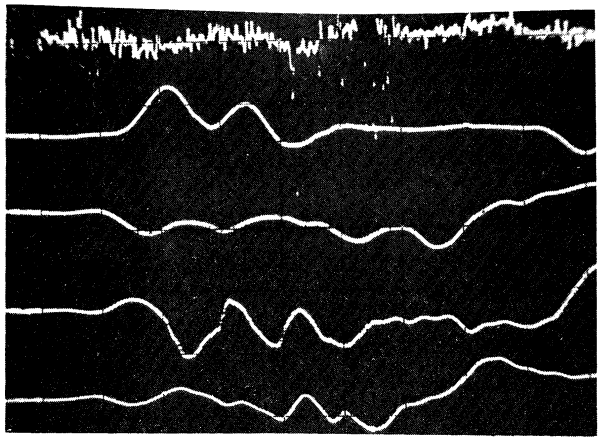

1	50m	86.4 $\frac{\text{ft-lb}}{\text{volt}}$
2	0.1	1.35 $\frac{\text{volt}}{\text{(in/s)}}$
3	20m	0.49
4	50m	1.28
5	50m	0.99

(b) Records Using Arrangement in Fig. 9.15(a).

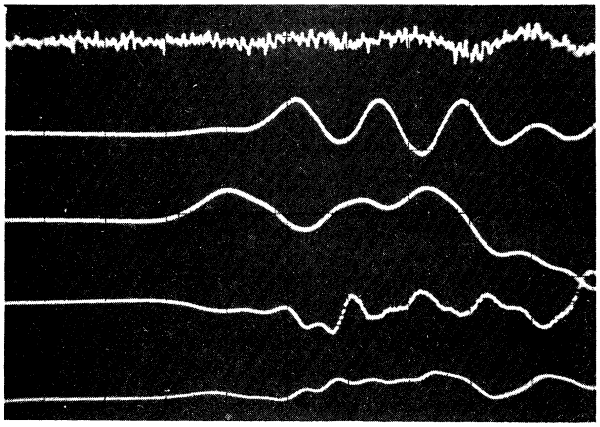

1	50m	61.9 $\frac{\text{ft-lb}}{\text{volt}}$
2	0.1	1.35 $\frac{\text{volt}}{\text{(in/s)}}$
3	10m	0.49
4	50m	1.28
5	50m	0.99

(c) Records Using Arrangement in Fig. 9.15(b).

Fig. 9.16: Records Showing Various Components of Load and Motion.

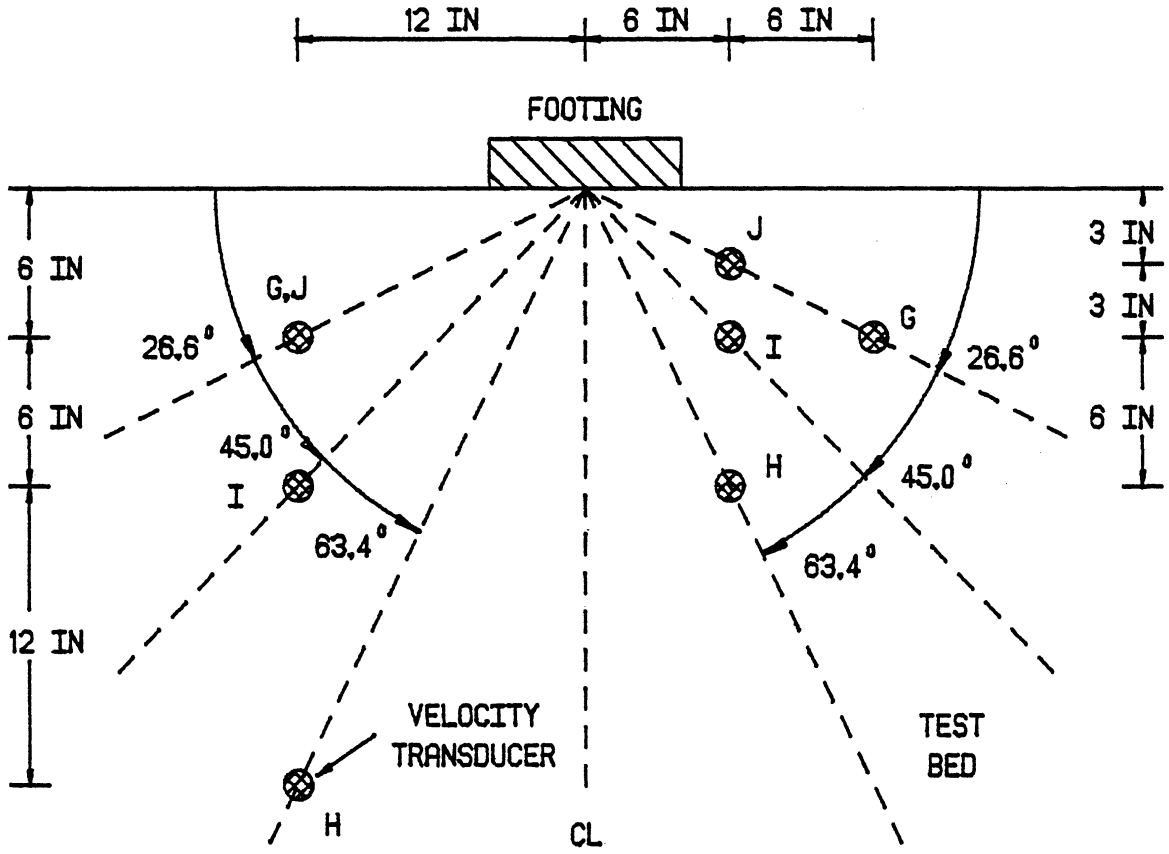

Fig. 9.17: Schematic Diagram of Test Bed Showing Arrangements of Velocity Transducers Used in Dynamic Model Footing Tests Along with Designations Corresponding to Main Tests.

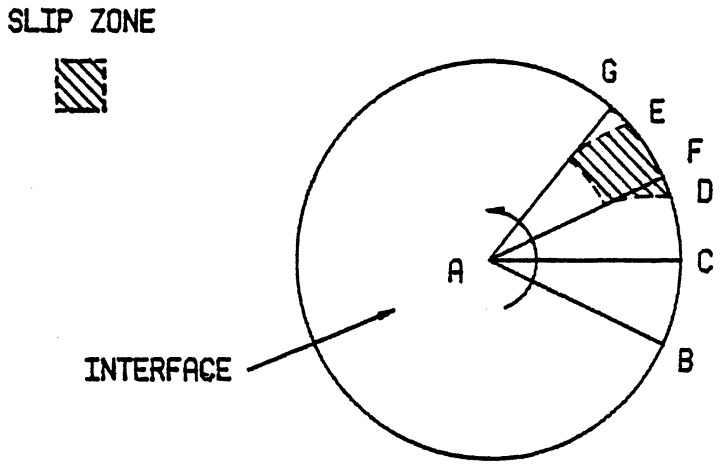

Fig. 9.18: Plan View of Half Space at Interface Demonstrating Rotation of Undeformed Slice of Half Space, ABC, to Deformed State, AED, With Slip. Slice Rotates Rigidly to AGF Without Slip.

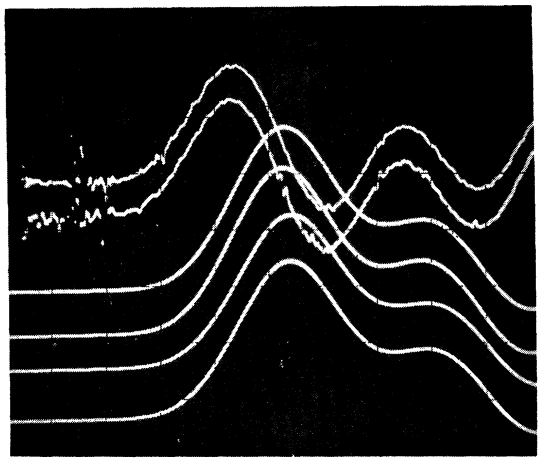

	Sensitivity (v/div)	Calibration Factors
1, 2	0.2	67.7 ft-lb/volt
3, 4	0.5	1.35 volt/(in/s)
5, 6	0.2	0.49

(a) First and Second Tests, Test J, Sweep =1ms/div.

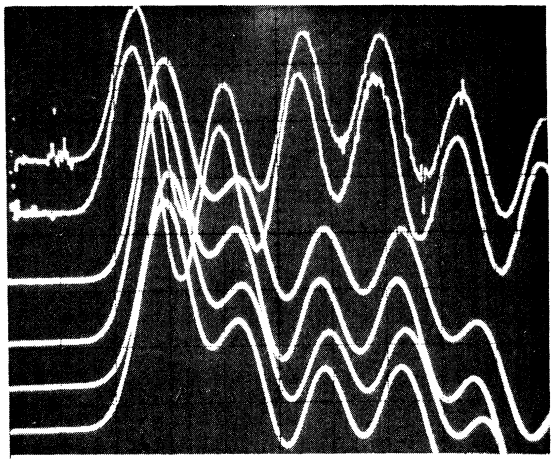

1, 2	0.2	67.7 ft-lb/volt
3, 4	0.5	1.35 volt/(in/s)
5, 6	0.2	0.49

(b) Second and Fifth Tests, Test G, Sweep = 2 ms/div.

Fig. 9.19: Records Used to Show Combined Effects of Incomplete Seating and Disturbances.

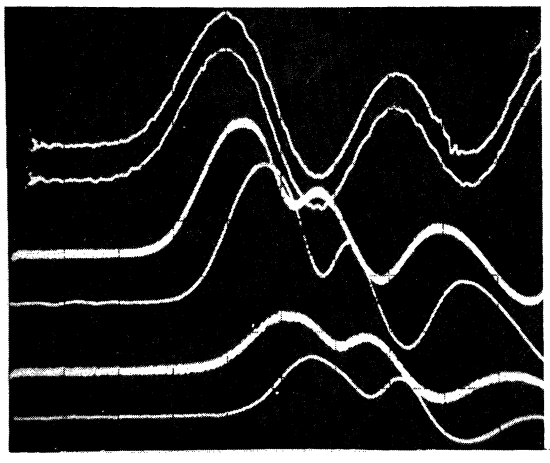

1, 2	0.2	67.7 ft-lb/volt
3, 4	5m	0.66 volt/(in/s)
5, 6	5m	0.66

Fig. 9.20: Records Showing Effects of Filtering on Information Obtained from Velocity Transducers within Test Bed. Test J, Sweep = 1 ms/div.

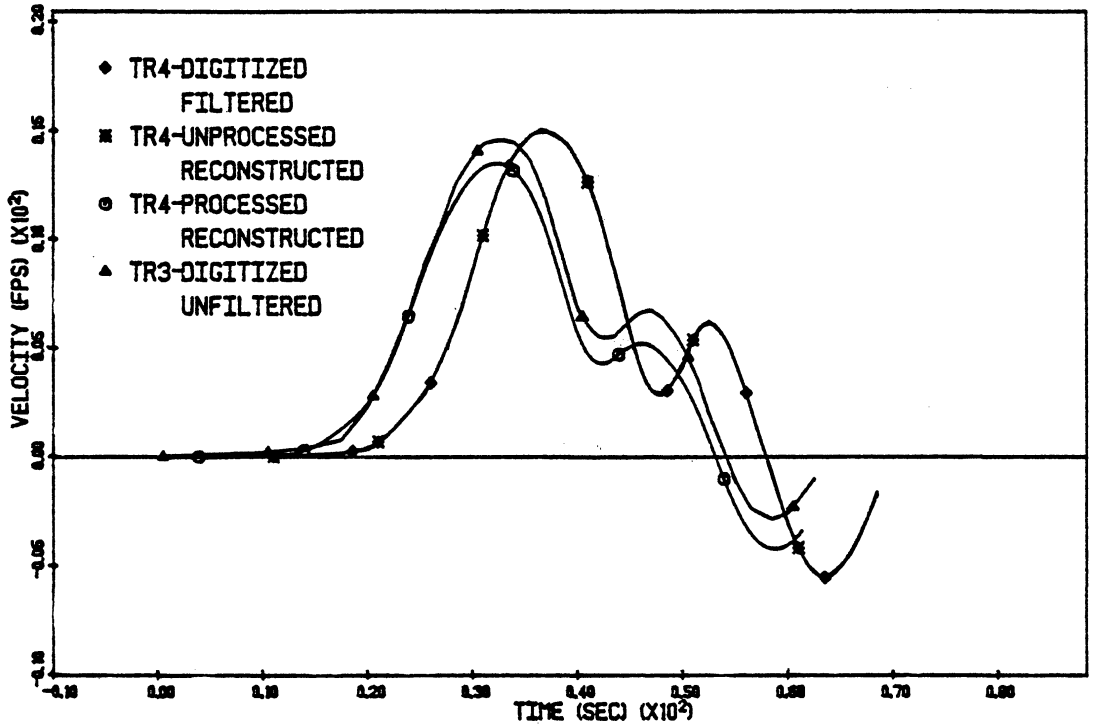

(a)

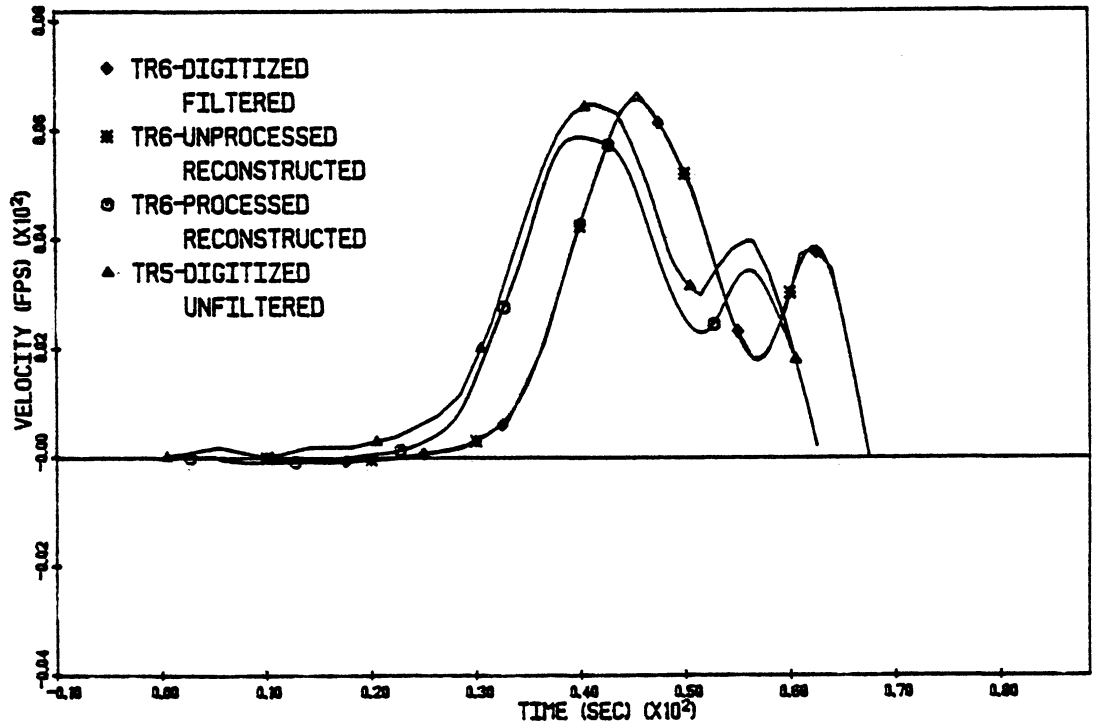

(b)

Fig. 9.21: Unprocessed Records from Fig. 9.20 and Processed Records.

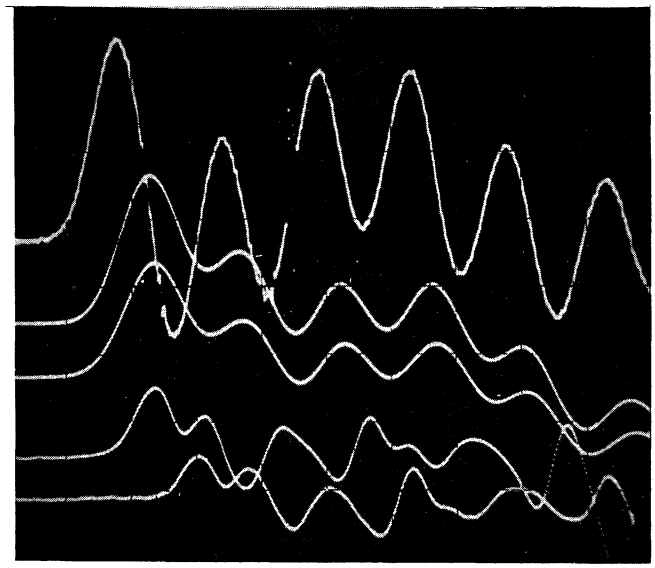

	Sensitivity (volts/div)	Calibration Factor
1	0.2	$67.7\frac{\text{ft-lb}}{\text{volt}}$
2	1	$1.35\frac{\text{volt}}{\text{(in/s)}}$
3	0.5	0.49
4	-	-
5	-	-

(a) Torsion

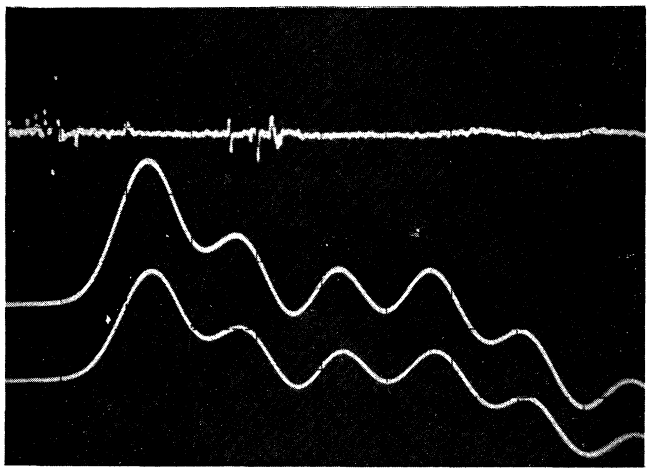

1	0.2	$61.9\frac{\text{ft-lb}}{\text{volt}}$
2	1	$1.35\frac{\text{volt}}{\text{(in/s)}}$
3	0.5	0.49

(b) Bending in y-z Plane

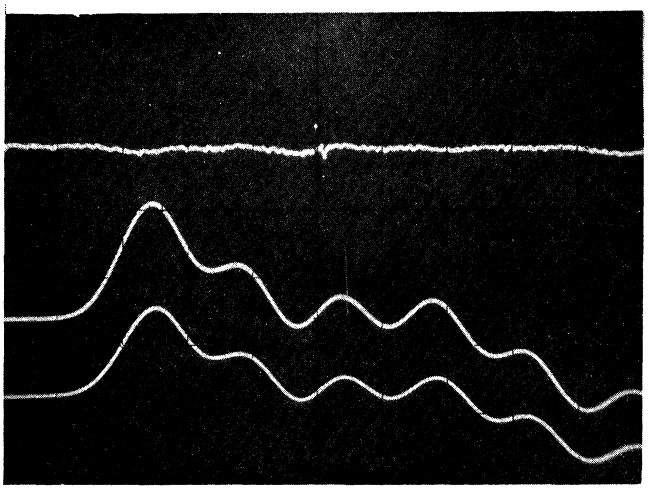

1	0.2	$86.4\frac{\text{ft-lb}}{\text{volt}}$
2	1	$1.35\frac{\text{volt}}{\text{(in/s)}}$
3	0.5	0.49

(c) Bending in x-z Plane

Fig. 9.22: Records Showing Various Components of Load. Test I, Sweep = 2 ms/div.

Sensitivity (volts/div)	Calibration Factors	
0.2	$67.7\frac{\text{ft-lb}}{\text{volt}}$	1
0.5	$1.35\frac{\text{volt}}{(\text{in/s})}$	2
0.2	0.49	3
5m	0.66	4
5m	0.66	5

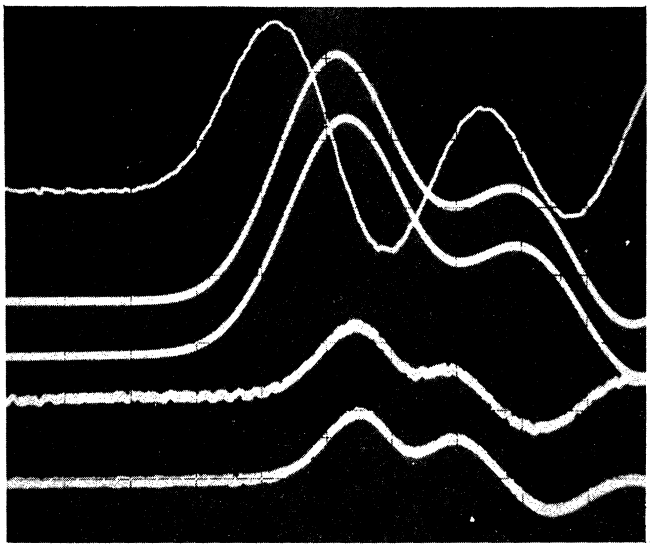

(a) Sweep Rate = 1 ms/div

0.2	$67.7\frac{\text{ft-lb}}{\text{volt}}$	1
1	$1.35\frac{\text{volt}}{(\text{in/s})}$	2
0.5	0.49	3
5m	0.66	4
5m	0.66	5

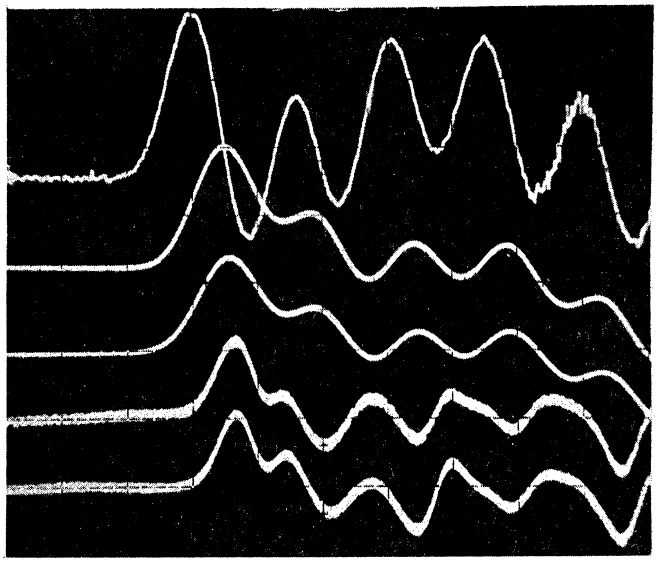

(b) Sweep Rate = 2 ms/div

Fig. 9.23: Records from Dynamic Model Footing Tests (Test G) and Schematic Diagram of Arrangement of Equipment in Test G.

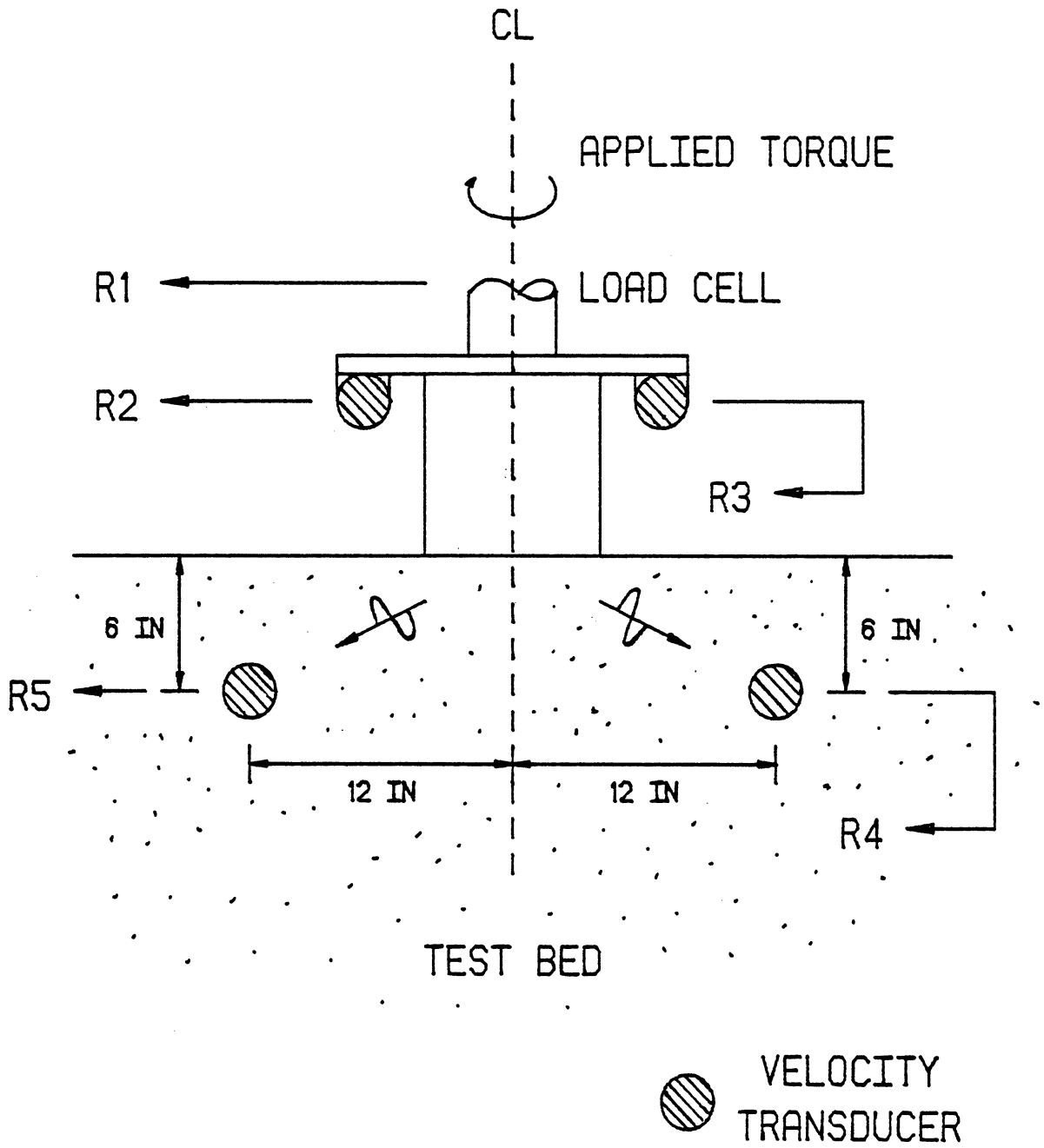

(c) Arrangement of Test G.
Fig. 9.23: (Continued)

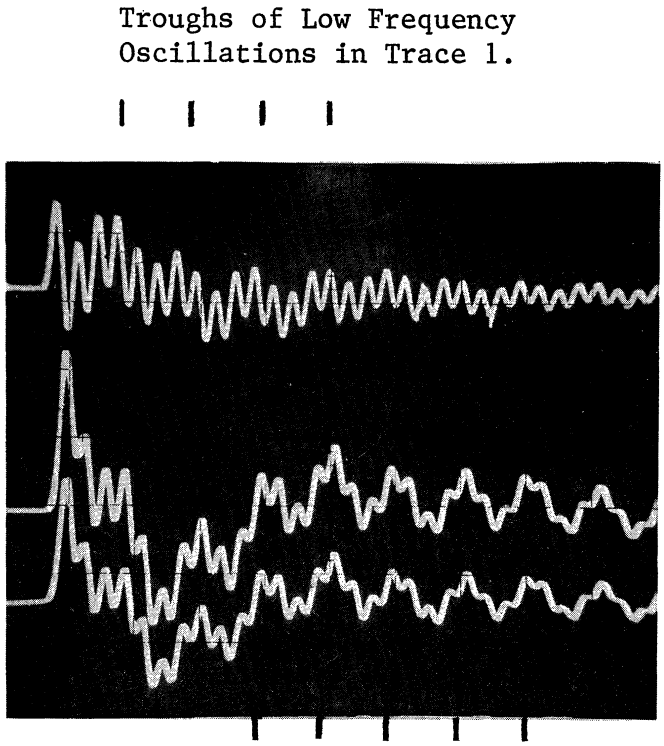

	Sensitivity (volts/div)	Calibration Factors
1	0.5	$67.7\frac{\text{ft-lb}}{\text{volt}}$
2	1	$1.35\frac{\text{volt}}{\text{(in/s)}}$
3	0.5	0.49

(a) Sweep Rate = 10 ms/div.

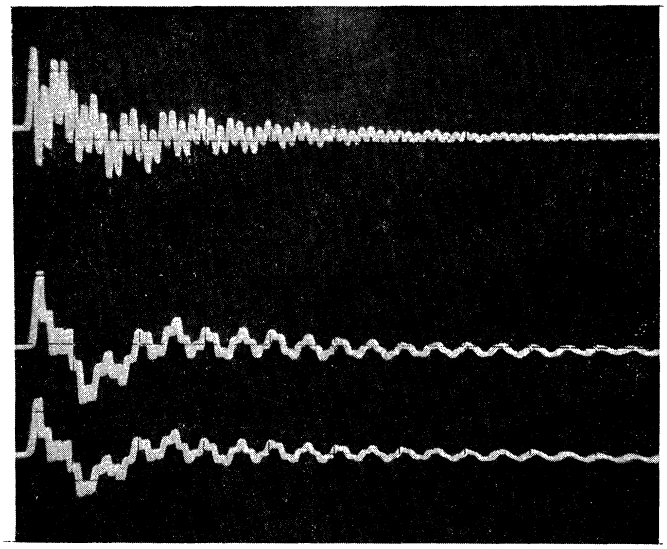

	Sensitivity (volts/div)	Calibration Factors
1	0.5	$67.7\frac{\text{ft-lb}}{\text{volt}}$
2	2	$1.35\frac{\text{volt}}{\text{(in/s)}}$
3	1	0.49

(b) Sweep Rate = 20 ms/div.

Fig. 9.24: Records from Dynamic Model Footing Tests (Test G) Obtained at Different Sweep Rates.

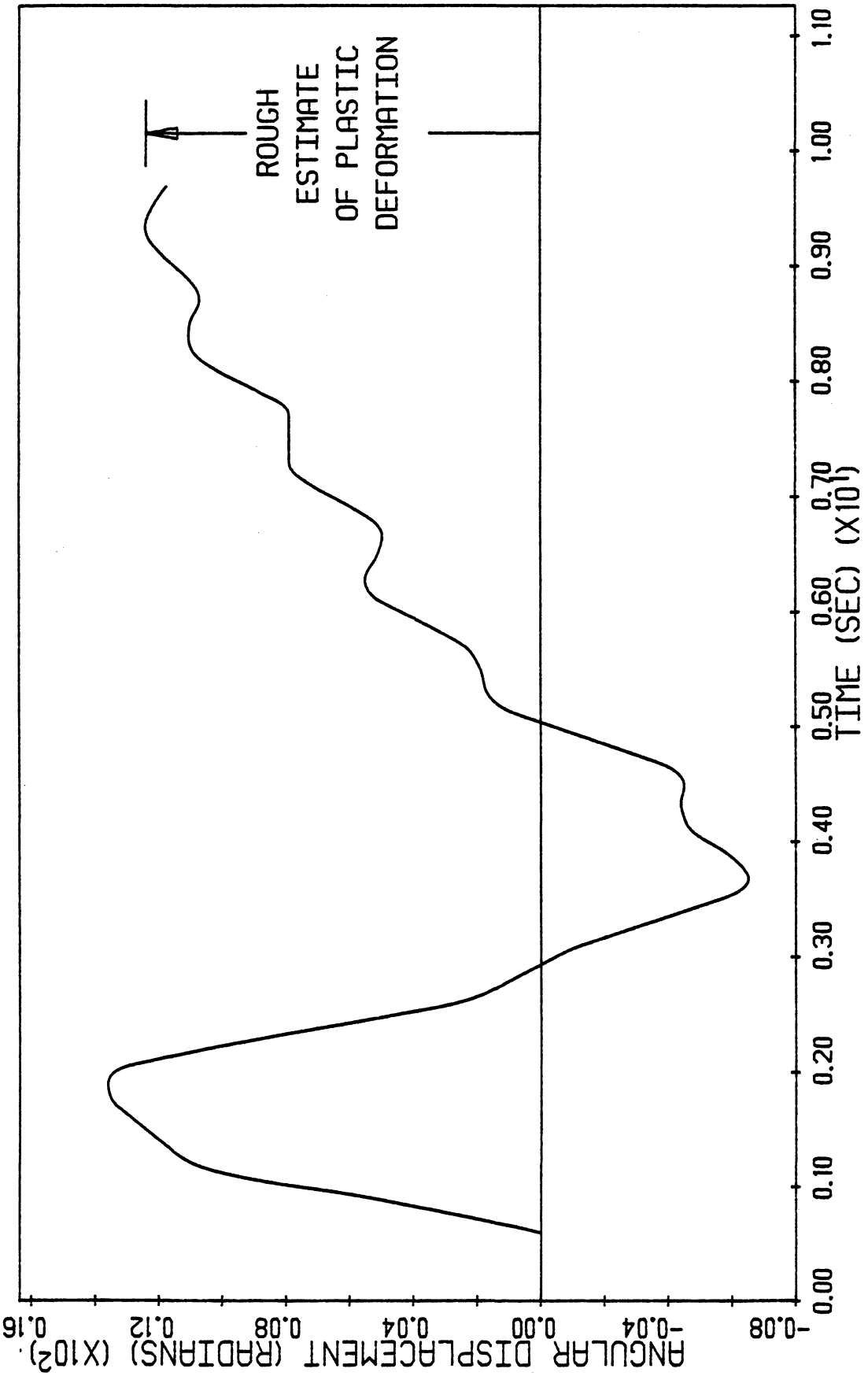

Fig. 9.25: Angular Displacement of Footing vs. Time.

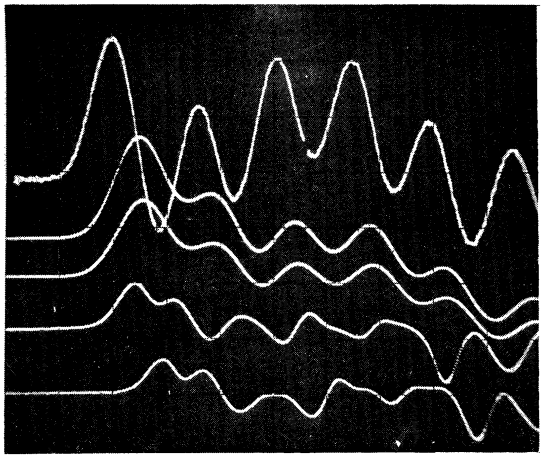

	Sensitivity (volt/div)	Calibration Factors
1	0.2	$67.7\frac{\text{ft-lb}}{\text{volt}}$
2	1	$1.35\frac{\text{volt}}{\text{(in/s)}}$
3	0.5	0.49
4	20m	0.66
5	10m	0.66

(a) Test J

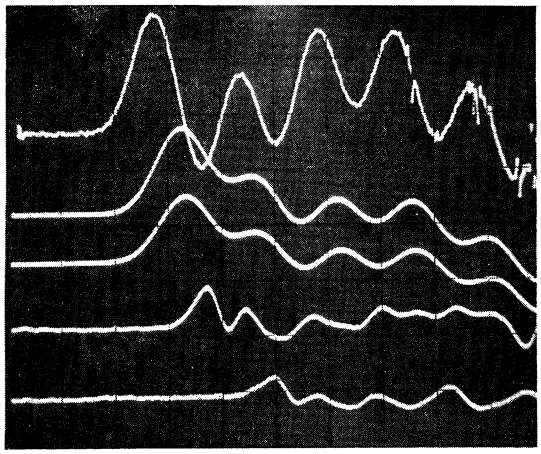

1	0.2	$67.7\frac{\text{ft-lb}}{\text{volt}}$
2	0.5	$1.35\frac{\text{volt}}{\text{(in/s)}}$
3	0.2	0.49
4	5m	0.66
5	2m	0.66

(b) Test I

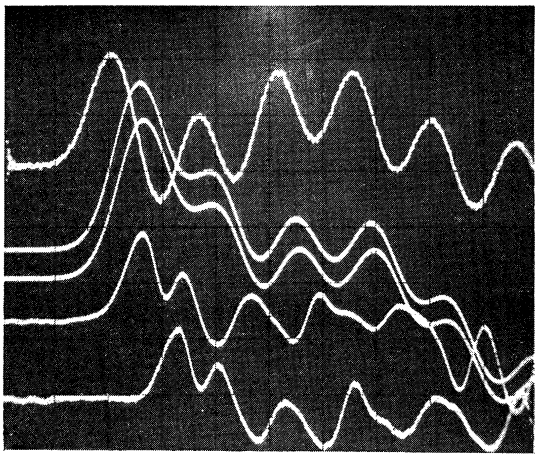

1	0.2	$67.7\frac{\text{ft-lb}}{\text{volt}}$
2	1	$1.35\frac{\text{volt}}{\text{(in/s)}}$
3	0.5	0.49
4	5m	0.66
5	5m	0.66

(c) Test H

Fig. 9.26: Records from Dynamic Model Footing Tests. Sweep Rate = 2 ms/div.

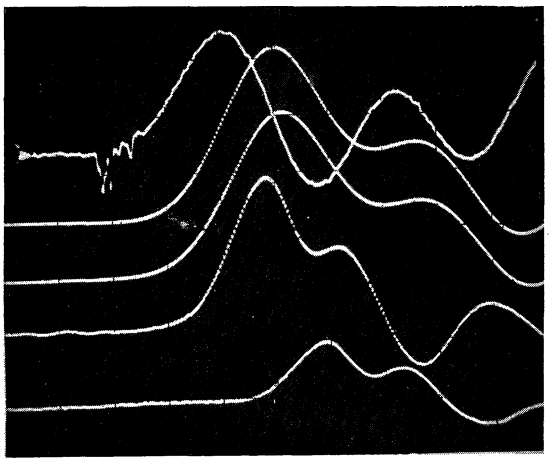

	Sensitivity (volts/div)	Calibration Factors
1	0.2	$67.7\frac{\text{ft-lb}}{\text{volt}}$
2	0.5	$1.35\frac{\text{volt}}{\text{(in/s)}}$
3	0.2	0.49
4	5m	0.66
5	5m	0.66

(a) Test J

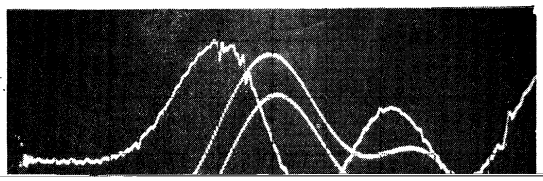

1	0.2	$67.7\frac{\text{ft-lb}}{\text{volt}}$
2	0.5	$1.35\frac{\text{volt}}{\text{(in/s)}}$

CHAPTER X

COMPARISONS BETWEEN EXPERIMENTAL AND NUMERICAL RESULTS

A. Introduction

In Chapter IX, the results were presented from several dynamic model footing tests (See Figs. 9.23(a) and 9.27). In this chapter, these experiments are simulated numerically using a nonlinear, inelastic half space to describe the test bed. In this half space, slip is permitted along the interface between the footing and the half space. In addition, Test G is modeled using a linearly elastic half space.

First, the details of these numerical models are given. Then numerical solutions, obtained using these models, are compared with experimental results. The discussion of solutions which was presented in Chapter VI, Section F applies equally to the solutions given in this chapter; therefore, very little discussion of results is presented.

B. Details of Numerical Models

1. Boundary Conditions

The boundary conditions which were used to obtain the numerical solutions presented in this chapter are identical to those given in Chapter VI, Section F.

2. Grids

Each numerical solution, except that based upon Test H, was obtained using a staggered grid consisting of 103 rows, each having 59 nodes. This grid and the footing are shown to scale with dimensions in Fig.10.1. The grid used to obtain the solution based on Test H consists of 127 rows, each having 71 nodes and represents a rectangular area having a depth of 2.80 ft and a width of 3.11 ft. In each grid, 8 nodes are located along the interface.

3. Properties of Test Bed

The properties of the test bed which were obtained experimentally and used in the numerical models include the average mass density, the average shear wave velocity and the average shearing strength along the interface. The values of these quantities are 3.17 slugs/ft^3, 470 fps and 150 psf (1.04 psi), respectively. The average shear wave velocity was based upon test results obtained from the upper two feet of the test

bed. It is the upper portion of the test bed which has the greatest effect upon the motion of the footing. Also, as shown in Fig. 9.17, it is the upper two feet of the test bed in which particle velocities were measured. All values of shear wave velocity from the appropriate profile are within 8.7% of the average value.

4. Properties of Half Space

a. Density--The mass density of the half space was given the value of the average mass density of the test bed: 3.17 slugs/ft^3.

b. Slip-Stress--The slip-stress, used in the nonlinear models, was given the value of the shearing strength of the test bed along the interface: 150 psf (1.04 psi).

c. Low Amplitude Shear Modulus--The entire half space in each of the models was assigned a single value of the low amplitude shear modulus. This value was calculated from the average shear wave velocity and is given as G_o = 700250 psf (4860 psi).

d. Shearing Strength--In order to define the nonlinear properties of the half space the values of the maximum shearing stresses which may be applied to the faces of an element, oriented as shown in Fig. 10.2, are needed. In torsion these maximum stresses,

designated as τ_{rm} and τ_{zm}, develop under conditions of constant normal stresses. Based upon the Mohr-Coulomb failure criterion, under the condition in which the lateral normal stresses are a fraction, K, of the vertical normal stresses, τ_{zm} may be given by

$$\tau_{zm} = \left\{\left[\frac{(1+K)}{2}\bar{\sigma}_v \sin\bar{\phi} + \bar{c}\cos\bar{\phi}\right]^2 - \left[\frac{(1-K)}{2}\bar{\sigma}_v\right]^2\right\}^{1/2} \qquad (10.1)$$

where $\bar{c}$ is the cohesion of the medium (Hardin and Drnevich, 1972). A similar equation may be derived giving τ_{rm}, which is determined by the lateral stresses alone, as

$$\tau_{rm} = K\bar{\sigma}_v \sin\bar{\phi} + \bar{c}\cos\bar{\phi} \qquad (10.2)$$

In each nonlinear model, the shearing strength of the half space was given the value of the shearing strength at one point within the test bed. In the numerical model of Test G this strength was based upon that obtained at a depth of 1 ft using Eq. (10.1). This depth is centered on the array of transducers within the test bed. The value of $\bar{\sigma}_v$, needed to calculate τ_{zm}, was obtained at this depth by assuming a

simplified distribution of vertical stresses developed within the central region of the test bed due to gravity and the loading from the surcharge pressure of 2 psi. Using the average value of the unit weight of the test bed, 102psf, this assumption gave a vertical stress of 390 psf at a depth of 1 ft. A value for K was obtained for this depth by using Eq. (9.1), Eq. (9.4) and the value of the shear wave velocity measured for this depth: 475 fps from Fig. 9.4. Using the average value of the void ratio of the test bed, 0.69, a value of 0.58 was obtained for K. The value of $\bar{\phi}$, 32.5°, was determined from a series of drained triaxial tests conducted on partially saturated samples of sand from the test bed.

Because the test bed was in a partially saturated state, during testing the sand had an apparent cohesion. The value of $\bar{c}$ which was used to determine τ_{zm} at a depth of 1 foot is that value of $\bar{c}$ which, when substituted into Eq. (10.1) along with the values of $\bar{\sigma}_v$ at the surface, $\bar{\phi}$ and K, gives the shearing strength along the interface as found by the torsional loading test. To determine this value of $\bar{c}$, the value of $\bar{\sigma}_v$ at the surface of the test bed, 288 psf (2psi), caused by the weight of the footing, the value of the shearing strength of the test bed along the

interface, 150 psf (1.04 psf), and the values of $\bar{\phi}$ and K were substituted into Eq. (10.1). This equation was solved for $\bar{c}$ giving a value of 47 psf (0.33 psi). Then the quantity τ_{zm} was obtained at the depth of 1 foot by substituting the value of the assumed vertical stress at this depth along with the values of K, $\bar{\phi}$, and $\bar{c}$ into Eq. (10.1). For the depth of one ft, τ_{zm} was calculated to be 187 psf (1.3 psi) by this procedure. Using these same values of $\bar{\sigma}_v$, K, and $\bar{c}$, a value of 160 psf (1.11 psi) was obtained for τ_{rm} from Eq. (10.2). Since, however, this value is reasonably close to that of τ_{zm}, for convenience, the value of τ_{zm} was also used for τ_{rm}.

In the numerical models of tests H, I and J, the shearing strength of the half space was given the value of the shearing strength along the interface: 150 psf (1.04 psi). This value is believed to be an improved estimate over the larger value used in the model of test G. This is because in a sand the shear wave velocity and the shearing strength depend strongly upon the same parameters: the confining pressure and void ratio. Thus, assuming uniform water contents, the curves of shear wave velocity vs. depth (see Fig. 9.4) may be used as rough guides indicating the nature of the variation of shearing strength within the test bed. As shown in Fig. 9.4, for the surcharge pressure of 2 psi, the shear

wave velocity within the test bed decreased slightly with depth. This indicates that the confining pressure decreased with depth (Eq. (9.1)). In a sand, shear wave velocity is a function of $\overline{\sigma_o}^{0.5}$ and shearing strength is a function of $\overline{\sigma_o}$ (Richart, 1977). Thus the shearing strength is also thought to have decreased with depth for this surcharge pressure. During the excavation of boreholes in preparation for the crosshole tests, at the maximum surcharge pressure, the upper surface of the test bed was noticeably more resistant to penetration of the hand auger than the test bed at depth. This observation indicates that the curves in Fig. 9.4 do give reasonable indications of trends in the shearing strength within the test bed.

A uniform rather than a decreasing profile of shearing strength was used in the numerical model of tests H, I and J primarily to maintain simplicity. This is a reasonable assumption because the profile of the shear wave velocity for the surcharge pressure of 2 psi is reasonably uniform (See Fig. 9.4).

To model linear behavior under the stresses developed, the shearing strength of the half space of the linear model was assigned the relatively large value of 6250 psf (43 psi).

e. Ramberg-Osgood Coefficients--For each of the nonlinear models the Ramberg-Osgood coefficients, α and R, were assigned values of 1.0 and 3.0, respectively. Richart (1975) has found that these values give stress-strain curves which give good agreement over a broad range of stress with stress-strain curves obtained from tests conducted on sands. To promote linear behavior, α was assigned the relatively low value of 0.1 in the linear model.

f. Discussion--In the nonlinear numerical model it was assumed that the parameters which define the nonlinear stress-strain curves in either of the coordinate directions are unaffected by the state of stress in the other direction. This assumption is not believed to be strictly valid for granular materials. Shearing stresses applied in either coordinate direction cause shearing stresses to develop at intergranular contacts which affect the elastic rigidity and the strength in the other direction. An improved model of the shearing stress-strain behavior at a point is believed to be one in which the behaviors in the two coordinate directions are interrelated.

g. Weak Zone--The weak zone surrounding the edge of the footing and caused by the lack of confining pressure in this zone was taken into account in the

nonlinear models. For these models a zone approximately 1/2 inch in depth and 1/2 inch wide located at the edge of the footing was given values of moduli equal to 70 psf. The size of this zone was based upon the width of the unconfined ring, 1/2 inch, and the manner in which stresses spread with depth.

5. Mass Moments of Inertia of Footing

For test G the mass moment of inertia of the footing was 0.155 slugs-ft^2. For tests H, I and J a pair of vertical velocity transducers attached to the footing had been removed causing a reduction in the mass moment of inertia to 0.145 slugs-ft^2.

6. Computing Information

In each analysis, results were obtained for a duration of 0.00718 sec. using a time step of 0.0000472 sec. Each solution was obtained using an Amdahl 470V/6 computer and a Fortran G-level compiler. A CPU time of 1090 sec was needed to obtain the solution corresponding to test H and 627 sec were required for each of the remaining solutions.

C. Results

1. Motion of Footing

The measured and computed responses of the footing to the measured applied moments are presented in

Figs. 10.3 through 10.10 for each test. The angular velocity of the footing vs. time is given in Figs. 10.3 through 10.6 and the angular displacement of the footing vs. time is given in Figs. 10.7 through 10.10. In each of these figures the measured applied moment vs. time is also presented for reference. In addition, corresponding results from the linear analysis are given in Figs. 10.3 and 10.7.

As indicated by these figures the agreement between experimental and nonlinear numerical results is good while that between experimental and linear numerical results is poor. As explained in Chapter VI, differences between results from the linear and nonlinear analyses are caused by the effects of the properties of the half space on the distribution of τ_z-stress along the interface. This stress distribution is plotted in Fig. 10.11 for the linear and the nonlinear models for times at which each distribution is at the maximum state.

2. Particle Velocities Within Half Space

The particle velocities vs. time, which were obtained for selected locations within the half space (see Fig. 9.17), are given in Figs. 10.12 through 10.16. In Figs. 10.14 through 10.16 (tests H, I and J) the

particle velocities which were obtained experimentally are presented as processed by Fourier analysis in the manner explained in Chapter VIII. Such processing was not needed for the records from test G, shown in Figs. 10.12 and 10.13, since the responses from the transducers in this test were not filtered. In each of Figs. 10.12 through 10.16, the measured and computed velocities of the edge of the footing vs. time are plotted as a reference.

Oscillations develop in the latter portions of the records from the numerical solutions corresponding to tests H, I and J. There are a number of possible reasons for these oscillations. The most probable reason is that the grid was not quite fine enough for the degree of nonlinearity developed in the models of these tests. Greater nonlinearity was developed in these models than in the model of test G because in the models of test H, I, and J the half space was treated as a weaker material. These oscillations did not influence the motion of the footing significantly.

As shown in Fig. 10.12, the nonlinear model gives much better agreement with measured results than the linear model. In general the peaks of the particle velocities from nonlinear models are approximately twice as large as those obtained experimentally. The motion

at the sites of the velocity transducers is believed to have been suppressed by the relatively large mass of the transducers. These transducers are approximately 2.5 inches long, 1.67 inches in diameter and roughly 3 times as dense as the surrounding soil. The excess mass provided by these transducers was not taken into account in the numerical models. The differences between the shapes of the waveforms given by the nonlinear models and the experiment (see Figs. 10.12 through 10.16) are also believed to have been caused by effects of the excess mass of the transducers.

As indicated in Figs. 10.12 through 10.16, each of the numerical models predicts fairly accurately the arrival time of the disturbance at points within the half space.

In Table 10.1 is given the ratio of the peak velocity of the edge of the footing to the peak of the particle velocity within the half space. This ratio is given for each of the locations within the half space designated in Fig. 9.17. These ratios are based upon results obtained from the nonlinear solutions and may also be obtained from Figs. 10.14 through 10.16. The information given in Table 10.1 indicates that particle velocities within the half space are much smaller than the velocity of the edge of the footing. Also geometric

decay of the disturbances is observed within the half space with increasing distance from the edge of the footing. As an example, the velocity of the edge of the footing is 26 times larger than the particle velocity computed for the site nearest to the edge of the footing (near transducer, test J) and 300 times larger than that for the site furthest from the edge of the footing (far transducer, test H).

Table 10.1: Ratio of Peak Velocity of Edge of Footing to Peak of Particle Velocity at Indicated Site within Half Space (See Fig. 9.17). Based on Results from Nonlinear Numerical Model.

Test	Site of Near Transducer	Site of Far Transducer
H	123	300
I	39	105
J	26	69

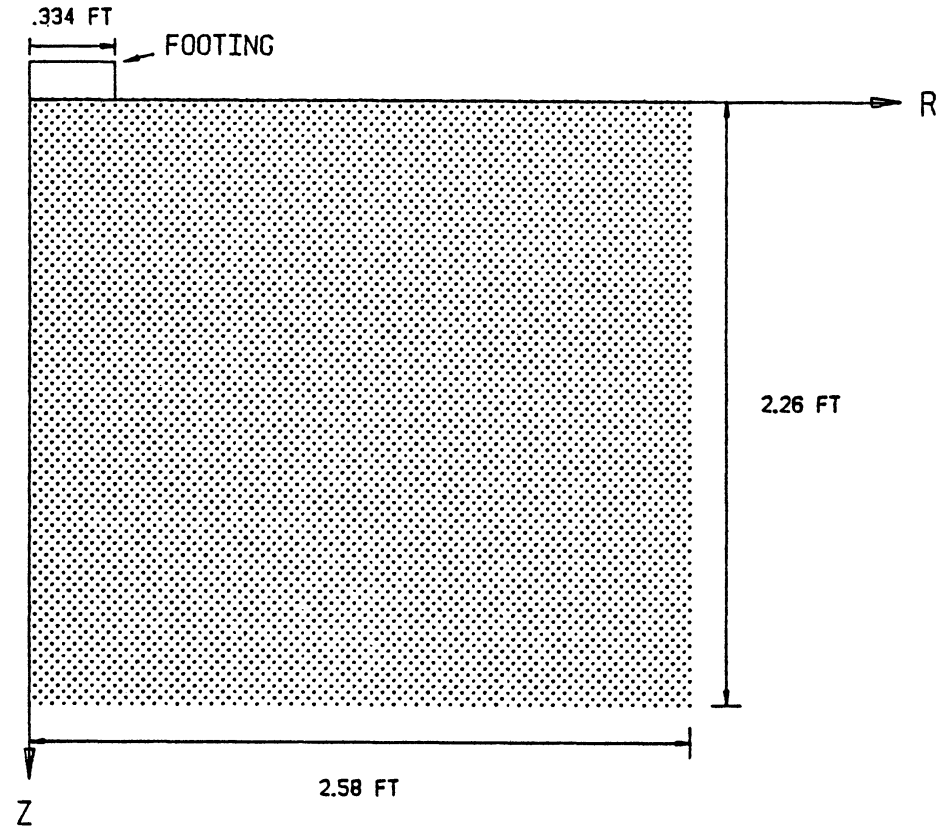

Fig. 10.1: Grid Used to Model Tests G, I, and J Numerically.

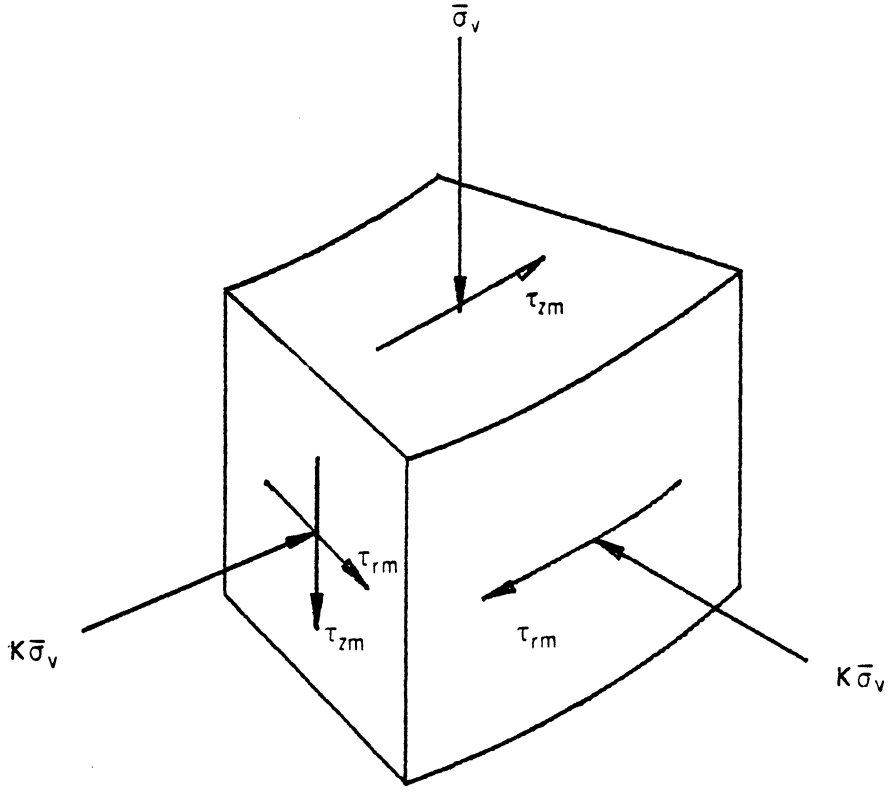

Fig. 10.2: Normal and Maximum Shearing Stresses Acting on Faces of Element.

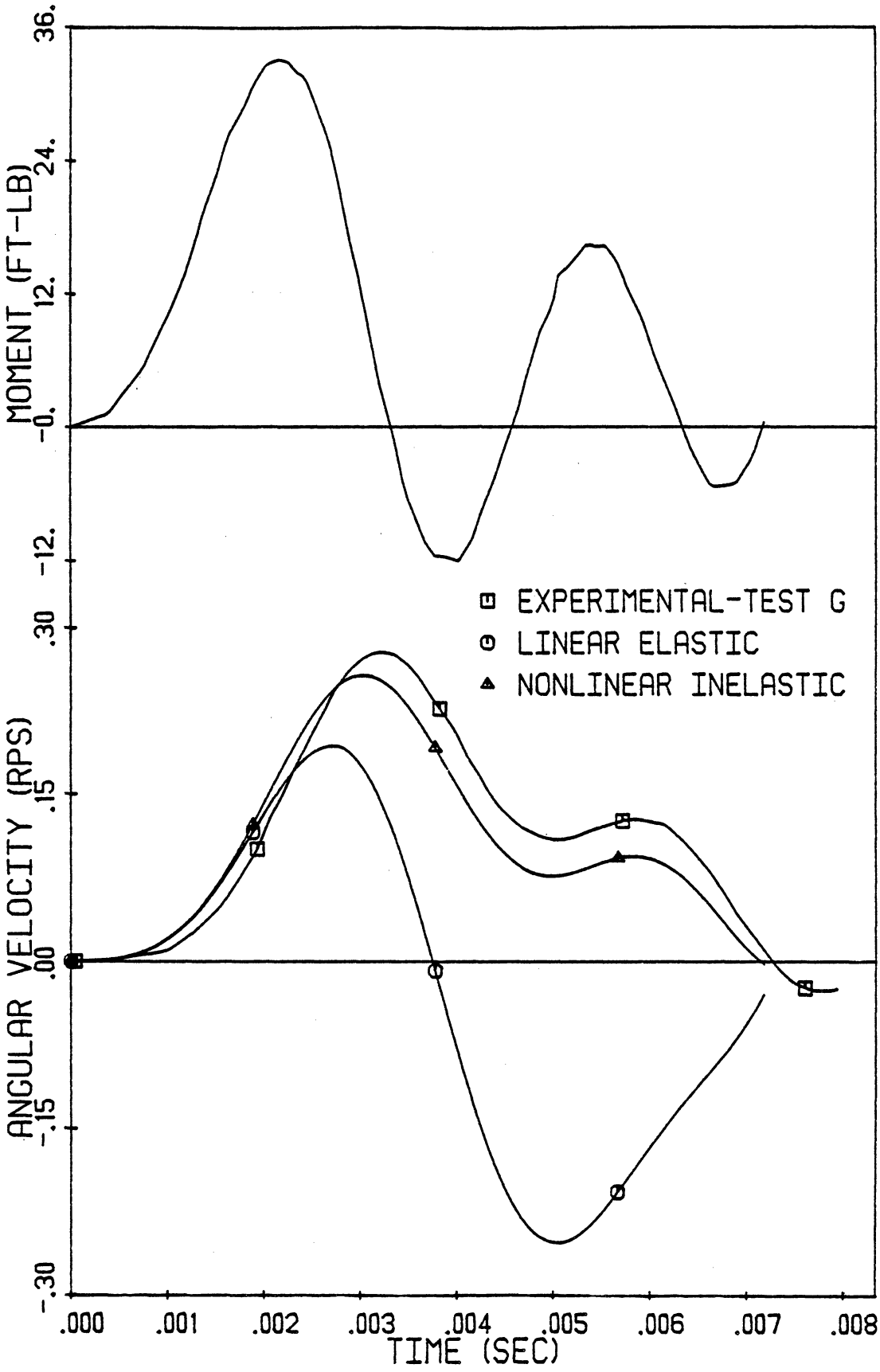

Fig. 10.3: Measured Applied Moment and Measured and Computed Response of Footing vs. Time (Test G).

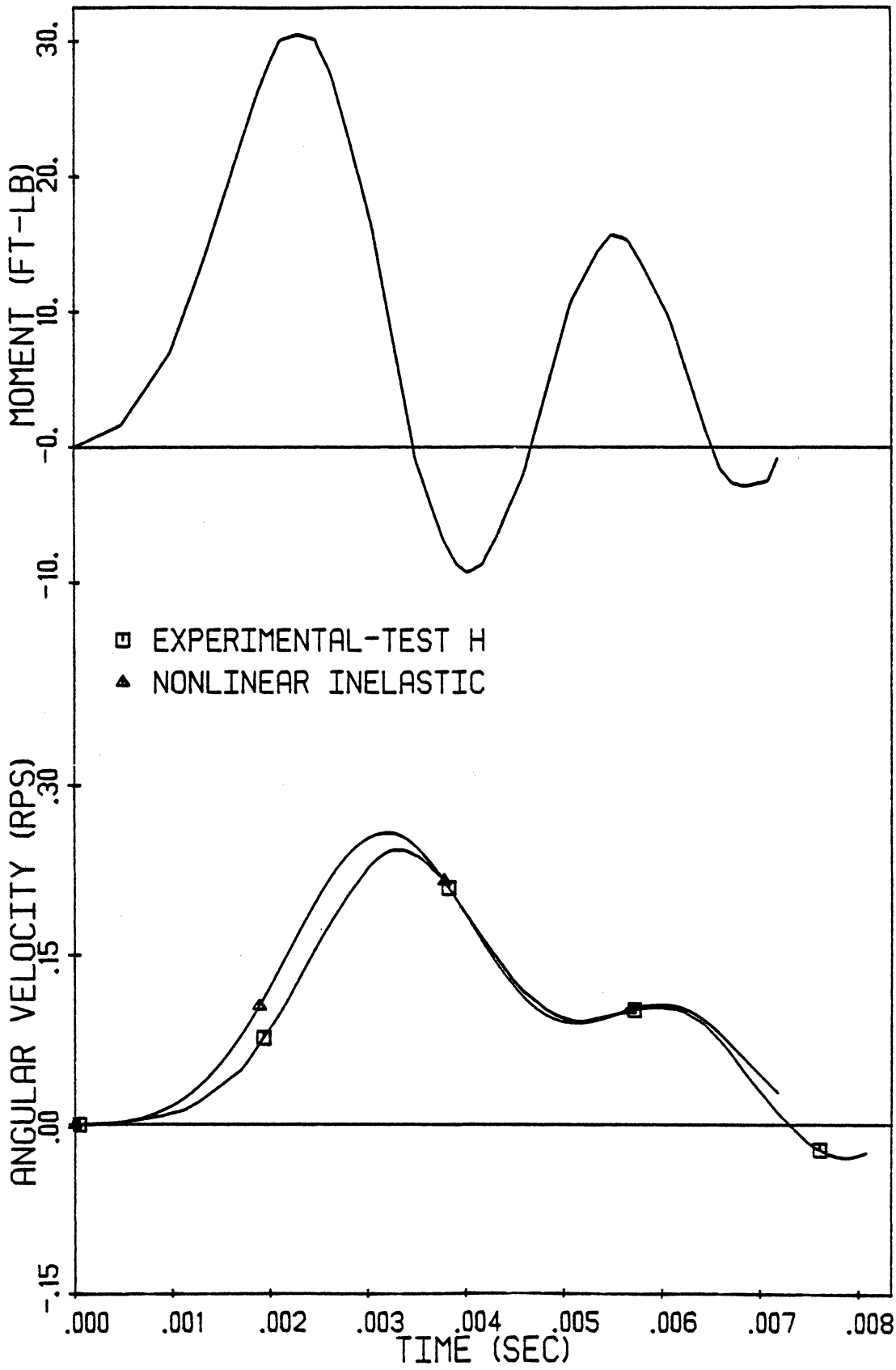

Fig. 10.4: Measured Applied Moment and Measured and Computed Response of Footing vs. Time (Test H).

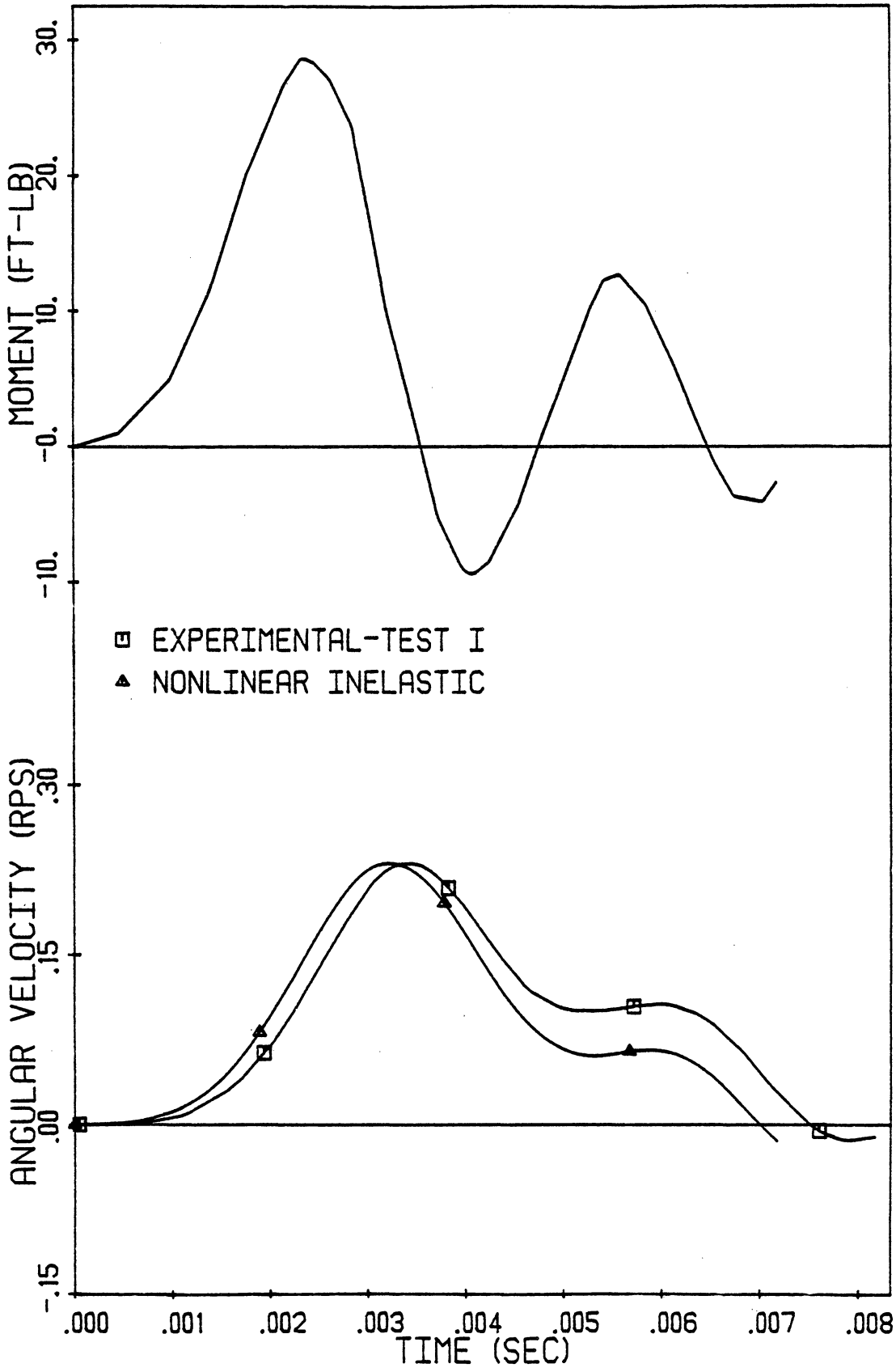

Fig. 10.5: Measured Applied Moment and Measured and Computed Response of Footing vs. Time (Test I).

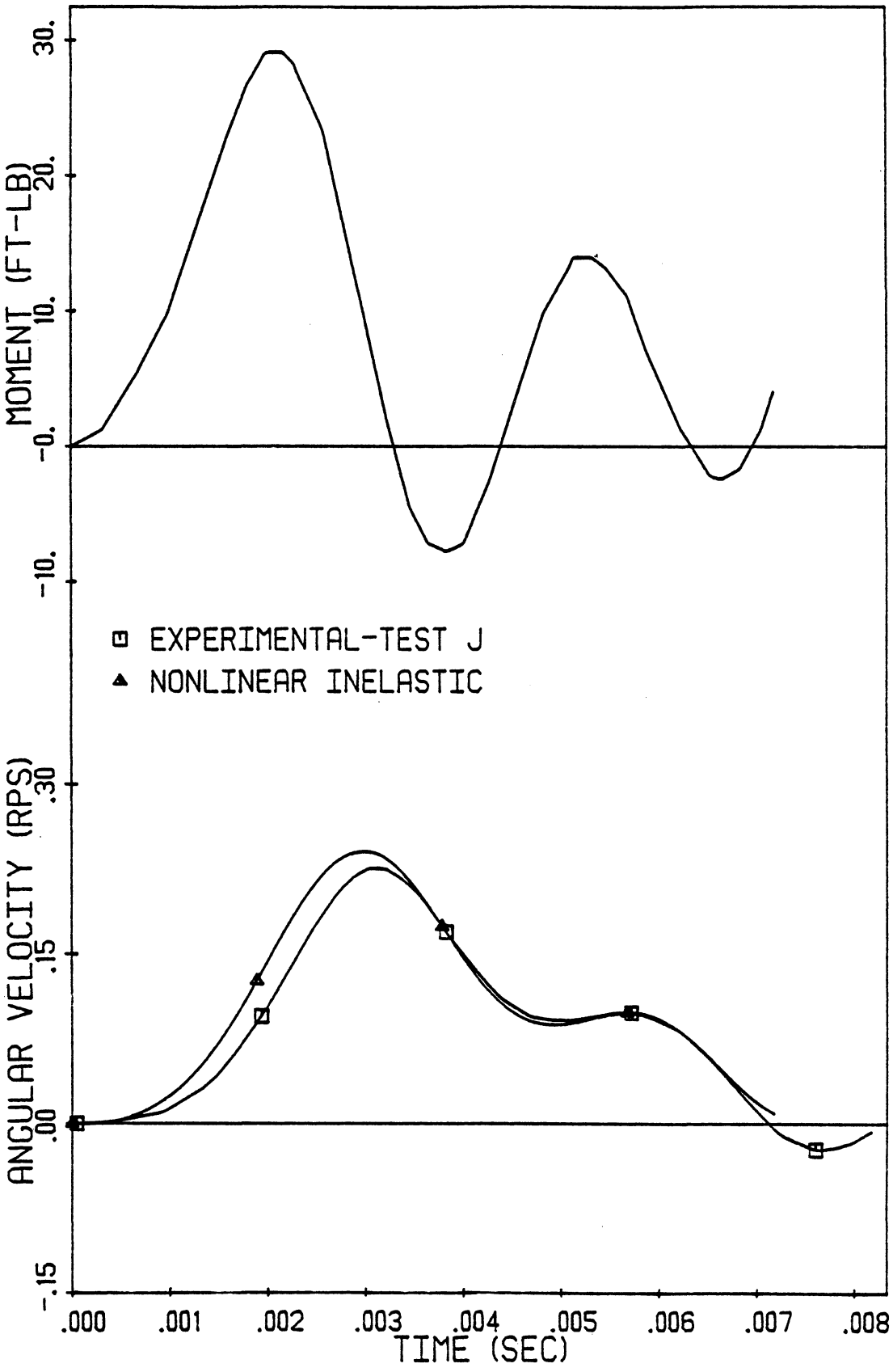

Fig. 10.6: Measured Applied Moment and Measured and Computed Response of Footing vs. Time (Test J).

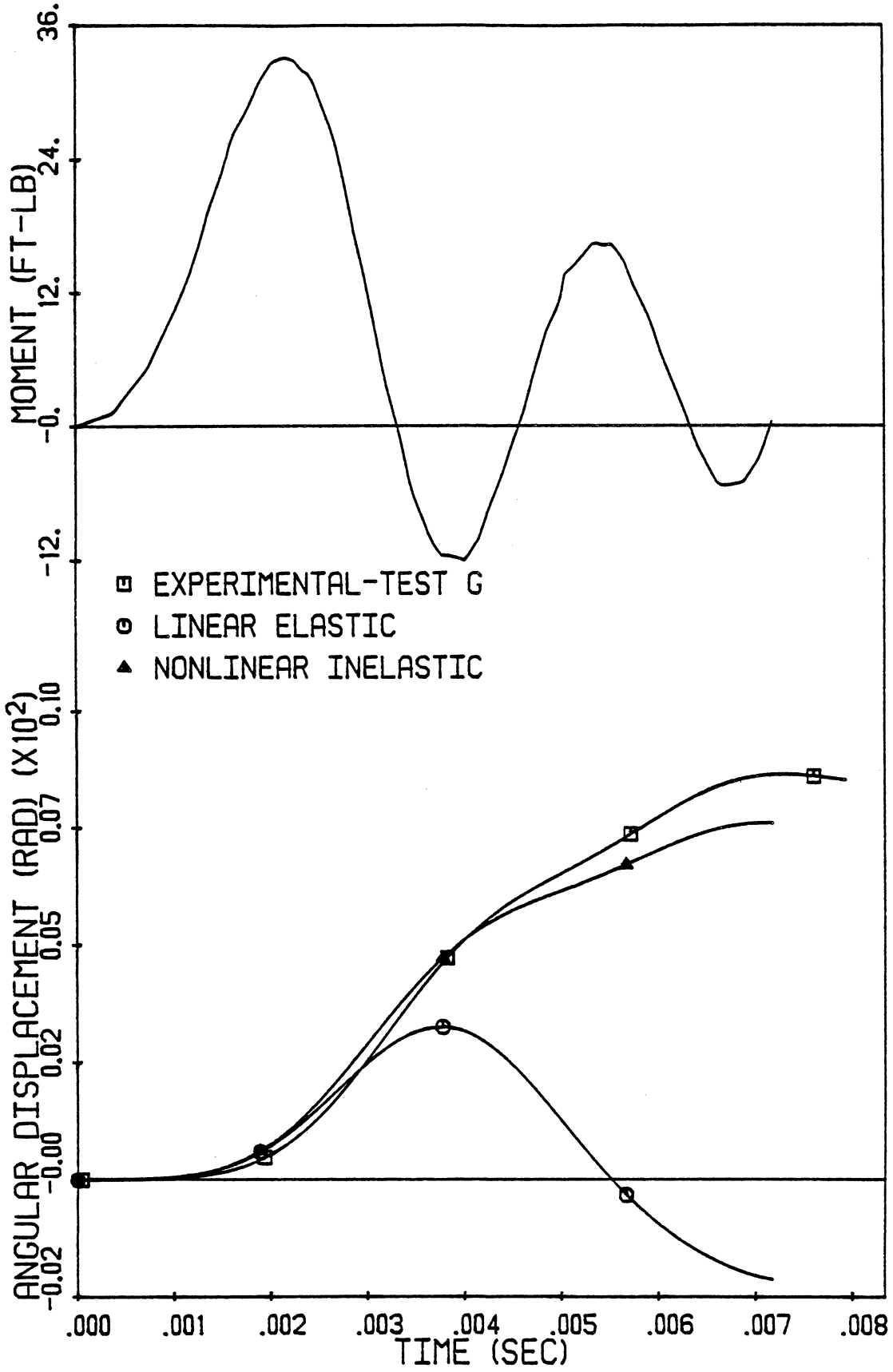

Fig. 10.7: Measured Applied Moment and Measured and Computed Response of Footing vs. Time (Test G).

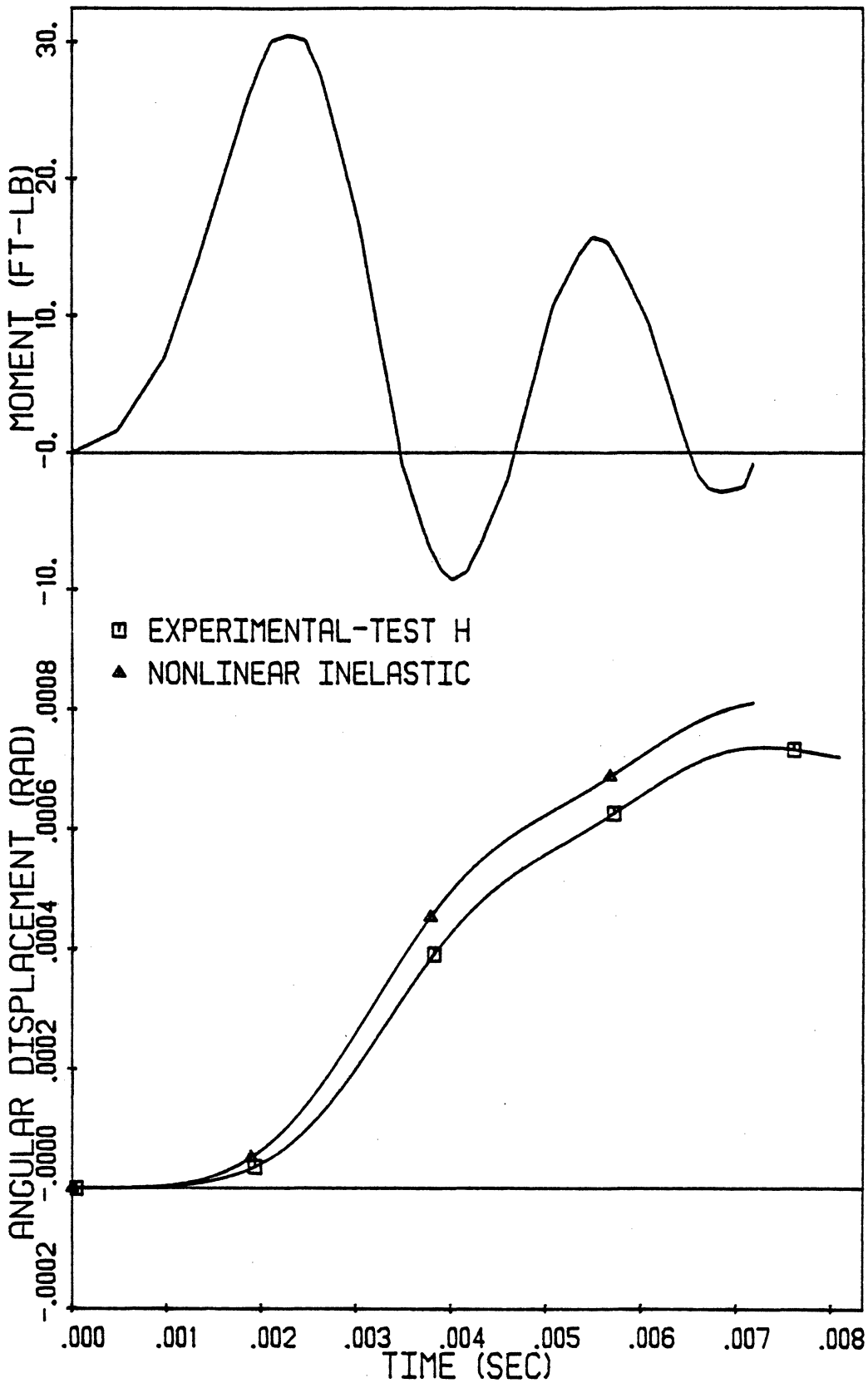

Fig. 10.8: Measured Applied Moment and Measured and Computed Response of Footing vs. Time (Test H).

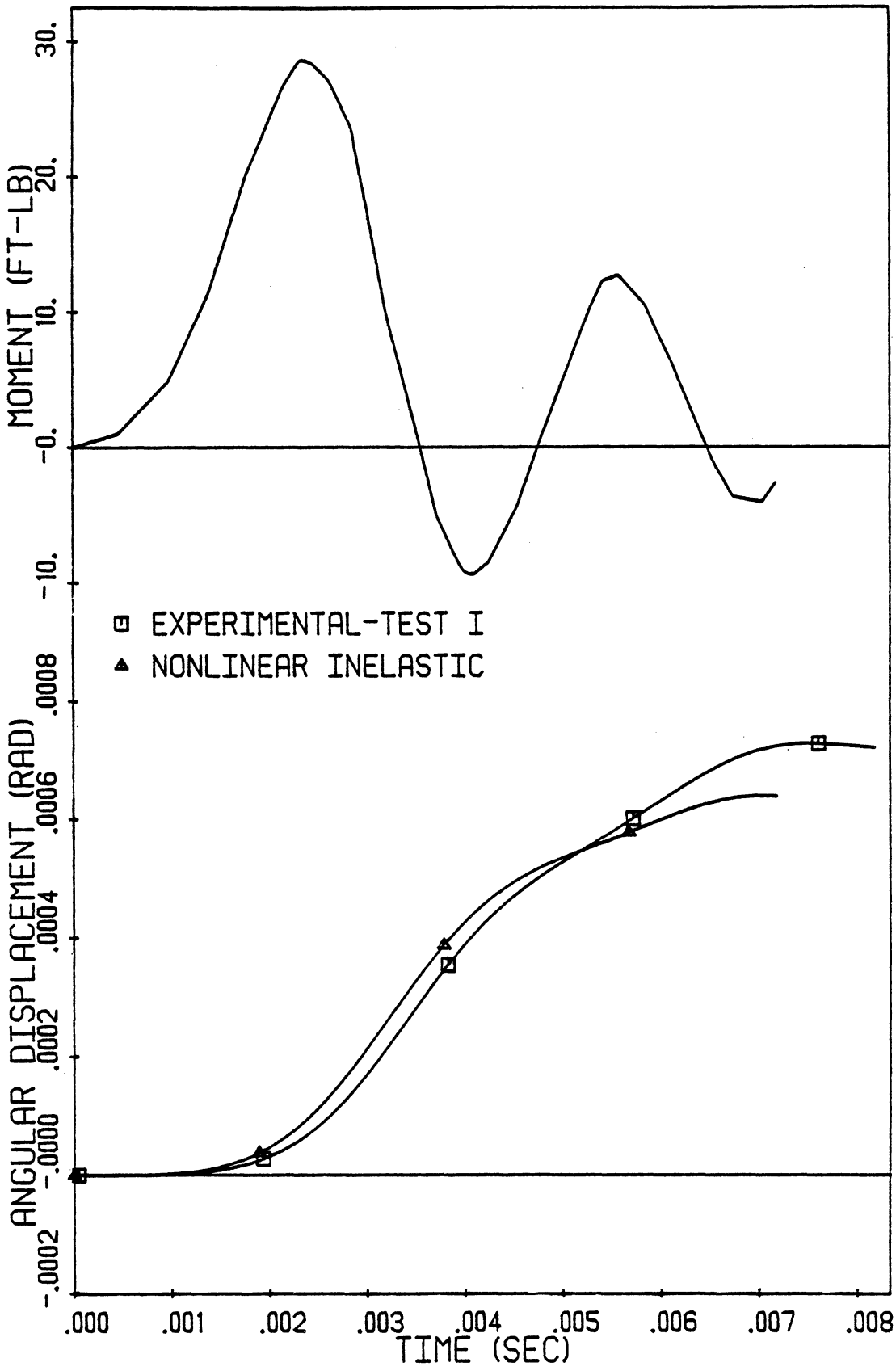

Fig. 10.9: Measured Applied Moment and Measured and Computed Response of Footing vs. Time (Test I).

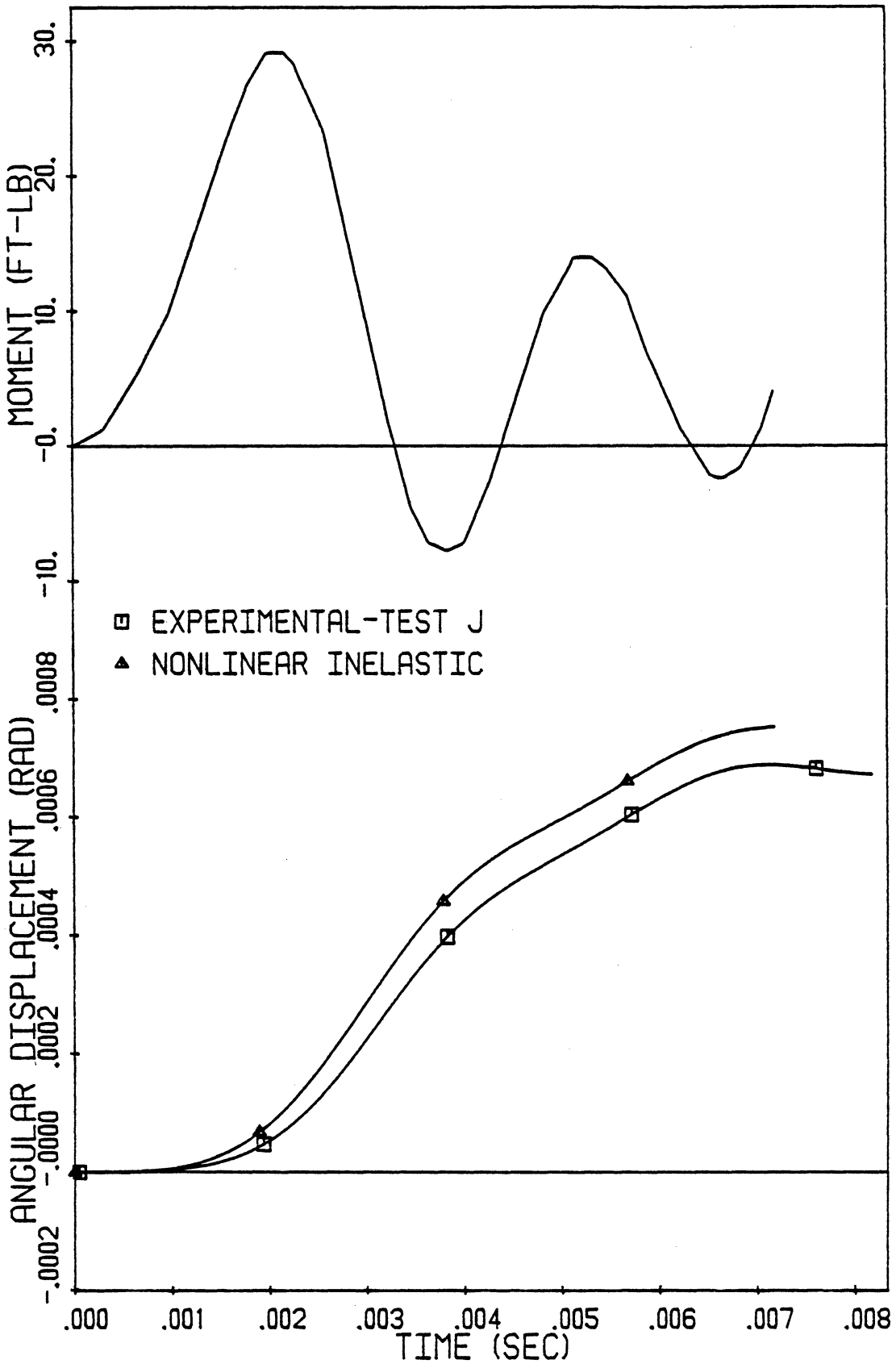

Fig. 10.10: Measured Applied Moment and Measured and Computed Response of Footing vs. Time (Test J).

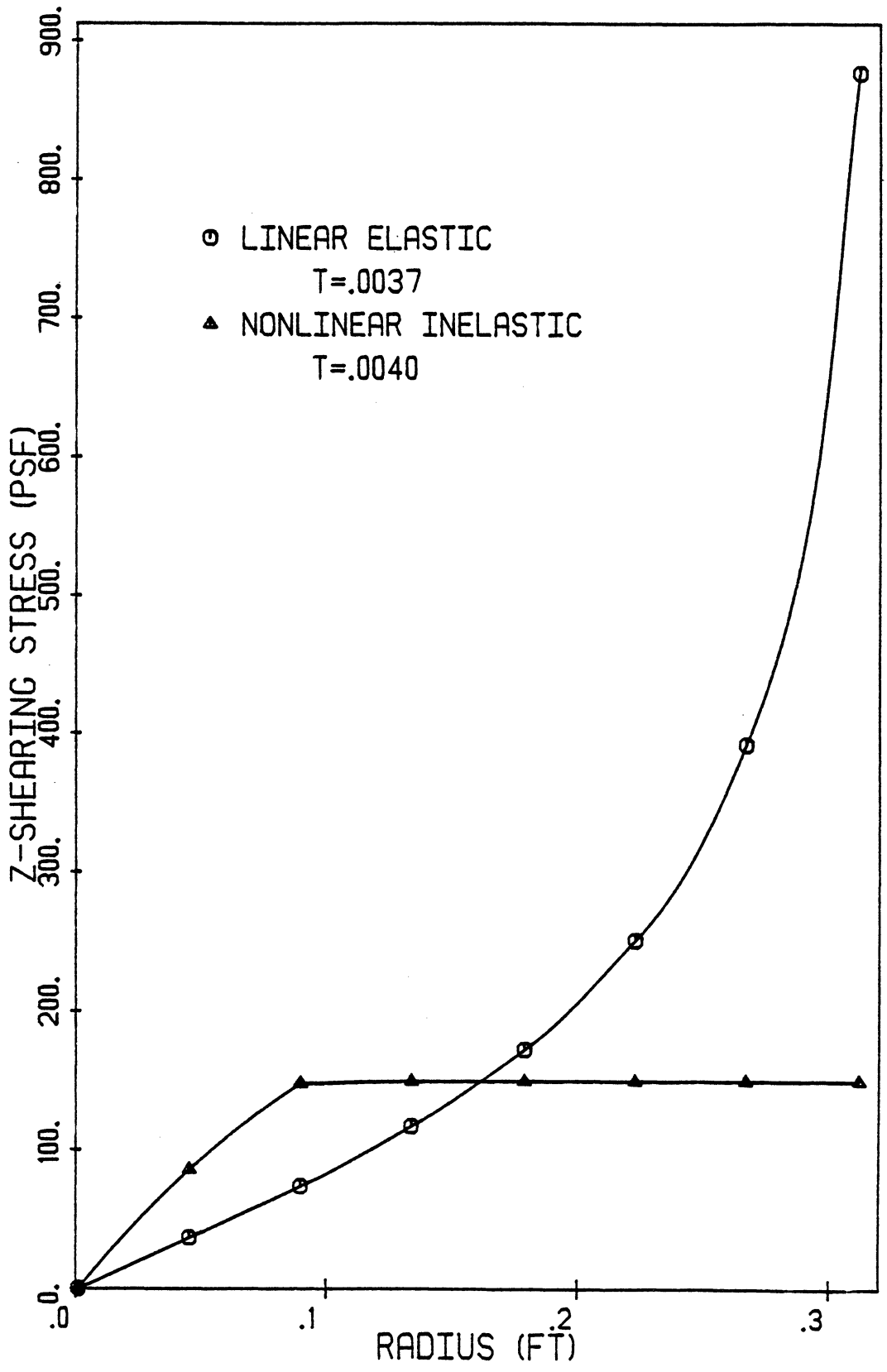

Fig. 10.11: τ_z-Stress vs. Radius Along Interface.

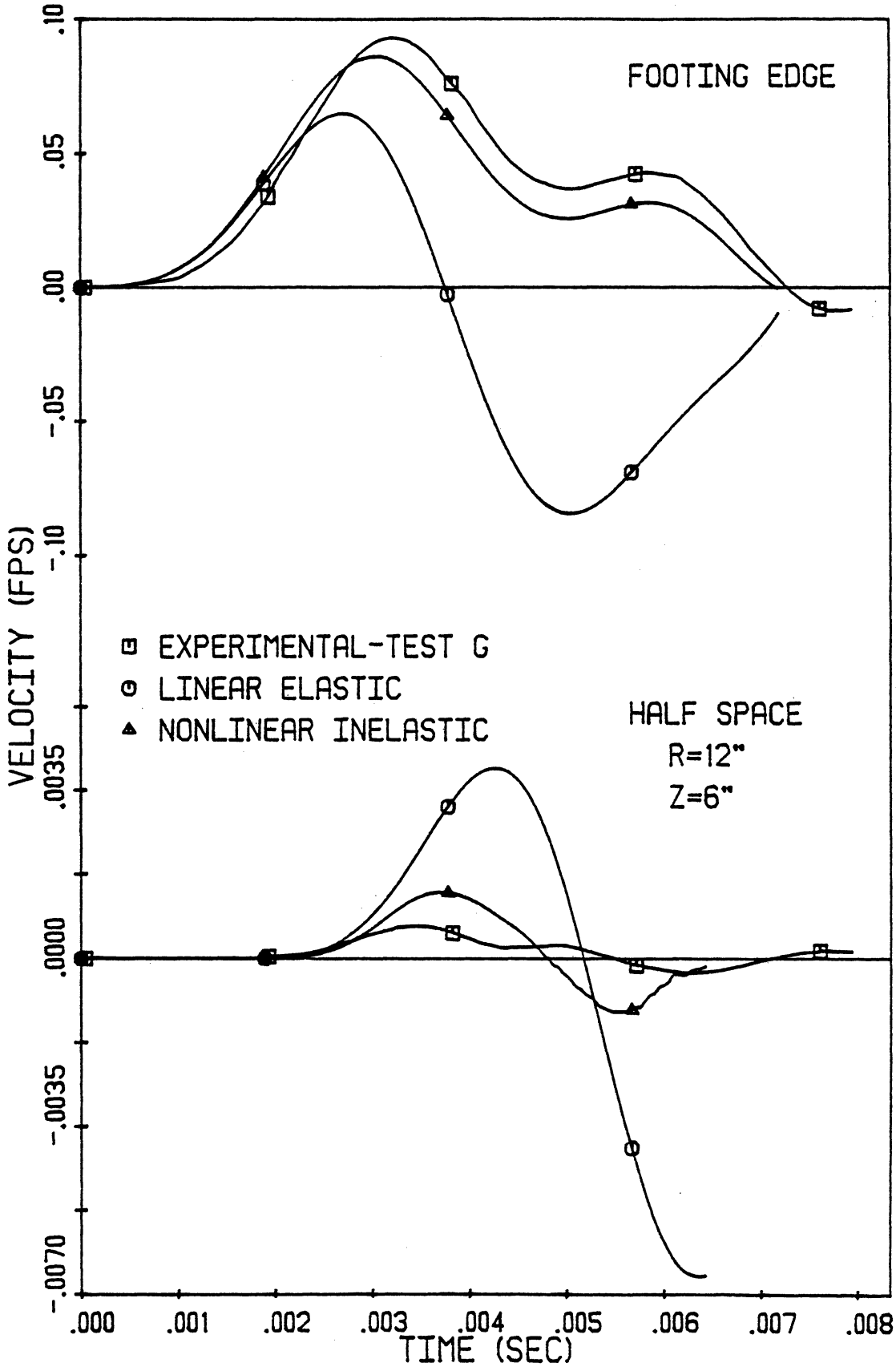

Fig. 10.12: Velocities of Edge of Footing and Particle Velocities Within Half Space (Test G).

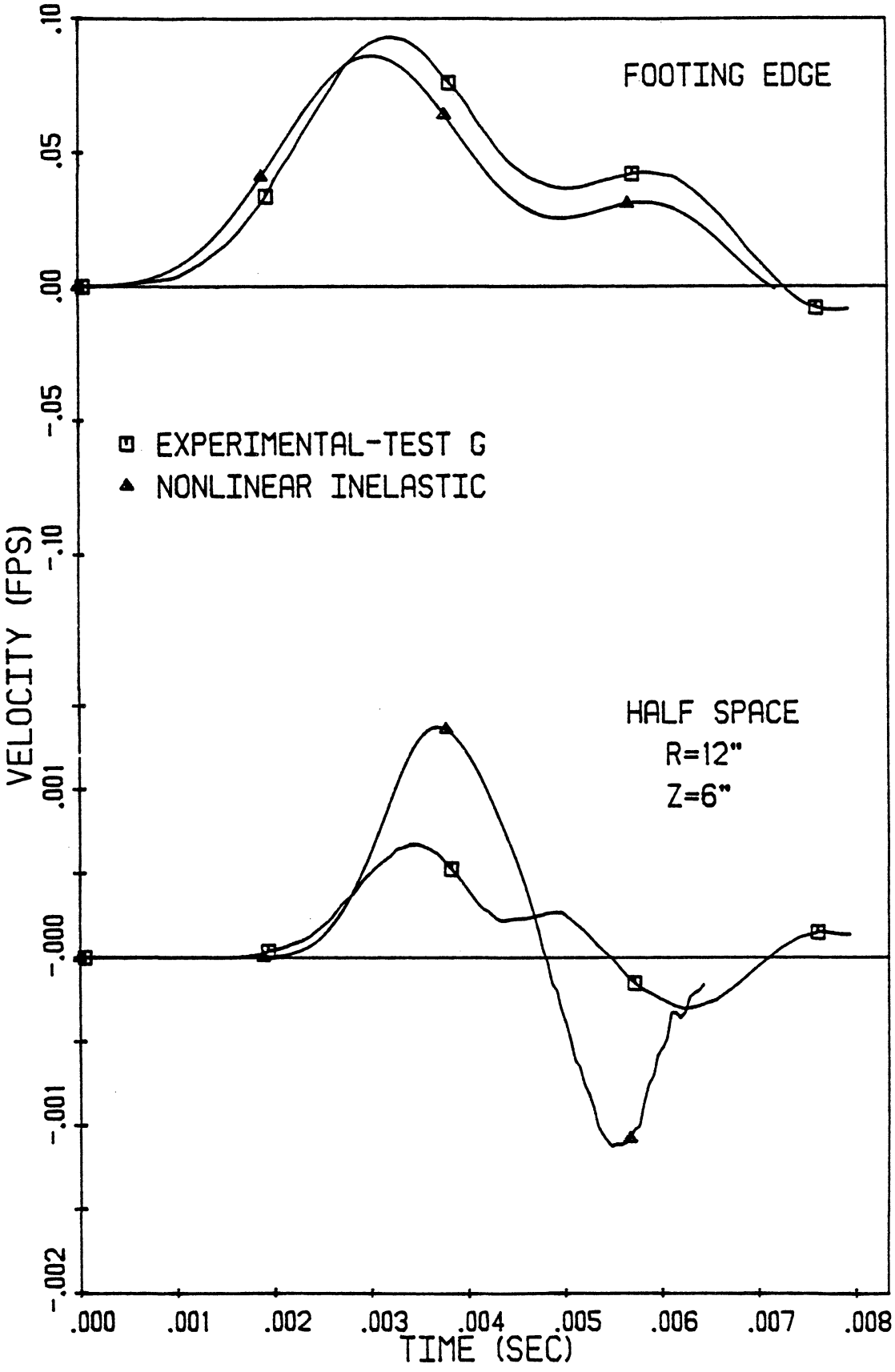

Fig. 10.13: Velocities of Edge of Footing and Particle Velocities Within Half Space (Test G).

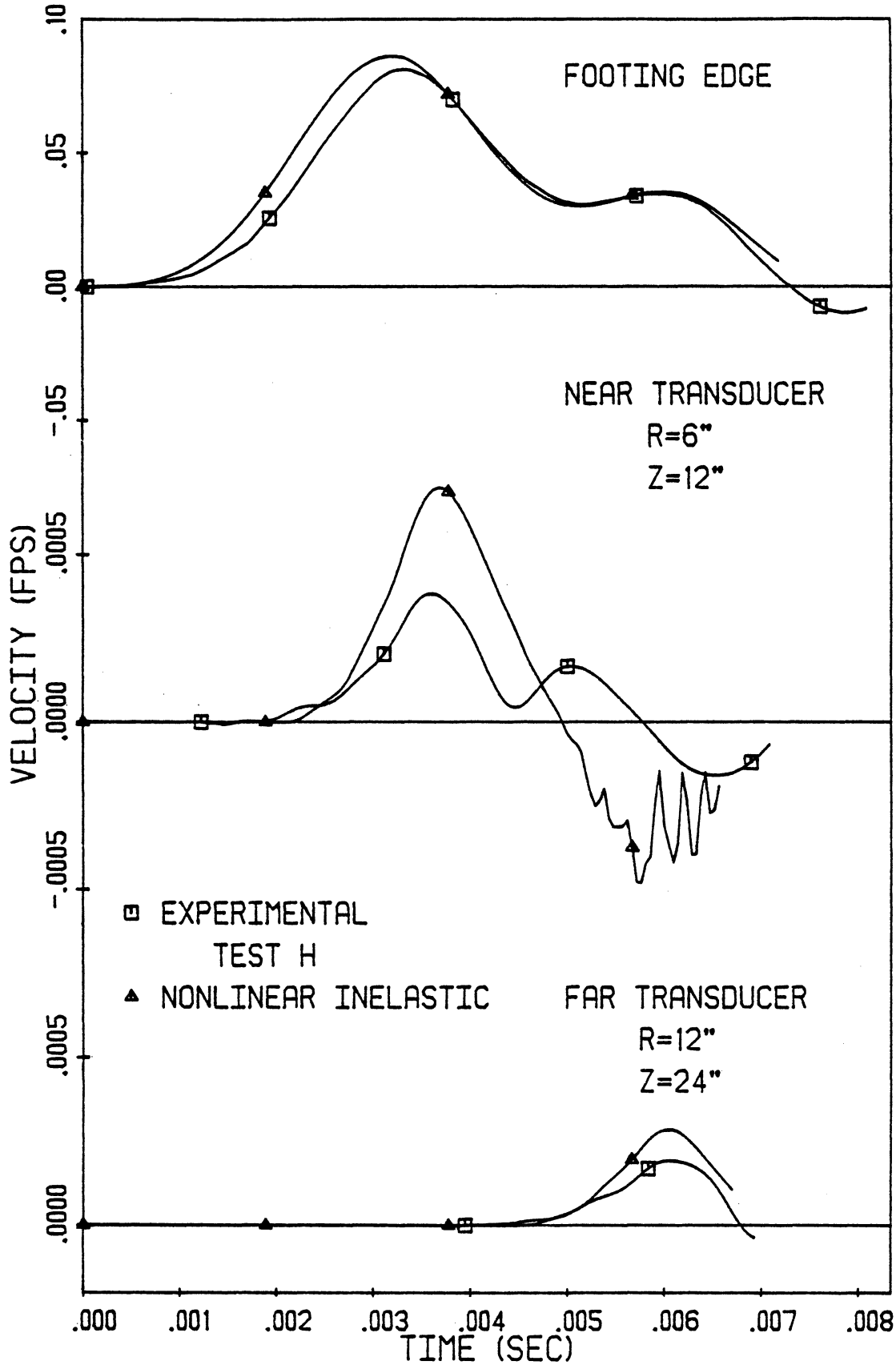

Fig. 10.14: Velocities of Edge of Footing and Particle Velocities Within Half Space (Test H).

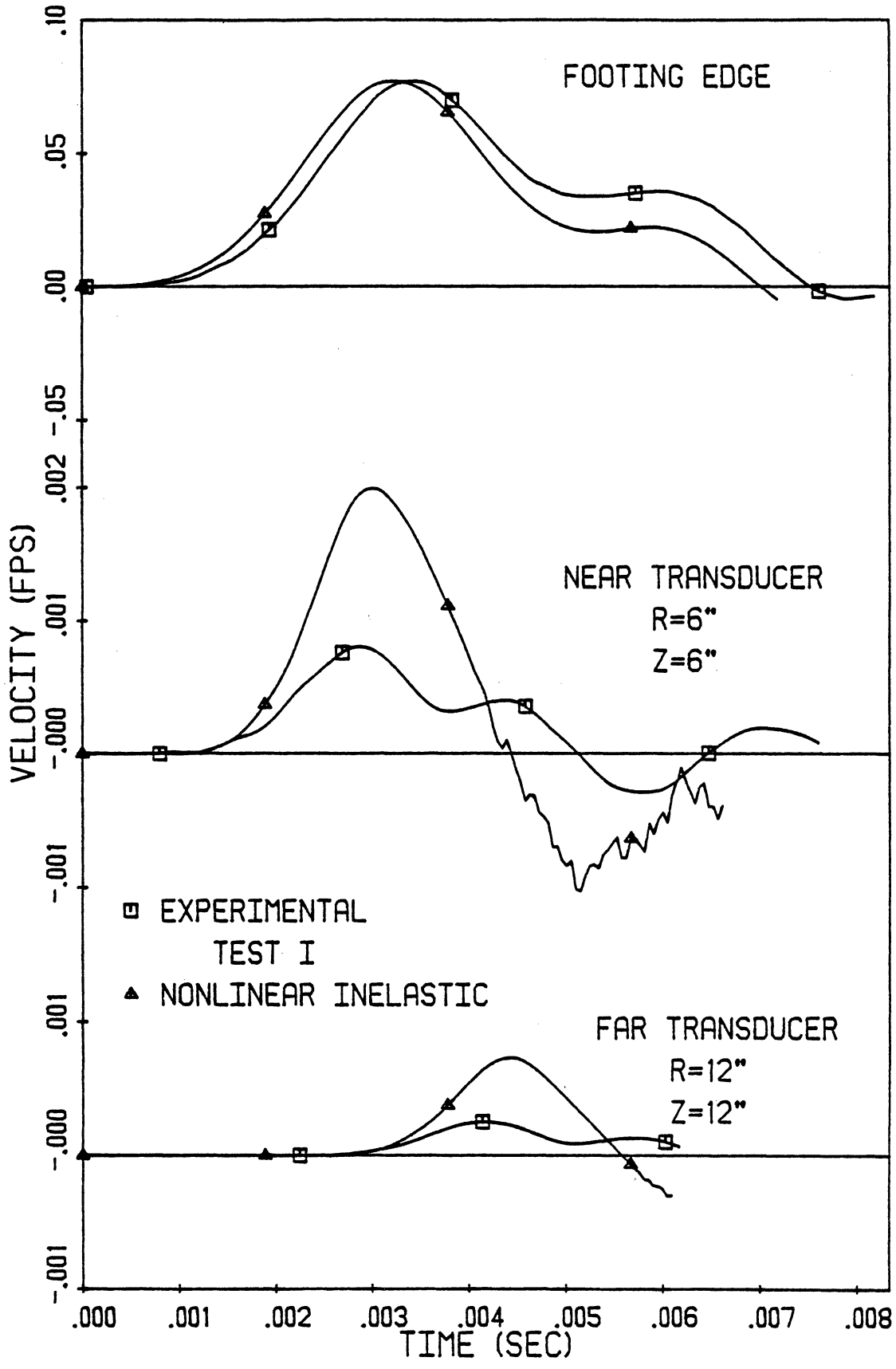

Fig. 10.15: Velocities of Edge of Footing and Particle Velocities Within Half Space (Test I).

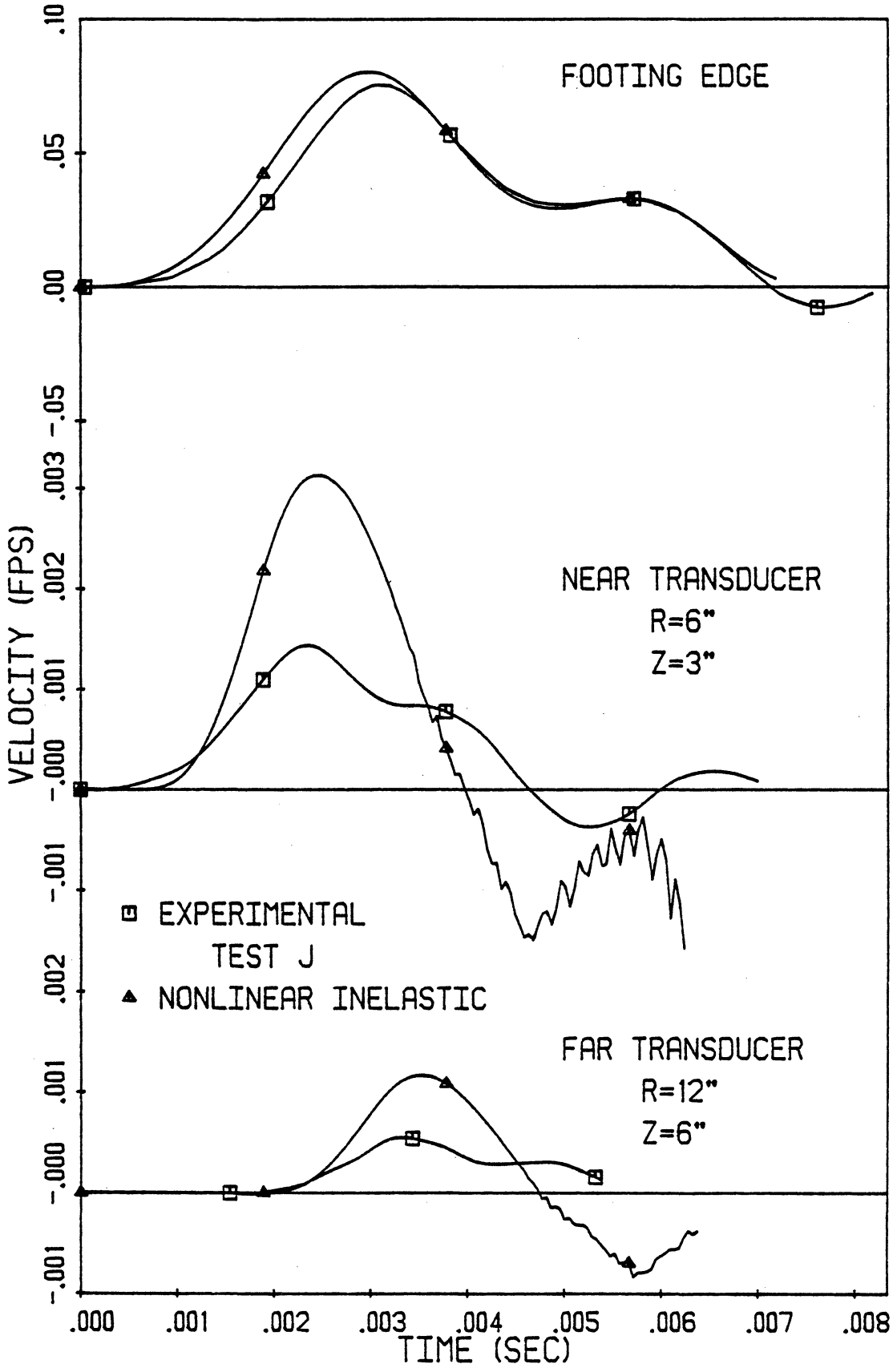

Fig. 10.16: Velocities of Edge of Footing and Particle Velocities Within Half Space (Test J).

CHAPTER XI

SUMMARY

Using the technique described in Chapter III, a numerical procedure capable of solving the equations governing axisymmetric, two-dimensional, torsional wave propagation within an elastic medium was formulated. Solutions obtained using this procedure was found to agree nearly exactly with several one-and two-dimensional theoretical solutions involving wave propagation in various elastic media. For one problem, however, that of a rigid disk on a half space, the theoretical solution, which gives infinite shearing stresses within the half space at the periphery of the disk, was only approached. Soils cannot withstand infinite stresses and since these stresses affect significantly the response of a disk having mass it was concluded that the elastic solution was not realistic for soils.

To limit the magnitudes of stresses the numerical procedure was reformulated to allow nonlinear inelastic shearing stress-strain properties. Also for the

disk on a half space problem, slip was permitted along the interface between the disk and the half space. Solutions were obtained for one-dimensional problems and two-dimensional problems involving a disk resting on a half space and excited torsionally. In each case the medium was treated as a linear elastic and nonlinear inelastic material. Ramberg-Osgood equations were used to describe the shearing stress-strain properties of the media. The adequacy of the grids and the correctness of these solutions were checked using an energy balance. Work and energy were found to approach a balanced state as the fineness of the grids was increased. The properties of the media were found to affect significantly the amplitudes and shapes of disturbances within the media and the response of the disk. The disk was found to undergo permanent angular displacements when treating the half space as a nonlinear inelastic material which permitted slip along the interface.

To verify the practical application of the numerical procedure, several experiments were conducted. In these experiments, torsional impulses inducing large strains were applied to a rigid model footing resting on a pressure confined granular test bed. The applied torque, the angular velocity of the footing, and the particle velocities within the test bed were measured.

These tests were similated numerically using linear elastic and nonlinear inelastic models for the half space. The low amplitude shear modulus and the shearing strength of the test bed, needed to define the stress-strain properties of the half space, were obtained by conducting torsional seismic crosshole tests and a static torsional loading test within the test bed, respectively.

In response to the measured loadings, the nonlinear model predicted the motion of the footing quite well while the linear model did not. Each model predicted accurately the arrival times of disturbances at selected sites within the test bed. However, the linear model overestimated the amplitudes of these disturbances by a factor of 7 and the nonlinear model, on the average, by a factor of 2. The excess mass of the transducers used to measure the motions of the test bed was believed to have suppressed particle motions at these locations. This factor was not taken into account in the numerical solutions. Because the amplitudes of the motions within the test bed were very small absolutely (measured as 0.0014 to 0.00019 fps) and relative to those of the edge of the footing (measured as 50 to 450 times larger) the agreement given by the nonlinear model was quite reasonable.

CHAPTER XII

CONCLUSIONS

The shearing stress-strain properties of the soil in a soil-structure system have a large effect on the response to dynamic loads of the structure and the soil. Nonlinear inelastic soil behavior, which develops at high amplitudes of strain, causes energy dissipation, affects the distribution of energy, affects the amplitudes and shapes of disturbances within the soil, affects the motion of the structure, and causes permanent deformation of the soil and permanent displacement of the structure. Thus, in order to predict accurately the dynamic response of soil-structure systems under conditions in which large shearing strains develop, nonlinear inelasticity of the soil must be taken into account.

A method leading to a practical numerical procedure was developed. This procedure may be used to predict accurately the torsional response of a soil-structure system consisting of a rigid circular footing resting on either a linear elastic or nonlinear

inelastic half space. Thus the method was applied to a two-dimensional system. This method is potentially general, perhaps permitting the solution of practical multi-dimensional problems involving compression as well as shearing disturbances. Such problems include the predictions of the vertical and rocking motions of various types of foundations as well as the motions of soil masses subjected to dynamic loadings. Effort must be directed towards reducing computational storage space and time needed to obtain solutions. Several possible and very significant means of meeting these goals include the use of grids with variable spacings between nodes, the use of boundaries within the half space and localized treatment of nonlinear inelasticity.

APPENDICES

APPENDIX I

NODAL POINT EQUATIONS AND COEFFICIENTS

The nodal point equations, which represent the integrated form of the differential equations [Eqs. (3.34) or Eqs. (5.25)], are given as

$$\begin{aligned} a_1\tau_{rp} + b_1\tau_{zp} + c_1 v_p + d_1 \frac{\partial \tau_z}{\partial r}\Big|_p &= e_1 \\ a_3\tau_{rp} + b_3\tau_{zp} + c_3 v_p + d_3 \frac{\partial \tau_z}{\partial r}\Big|_p &= e_3 \\ a_5\tau_{rp} + b_5\tau_{zp} + c_5 v_p + d_5 \frac{\partial \tau_z}{\partial r}\Big|_p &= e_5 \\ a_7\tau_{rp} + b_7\tau_{zp} + c_7 v_p + d_7 \frac{\partial \tau_z}{\partial r}\Big|_p &= e_7 \end{aligned} \tag{3.37}$$

For the linearly elastic model the coefficients in Eqs. (3.37) are given as

$$\begin{aligned} a_1 &= 2 - \frac{r_B}{r_p} \\ b_1 &= -\frac{3}{2} + \frac{r_B}{2r_p} \\ c_1 &= \rho v_s \left(-\frac{1}{2} - \frac{r_B}{2r_p}\right) \\ d_1 &= r_p - r_B \\ e_1 &= \left(2 - \frac{r_p}{r_B}\right)\tau_{rB} + \left(-\frac{3}{2} + \frac{r_p}{2r_B}\right)\tau_{zB} + \\ &\quad \rho v_s \left(-\frac{1}{2} - \frac{r_p}{2r_B}\right) v_B - (r_p - r_B)\frac{\partial \tau_z}{\partial r}\Big|_B \end{aligned} \tag{A.1.1}$$

$$a_3 = 2 - \frac{r_A}{r_p}$$

$$b_3 = \frac{3}{2} - \frac{r_A}{2r_p}$$

$$c_3 = -\frac{\rho V_s}{2}\left(1 + \frac{r_A}{r_p}\right)$$

$$d_3 = -(r_p - r_A)$$

$$e_3 = \left(2 - \frac{r_p}{r_A}\right)\tau_{rA} + \left(\frac{3}{2} - \frac{r_p}{2r_A}\right)\tau_{zA} - \frac{\rho V_s}{2}\left(1 + \frac{r_p}{r_A}\right)V_A + \left.\frac{\partial \tau_z}{\partial r}\right|_A (r_p - r_A)$$

$$a_5 = 2 - \frac{r_D}{r_p} \qquad \text{(A.1.1)}$$

$$b_5 = -\frac{3}{2} + \frac{r_D}{2r_p}$$

$$c_5 = \rho V_s\left(\frac{1}{2} + \frac{r_D}{2r_p}\right)$$

$$d_5 = r_p - r_D$$

$$e_5 = \left(2 - \frac{r_p}{r_D}\right)\tau_{rD} + \left(-\frac{3}{2} + \frac{r_p}{2r_D}\right)\tau_{zD} + \rho V_s\left(\frac{1}{2} + \frac{r_p}{2r_D}\right)V_D - (r_p - r_D)\left.\frac{\partial \tau_z}{\partial r}\right|_D$$

$$a_7 = 2 - \frac{r_c}{r_p}$$

$$b_7 = \frac{3}{2} - \frac{r_c}{2r_p}$$

$$c_7 = \rho V_s\left(\frac{1}{2} + \frac{r_c}{2r_p}\right)$$

$$d_7 = -(r_p - r_c)$$

$$e_7 = \left(2 - \frac{r_p}{r_c}\right)\tilde{\tau}_{rc} + \left(\frac{3}{2} - \frac{r_p}{2r_c}\right)\tilde{\tau}_{zc} + \rho V_s \left(\frac{1}{2} + \frac{r_p}{2r_c}\right) V_c + (r_p - r_c)\left.\frac{\partial \tilde{\tau}_z}{\partial r}\right|_c$$

For the nonlinear inelastic model the coefficients in Eqs. (3.37) are given as

$$a_1 = 2 - \frac{r_B}{r_p}$$

$$b_1 = -\frac{V_{sr_B}}{V_{sz_B}} - \frac{\rho V_{sr_B} V_{sz_B}}{2 G_{zs_B}}\left(1 - \frac{r_B}{r_p}\right)$$

$$c_1 = -\frac{\rho V_{sr_B}}{2}\left(1 + \frac{r_B}{r_p}\right)$$

$$d_1 = \frac{V_{sr_B}}{V_{sz_B}}(r_p - r_B)$$

$$e_1 = \left(2 - \frac{r_p}{r_B}\right)\tilde{\tau}_{r_B} - \left[\frac{V_{sr_B}}{V_{sz_B}} - \frac{\rho V_{sr_B} V_{sz_B}}{2 G_{zs_B}}\left(\frac{r_p}{r_B} - 1\right)\right]\tilde{\tau}_{z_B} - \frac{\rho V_{sr_B}}{2}\left(1 + \frac{r_p}{r_B}\right) V_B - \frac{V_{sr_B}}{V_{sz_B}}(r_p - r_B)\left.\frac{\partial \tilde{\tau}_z}{\partial r}\right|_B \qquad \text{(A.1.2)}$$

$$a_3 = 2 - \frac{r_A}{r_p}$$

$$b_3 = \frac{V_{sr_A}}{V_{sz_A}} + \frac{\rho V_{sr_A} V_{sz_A}}{2 G_{zs_A}}\left(1 - \frac{r_A}{r_p}\right)$$

$$c_3 = -\frac{\rho V_{srA}}{2}\left(1 + \frac{r_A}{r_p}\right)$$

$$d_3 = -\frac{V_{srA}}{V_{szA}}\left(r_p - r_A\right)$$

$$e_3 = \left(2 - \frac{r_p}{r_A}\right)\tau_{rA} + \left[\frac{V_{srA}}{V_{szA}} - \frac{\rho V_{srA} V_{szA}}{2 G_{zsA}}\left(\frac{r_p}{r_A} - 1\right)\right]\tau_{zA} - \frac{\rho V_{srA}}{2}\left(1 + \frac{r_p}{r_A}\right)V_A + \frac{V_{srA}}{V_{szA}}\left(r_p - r_A\right)\left.\frac{\partial \tau_z}{\partial r}\right|_A$$

$$a_5 = 2 - \frac{r_D}{r_p}$$

$$b_5 = -\frac{V_{srD}}{V_{szD}} - \frac{\rho V_{srD} V_{szD}}{2 G_{zsD}}\left(1 - \frac{r_D}{r_p}\right) \quad \text{(A.1.2)}$$

$$c_5 = \frac{\rho V_{srD}}{2}\left(1 + \frac{r_D}{r_p}\right)$$

$$d_5 = \frac{V_{srD}}{V_{szD}}\left(r_p - r_D\right)$$

$$e_5 = \left(2 - \frac{r_p}{r_D}\right)\tau_{rD} - \left[\frac{V_{srD}}{V_{szD}} - \frac{\rho V_{srD} V_{szD}}{2 G_{zsD}}\left(\frac{r_p}{r_D} - 1\right)\right]\tau_{zD} + \frac{\rho V_{srD}}{2}\left(1 + \frac{r_p}{r_D}\right)V_D - \frac{V_{srD}}{V_{szD}}\left(r_p - r_D\right)\left.\frac{\partial \tau_z}{\partial r}\right|_D$$

$$a_7 = 2 - \frac{r_c}{r_p}$$

$$b_7 = \frac{V_{src}}{V_{szc}} + \frac{\rho V_{src} V_{szc}}{2 G_{zsc}}\left(1 - \frac{r_c}{r_p}\right)$$

$$c_7 = \frac{\rho V_{src}}{2}\left(1 + \frac{r_c}{r_p}\right)$$

$$d_7 = -\frac{V_{src}}{V_{szc}}(r_p - r_c)$$

$$e_7 = \left(2 - \frac{r_p}{r_c}\right)\tilde{\tau}_{rc} + \left[\frac{V_{src}}{V_{szc}} - \frac{\rho V_{src} V_{szc}}{2 G_{zsc}}\left(\frac{r_p}{r_c} - 1\right)\right]\tilde{\tau}_{zc} + \frac{\rho V_{src}}{2}\left(1 + \frac{r_p}{r_c}\right) V_c + \frac{V_{src}}{V_{szc}}(r_p - r_c)\left.\frac{\partial \tilde{\tau}_z}{\partial r}\right|_c$$

(A.1.2)

APPENDIX II

LIST OF MAJOR EQUIPMENT

A list of the major equipment used in the various experiments described in Chapters VII, VIII and IX is given in Table A.2.1.

Table A.2.1: List of Major Equipment used in Designated Tests

Test	Equipment	Manufacturer	Model	Remarks
Calibration of Velocity Transducers	Optical Displacement Transducer	Optron	701	Used with Model 711 Lens (0.050 inch range)
	Vibration Exciter	MB	C31	
	Variable Filter	Krohn-Hite Cambridge, Mass.	335	
	A.C. Voltmeters	Hewlett-Packard, Inc. P.O. Box 301 Loveland, CO 80537	400AE 427A	
	Storage Oscilloscope	Tektronix, Inc. Portland, OR	Display-5103N Time Base-5B12N Amplifier-5A14N Amplifier-5A20N	
	Period Counter	Hewlett-Packard, Inc. P.O. Box 301 Loveland, CO 80537	5223L	

Table A.2.1 (Continued)

Test	Equipment	Manufacturer	Model	Remarks
	Power Amplifier	MB	T132534 Amplifier-PA13 Oscillator-A25 Field Supply-F34 Power Supply-PP13	
Filter Tests	Frequency Generator	Hewlett-Packard	202A	
	Oscillator	Hewlett-Packard	200CD	
	Period Counter	Hewlett-Packard	5223L	
	A.C. Voltmeter	Hewlett-Packard	427A	
	Storage Oscilloscope	Tektronix, Inc. Portland, OR	Display-5103N Time Base-5B12N Amplifier-5A14N Amplifier-5A20N	
	Oscilloscope Camera	Tektronix, Inc.	C-5A	
Dynamic Model Footing Tests	Strain Gages	Micro-Measure-ments Box 306 38905 Chase Rd. Romulus, MI 48174	EA-06-250BK-10C	

Table A.2.1 (Continued)

Test	Equipment	Manufacturer	Model	Remarks
	Velocity Transducers	Mandrel Ind., Inc. 5134 Glenmont Houston, TX	EVS-4BH	
	Triggering Circuit	Constructed by L. North at Univ. of Michigan		
	Filters	Constructed by L. North at Univ. of Michigan		
	Storage Oscilloscope	Tektronix, Inc. Portland, OR	Display-5103N Time Base-5B12N Amplifiers-5A14N Amplifiers-5A20N	
	Strain Gage Preamplifier	Tektronix, Inc.	Power Supply-Type 127 Preamplifier-Type Q	
	Oscilloscope Camera	Tektronix, Inc.	C-5A	
	Digitizer	Houston Instruments Austin, TX 78753		Resolution 0.005 in Accuracy ± 0.015 in

Table A.2.1 (Continued)

Test	Equipment	Manufacturer	Model	Remarks
Torsional Seismic Crosshole Test	Velocity Transducers	Mandrel Ind., Inc. 5134 Glenmont Houston, TX	EVS-4BH	
	Triggering Circuit	Constructed by L. North at Univ. of Michigan		
	Storage Oscilloscope	Tektronix, Inc. Portland, OR	Display-5103N Time Base-5B12N Amplifiers-5A20N	
	Oscilloscope Camera	Tektronix, Inc.	C-5A	

APPENDIX III

SYSTEM FOR APPLYING SURCHARGE PRESSURE

A. Introduction

The system for applying a surcharge pressure consisted of four major subsystems: a system of three flexible rubber air bags, a structural restraining system, a system for distributing air and a system for measuring the pressures in the air bags. The various components of these subsystems are shown schematically in Figs. A.3.1, A.3.2, A.3.3, A.3.6 and A.3.7. Details of the construction, maintenance and installation of these subsystems are given in the following sections.

Fully assembled in the quicksand tank and under testing conditions, surcharge pressures of up to 5 psi have been applied safely. This represents a force of approximately 32,000 lbs distributed uniformly over the surface of the test bed.

B. Air Bags

Three air bags, shown in Fig. A.3.1 through A.3.3, were used to apply surcharge pressures to the surface of the test bed.

1. Construction

a. General--The air bags were constructed from Goodrich pure gum rubber sheets 36 inches wide and 3/32 inch thick. This material is durable but deteriorated in the presence of oil. Patterns were cut, joined and folded to give the shapes shown in Fig. A.3.3. All rubber to rubber joints were bonded using Rema Tip Top Special Vulcanizing Cement #54 manufactured by Remaco Incorporated, Northvale, New Jersey 07647. The following outline gives the steps for bonding two rubber surfaces.

1) Wash, rinse, dry, roughen and brush off bonding surfaces.
2) Apply thin coat of cement to bonding surfaces.
3) Let cement dry 15 minutes.
4) Join bonding surfaces carefully.
5) Sandwich entire joint between boards.
6) Place weights on boards to clamp joint.
7) Allow 30 minutes set time.

b. Valve Stems--Valves from automotive tire tubes were used in the air bags as inlets for supplying air and outlets for measuring pressure. As shown in Fig. A.3.4, these valves were centered on circles cut 6 inches in diameter from the tubes. These circles were

bonded to the inside of the skin of the air bags with the stems protruding outwards. As shown in Fig. A.3.4, a reinforcing layer of rubber 6 inches in diameter and centered on the valve was bonded to the outer skin of the air bags.

c. Joints--As shown in Fig. A.3.3, the air bags were assembled using various types of joints. These joints are shown in detail in Fig. A.3.5. Lap joints 3 inches wide were used to join rubber sheets together to form large shapes. A number of strips 3 inches wide were needed to provide reinforcement, to reduce the sharpness of folds and to eliminate steps created by lap joints. Butt joints, shown in Fig. A. 3.5, were used in joining these strips to other strips, to sheets or to the inside of a fold. Edge joints were used along the unfolded edges of the air bags.

Unlike lap joints, edge joints were weak under pressure and required external clamping. As shown in Fig. A.3.5(c), clamping was provided by two 3/8 by 3/8 inch aluminum bars. Each bar was centered on the reinforcing strip on each side of the joint. Aluminum was selected to minimize corrosion. The clamping force was provided by 2 inch long No. 6-32 machine screw and nut systems spaced at 2 inches along the bars. These

bars were shaped to conform to the air bags by repeatedly pulling these bars through an adjustable bender. Matched clamps were aligned and clamped together and then vertical holes for the screws were drilled through these matched clamps. To prevent damage to adjacent air bags the ends of the clamps were rounded as shown in Fig. A.3.5 (d). Circular clamps for the central access hole were machined from aluminum plates.

To clamp a joint, matched bars were appropriately located and the ends of the bars were fastened as shown in Fig. A.3.5 (d). Holes for the clamping screws were punched through the layers of the joint using a punch with a slanted face. After each hole was punched, a threaded fastener was inserted and its nut hand tightened. After placing all the fasteners these fasteners were tightened sequentially and repeatedly to give an air tight seal without excessive squeezing of the joint. To prevent damage to other air bags, the ends of the screws protruding from the nuts were clipped and filed flush. For additional security against loosening, nuts were taped to the bars using a waterproof tape. Then the outer edges of the joints were trimmed to within 1/2 inch of the clamping bars to improve the fit of the air bags in the quicksand tank.

d. Folds--The folds of the air bags were particularly susceptable to abrasion and damage caused by handling and testing. As shown in Fig. A.3.3, reinforcing layers were cemented to the air bags along the folds.

e. Leakage Tests--Following construction, each air bag was tested for leakage by pressurizing each bag to an expanded state and then submerging each bag in a large tub of water. Leakage was detected by the formation of bubbles and corrections were carried out as needed.

2. Maintenance

The gum rubber was found to develop cracks with time. To eliminate this problem the air bags were washed, rinsed and dried regularly and then coated liberally with talcum powder. The insides of the air bags were also treated by introducing talcum powder into the air bags through the valve stems.

C. Restraining System

A restraining system transmitted the upward pressure from the air bags to the wall of the quicksand tank. This system also limited the expanded volume of the air bags.

The restraining system, shown in Fig. A.3.6, consisted of two semi-circular, 1/4 inch thick, plywood sheets reinforced with expanded metal mesh (See Fig. A.3.7) and held down by a grid of I-beams. This grid was attached to the wall of the quicksand tank by brackets.

The basic shape and size of the covers were designed to give a snug fit inside the quicksand tank. All edges of the plywood covers were rounded and to further protect the air bags a split garden hose was slipped over the edges. Also round headed bolts were used for fasteners passing through the covers and contacting the air bags.

In order to provide freedom in the placement of the air bags and covers, holes in the covers through which the valve stems protruded were made much larger than the stems. Plywood disks somewhat larger in area than these holes were used to avoid localized bulging of the air bags in this zone. These disks, provided with holes for the valve stems, were sandwiched between the air bags and the underside of the covers.

At times it was necessary to totally deflate the air bags with all equipment in place. To prevent the empty air bags and soil from supporting a large fraction of the weight of the grid small angles were welded to

the top of each secondary I-beam. With this arrangement it was possible to suspend these beams from the primary I-beams.

D. System for Supplying Air

The system for supplying air to the air bags is shown in Fig. A.3.1. Air was drawn from the building supply and the pressure of the air was regulated by a pressure regulator. The air was routed past a pressure gage used for coarse measurements and through a manifold. This manifold, which distributed air to the air bags, was connected to the air bags using flexible Tygon tubing.

E. System for Measuring Air Pressure

The system for measuring independently the pressures of the air bags, shown in Fig. A.3.1, consisted of a detachable mercury manometer, a line of Tygon tubing, and a bleed valve. The end fitting from a bicycle tire pump was attached to the end of the tubing leading from the manometer. This fitting permitted the pressure in each air bag to be measured rapidly. The bleed valve was inserted in this line to minimize the oscillations of the mercury brought about by sudden changes in pressure.

F. Installation of System for Applying Surcharge Pressure

[redacted]

8) Engage suspending angles of secondary I-beams.

9) Align central access hole with plumbline defining centerline of test bed.

10) To connect air lines without excessive loss of air from air bags first adjust pressure regulator to give fairly high rate of flow. Remove inlet valve from one air bag and slip end of matched air line over threaded length of valve stem rapidly. Tape and clamp joint using screw clamp for additional security against leakage. Repeat process for remaining air bags. Reduce flow of air after making each connection to prevent buildup of pressure in air bags over that needed to support grid.

The system for applying surcharge pressure is disassembled by reversing the steps for assembly. The pressure in the air bags should be negligible during disassembly.

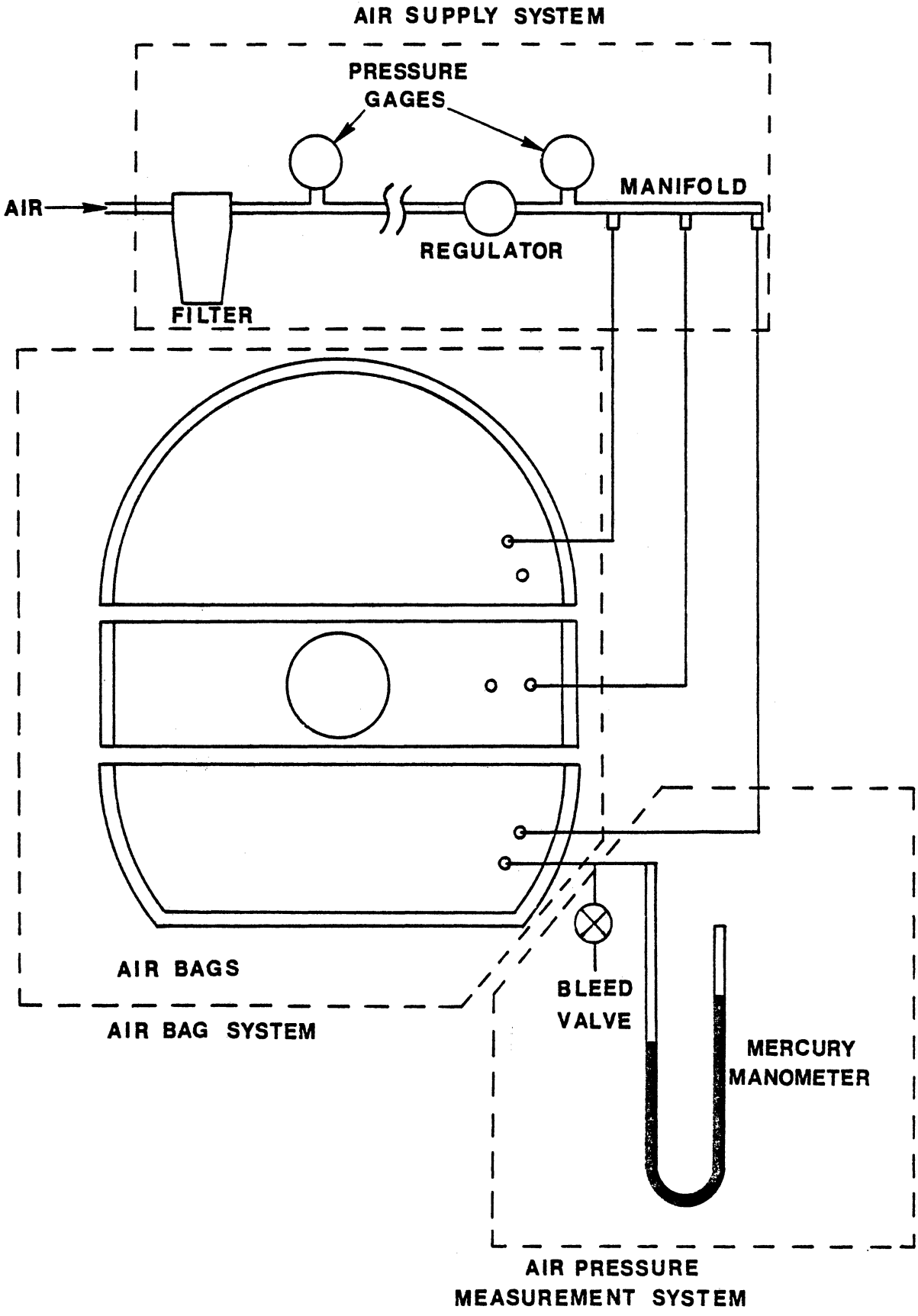

Fig. A.3.1: Schematic Diagram of Components of System for Applying Surcharge Pressure.

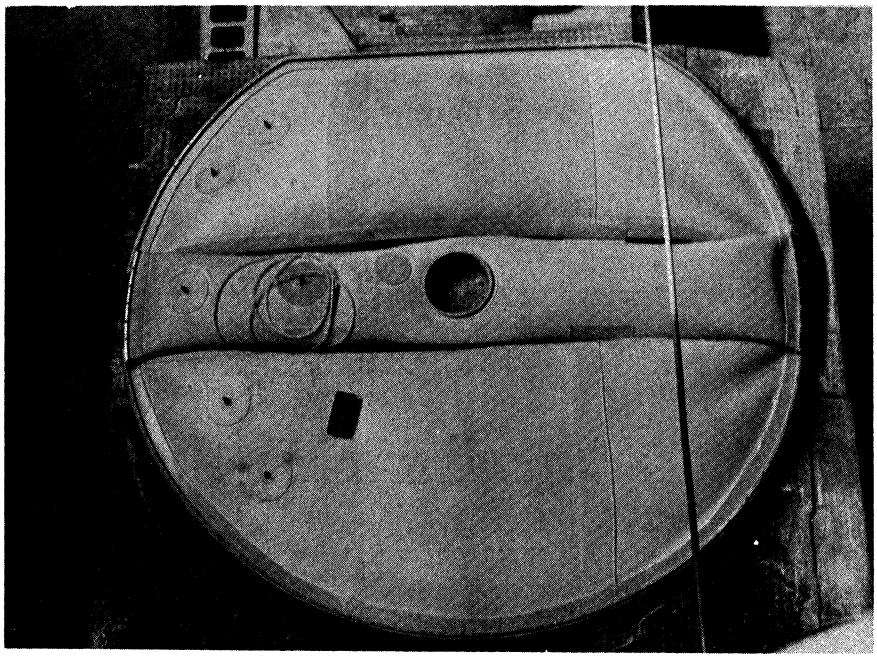

(a) Plan View.

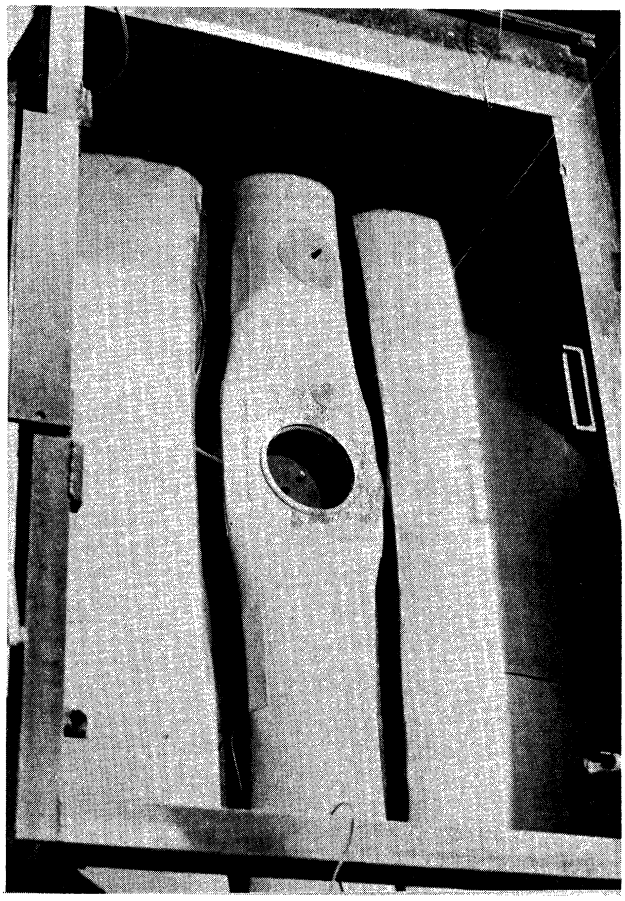

(b) Positioned in Quicksand Tank.
Fig. A.3.2: Photographs of Air Bags.

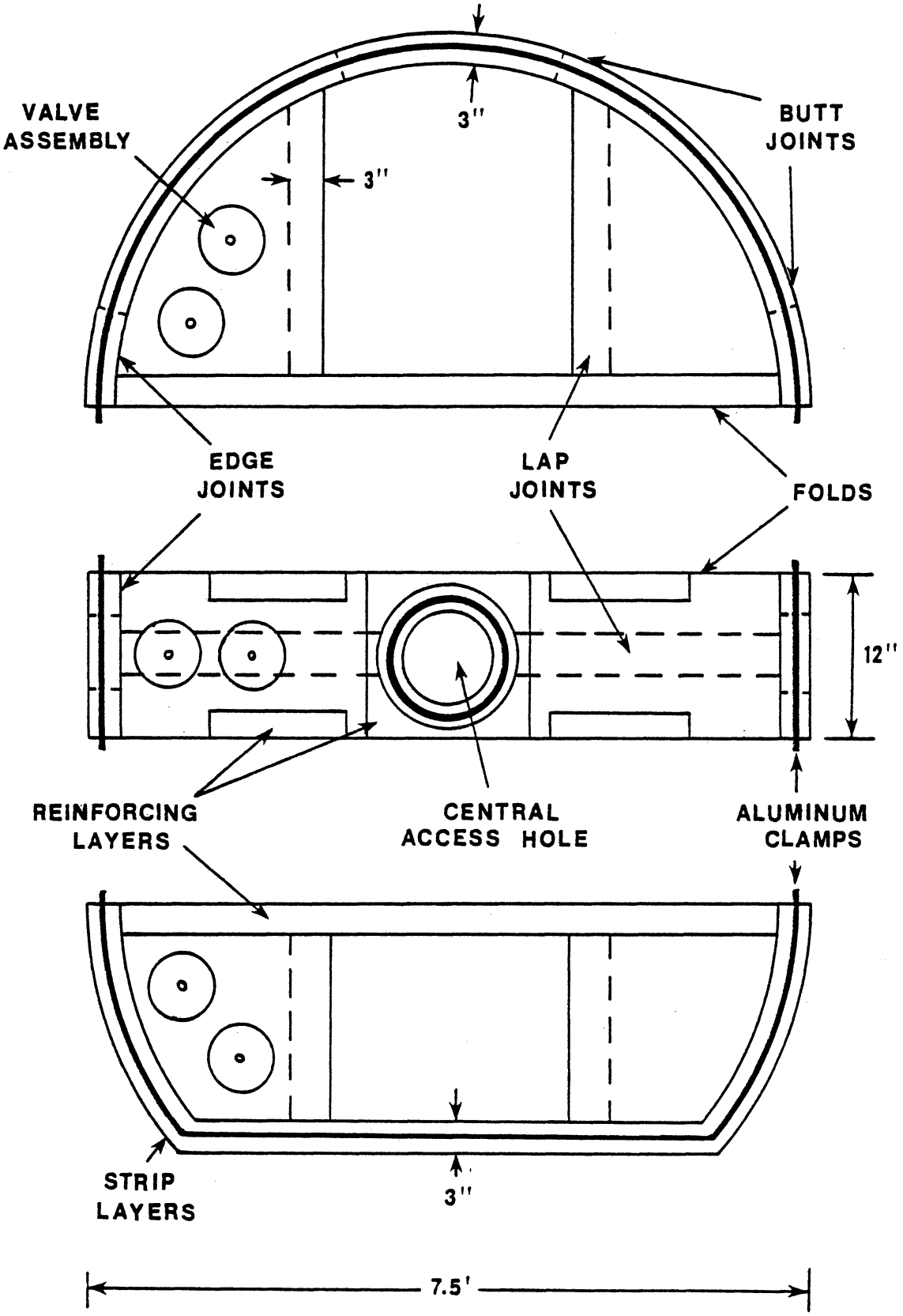
VALVE ASSEMBLY
3"
3"
BUTT JOINTS
EDGE JOINTS
LAP JOINTS
FOLDS
12"
REINFORCING LAYERS
CENTRAL ACCESS HOLE
ALUMINUM CLAMPS
STRIP LAYERS
3"
7.5'

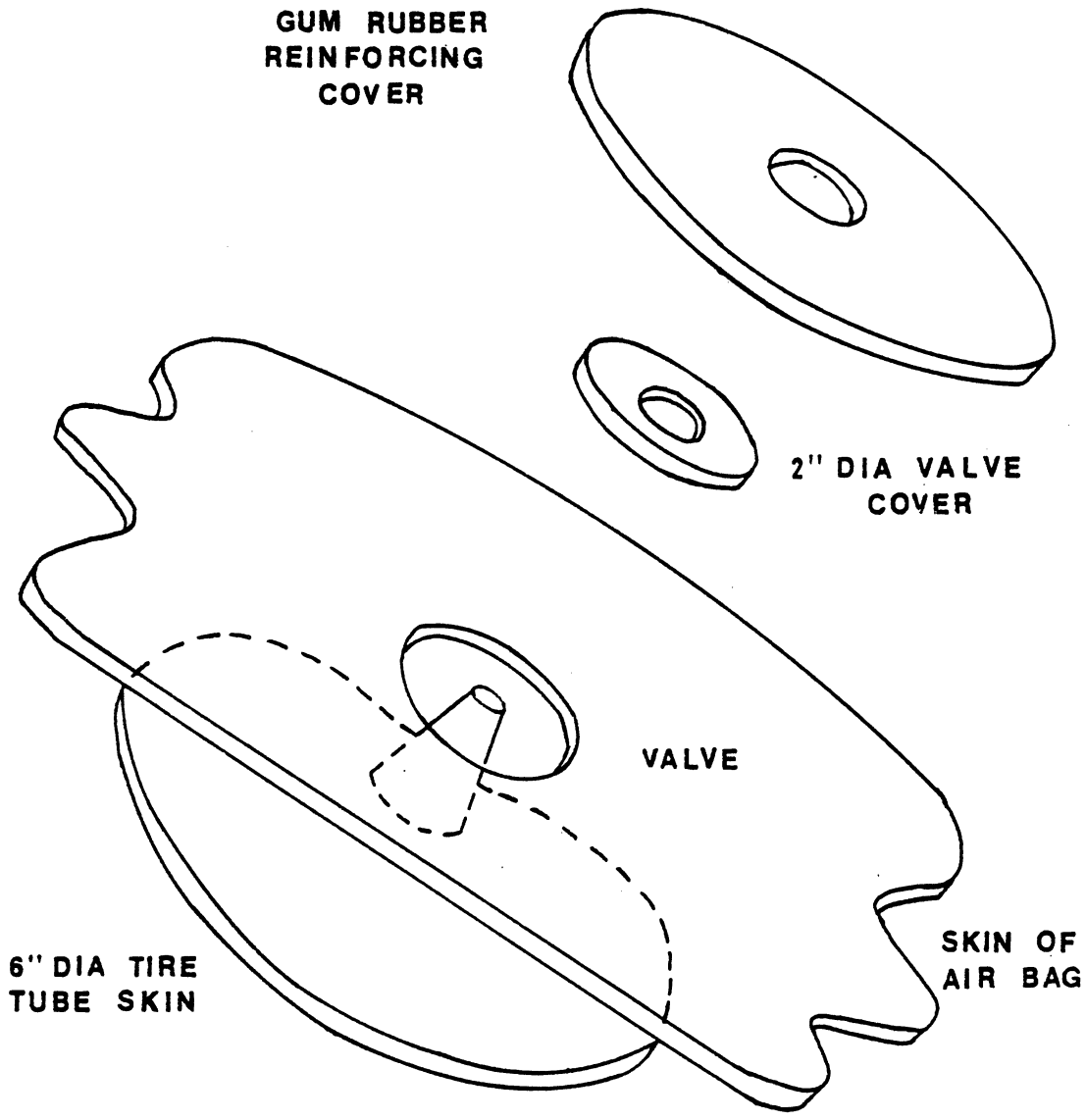

'ig. A.3.4: Inlet/Outlet Assemblies for Air Bags.

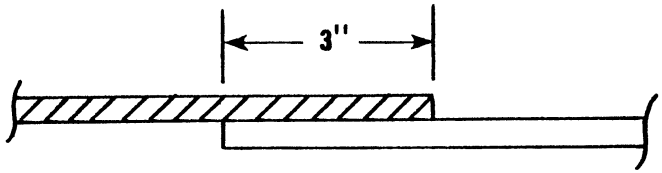

(a) Lap Joint: Cross Sectional View.

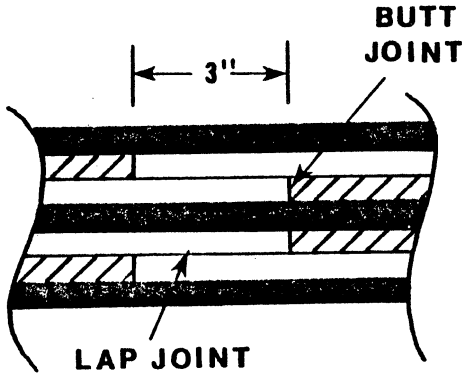

(b) Lap and Butt Joint: Edge View.

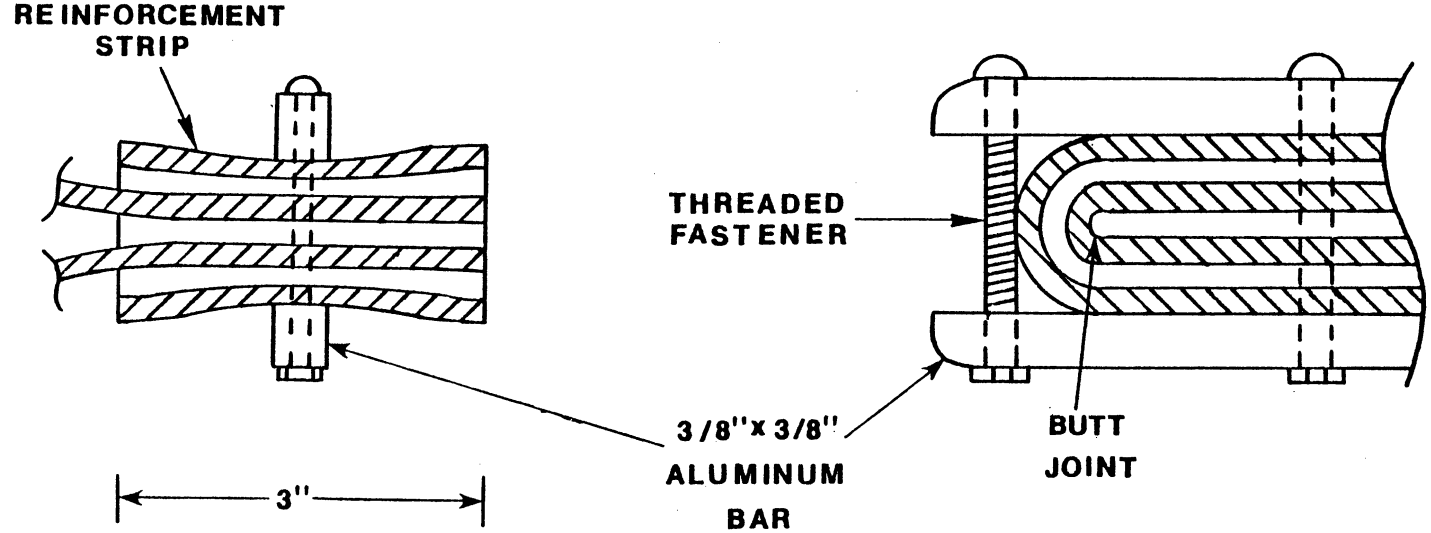

(c) Edge Joint: Cross Sectional View.

(d) Edge and Butt Joints at Fold: Edge View.

Fig. A.3.5: Details of Joints of Air Bags.

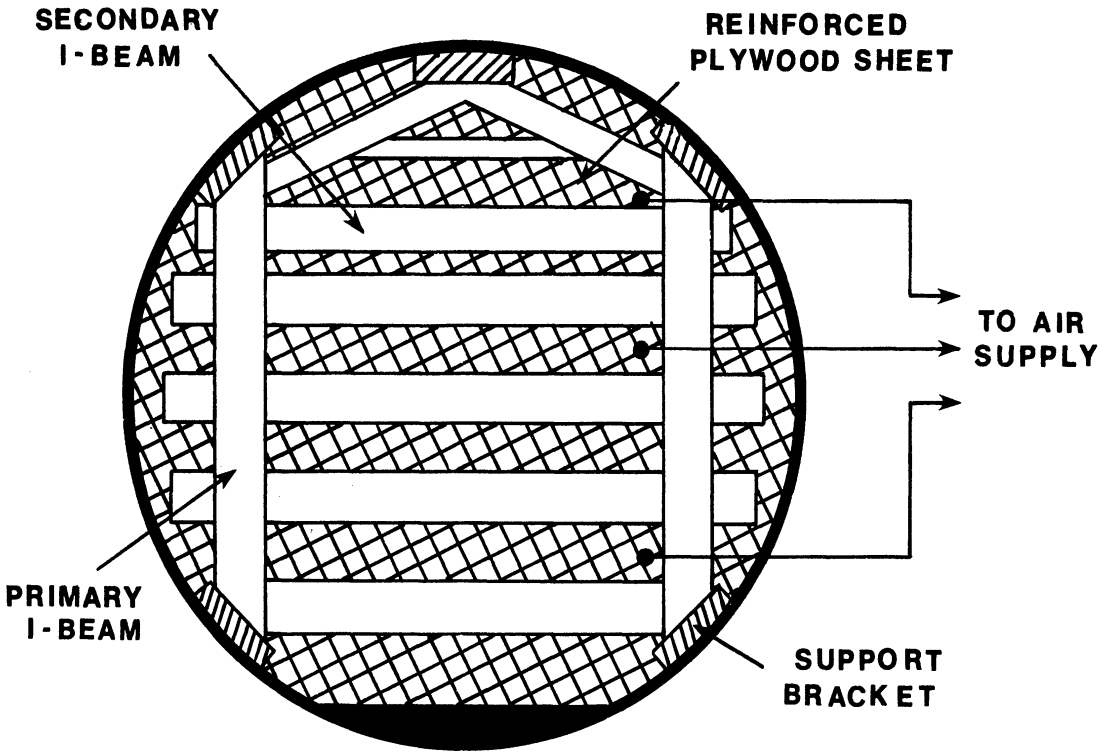

(a) Plan View.

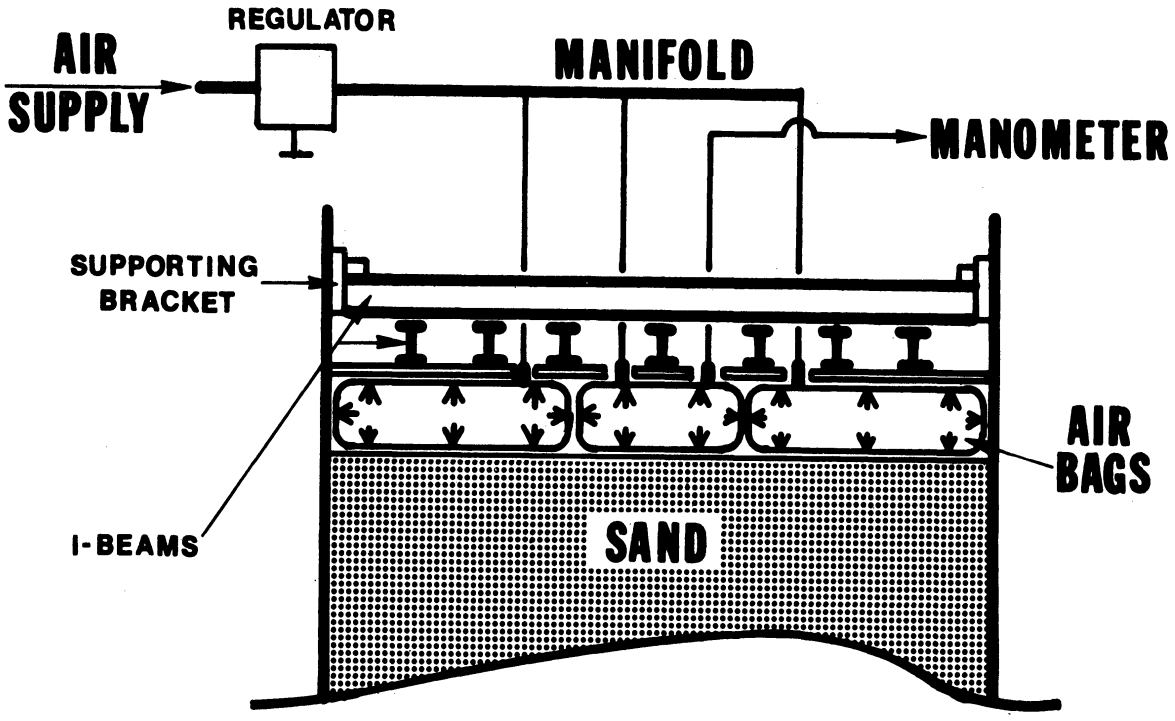

(b) Elevation View.

Fig. A.3.6: Schematic Diagram of Restraining System as Assembled in Quicksand Tank.

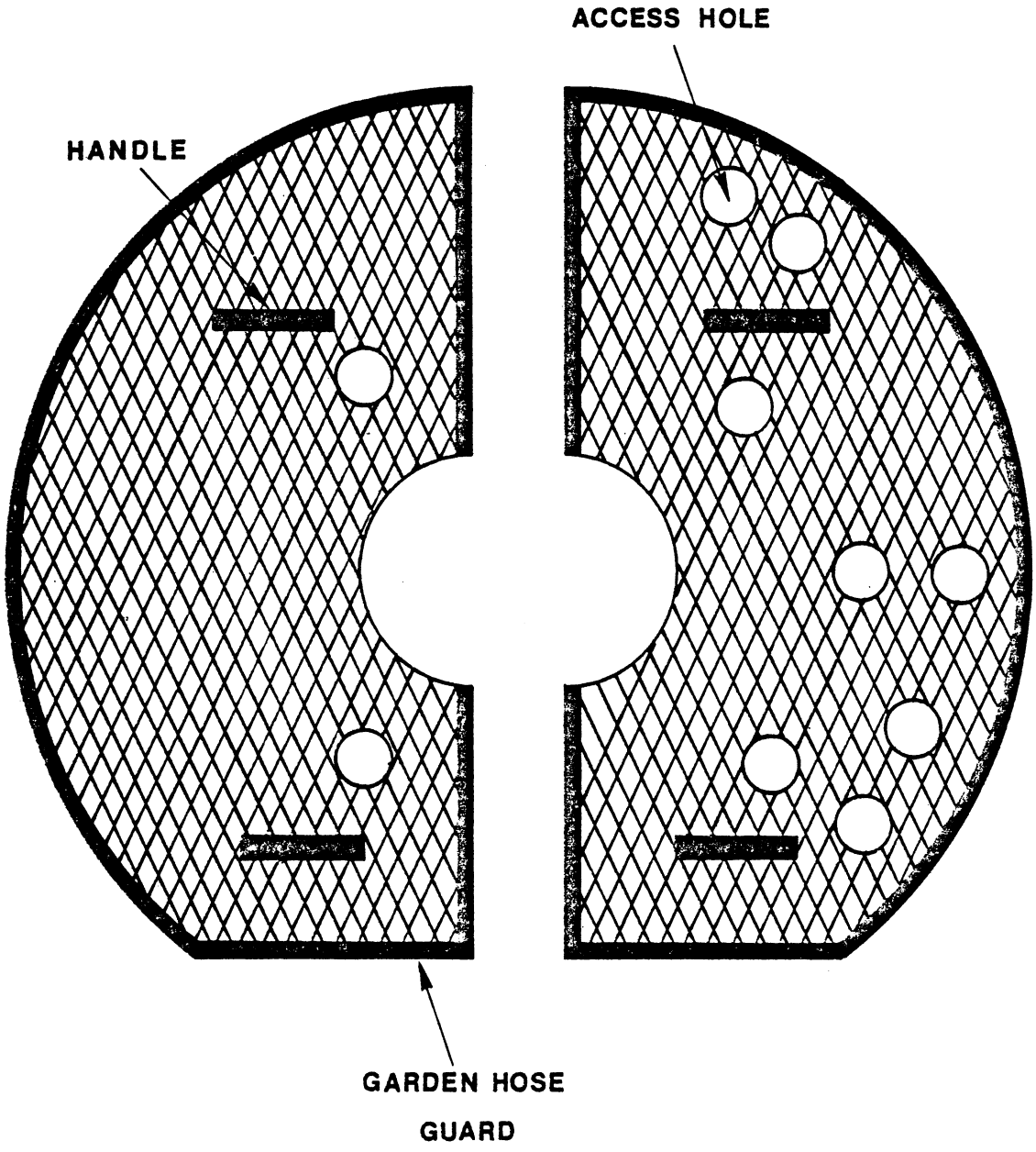

Fig. A.3.7: Plan View of Covers for Air Bags.
Approximate Diameter = 7.5 ft.

APPENDIX IV

COMPUTER PROGRAM USED FOR PROBLEM OF FOOTING ON NONLINEAR INELASTIC HALF SPACE WITH SLIP ALONG INTERFACE

```
C
C  DIMENSIONING AND INITIALIZATION OF ARRAYS
C
      DIMENSION V(127,71),TR(127,71),TZ(127,71),PDR(127,71),
     1VP(127,71),TRP(127,71),TZP(127,71),PDRP(127,71),
     2U(127,71),R(141),TRAVE(126,140),TZAVE(126,140),
     3GMZAVE(126,140),GMRAVE(126,140),GZT(126,140),
     4GRT(126,140),IVCR(126,140),Z(127),A(8),RO(8),RI(8)
     5,IVCZ(126,140),DVCI(140),ISLIP(8),UO(8)
     6,PRAMOM(165),PRCMP(165),PRRMOM(165),PRT(165),
     7PRTZFT(165,8),PRVP1(165),PRVP2(165),PRTRA(165),
     8PRGMRA(165),PRTZA(165),PRGMZA(165),PRUS(165,71),
     9PRWORK(165),PRDISK(165),PRHSWO(165),PRSLWO(165),
     9PRENKE(165),PRPEPH(165),PRENRA(165),PRENRH(165),
     9PRUFTE(165)
      COMMON AI,TY,GO,RR
      COMMON/CCCEFF/A1,B1,C1,D1,E1,A3,B3,C3,D3,E3,
     1A5,B5,C5,D5,E5,A7,E7,C7,D7,E7
      DATA V,TR,TZ,PDR,VP,TRP,TZP,PDRP,U/81153*0./
      DATA TRAVE,TZAVE,GMZAVE,GMRAVE,GZT,GRT,
     1IVCZ,IVCR/70560*0.,35280*700253.,35280*1/
      DATA INDE,INDC,INDG,INDH,INDI,INDM,ISLIP,NROW/14*0,1/
      DATA T,UC,AMOM,AMCMP,RMCM,RMOMP,OM,OMP,WORK,
     1PEPHI,ENRAT,HSWORK,ENRAHS,SLWORK,TTR,TTZ,GMR,
     2UFTE,GMZ/26*0./
      DATA PRAMCM,PRCMP,PRRMCM,PRT,PRTZFT,PRVP1,PRVP2,
     1PRTRA,PRGMRA,PRTZA,PRGMZA,PRUS,PRWORK,PRDISK,PRHSWO,
     1PRSLWO,PRENKE,PRPEPH,PRENRA,PRENRH,PRUFTE/16170*0./
C
C  INPUT OF DATA
C
      INTEGER RN
      NAMELIST/DATA/GO,RHO,AL,RR,TY,R,REND,
     1IMAX,KPR,PN,NRW,NCL,XMI,IZMAX,NDP
     2,MPR1,NPR1,MPR2,NPR2,MPR3,NPR3,JPR,INDN
     3,NDVC,NSCC
   10 READ(10,DATA,END=99)
      READ(11,4500) (PRAMOM(I),I=2,NDP)
C
C  PRELIMINARY COMPUTATIONS AND INITIALIZATIONS
C
      NRWM1=NRW-1
      NCT2M1=2*NCL-1
      NCT2M2=2*NCL-2
      DR=(REND-R(1))/NCT2M2
      DZ=DR
      DO 50 N=1,NCT2M1
   50 R(N)=R(1)+(N-1)*DR
      DO 55 M=1,NRW
```

```
   55 Z(M)=(M-1)*DZ
      GZS=G0
      VS0=SQRT(G0/RHO)
      DT=DR/VS0
      DZR=DR*DZ
      CXMI=2.*XMI/DT
      PI=3.14159
      DO 60 N=2,RN
      RI(N)=R(2*N-1)-DR
      RO(N)=R(2*N-1)+DR
   60 A(N)=PI*((RO(N)**2)-(RI(N)**2))
      DO 65 N=1,NCT2M2
   65 DVOL(N)=PI*((R(N+1)**2)-(R(N)**2))*DZ
      NCOL=RN
C
C  PRINTING OUT OF INPUT DATA AND RESULTS
C
      WRITE(6,4000) G0,RHO,R(1),REND,TMAX,
     1VS0,DR,DT,KPR,RN,XMI,AL,RR,TY,NRW,NCL,TZMAX,
     2NDP,MPR1,NPR1,MPR2,NPR2,MPR3,NPR3,NDVC,NSCC,JPR
      WRITE(6,4200) (R(N),N=1,NCT2M1)
      WRITE(6,4510) NDP,(PRAMCM(I),I=1,NDP)
      IF(INDN.EQ.1) GO TO 100
      WRITE(19,4630)
      WRITE(18,4600) NDVC,NSCC
   30 WRITE(18,4613) T
      DO 4611 M=44,45
      DO 4611 N=11,12
 4611 WRITE(18,4616) TR(M,N),TZ(M,N),V(M,N),PDR(M,N),U(M,N)
      WRITE(18,4614)
      DO 4612 M=44,45
      DO 4612 N=22,23
 4612 WRITE(18,4617) TRAVE(M,N),TZAVE(M,N),GMRAVE(M,N),
     1GMZAVE(M,N),GRT(M,N),GZT(M,N),GZS
      IF(NROW.EQ.0) NCOL=RN
      INDM=INDM+1
      PRT(INDM)=T
      PROMP(INDM)=CMP
      PRMOM(INDM)=RMCMP
      DO 5000 I=1,RN,JPR
 5000 PRTZFT(INDM,I)=TZ(1,I)
      PRVP1(INDM)=V(MPR1,NPR1)
      PRVP2(INDM)=V(MPR2,NPR2)
      PRTRA(INDM)=TRAVE(MPR3,NPR3)
      PRTZA(INDM)=TZAVE(MPR3,NPR3)
      PRGMRA(INDM)=GMRAVE(MPR3,NPR3)
      PRGMZA(INDM)=GMZAVE(MPR3,NPR3)
      DO 5010 I=1,NCOL,JPR
 5010 PRUS(INDM,I)=U(1,I)
      PRUFTE(INDM)=UFTE
      PRWORK(INDM)=WORK
      PRDISK(INDM)=DISCKE
      PRHSWO(INDM)=HSWORK
```

```
      PRSLWC(INIM)=SIWORK
      PRENKE(INIM)=ENKE
      PRPEPH(INIM)=PEPHI
      PRENBA(INIM)=ENBAT
      PRENRH(INIM)=ENRAHS
      IF(NROW.EQ.0) GO TO 10
C  DEVELOPMENT OF MATERIAL PROPERTY MATRICES
C  AND ENERGY COMPUTATIONS
C
   20 T=T+DT
      INDC=INDC+1
      INDI=INDI+1
      IF((NROW/2)*2.EQ.NROW) GO TO 8010
      NUMBN=2*NCCI-2
      INDG=1
      GO TO 8020
 8010 NUMEN=2*NCCL-1
      INDG=2
 8020 NUMBM=NRCW-1
      IF(INDE.EQ.0) GO TO 8040
      NUMBM=NRCW
      NUMEN=2*NCCI
 8040 IF(INDI.EQ.1) GO TO 9805
      ENKE=0.
      DO 2000 M=1,NUMBM
      DO 2000 N=1,NUMBN
      INDPAR=1
      CALL NDLPEI(TVA,TVE,TVC,TVD,TR,M,N,NRW,NCL,
     1NROW,NCCI,INDB,INDG,RN,INDPAR,CMP,R,NCT2M1)
      TTB=(TVA+TVE+TVC+TVD)/4.
      INDPAR=2
      CALL NDLPEI(TVA,TVB,TVC,TVD,TZ,M,N,NRW,NCL,
     1NROW,NCCI,INDB,INDG,RN,INDPAR,CMP,R,NCT2M1)
      TTZ=(TVA+TVE+TVC+TVD)/4.
      INDPAR=5
      CALL NDLPEI(TVA,TVE,TVC,TVD,U,M,N,NRW,NCL,
     1NROW,NCCI,INDB,INDG,RN,INDPAR,CMP,R,NCT2M1)
      GMB=-(ALOG(R(N+1)/R(N))/(2.*DR**2))*
     1(R(N+1)*(TVA+TVB)-R(N)*(TVC+TVD))
      GMZ=(TVE-TVA+TVC-TVD)/(2.*DZ)
      CALL ZMOD(TTZ,TZAVE,GMZ,GMZAVE,M,N,NRWM1,NCT2M2,
     1GZT,IVCZ)
      CALL RMOD(TTB,TRAVE,GMB,GMBAVE,M,N,NRWM1,NCT2M2,
     1GRT,IVCB)
      IF(INDB.EQ.1) GO TO 8560
      INDPAR=3
      CALL NDLPEI(TVA,TVB,TVC,TVD,V,M,N,NRW,NCL,
     1NROW,NCCI,INDB,INDG,RN,INDPAR,CMP,R,NCT2M1)
      VAVE=(TVA+TVE+TVC+TVD)/4.
      CALL ENERGY(M,N,AMCMP,OMP,AMOM,OM,DT,T,
     1WORK,XMI,TTB,GMB,TTZ,GMZ,TRAVE,TZAVE,GMBAVE,
     2GMZAVE,NRWM1,NCT2M2,PEPHI,RHO,VAVE,DVOL,
     3ENKE,DISCPE,RMCMP,PMOM,HSWORK,ISLIP
```

```
     4,RN,UO,TZ,R,NCT2M1,A,SLWORK,NRW,NCL,U)
 8560 TZAVE(M,N)=TTZ
      TRAVE(M,N)=TTR
      GMZAVE(M,N)=GMZ
 2000 GMRAVE(M,N)=GMR
      AMOM=AMOMP
      RMOM=RMOMP
      OM=OMP
      IF(WORK.NE.0.) GO TO 9000
      ENRAT=0.
      GO TO 9020
 9000 ENRAT=(DISSKE+ENKE+PEPHI+SLWORK)/WORK
 9020 IF(HSWORK.NE.0.) GO TO 9030
      ENRAHS=0.
      GO TO 9805
 9030 ENRAHS=(ENKE+PEPHI+SLWORK)/HSWORK
 9805 DO 9800 M=1,2
      DO 9800 N=16,17
      GRT(M,N)=.0001*GO
 9800 GZT(M,N)=.0001*GO
C
C  NODAL POINT SOLUTION
C
 8030 M=1
      RMOMSL=0.
      DO 3410 N=2,RN
 3410 ISLIP(N)=0
      INDS=0
      INDA=0
      INDK=0
      INDL=0
      P7=0.
      P8=0.
 3050 N=2
 3040 CALL COEFF(M,N,GRT,GZT,NRW,NCL,RHO,R,DZR,
     1Z,DT,V,TR,TZ,PDR,GZS,NRWM1,NCT2M2,NCT2M1
     2,NRCW,NCCT,INDB,INDG,RN,INDPAR,OM)
      P13=D7*E1-D1*B7
      P14=-(D7*A1-D1*A7)/P13
      P15=-(D7*C1-D1*C7)/P13
      P16=(D7*E1-D1*E7)/P13
      IF(INDA.NE.0) GO TO 3060
      P7=P7+(R(2*N-1)**2)*A(N)*P15
      P8=P8+(R(2*N-1)*A(N))*(TR(1,N)*P14+P16)
      IF(INDK.EQ.1) GO TO 3470
      N=N+1
      IF(N.LE.RN) GO TO 3040
      AMOMP=PEAMOM(INDI+1)
      OMP=(AMOMP+P8+AMOM+RMOM+CXMI*OM)/(CXMI-P7)
      N=2
      INDA=1
      GO TO 3040
 3060 VP(M,N)=R(2*N-1)*OMP
```

```
      TRP(M,N)=TR(M,N)
      TZP(M,N)=P14*TRP(M,N)+P15*VP(M,N)+P16
      PDRP(M,N)=(E1-A1*TRP(M,N)-B1*TZP(M,N)-C1*VP(M,N))/D1
      IF(INDL.EQ.1) GO TO 3490
      N=N+1
      IF(N.LE.RN) GO TO 3040
 9999 N=2
 3460 IF(ISLIP(N).EQ.1) GO TO 3400
      IF(ABS(TZP(M,N)).LE.TZMAX) GO TO 3400
      IF(TZP(M,N).GE.0.) TZP(M,N)=TZMAX
      IF(TZP(M,N).LT.0.) TZP(M,N)=-TZMAX
      ISLIP(N)=1
      INDS=1
      CALL COEFF(M,N,GRT,GZT,NRW,NCL,RHO,R,DZR,
     1Z,DT,V,TR,TZ,PDR,GZS,NRWM1,NCT2M2,NCT2M1
     2,NBCW,NBCL,INDE,INDG,RN,INDPAR,CM)
      P10=C7*A1-C1*A7
      P11=-(C7*E1-C1*B7)/P10
      P12=(C7*F1-C1*E7)/P10
      TRP(M,N)=P11*TZP(M,N)+P12
      VP(M,N)=(E1-E1*TZP(M,N)-A1*TRP(M,N))/C1
      PDRP(M,N)=0.
      RMOMSL=RMOMSL+R(2*N-1)*A(N)*TZP(M,N)
 3400 N=N+1
      IF(N.LE.RN) GO TO 3460
      IF(INDS.EQ.0) GO TO 3540
 3530 P7=0.
      P8=0.
      INDA=0
      INDK=1
      INDI=0
      N=2
 3440 IF(N.GT.RN) GO TO 3450
      IF(ISLIP(N).EQ.1) GO TO 3470
      GO TO 3040
 3470 N=N+1
      GO TO 3440
 3450 OMP=(AMOMP+P8+RMOMSL+AMOM+RMOM+CXMI*OM)/
     1(CXMI-P7)
      INDK=0
      N=2
      INDA=1
      INDI=1
 3500 IF(N.GT.RN) GO TO 3510
      IF(ISLIP(N).EQ.1) GO TO 3490
      GO TO 3040
 3490 N=N+1
      GO TO 3500
 3510 INDI=0
      N=2
      INDS=0
      INDA=0
      GO TO 3460
```

```
3540 RMCMP=P7*CMP+P8+RMCMSL
     CALL COEFF(M,1,GRT,GZT,NRW,NCL,RHC,R,DZR,
    1Z,DT,V,TR,TZ,PDR,GZS,NRWM1,NCT2M2,NCT2M1
    2,NROW,NCCI,INDB,INDG,RN,INDPAR,CM)
     TZP(M,1)=C.
     TRP(M,1)=C.
     VP(M,1)=R(1)*CMP
     PDRP(M,1)=(E7-C7*VP(M,1))/D7
3070 CALL COEFF(M,N,GRT,GZT,NRW,NCL,RHC,R,DZR,
    1Z,DT,V,TR,TZ,PDR,GZS,NRWM1,NCT2M2,NCT2M1
    2,NROW,NCCI,INDB,INDG,RN,INDPAR,CM)
     TZP(M,N)=C.
     PDRP(M,N)=C.
     VP(M,N)=(A7*E1-A1*E7)/(A7*C1-A1*C7)
     TRP(M,N)=(E1-C1*VP(M,N))/A1
     N=N+1
     IF(N.LE.NCCI) GO TO 3070
     IF(NROW.EQ.1) GO TO 3800
3100 M=M+1
     N=1
3090 CALL COEFF(M,N,GRT,GZT,NRW,NCL,RHC,R,DZR,
    1Z,DT,V,TR,TZ,PDR,GZS,NRWM1,NCT2M2,NCT2M1
    2,NROW,NCCI,INDB,INDG,RN,INDPAR,CM)
     IF((M/2)*2.EQ.M) GO TO 3080
     IF(N.NE.1) GO TO 3080
     TZP(M,N)=C.
     VP(M,N)=C.
     TRP(M,N)=(D7*E5-D5*E7)/(D7*A5-D5*A7)
     PDRP(M,N)=(E5-A5*TRP(M,N))/D5
     N=N+1
     GO TO 3090
3080 F1=D1*A3-D3*A1
     F2=D1*B3-D3*B1
     F3=D1*C3-D3*C1
     F4=D1*E3-D3*E1
     F5=D5*A1-D1*A5
     F6=D5*B1-D1*B5
     F7=D5*C1-D1*C5
     F8=D5*E1-D1*E5
     F9=D7*A5-D5*A7
     F10=D7*B5-D5*B7
     F11=D7*C5-D5*C7
     F12=D7*E5-D5*E7
     G1=F5*F2-F1*F6
     G2=F5*F3-F1*F7
     G3=F5*F4-F1*F8
     G4=F9*F6-F5*F10
     G5=F9*F7-F5*F11
     G6=F9*F8-F5*F12
     VP(M,N)=(G4*G3-G1*G6)/(G4*G2-G1*G5)
     TZP(M,N)=(G3-G2*VP(M,N))/G1
     TRP(M,N)=(F8-F6*TZP(M,N)-F7*VP(M,N))/F5
     PDRP(M,N)=(E3-A3*TRP(M,N)-B3*TZP(M,N)-
```

```
     1C3*VP(M,N))/D3
      N=N+1
      IF(INDE.EQ.1) GO TO 3200
      IF((NROW/2)*2.EQ.NECW) GO TO 3200
      IF((M/2)*2.EQ.M.AND.N.EQ.NCOL) GO TO 3095
3200  IF(N.LE.NCCI) GO TO 3090
3095  IF(M.LT.NECW) GO TO 3100
      DO 3210 N=2,RN
3210  UO(N)=U(1,N)
      UFTE=UFTE+R(2*RN)*(OMP+CM)*DT/2.
3800  DO 3110 M=1,NROW
      DO 3110 N=1,NCCL
      U(M,N)=U(M,N)+(VP(M,N)+V(M,N))*DT/2.
      TR(M,N)=TEP(M,N)
      TZ(M,N)=TZP(M,N)
      V(M,N)=VP(M,N)
      PDR(M,N)=PDEP(M,N)
3110  CONTINUE
      IF(INDB.NE.0) GO TO 3120
      NRCW=NECW+1
      IF((NRCW/2)*2.NE.NECW) NCCI=NCCL+1
      IF(NROW.LE.NEWM1) GO TO 3130
      WRITE(19,4640) T
      I=1
      J=RN
3820  WRITE(19,4650) R(2*J-1),Z(I),TR(I,J),TZ(I,J),
     1V(I,J),PDE(I,J),U(I,J)
      IF(I.EQ.NEW) GO TO 3830
      IP1=I+1
      WRITE(19,4650) R(2*J),Z(IP1),TR(IP1,J),TZ(IP1,J),
     1V(IP1,J),PDR(IP1,J),U(IP1,J)
      I=IP1+1
      J=J+1
      GO TO 3820
3830  INDB=1
      NECW=NRCW-3
      NCCL=NCCI-2
      GO TO 3130
3120  NRCW=NECW-2
      NCCI=NCCI-1
3130  IF(INDC.NE.KEB) GO TO 20
      INDC=0
      IF(T.LE.TMAX) GO TO 30
      GO TO 10
  99  WRITE(12,4520) (PRT(I),PRAMOM(I),PROMP(I),
     1PREMOM(I),I=1,INDM)
      WRITE(13,4530) (R(2*I-1),I=1,RN,JPR)
      WRITE(13,4535)
      DO 5110 I=1,INDM
5110  WRITE(13,4540) PRT(I),(PRTZFT(I,J),J=1,RN,JPR)
      WRITE(14,4550) MPR1,NPR1,MPR2,NPR2,(PRT(I),
     1PRVP1(I),PRVP2(I),I=1,INDM)
      WRITE(15,4560) MPR3,NPR3,(PRT(I-1),PRTRA(I),
```

```
     1PRGMBA(I),PRTZA(I),PRGMZA(I),I=2,INDM)
      WRITE(16,4570) (PRT(I-1),PRWORK(I),PRDISK(I),
     1PRHSWO(I),PRSIWC(I),PRENKE(I),PRPEPH(I),
     2PRENBA(I),PRENRH(I),I=3,INDM)
      WRITE(17,4580) (R(2*I-1),I=1,NCL,JPR)
      WRITE(17,4585)
      DO 5120 I=1,INDM
 5120 WRITE(17,4590) PRT(I),PRUFTE(I),(PRUS(I,J),
     1J=1,NCL,JPR)
  100 STOP
C
C  FORMAT SPECIFICATIONS
C
 4000 FORMAT('1G0=',E20.2/' REC=',F10.5/' R(1)=',
     1E13.6/' REND=',E13.6/' IMAX=',F12.9/
     2' VS0=',F12.6/' DR=',
     3E13.6/' DT=',E13.6/' KPR=',I5/' RN=',I5/' XMI='
     4,F12.9/' AI=',E13.6/
     5' RR=',E13.6/' TY=',E13.6/' NRW=',I5/' NCL=',I5/
     6' TZMAX=',E13.6/' NDP=',I5/' MPR1=',I5/' NPR1=',I5/
     7' MPR2=',I5/' NPR2=',I5/' MPR3=',I5/' NPR3=',I5/
     8' NDVC=',I5/' NSCC=',I5/' JPR=',I5)
 4200 FORMAT('0',50X,'NODAL COLUMN RADII'/'0',(9F13.6))
 4500 FORMAT(20X,E20.10)
 4510 FORMAT('CODE=',I5/'0PRAMOM'/(' ',E13.6))
 4520 FORMAT(6X,'TIME',12X,'AMOM',13X,'OMP',13X,
     1'RMOM'/(4(2X,E13.6)))
 4530 FORMAT(' SHEAR STRESS DISTRIBUTION BENEATH FOOTING '
     1/50X,'RADII'/(15X,7(2X,E13.6)))
 4535 FORMAT('0',5X,'TIME',40X,'STRESS')
 4540 FORMAT(8(2X,E13.6)/(15X,7(2X,E13.6)))
 4550 FORMAT(2X,'SELECTED MEDIUM VELOCITY RECORDS'/
     16X,'TIME',8X,'NODE(',I2,',',I2,')',4X,'NODE(',
     2I2,',',I2,')'/(3(2X,E13.6)))
 4560 FORMAT(2X,'STRESS STRAIN CURVE FOR SUBCELL(',I2,','
     1,I2,')'/6X,'TIME',14X,'TR',13X,'GMR',14X,'TZ',
     213X,'GMZ'/(5(2X,E13.6)))
 4570 FORMAT(50X,'ENERGY ACCOUNT'/5X,'TIME',10X,'WORK',
     110X,'DKKE',10X,'HSWC',10X,'SLWC',10X,'ENKE',10X,
     2'PEHL',10X,'ENBA',10X,'ENBH'/(9(1X,E13.6)))
 4580 FORMAT(25X,'ROCKING EDGE AND SURFACE DISPLACEMENTS'
     1/'0',40X,'RADII'/(30X,6(2X,E13.6)))
 4585 FORMAT('0',6X,'TIME',12X,'UFTE',12X,'SURFACE
     1DISPLACEMENTS')
 4590 FORMAT(8(2X,E13.6)/(30X,6(2X,E13.6)))
 4600 FORMAT(' PRINT OUT COLUMN'/' NODAL COLUMN=',
     1I5/' SUBCELL COLUMN=',I5/'0',6X,'TR',13X,'TZ',
     213X,'V',13X,'PDR',13X,'U'/'0',5X,'TRAVE',10X,
     3'TZAVE',9X,'GMRAVE',9X,'GMZAVE',11X,'GRT',
     412X,'GZT',12X,'GZS')
 4613 FORMAT('CT=',E13.6/'0DV'/' ')
 4614 FORMAT('CMP'/' ')
 4616 FORMAT(5(2X,E13.6))
```

```
 4617 FORMAT(7(2X,E13.6))
 4630 FORMAT(' DEPENDENT VARIABLE RECORDS AT INSTANT IN TIME'/
     1' RECORD LINE EXTENDS FROM FOOTING EDGE AT 45 DEG ')
 4640 FORMAT('CI=',E13.6/7X,'R',14X,'Z',13X,'TR',14X,'TZ',
     114X,'V',12X,'PDR',13X,'U')
 4650 FORMAT(7(2X,E13.6))
      END
C
C  SUBROUTINES
C
C
C SUBROUTINE NDIPHI
C
      SUBROUTINE NDIPHI(PHIA,PHIB,PHIC,PHID,PHI,M,N,
     1NRW,NCL,NFCW,NCCL,INDB,INDG,RN,INDPAR,OM,R,NCT2M1)
      DIMENSION PHI(NRW,NCL),R(NCT2M1)
      INTEGER RN
      MM1=M-1
      NM1D2=(N-1)/2
      NP1D2=(N+1)/2
      MP1=M+1
      NP3D2=(N+3)/2
      MP2=M+2
      ND2=N/2
      NP2D2=(N+2)/2
      IF((M/2)*2.EQ.M) GO TO 1000
      IF((N/2)*2.EQ.N) GO TO 1010
      IF(N.NE.1) GO TO 1020
      IF(M.NE.1) GO TO 1030
      PHIB=(PHI(M,N)+PHI(MP2,N))/2.
      PHID=(PHI(M,NP1D2)+PHI(M,NP3D2))/2.
      GO TO 1040
 1030 PHIB=(PHI(M,N)+PHI(MP2,N))/2.
      PHID=(PHI(M,NP1D2)+PHI(MM1,NP1D2)+PHI(M,NP3D2)
     1+PHI(MP1,NP1D2))/4.
      GO TO 1040
 1020 IF(M.NE.1) GO TO 1050
      PHIB=(PHI(MP1,NM1D2)+PHI(M,NP1D2)+PHI(MP1,NP1D2)
     1+PHI(MP2,NP1D2))/4.
      PHID=(PHI(M,NP1D2)+PHI(M,NP3D2))/2.
      GO TO 1040
 1050 PHIB=(PHI(MP1,NM1D2)+PHI(M,NP1D2)+PHI(MP1,NP1D2)
     1+PHI(MP2,NP1D2))/4.
      PHID=(PHI(M,NP1D2)+PHI(MM1,NP1D2)+PHI(M,NP3D2)
     1+PHI(MP1,NP1D2))/4.
 1040 PHIA=PHI(M,NP1D2)
      PHIC=PHI(MP1,NP1D2)
      GO TO 1110
 1010 IF(M.NE.1) GO TO 1060
      PHIA=(PHI(M,ND2)+PHI(M,NP2D2))/2.
      GO TO 1070
 1060 PHIA=(PHI(M,ND2)+PHI(MM1,ND2)+PHI(M,NP2D2)
     1+PHI(MP1,ND2))/4.
```

```
 1070 PHIC=(PHI(MP1,ND2)+PHI(M,NP2D2)+PHI(MP1,NP2D2)
     1+PHI(MP2,NP2D2))/4.
      PHIB=PHI(MP1,ND2)
      PHID=PHI(M,NP2D2)
      GO TO 1110
 1000 IF((N/2)*2.EQ.N) GO TO 1080
      IF(N.NE.1) GO TO 1090
      PHIA=(PHI(MM1,NP1D2)+PHI(MP1,NP1D2))/2.
      GO TO 1100
 1090 PHIA=(PHI(M,NM1D2)+PHI(MM1,NP1D2)+PHI(M,NP1D2)
     1+PHI(MP1,NP1D2))/4.
 1100 PHIC=(PHI(MP1,NP1D2)+PHI(M,NP1D2)+PHI(MP1,NP3D2)
     1+PHI(MP2,NP1D2))/4.
      PHIB=PHI(MP1,NP1D2)
      PHID=PHI(M,NP1D2)
      GO TO 1110
 1080 PHIB=(PHI(MP1,ND2)+PHI(M,ND2)+PHI(MP1,NP2D2)
     1+PHI(MP2,ND2))/4.
      PHID=(PHI(M,ND2)+PHI(MM1,NP2D2)+PHI(M,NP2D2)
     1+PHI(MP1,NP2D2))/4.
      PHIA=PHI(M,ND2)
      PHIC=PHI(MP1,NP2D2)
 1110 IF(INDB.EQ.1) GO TO 1120
      IF(M.LT.NROW-1.AND.N.LT.NCOL*2-2) GO TO 1120
      IF(INDG.EQ.2) GO TO 1130
      IF(M.NE.NROW-1) GO TO 1140
      IF((N/2)*2.NE.N) PHIC=0.
      IF((N/2)*2.EQ.N) PHIB=0.
 1140 IF(N.NE.NCOL*2-2) GO TO 1120
      IF((M/2)*2.NE.M) PHIC=0.
      IF((M/2)*2.EQ.M) PHID=0.
      GO TO 1120
 1130 IF(M.NE.NROW-1) GO TO 1150
      IF((N/2)*2.NE.N) PHIB=0.
      IF((N/2)*2.EQ.N) PHIC=0.
 1150 IF(N.NE.2*NCOL-1) GO TO 1120
      IF((M/2)*2.NE.M) PHID=0.
      IF((M/2)*2.EQ.M) PHIC=0.
 1120 IF(M.NE.1) GO TO 1200
      IF(N.NE.2*BN-1) GO TO 1210
      CALL PARAE(BN,N,INDPAR,PHID,OM,R,NCT2M1,
     1NRW,NCL,PEI)
 1210 IF(N.NE.2*BN) GO TO 1200
      CALL PARAE(BN,N,INDPAR,PHIA,OM,R,NCT2M1,
     1NRW,NCI,PEI)
 1200 RETURN
      END
C
C  SUBROUTINE ZMOI
C
      SUBROUTINE ZMOI(TT,CTT,GAM,OGAM,M,N,
     1NRWM1,NCT2M2,G,IVC)
      COMMON AI,TY,GC,RR
      DIMENSION CTT(NRWM1,NCT2M2),OGAM(NRWM1,NCT2M2),G(NRWM1,NCT2M2),
```

```
     1UPP(126,140),IVC(NBWM1,NCT2M2),IC(126,140),
     2YM(7,126,140)
      GV(DY)=1./(1.+RR*AI*ABS(DY)**(RR-1.))
      GRC(DY,DYC)=1./(1.+RR*AI*ABS((DY-DYC)/2.)**(RR-1.))
      T=TT/TY
      OT=OTT(M,N)/TY
      IF(IVC(M,N).EQ.0) GO TO 30
      IF(ABS(GAM).LT.ABS(OGAM(M,N))) GO TO 20
   10 G(M,N)=GC*GV(T)
      IC(M,N)=0
      RETURN
   20 IVC(M,N)=0
      UPP(M,N)=1.
      IF(GAM.LT.OGAM(M,N)) UPP(M,N)=-1.
      IC(M,N)=2
      YM(1,M,N)=-CT
      YM(2,M,N)=CT
      G(M,N)=GC*GRC(T,CT)
  120 RETURN
   30 IF(ABS(T).GE.ABS(YM(1,M,N))) GO TO 45
      IF(UPP(M,N)*(GAM-CGAM(M,N)).GE.0.) GO TO 50
      UPP(M,N)=1.
      IF(GAM.LT.OGAM(M,N)) UPP(M,N)=-1.
      IC(M,N)=IC(M,N)+1
      IF(IC(M,N).GT.6) IC(M,N)=5
      IF(UPP(M,N)*(T-YM(IC(M,N)-1,M,N)).GT..0) GO TO 60
      YM(IC(M,N),M,N)=CT
   40 G(M,N)=GC*GRC(T,YM(IC(M,N),M,N))
  160 RETURN
   45 IVC(M,N)=1
      IF(ABS(GAM).LT.ABS(OGAM(M,N))) GO TO 20
      GO TO 10
   50 IF(UPP(M,N)*(T-YM(IC(M,N)-1,M,N)).LT.0.) GO TO 40
   60 IC(M,N)=IC(M,N)-2
      IF(IC(M,N).EQ.1) IC(M,N)=2
      IF(IC(M,N).EQ.2) GO TO 40
      IF(IC(M,N).EQ.0) GO TO 45
      GO TO 50
      END
C
C  SUBROUTINE RMOD
C
      SUBROUTINE RMOD(TT,OTT,GAM,OGAM,M,N,
     1NBWM1,NCT2M2,G,IVC)
      COMMON AI,TY,GC,RR
      DIMENSION CTT(NBWM1,NCT2M2),OGAM(NBWM1,NCT2M2),G(NBWM1,NCT2M2),
     1UPP(126,140),IVC(NBWM1,NCT2M2),IC(126,140),
     2YM(7,126,140)
      GV(DY)=1./(1.+RR*AI*ABS(DY)**(RR-1.))
      GRC(DY,DYC)=1./(1.+RR*AI*ABS((DY-DYC)/2.)**(RR-1.))
      T=TT/TY
      CT=OTT(M,N)/TY
      IF(IVC(M,N).EQ.0) GO TO 30
```

```
      IF(ABS(GAM).LT.ABS(OGAM(M,N))) GO TO 20
   10 G(M,N)=GC*GV(I)
      IC(M,N)=0
      RETURN
   20 IVC(M,N)=0
      UPP(M,N)=1.
      IF(GAM.LT.OGAM(M,N)) UPP(M,N)=-1.
      IC(M,N)=2
      YM(1,M,N)=-CI
      YM(2,M,N)=CI
      G(M,N)=GC*GRC(I,CI)
      RETURN
   30 IF(ABS(I).GE.ABS(YM(1,M,N))) GO TO 45
      IF(UPP(M,N)*(GAM-CGAM(M,N)).GE.0.) GO TO 50
      UPP(M,N)=1.
      IF(GAM.LT.OGAM(M,N)) UPP(M,N)=-1.
      IC(M,N)=IC(M,N)+1
      IF(IC(M,N).GT.6) IC(M,N)=5
      IF(UPP(M,N)*(I-YM(IC(M,N)-1,M,N)).GT..0) GO TO 60
      YM(IC(M,N),M,N)=CI
   40 G(M,N)=GC*GRC(I,YM(IC(M,N),M,N))
      RETURN
   45 IVC(M,N)=1
      IF(ABS(GAM).LT.ABS(OGAM(M,N))) GO TO 20
      GO TO 10
   50 IF(UPP(M,N)*(I-YM(IC(M,N)-1,M,N)).LT.0.) GO TO 40
   60 IC(M,N)=IC(M,N)-2
      IF(IC(M,N).EQ.1) IC(M,N)=2
      IF(IC(M,N).EQ.2) GO TO 40
      IF(IC(M,N).EQ.0) GO TO 45
      GO TO 50
      END
C
C  SUBROUTINE CCEFF
C
      SUBROUTINE CCEFF(M,N,GRI,GZI,NRW,NCL,RHO,R,DZR,
     1Z,CI,V,IB,IZ,PDR,GZS,NRWM1,NCI2M2,NCI2M1
     2,NROW,NCCI,INDB,INDG,RN,INDPAR,CM)
      INTEGER RN
      DIMENSION GRI(NRWM1,NCI2M2),GZI(NRWM1,NCI2M2),Z(NRW)
     1,V(NRW,NCI),IB(NRW,NCL),IZ(NRW,NCL)
     2,PDR(NRW,NCI),R(NCI2M1)
      COMMON/CCCEFF/A1,B1,C1,D1,E1,A3,B3,C3,D3,E3,
     1A5,B5,C5,D5,E5,A7,B7,C7,D7,E7
      MP1=M+1
      MM1=M-1
      NI2M2=2*N-2
      NI2M1=2*N-1
      NI2=2*N
      NI2P1=2*N+1
      IF((M/2)*2.EQ.M) GO TO 1000
      BP=R(NI2M1)
      IF(M*N.EQ.1) GO TO 1010
```

```
      IF(M.EQ.1) GO TO 1030
      IF(N.EQ.1) GO TO 1010
      CALL SHFUN(MM1,NT2M2,NT2M1,M,NT2M1,M,MM1,NT2M2,
     1NRWM1,NCT2M2,NCT2M1,NBW,NCL,DZR,DT,V,TR,TZ,PDR,VA,
     2TRA,TZA,PDRA,GRT,GZS,GZT,RHO,R,Z,-1,-1,RAP,ZAP
     3,VSRAP,VSZAP,GZSAP,NBOW,NCOL,INDB,INDG,RN,INDPAR,OM)
 1030 CALL SHFUN(M,NT2M2,NT2M1,M,NT2M1,MP1,M,NT2M2,NRWM1,
     1NCT2M2,NCT2M1,NBW,NCL,DZR,DT,V,TR,TZ,PDR,VB,TRB,
     2TZB,PDRB,GRT,GZS,GZT,RHO,R,Z,-1,1,RBP,ZBP
     3,VSREP,VSZBP,GZSBP,NBOW,NCOL,INDB,INDG,RN,INDPAR,OM)
 1010 CALL SHFUN(M,NT2M1,NT2M1,M,NT2,MP1,M,NT2M1,NRWM1,
     1NCT2M2,NCT2M1,NRW,NCL,DZR,DT,V,TR,TZ,PDR,VC,TRC,TZC,
     2PDRC,GRT,GZS,GZT,RHO,R,Z,1,1,RCP,ZCP
     3,VSRCP,VSZCP,GZSCP,NBOW,NCOL,INDB,INDG,RN,INDPAR,OM)
      IF(M*N.EQ.1) GO TO 1020
      IF(M.EQ.1) GO TO 1040
      CALL SHFUN(MM1,NT2M1,NT2M1,M,NT2,M,MM1,NT2M1,NRWM1,
     1NCT2M2,NCT2M1,NRW,NCL,DZR,DT,V,TR,TZ,PDR,VD,TRD,TZD,
     2PDRD,GRT,GZS,GZT,RHO,R,Z,1,-1,RDP,ZDP
     3,VSRDP,VSZDP,GZSDP,NBOW,NCOL,INDB,INDG,RN,INDPAR,OM)
      IF(N.EQ.1) GO TO 1020
      GO TO 1050
 1000 BP=R(NT2)
      CALL SHFUN(MM1,NT2M1,NT2,M,NT2,M,MM1,NT2M1,NRWM1,
     1NCT2M2,NCT2M1,NRW,NCL,DZR,DT,V,TR,TZ,PDR,VA,TRA,TZA,
     2PDRA,GRT,GZS,GZT,RHO,R,Z,-1,-1,RAP,ZAP
     3,VSRAP,VSZAP,GZSAP,NBOW,NCOL,INDB,INDG,RN,INDPAR,OM)
      CALL SHFUN(M,NT2M1,NT2,M,NT2,MP1,M,NT2M1,NRWM1,
     1NCT2M2,NCT2M1,NBW,NCL,DZR,DT,V,TR,TZ,PDR,VB,TRB,TZB,
     2PDRB,GRT,GZS,GZT,RHO,R,Z,-1,1,RBP,ZBP
     3,VSREP,VSZBP,GZSBP,NBOW,NCOL,INDB,INDG,RN,INDPAR,OM)
      CALL SHFUN(M,NT2,NT2,M,NT2P1,MP1,M,NT2,NRWM1,
     1NCT2M2,NCT2M1,NRW,NCL,DZR,DT,V,TR,TZ,PDR,VC,TRC,
     2TZC,PDRC,GRT,GZS,GZT,RHO,R,Z,1,1,RCP,ZCP
     3,VSRCP,VSZCP,GZSCP,NBOW,NCOL,INDB,INDG,RN,INDPAR,OM)
      CALL SHFUN(MM1,NT2,NT2,M,NT2P1,M,MM1,NT2,NRWM1,
     1NCT2M2,NCT2M1,NBW,NCL,DZR,DT,V,TR,TZ,PDR,VD,TRD,
     2TZD,PDRD,GRT,GZS,GZT,RHO,R,Z,1,-1,RDP,ZDP
     3,VSRDP,VSZDP,GZSDP,NBOW,NCOL,INDB,INDG,RN,INDPAR,OM)
 1050 A3=2.-RAP/RP
      B3=VSRAP/VSZAP+RHO*VSRAP*VSZAP*(1.-RAP/RP)/
     1(2.*GZSAP)
      C3=-RHO*VSRAP*(1.+RAP/RP)/2.
      D3=-VSRAP*(RP-RAP)/VSZAP
      E3=(2.-RP/RAP)*TRA+(VSRAP/VSZAP-RHO*VSRAP*
     1VSZAP*(RP/RAP-1.)/(2.*GZSAP))*TZA-RHO*VSRAP
     2*(1.+RP/RAP)*VA/2.+VSRAP*(RP-RAP)*PDRA/VSZAP
 1040 A1=2.-REP/RP
      B1=-VSREP/VSZBP-RHO*VSRBP*VSZBP*(1.-RBP/RP)/
     1(2.*GZSBP)
      C1=RHO*VSRBP*(-1.-RBP/RP)/2.
      D1=VSREP*(RP-REP)/VSZBP
      E1=(2.-RP/RBP)*TRB-(VSRBP/VSZBP-RHO*VSRBP*
     1VSZBP*(RP/REP-1.)/(2.*GZSBP))*TZB-RHO*VSRBP
```

```
     2*(1.+RP/REP)*VE/2.-VSRBE*(RP-REP)*PDRB/VSZBP
 1020 A7=2.-RCE/EE
      E7=VSRCE/VSZCP+RHO*VSRCE*VSZCP*(1.-RCP/RP)/
     1(2.*GZSCE)
      C7=RHO*VSRCE*(1.+RCP/RP)/2.
      D7=-VSRCE*(RP-RCP)/VSZCE
      E7=(2.-EE/RCE)*TRC+(VSRCP/VSZCE-RHO*VSRCE*
     1VSZCP*(RP/RCP-1.)/(2.*GZSCP))*TZC+RHO*VSRCP
     2*(1.+RP/ECE)*VC/2.+VSRCE*(RP-RCP)*PDRC/VSZCP
      IF(M.EQ.1) RETURN
      A5=2.-RDE/EE
      B5=-VSRDE/VSZDP-RHO*VSRDE*VSZDE*(1.-RDP/RP)/
     1(2.*GZSDE)
      C5=RHO*VSRDE*(1.+RDP/RP)/2.
      D5=VSRDP*(RP-RDP)/VSZDP
      E5=(2.-EE/RDE)*TRD-(VSRDP/VSZDE-RHO*VSRDE*
     1VSZDE*(EE/RDE-1.)/(2.*GZSDE))*TZD+RHO*VSRDP
     2*(1.+RP/RDE)*VD/2.-VSRDE*(RP-RDE)*PDRD/VSZDP
      RETURN
      END
C  SUBROUTINE SEFUN
C
      SUBROUTINE SEFUN(I,J,K,L,II,JJ,KK,LL,NRWM1,
     1NCT2M2,NCT2M1,NRW,NCL,DZR,DT,V,TR,TZ,PDR,VE,
     2TRE,TZE,PDRE,GRT,GZS,GZT,RHO,R,Z,INDR,INDZ,RP,ZP
     3,VSRE,VSZE,GZSP,NRCW,NCCL,INDB,INDG,RN,INDPAR,CM)
      INTEGER RN
      REAL NA,NB,NC,ND
      DIMENSION GRT(NRWM1,NCT2M2),
     1GZT(NRWM1,NCT2M2),R(NCT2M1),Z(NRW),V(NRW,NCL),
     2TR(NRW,NCL),TZ(NRW,NCL),PDR(NRW,NCL)
      SFVAL(TVA)=(NA*TVA+NB*TVB+NC*TVC+ND*TVD)/DZR
      GZSP=GZS
      IF(I.GT.2) GO TO 100
      IF(J.LT.16.OR.J.GT.17) GO TO 100
      GZSP=.0001*GZS
  100 VSRP=SQRT(GRT(I,J)/RHO)
      VSZP=SQRT(GZT(I,J)/RHO)
      RP=R(K)+VSRP*DT*INDR
      ZP=Z(L)+VSZP*DT*INDZ
      NA=(RP-R(II))*(ZP-Z(JJ))
      NB=-(RP-R(II))*(ZP-Z(KK))
      NC=(RP-R(II))*(ZP-Z(KK))
      ND=-(RP-R(II))*(ZP-Z(JJ))
      INDPAR=3
      CALL NDIPRI(TVA,TVB,TVC,TVD,V,I,J,NRW,NCL
     1,NRCW,NCCL,INDB,INDG,RN,INDPAR,CM,R,NCT2M1)
      VE=SFVAL(TVA)
      INDPAR=1
      CALL NDIPRI(TVA,TVB,TVC,TVD,TR,I,J,NRW,NCL
     1,NRCW,NCCL,INDB,INDG,RN,INDPAR,CM,R,NCT2M1)
      TRE=SFVAL(TVA)
      INDPAR=2
```

```
      CALL NDLPEI(IVA,IVE,IVC,IVD,IZ,I,J,NRW,NCL
     1,NBCW,NCCI,INDE,INDG,RN,INDPAR,CM,R,NCT2M1)
      IZE=SFVAI(IVA)
      INDPAR=4
      CALL NDLPEI(IVA,IVE,IVC,IVD,PDR,I,J,NRW,NCL
     1,NBCW,NCCI,INDE,INDG,RN,INDPAR,CM,R,NCT2M1)
      PDRE=SFVAI(IVA)
      RETURN
      END
C
C   SUBROUTINE ENERGY
C
      SUBROUTINE ENERGY(E,N,AMCMP,CMP,AMCM,CM,DT,T,
     1WORK,XMI,TIE,GMR,TIZ,GMZ,TRAVE,TZAVE,GMRAVE,
     2GMZAVE,NRWM1,NCT2M2,PEPHI,RHO,VAVE,DVOL,ENKE,DISCKE,
     3EMCMP,EMCM,ESWORK,ISLIP,RN,UO,TZ,R,
     4NCT2M1,A,SIWORK,NRW,NCL,U)
      INTEGER RN
      DIMENSION TRAVE(NRWM1,NCT2M2),TZAVE(NRWM1,NCT2M2),
     1GMZAVE(NRWM1,NCT2M2),GMRAVE(NRWM1,NCT2M2),DVOL(NCT2M2)
     2,ISLIP(RN),UO(RN),TZ(NRW,NCL),R(NCT2M1),A(RN)
     3,U(NRW,NCI)
      IF(E**N.NE.1) GO TO 1000
      DWORK=.5*(AMCMI*CMP+AMCM*CM)*DT
      DESWOR=.5*((-EMCMP)*CMP+(-EMCM)*CM)*DT
      WORK=WORK+DWORK
      ESWORK=ESWORK+DESWOR
      DISCKE=.5*XMI*(CMP**2)
      DO 1030 I=2,RN
      IF(ISLIP(I).EQ.0) GO TO 1030
      DFTDIS=(CMP+CM)*R(2*I-1)*DT/2.
      SIWORK=SIWORK+((U(1,I)-UO(I))-DFTDIS)*TZ(1,I)*A(I)
 1030 CONTINUE
      TMDT=T-DT
 1000 DPEPHL=.5*((TIR+TRAVE(M,N))*(GMR-GMRAVE(M,N))+
     1(TIZ+TZAVE(M,N))*(GMZ-GMZAVE(M,N)))*DVOL(N)
      PEPEL=PEPEL+DPEPHL
      DENKE=.5*EMC*(VAVE**2)*DVOL(N)
      ENKE=ENKE+DENKE
      RETURN
      END
C
C   SUBROUTINE PARAB
C
      SUBROUTINE PARAB(RN,N,INDPAR,PHIE,CM,R,NCT2M1,
     1NRW,NCL,PEI)
      INTEGER RN
      DIMENSION R(NCT2M1),PHI(NRW,NCI)
      A(R1)=(Y1*(R2-R3)+Y2*(R3-R1)+Y3*(R1-R2))/
     1((R1**2)*(R2-R3)+(R2**2)*(R3-R1)+(R3**2)*(R1-R2))
      B(R1)=(Y2-Y3-A(R1)*((R2**2)-(R3**2)))/(R2-R3)
      C(R1)=Y1-A(R1)*(R1**2)-B(R1)*R1
      IF(N.EQ.2*RN) GO TO 100
```

```
      IF(INDPAR.NE.1) GO TO 110
      PHIE=0.
      RETURN
  110 IF(INDPAR.NE.3) GO TO 115
      PHIE=OM*E(2*RN)
      RETURN
  115 IF(INDPAR.NE.5) GO TO 120
      PHIE=PHI(1,RN)+.5*(PHI(1,RN)-PHI(1,RN-1))
      RETURN
  120 R1=R(2*RN-5)
      R2=R(2*RN-3)
      R3=R(2*RN-1)
      Y1=PHI(1,RN-2)
      Y2=PHI(1,RN-1)
      Y3=PHI(1,RN)
      PHIE=A(R1)*(R(2*RN)**2)+B(R1)*R(2*RN)+C(R1)
      RETURN
  100 IF(INDPAR.NE.2.AND.INDPAR.NE.4) GO TO 140
      PHIE=0.
      RETURN
  140 IF(INDPAR.NE.3) GO TO 145
      PHIE=OM*E(2*RN)
      RETURN
  145 IF(INDPAR.NE.5) GO TO 150
      PHIE=PHI(1,RN)+.5*(PHI(1,RN)-PHI(1,RN-1))
      RETURN
  150 R1=R(2*RN+1)
      R2=R(2*RN+3)
      R3=R(2*RN+5)
      Y1=PHI(1,RN+1)
      Y2=PHI(1,RN+2)
      Y3=PHI(1,RN+3)
      PHIE=A(R1)*(R(2*RN)**2)+B(R1)*R(2*RN)+C(R1)
      RETURN
      END
```

BIBLIOGRAPHY

BIBLIOGRAPHY

Butler, D.S. (1960), "The Numerical Solution of Hyperbolic Systems of Partial Differential Equations in Three Independent Variables," Proceedings of the Royal Society of London, Series A, Vol. 255, pp. 232-252.

Chon, C. (1977), "Dynamic Response of Friction Piles," Ph.D. Dissertation, University of Michigan, 212 pp.

Dally, J.W., Riley, W.F. (1978), Experimental Stress Analysis, McGraw-Hill, New York.

Dobrin, M.B. (1960), Introduction to Geophysical Prospecting, McGraw-Hill, New York.

Drnevich, V.P., Hall, J.R., Jr., and Richart, F.E., Jr. (1965), "Transient Loading Tests on a Rigid Circular Footing," Report No. 3-146 prepared at the University of Michigan under contract No. DA-22-079-ENG-340 for the U.S. Army Engr. Waterways Experiment Sta., Vicksburg, Miss.

Fox, L. (1962), Numerical Solution of Ordinary and Partial Differential Equations, Pergamon Press; Addison-Wesley Publishing Co., Inc., pp. 366-377.

Gallagher, R.H. (1975), "Finite Element Analysis Fundamentals," Prentice-Hall, Inc., Englewood Cliffs, N.J., 420 pp.

Hardin, B.O., and Drnevich, V.P. (1972a), "Shear Modulus and Damping in Soils: Measurement and Parameter Effects," J. Soil Mech. and Found. Div. Proc. ASCE, Vol. 98, No. SM6, June, pp. 603-624.

Hardin, B.O., and Drnevich, V.P. (1972b), "Shear Modulus and Damping in Soils: Design Equations and Curves," J. Soil Mech. and Found. Div. Proc. ASCE, Vol. 98, No. SM7, July, pp. 667-692.

Kolsky, H. (1963), "Stress Waves in Solids," Dover Publications, Inc., New York, New York.

Lai, C. (1977), "Computer Simulation of Two-Dimensional Unsteady Flows in Estuaries and Embayments by the Method of Characteristics--Basic Theory and the Formulation of the Numerical Method," Report No. USGS/WRI 77-85 for the U.S. Geological Survey, Reston, Virginia.

Papadakis, C.N., Streeter, V.L., and Wylie, E.B. (1974), "Bedrock Motions Computed from Surface Seismograms," J. Geotechnical Eng. Div. Proc. ASCE, Vol. 100, No. GT10, Oct., pp. 1091-1106.

Papadakis, C.N., and Wylie, E.B. (1975), "Seismic Shear Wave Propagation through Earth Dams," Soils and Foundations, Vol. 15, No. 2, June, pp. 47-61.

Reissner, E. (1937), "Freie und erzwungene Torsionschwingungen des elastischen Halbraumes," Ingenieur-Archiv, Vol. 8, No. 4, pp. 229-245.

Reissner, E., and Sagoci, H.F. (1944), "Forced Torsional Oscillations of an Elastic Half-Space. I," J. of Appl. Phys., Vol. 15, pp. 652-654.

Richardson, D.J. (1964), "Solutions of Two-Dimensional Hydrodynamic Equations by the Method of Characteristics," Methods in Computational Physics, Vol. 3, Alder, B., Fernbach, S., and Rotenberg, M., eds., Academic Press, New York, pp. 295-318.

Richart, F.E., Jr. (1975), Some Effects of Dynamic Soil Properties on Soil-Structure Interaction, The 10th Terzaghi Lecture, ASCE, Report of Civil Eng. Dep't, Univ. of Michigan, UMEE-75RI, April, 1975, pp. 1-81.

Richart, F.E., Jr. (1977), "Dynamic Stress-Strain Relationships for Soils," Soil Dynamics and its Application to Foundation Engineering, State-of-the-Art Report IX ICSMFE, Tokyo, 1977, pp. 605-612.

Richart, F.E., Jr., Hall, J.R., Jr., and Woods, R.D. (1970), Vibrations of Soils and Foundations, Prentice-Hall, Englewood Cliffs, N.J., 414 pp.

Richart, F.E., Jr., and Wylie, E. B. (1975), "Influence of Dynamic Soil Properties on Response of Soil Masses," Symp. Struc. and Geotech. Mech., U. of Ill., Urbana, Ill., Oct. 2-5.

Sagoci, H.F. (1944), "Forced Torsional Oscillations of an Elastic Half-Space. II," J. of Appl. Phys., Vol. 15, pp. 655-662.

Shin, Y.W., and Valentin, R.A. (1978), "A Numerical Method Based on the Method of Characteristics for Two-Dimensional Fluid Transients," Presented at ASME/CSME Pressure Vessels and Piping Conference, Montreal, Canada, June 25-30, 1978.

Streeter, V.L., Wylie, E.B., and Richart, F.E., Jr. (1974), "Soil Motion Computations by Characteristic Method," J. Geotechnical Eng. Div. Proc. ASCE, Vol. 100, No. GT3, March, pp. 247-263.

Terzaghi, K. (1943), "Theoretical Soil Mechanics," J. Wiley and Sons, Inc., New York.

Wylie, E.B., and Henke, R. (1979), "Nonlinear Soil Dynamics by Characteristics Method," Proceedings on 2nd U.S. National Conference on Earthquake Engineering, EERI, Stanford University, Aug. 22-24, 1979, pp. 563-572.

Wylie, E.B., and Streeter, V.L. (1978), "Fluid Transients," McGraw-Hill Book Co., New York.

Wylie, E.B., Streeter, V.L., Papadakis, C.N., and Richart, F.E., Jr. (1974), "Transient Two-Dimensional Analysis of Soils by Lattice-Work Method, Lopez Dam Case Study," The University of Michigan, Dept. of Civil Engineering, Report UMEE-74R3, Oct., 1974.

Woods, R.D. (1978), "Measurement of Dynamic Soil Properties," Proceedings of the ASCE Geotechnical Engineering Division Specialty Conference, Volume 1, Pasadena, Ca., June 19-21, 1978.

Zienkiewicz, O.C. (1971), "The Finite Element Method in Engineering Science," McGraw-Hill Book Co., New York, New York, 521 pp.

Ziv, M. (1969), "Two-Spatial Dimensional Elastic Wave Propagation by the Theory of Characteristics," Intern. J. Solids Struct., Vol. 5, pp. 1135 to 1151.